XDC 60-6-70

AIRCRAFT NUCLEAR PROPULSION DEPARTMENT

TID-6302

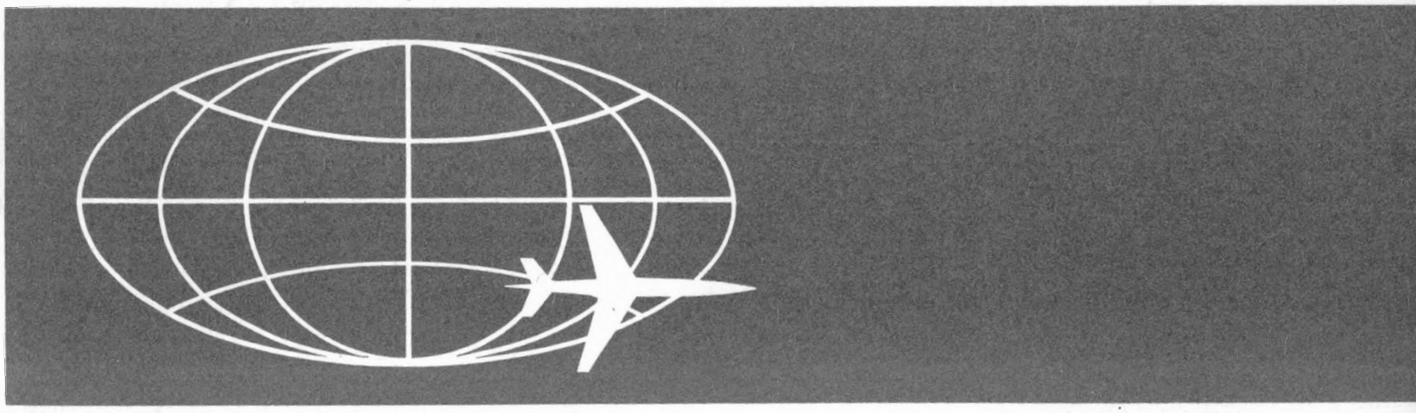

PAPERS FROM SEVENTH SEMIANNUAL SHIELDING INFORMATION MEETING OCTOBER 14-15, 1959

GENERAL ELECTRIC

PAPERS FROM SEVENTH SEMIANNUAL SHIELDING INFORMATION MEETING OCTOBER 14-15, 1959

Sponsored By
Air Research and Development Command
(U.S. Air Force)

and
Aircraft Nuclear Propulsion Office
United States Atomic Energy Commission

Host
Aircraft Nuclear Propulsion Division
General Electric Company

GENERAL ELECTRIC
AIRCRAFT NUCLEAR PROPULSION DEPARTMENT
Cincinnati 15, Ohio

CONTENTS

1. A METHOD FOR COMPUTING A GENERALIZED EFFECTIVE FAST NEUTRON REMOVAL CROSS SECTION

K. B. Hanchon

General Electric Company
Aircraft Nuclear Propulsion Department
Evendale, Ohio

A METHOD FOR COMPUTING A GENERALIZED EFFECTIVE FAST NEUTRON REMOVAL CROSS SECTION

by

K. B. Hanchon

General Electric Company
Aircraft Nuclear Propulsion Department
Evendale, Ohio

An analytical method for computing a generalized effective neutron removal cross section is discussed. Such a cross section would be a function of backing material and source-receiver distance, and would be specifically oriented toward a slab geometry. Discussion of results obtained from the method are presented.

The point kernel approach to the calculation of dose rates at a point is based on the assumption that the dose rate from an isotropic point source in an infinite medium may be calculated by finding an attenuation function along a source-receiver path. The dose rate from a volume distributed source is then considered to be the integrated dose rate from an assembly of point sources. Slab geometry effects have generally been taken into account by making the parameters of the kernel fit to data, for example, BSR data.

Suppose that we have a hydrogen point kernel, or, as it is sometimes called, an influence function which is capable of calculating the total response of a fast neutron detector at a point, integrated over all source energies, and such that the effects of nonhydrogenous material may be expressed by the exponential

$$\exp\left(\left\{-\rho\sum_{i=1}^{M}\theta_i\,\Sigma_i\right\}\right)$$

of a sum (where ρ is the source-receiver distance, θ_i is the probability of seeing the material along the path length, and Σ_i is the macroscopic fast neutron removal cross section). Geometric attenuation is represented by $1/4\pi\rho^2$ (giving an expression of the form

$$\frac{G(\rho)\exp\left\{-\rho\sum_{i=1}^{M}\theta_i\,\Sigma_i\right\}}{4\pi\rho^2}\Bigg)$$

This model implies that the effects of nonhydrogenous materials are energy-independent, additive, and commutative.

As an example of such a function, the Albert Welton point kernel combines a theoretical hydrogen cross section with an integration over an experimentally determined fission spectrum to obtain the uncollided neutron flux as a function

of penetration distance. The attenuation effects of materials other than hydrogen are included by assuming exponential attenuation and treating the cross sections as energy independent parameters to be determined by a fit to data.

Having once determined the parameters of the hydrogenous material, the fast neutron removal cross sections of the other materials are determined from the effect on the dose rate along a lid tank source plate centerline combining a slab of material whose cross section is unknown with a given thickness of water, when the dose rate behind that thickness of water is known.

This effect has usually been calculated at distances greater than one hundred centimeters from the source plate, partly to simplify the computations, partly because fast neutron dose rates are usually obtained for the purpose by conversion from thermal neutron fluxes, which do not reach equilibrium with fast neutron dose rates at less than considerable distances from the source.

We should like to have a parameter to express the attenuation of nonhydrogenous materials which makes as few assumptions as possible about the range of validity of any of the expressions involved, or the slope of the dose rate curves at any point. If we used the Moments Method results, for example, to get a hydrogen kernel, we might find that the cross sections become slowly varying functions. The problem involves using the dose rate from a volume distributed source to determine a parameter to be used in a point-to-point attenuation function.

Let us combine the point kernel

$$\frac{G(\rho)\ \exp\left\{-\rho \sum_{i=1}^{M} \theta_i\ \Sigma_i\right\}}{4\pi\rho^2}$$

with a function $S(\vec{\rho})$ which expresses the spatial distribution of the source, and integrates over the source volume. Then the total fast neutron dose rate may be represented by

$$D_n = \int_{\substack{\text{source}\\ \text{volume}}} \frac{S(\vec{\rho})\ G(\rho)\ \exp\left\{-\rho \sum_{i=1}^{M} \theta_i\ \Sigma_i\right\}}{4\pi\rho^2}\, dV_s$$

if, of course, the other entires are given in appropriate units. Here we intend to use this kernel as a model for the effect at the detector of a unit concentrated cause at the source and to determine a macroscopic removal cross section of the unknown material, to be called the M^{th} material for convenience, by determining the corresponding parameter in the influence function.

The method reported here uses a generalized mean value theorem. In its full generalization, this theorem holds for functions which are integrable in the Lebesgue sense. For all practical purposes, however, we may restrict ourselves to continuous functions. The theorem status: $f(x)$ and $p(x)$ are continuous functions in $a \leq x \leq b$, and $p(x) \geq 0$, then

$$\int_a^b f(x)\, p(x)\, dx = f(\xi) \int_a^b p(x)\, dx$$

where $a \leq \xi \leq b$

In the case of a lid tank source plate, the dose rate D_n at a fixed distance k, from the source plate takes the form

$$D_n = 2\pi \int_{r_{sl}}^{r_{su}} \frac{r_s\, S(\vec{\rho})\, G(\rho) \exp\left\{-\rho \sum_{i=1}^{M} \theta_i\, \Sigma_i\right\}}{4\pi\rho^2}\, dr_s$$

The geometry of the situation is shown in Figure 1.

Making appropriate substitutions in the mean value theorem enables us to calculate the number of relaxation lengths through any subset of the set of materials in a path from the source to the detector which is, in some sense, an average path. The source plate is effectively reduced to a circle of point sources with cylindrical symmetry. For example, the number of relaxation lengths of the unknown material can be deduced from

$$D_n = \frac{\exp\,(-\Sigma_M\, \theta_M\, \bar{\rho})}{2} \int_{r_{sl}}^{r_{su}} \frac{r_s\, S(\vec{\rho})\, G(\rho) \exp\left\{-\rho \sum_{i=1}^{M-1} \theta_i\, \Sigma_i\right\}}{\rho^2}\, dr_s$$

where $k \leq \bar{\rho} \leq +(k^2 + r_{sl}^2)^{\frac{1}{2}}$. From this, we can solve for $(\Sigma_M\, \theta_M\, \bar{\rho})$

$$\Sigma_M\, \theta_M\, \bar{\rho} = -\ln \frac{2\, D_n}{\int_{r_{sl}}^{r_{su}} \frac{r_s\, S(\vec{\rho})\, G(\rho) \exp\left\{-\rho \sum_{i=1}^{M-1} \theta_i\, \Sigma_i\right\}}{\rho^2}\, dr_s}$$

By similar reasoning, the total number of relaxation lengths through all materials along $\bar{\rho}$ is

$$\bar{\rho} \sum_{i=1}^{M} \theta_i\, \Sigma_i = -\ln \frac{2\, D_n}{\int_{r_{sl}}^{r_{su}} \frac{r_s\, S(\vec{\rho})\, G(\rho)}{\rho^2}\, dr_s}$$

This procedure gives two simultaneous equations in the unknowns Σ_M and $\bar{\rho}$, so that we are able to solve for the desired parameter Σ_M.

The theorem and the method generalize readily to the three dimensional case, except that another equation is required, since the location of the "average" source point must be located in a three dimensional space, rather than merely on a plane.

This procedure was applied to an experimental configuration measured in the Oak Ridge Lid Tank under the direction of R. W. Peele and reported in CF 57-2-8 and DC 57-3-99. The configuration was 3 inches of lead backed by transformer oil.

ast neutron dose rates were measured along the source plate centerline. The alculated cross sections, using the Albert-Welton influence function as a odel, were

Z	Materials Seen	Removal Cross Section
30 cm	7.62 cm Pb + 22.38 cm Oil	.083
40 cm	7.62 cm Pb + 32.38 cm Oil	.096
50 cm	7.62 cm Pb + 42.38 cm Oil	.106
70 cm	7.62 cm Pb + 62.38 cm Oil	.106
80 cm	7.62 cm Pb + 72.38 cm Oil	.118
90 cm	7.62 cm Pb + 82.38 cm Oil	.126

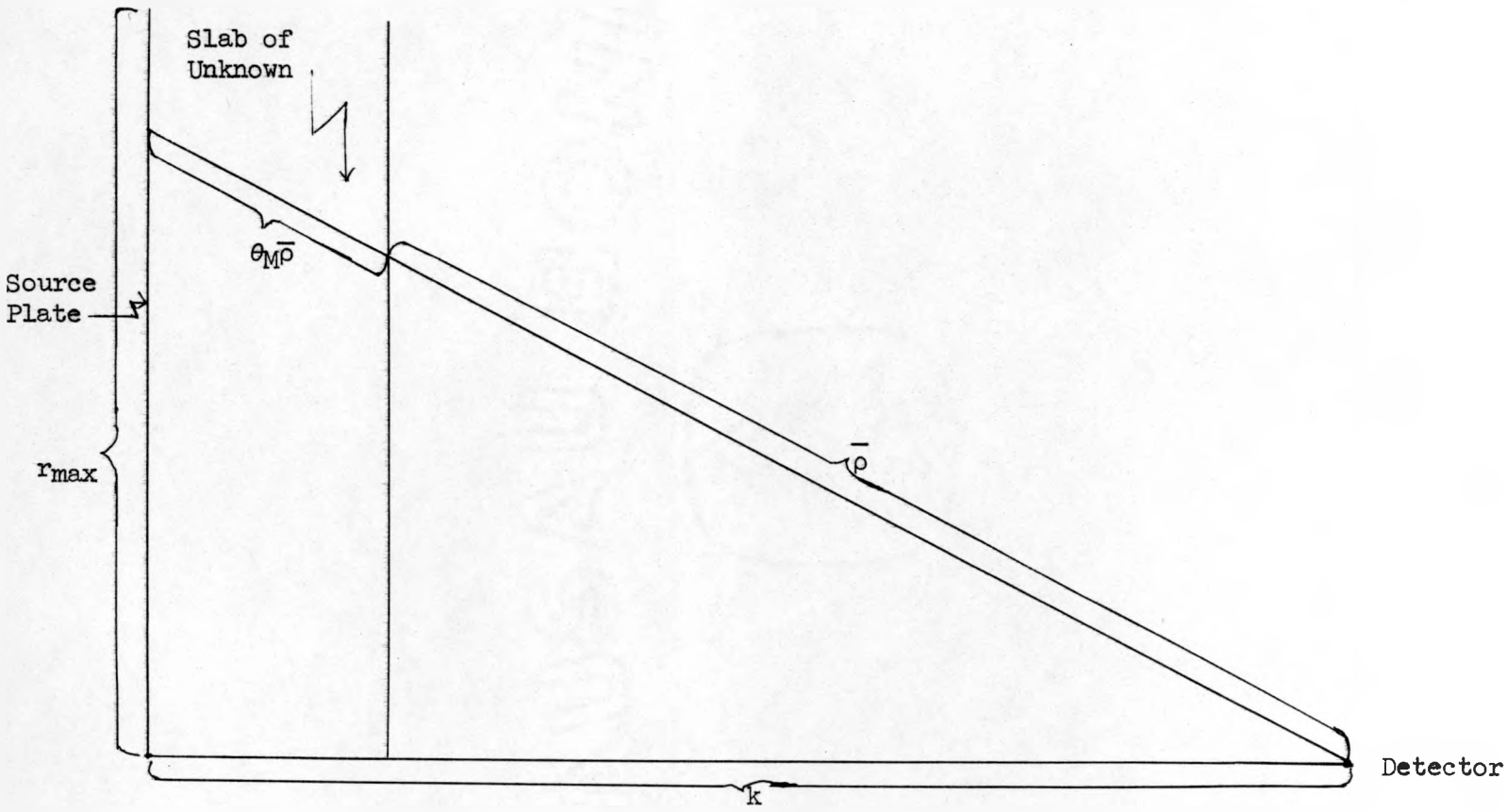
Slab of
Unknown
$\theta_M\bar{\rho}$
Source
Plate
r_{max}
$\bar{\rho}$
Detector
k

FIGURE 1

2. A MONTE CARLO PROGRAM FOR AIR-SCATTERED NEUTRONS

J. E. MacDonald
A. Trampus

General Electric Company
Aircraft Nuclear Propulsion Department
Evendale, Ohio

A MONTE CARLO PROGRAM FOR AIR-SCATTERED NEUTRONS

by

J. E. MacDonald
A. Trampus

General Electric Company
Aircraft Nuclear Propulsion Department
Evendale, Ohio

This paper is devoted to a description of the application of the Monte Carlo method in the calculation of the energy and angular distribution of neutrons scattered in air. The events considered are: isotropic elastic scattering, anisotropic elastic scattering, inelastic scattering, radiative capture, and absorption without subsequent particle emission. Gamma rays born during the course of a neutron problem are recorded for future use in a gamma air-scattering program.

This paper exhibits the probability density and scoring functions which will make up the expected values that are to be estimated by random sampling techniques. It is shown that these basic equations yield to such variance reducing methods as statistical estimation, importance sampling, and quota sampling.

A Monte Carlo program is being written for the calculation of the angular distribution and energy spectrum of air-scattered neutrons. This program will be general enough to be applicable to source energies up to about 18 Mev. The neutron events that may occur are: isotropic elastic scattering with each element, anisotropic elastic scattering with each element, inelastic scattering with each element and radiative capture; all other possible neutron events in air are treated as absorption without subsequent particle emission. Records of gamma rays born in air are stored on tape for future use in a gamma air-scattering program.

The response of a detector due to a point source of neutrons located a fixed distance from the detector may be expressed as an expected (or average) value in many ways, all of which may be derived from a proper mathematical formulation of the direct analogue procedure of tracing typical life histories of neutrons and recording the per cent that succeed in striking the detector.

Let us consider a monodirectional, monoenergetic point source. Figure 1 shows the first two collisions of a possible neutron history from such a source and the notation to be used. A typical neutron history is obtained by sampling in succession the distance $\rho_{0,1}$, the kind of first event e_1, the direction Ω_1 of the neutron after the collision (if e_1 is a scattering event), the energy E_1 of the neutron after the collision (if e_1 is an elastic scattering E_1 is determined by Ω_1), the distance $\rho_{1,2}$, event e_2, direction Ω_2, energy E_2, etc. The subscripts refer to the number of the collision and primed quantities refer to scattering toward the detector. These random variables and the probability distributions from which they are chosen are shown below.

FIGURE 1
BEGINNING OF A NEUTRON HISTORY

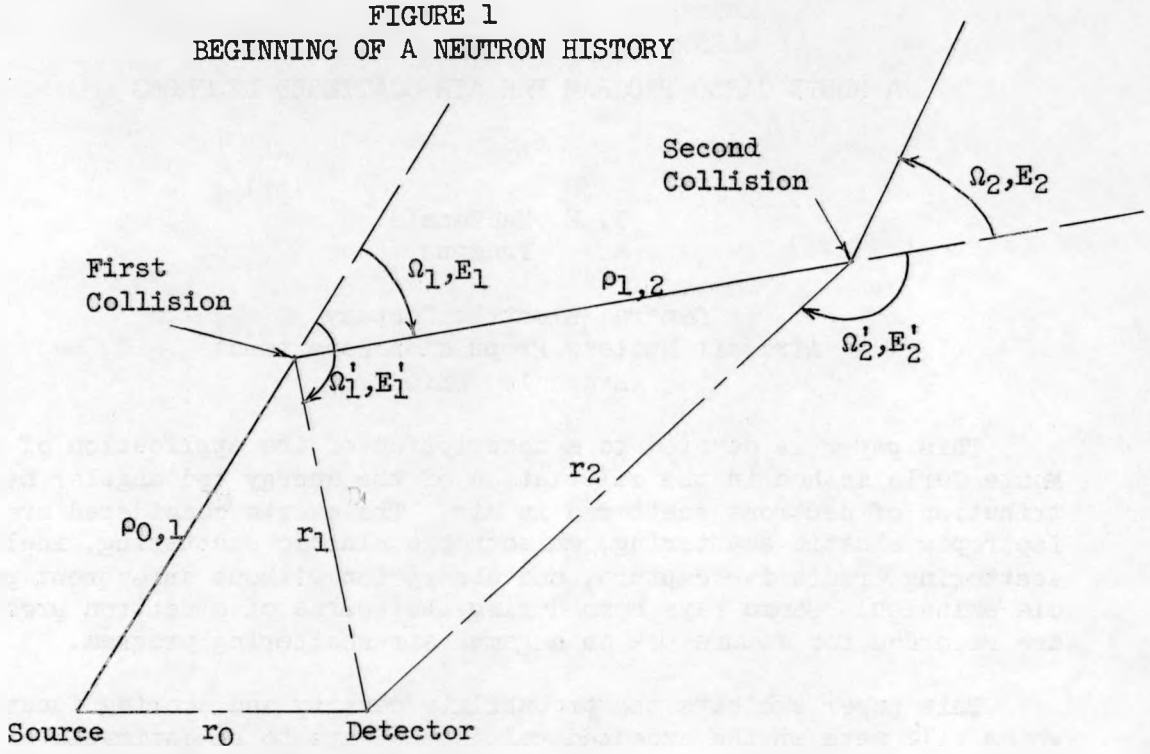

$$\rho_{i-1,i} \text{ from } \Sigma_t(E_{i-1})\, e^{-\Sigma_t(E_{i-1})\rho_{i-1,i}}, \quad 0 \le \rho_{i-1,i} < \infty$$

$$e_i \text{ from } \frac{\Sigma(E_{i-1};e_i)}{\Sigma_t(E_{i-1})},$$

i is one of the events: elastic scattering with one element, inelastic scattering with one element, relative capture or absorption.

$$\Omega_i \text{ from } \frac{\Sigma(E_{i-1},e_i;\Omega_i)}{\Sigma(E_{i-1};e_i)},$$

$$E_i \text{ from } P(E_{i-1},e_i;E_i), \quad 0 < E_i \le E_{i-1}$$

here i denotes the number of the collision, i=1, 2, ..., n. The distributions re assumed to be normalized as shown below.

$$\int_0^\infty \Sigma_t(E_{i-1})\, e^{-\Sigma_t(E_{i-1})\rho_{i-1,i}}\, d\rho_{i-1,i} = 1 \quad \text{for all } E_{i-1}$$

$$\sum_{\text{All } e_i} \frac{\Sigma(E_{i-1};e_i)}{\Sigma_t(E_{i-1})} = 1, \quad \text{for all } E_{i-1}.$$

$$\int_{\substack{\text{all}\\ \text{directions}}} \frac{\Sigma(E_{i-1},e_i;\Omega_i)}{\Sigma(E_{i-1};e_i)}\, d\Omega_i = 1 \text{ for all } E_{i-1} \text{ and scattering events } e_i.$$

$$\int_0^{E_0} P(E_{i-1},e_i,E_i)\, dE_i = 1 \text{ for all } E_{i-1} \text{ and scattering events } e_i.$$

Assuming one can obtain random samples from these probability distributions, let us define

$$Q(\Omega_i,\Omega_i') = \begin{cases} 1, \text{ if } \Omega_i = \Omega_i' \\ 0, \text{ otherwise.} \end{cases}$$

$$H(\rho_{i,i+1},r_i) = \begin{cases} 1, \text{ if } \rho_{i,i+1} \geq r_i \\ 0, \text{ otherwise} \end{cases}$$

where i = 1, 2, ..., n. Then

$$Y = \sum_{i=1}^{n-1} Q(\Omega_i,\Omega_i')\, H(\rho_{i,i+1}, r_i)$$

= 1 if neutron strikes detector (success)

= 0 otherwise (failure).

This Y then is the scoring function for the direct analogue Monte Carlo approach to the neutron air-scattering problem. Y is a function of the phase space variable X associated with a neutron history.

$$X = (\rho_{0,1},e_1,\Omega_1,E_1,\rho_{1,2},e_2,\Omega_2,E_2,\ldots,e_{n-1},\Omega_{n-1},E_{n-1},\rho_{n-1,n})$$

and is distributed according to the probability density function

$$F(X) = \Sigma_t(E_0)e^{-\Sigma_t(E_0)\rho_{0,1}} \prod_{i=1}^{n-1} \left[\frac{\Sigma(E_{i-1};e_i)}{\Sigma_t(E_{i-1})} \cdot \frac{\Sigma(E_{i-1},e_i;\Omega_i)}{\Sigma(E_{i-1};e_i)} P(E_{i-1},e_i;E_i)\, \Sigma_t(E_i)\, e^{-\Sigma_t(E_i)\rho_{i,i+1}} \right],$$

$$\int_{\substack{\text{all possible} \\ \text{neutron histories}}} F(X)\, dX = 1$$

Now the response of the detector is given by the expression

$$\bar{Y} = \int_{\substack{\text{all possible} \\ \text{neutron histories}}} Y(X)\, F(X)\, d(X).$$

Hence, to estimate the response $\bar{Y}$ one may trace a large number N of neutron histories, evaluate Y for each and calculate the fraction of successes

$$\bar{Y} = \frac{1}{N} \sum_{j=1}^{N} Y_j.$$

If one observes that $Q(\Omega_i,\Omega_i')$ behaves like a delta function and $H(\rho_{i,i+1},r_i)$ s the Heaviside unit function, another estimate of the response $\bar{Y}$ can be obtained y simply integrating these quantities out. This yields a sum of expected values.

$$\bar{Y} = \int_{\substack{\text{all possible}\\ \text{neutron histories}}} Y(X)\, F(X)\, dX$$

$$\sum_{\substack{\text{all } e_1,\ldots,\\ e_{n-1}}} \int_{\substack{E_1,\ldots,\\ E_{n-1}=0}}^{E_0} \int_{\substack{\text{all directions}\\ \Omega_1,\ldots,\Omega_{n-1}}} \int_{\substack{\rho_{0,1},\ldots,\\ \rho_{n-1,n}=0}}^{\infty} \left\{ \sum_{i=1}^{n-1} Q(\Omega_i,\Omega_i')\, H(\rho_{i,i+1},r_i) \right\}$$

$$\Sigma_t(E_0)e^{-\Sigma_t(E_0)\rho_{0,1}} \prod_{i=1}^{n-1} \left[\frac{\Sigma(E_{i-1};e_i)}{\Sigma_t(E_{i-1})} \cdot \frac{\Sigma(E_{i-1},e_i;\Omega_i)}{\Sigma(E_{i-1};e_i)} \cdot P(E_{i-1},e_i;E_i)\, \Sigma_t(E_i)e^{-\Sigma_t(E_i)\rho_{i,i+1}} \right]$$

$$dE_1 \cdots dE_{n-1} d\Omega_1 \cdots d\Omega_{n-1} d\rho_{0,1} \cdots d\rho_{n-1,n}$$

$$= \sum_{i=1}^{n-1} \bar{Y}_{(i)}$$

hese $\bar{Y}_{(i)}$ are expected values of the $Y_{(i)}(X_{(i)})$ as shown below.

$$_{(i)} = \int_{\substack{\text{all possible}\\ \text{i-collision histories}}} Y_{(i)}\,(X_{(i)})\, F_{(i)}\,(X_{(i)})\, dX_{(i)},$$

$$_{(1)} = (\rho_{0,1},\, e_1,\, E_1')$$

$$_{(i)} = (\rho_{0,1},e_1,\Omega_1,E_1,\rho_{1,2},\ \cdots,\ e_{i-1},\Omega_{i-1},E_{i-1},\rho_{i-1,i},e_i,E_i'),\quad i > 1$$

$$_{(1)}(X_{(1)}) = \Sigma_t(E_0)e^{-\Sigma_t(E_0)\rho_{0,1}} \left[\frac{\Sigma(E_0;e_1)}{\Sigma_t(E_0)} \cdot P(E_0,e_i;E_i') \right]$$

$$_{(i)}(X_{(i)}) = \Sigma_t(E_0)e^{-\Sigma_t(E_0)\rho_{0,1}} \prod_{j=1}^{i-1} \left[\frac{\Sigma(E_{j-1};e_j)}{\Sigma_t(E_{j-1})} \cdot \frac{\Sigma(E_{j-1},e_j;\Omega_j)}{\Sigma(E_{j-1};e_j)} \cdot P(E_{j-1},e_j;E_j) \right.$$

$$\left. \Sigma_t(E_j)e^{-\Sigma_t(E_j)\rho_{j,j+1}} \right] \cdot \frac{\Sigma(E_{i-1},e_i)}{\Sigma_t(E_{i-1})} \cdot P(E_{i-1},e_i,E_i'),$$

$$Y_{(i)}(X_{(i)}) = \left\{\frac{\Sigma(E_{i-1},e_i;\Omega_i')}{\Sigma(E_{i-1};e_i)} \cdot e^{-\Sigma_t(E_i')\, r_i}\right\},$$

i=1, 2, ..., n-1. In this case then an estimate of the response $\bar{Y}$ is obtained by selecting neutron histories randomly, scoring $Y_{(i)}(X_{(i)})$ at the i-th collision point, summing this over all collisions and all histories and dividing by the number of neutron histories sampled. This scoring function is more difficult to evaluate than the scoring function for the direct analogue approach which involved the Q and H functions, but it can be shown that for a given sample size the statistical variance of the estimate is greatly reduced in the latter case.

Instead of sampling for E_i' (which is done only when the event e_i is an inelastic scattering) one may use the sampling scheme shown below.

$$X_{(1)} = (\rho_{0,1}, e_1)$$

$$X(i) = (\rho_{0,1}, e_1, \Omega_1, E_1, \ldots, e_{i-1}, \Omega_{i-1}, E_{i-1}, \rho_{i-1,i}, e_i), \quad i > 1$$

$$F_{(1)}(X_{(1)}) = \Sigma_t(E_0) e^{-\Sigma_t(E_0)\rho_{0,1}} \frac{\Sigma(E_0,e_1)}{\Sigma_t(E_0)}$$

$$F_{(i)}(X_{(i)}) = \Sigma_t(E_0) e^{-\Sigma_t(E_0)\rho_{0,1}} \prod_{j=1}^{i-1} \left[\frac{\Sigma(E_{j-1};e_j)}{\Sigma t(E_{j-1})} \cdot \frac{\Sigma(E_{j-1},e_j;\Omega_j)}{(E_{j-1};e_j)} \cdot P(E_{j-1},e_j;E_j) \right.$$

$$\left. \Sigma_t(E_j) e^{-\Sigma_t(E_j)\rho_{j,j+1}}\right] \frac{\Sigma(E_{i-1};e_i)}{\Sigma_t(E_{i-1})}$$

$$Y_{(i)}(X_{(i)}) = \left\{\frac{\Sigma(E_{i-1},e_i;\Omega_i')}{\Sigma(E_{i-1};e_i)} \cdot \int_0^{E_0} P(E_{i-1},e_i;E_i')\, e^{-\Sigma_t(E_i')r_i}\, dE_i'\right\}$$

The expected value of this scoring function is the same as the expected value of the preceding scoring function as can be shown by carrying out the multiplications and integrations. The difference here is essentially one of integrating analytically over one of the variables versus an integration by random sampling.

Similarly, instead of selecting the event e_i at the i-th collision point, we may score every possible scattering event by weighting properly as shown below.

$$X_{(1)} = \rho_{0,1}$$

$$X(i) = (\rho_{0,1}, e_1, \Omega_1, E_1, \ldots, e_{i-1}, \Omega_{i-1}, E_{i-1}, \rho_{i-1,i}), \quad i > 1$$

$$F_{(1)}(X_{(1)}) = \Sigma_t(E_0) e^{-\Sigma_t(E_0)\rho_{0,1}}$$

$$_{i)}(X_{(i)}) = \Sigma_t(E_0)e^{-\Sigma_t(E_0)\rho_{0,1}} \prod_{j=1}^{i-1} \left[\frac{\Sigma(E_{j-1};e_j)}{\Sigma t(E_{j-1})} \cdot \frac{\Sigma(E_{j-1},e_j;\Omega_j)}{\Sigma(E_{j-1};e_j)} P(E_{j-1},e_j;E_j) \right.$$

$$\left. \Sigma_t(E_j)e^{-\Sigma_t(E_j)\rho_{j,j+1}} \right]$$

$$_{i)}(X_{(i)}) = \left\{ \sum_{\text{all } e_i} \frac{\Sigma(E_{i-1};e_i)}{\Sigma_t(E_{i-1})} \cdot \frac{\Sigma(E_{i-1},e_i;\Omega_i')}{\Sigma(E_{i-1},e_i)} \cdot \int_0^{E_0} P(E_{i-1},e_i;E_i')e^{-\Sigma_t(E_i')r_i} \, dE_i \right\}$$

ote that the scoring function $Y(i)(X_{(i)})$ becomes progressively more difficult evaluate and if this procedure were carried to its limit, it would amount to solution in the form of a multi-dimensional integral. The present program has ptions of employing any one of the three scoring functions shown above. Some esting will be done to find the most efficient method of calculation. This pro-ram uses most of the techniques employed in our gamma air-scattering program hich we reported at the 1958 Atlanta meeting. These techniques include: the alculation of the single collision contribution by numerical integration, the ystematic sampling of first collision points, and the use of quota sampling at hese points, the removal of the singularity appearing in other programs, the alculation of variance and the method of tabulating the angular distribution nd energy spectrum at the detector.

018

3. RECENT FISSION GAMMA-RAY SPECTRAL MEASUREMENTS

F. C. Maienschein
R. W. Peelle
T. A. Love

Oak Ridge National Laboratory
Oak Ridge, Tennessee

RECENT FISSION GAMMA-RAY SPECTRAL MEASUREMENTS

by

F. C. Maienschein, R. W. Peelle, and T. A. Love

Oak Ridge National Laboratory*
Oak Ridge, Tennessee

Measurements of the gamma-ray spectrum closely associated in time with the fission of U^{235} by thermal neutrons have been extended down to 10 kev with a single-crystal spectrometer. Preliminary results indicate a photon yield which varies between 6 and 15 photons·fission^{-1}·Mev^{-1} for all energies from 10 to approximately 600 kev except at the heavy fission-fragment x-ray peak where the yield increases to about 24 photons·fission^{-1}·Mev^{-1}. In an additional investigation, an unrefined measurement of the gross spectrum of gamma rays associated with the thermal fission of U^{235} has been made with a three-crystal pair spectrometer and an irradiated U^{235} foil. Within the many limitations, the results roughly agree in spectral shape with the data of Motz (Phys. Rev. 86, 753, 1952) and also with a summation of the earlier prompt-fission and fission-product data. These two investigations are discussed separately in the paper which follows.

PRELIMINARY RESULTS FROM A DETERMINATION OF THE LOW-ENERGY PORTION OF THE GAMMA-RAY SPECTRUM EMITTED PROMPTLY AFTER FISSION OF U^{235} BY THERMAL NEUTRONS

The energy spectrum of gamma rays emitted promptly ($< 5 \times 10^{-8}$ sec) after fission of U^{235} by thermal neutrons has previously been studied for energies above 400 kev, and the results obtained from a preliminary analysis of part of the data have been reported.[1,2] The final analysis has been carried forward and is complete except for corrections for the nonunique spectrometer response and for the variation of spectrometer efficiency with gamma-ray energy. At the lowest energies considered in these measurements (~ 350 kev) a peak in the spectrum was observed. In order to verify the reality of this peak and the possible existence of

---

* Operated by Union Carbide Corporation for the U. S. Atomic Energy Commission.

1. Peelle, R. W., Zobel, W., Love, T. A., and Maienschein, F. C., "Recent Results for the Energy Spectra of Fission-Associated Radiation, 5th Semi-Annual ANP Shielding Information Meeting, May 14-15, 1958, Paper 25, Vol. III, LNP-NR-47.

2. Maienschein, F. C., Peelle, R. W., Zobel, W., Love, T. A., Proc. U.N. Intern. Conf. Peaceful Uses Atomic Energy, Geneva, 1958, Vol. 15, 366-372 (1959).

other peaks, an additional measurement of gamma rays in the 10- to 800-kev range was initiated. (A similar measurement, not on an absolute yield basis and without discrimination against neutron effects, has been reported elsewhere.[3])

Knowing the low-energy prompt-fission spectrum is important for reactor heating considerations, since the energy of these gamma rays can be deposited in a relatively thin layer of reactor material. For the study of this lower energy region it appeared feasible to employ a single-crystal spectrometer since the peak-to-total ratios are not too small (for the crystal used the ratio was > 0.5 for energies below ~ 0.5 Mev). A time-of-flight technique, made possible because the high inherent efficiency of the single crystal allowed a sufficiently long flight path, was utilized to exclude pulses from neutron interaction effects in the scintillator. Without this extra discrimination, the neutron effects in the single crystal would have been appreciably greater than those which have been observed for a multiple-crystal spectrometer.[4]

The crystal used in the spectrometer was a NaI(Tl) scintillation crystal 1.75 in. in diameter by 1.0 in. thick, protected on the end by a thin cover. It examined the gamma rays from a four-plate fission chamber, containing approximately 14.0 mg of U^{235}, through a 342-cm flight path of helium contained within thin foils. A largely thermal neutron beam from the Oak Ridge Graphite Reactor produced about 25,000 fission counts per second in the fission chamber. Extensive shielding of lead and lithiated paraffin reduced the background to an unimportant level. Studies were made of the response of the spectrometer to numerous monoenergetic gamma-ray sources in order to ascertain the pulse-height spectral response in the presence of the shielding and collimator system. Gamma-ray and x-ray sources were also used repeatedly to determine the energy vs pulse-height calibrations for the spectrometer.

In order to discriminate against fission neutrons which might travel down the flight path and interact exoergically in the scintillator, the output of the gamma-ray spectrometer was examined at a time after a fission event corresponding to the flight time for a photon ($\sim 10^{-8}$ sec). The resolving time employed in the coincidence circuit used to establish time coincidence was $(7.0 \pm 0.1) \times 10^{-8}$ sec. Because of the jitter in time due to the poor electron statistics at the photocathode of the electron multiplier for the low-energy gamma rays studied, it was necessary to determine the "efficiency" of the coincidence circuit as a function of gamma-ray energy. This determination was made using a short flight path (~ 15 cm) and a variable time delay between the two signals. Representative preliminary values for the coincidence-circuit efficiency are given in Table I.

---

3. Voitovetskii, U. K., Levin, B. A., and Marchenkov, E. U., J. Exp. Theoret. Phys. (U.S.S.R.) 5, 184-188 (1957).

4. Maienschein, F. C., Peelle, R. W., Love, T. A., Appl. Nuc. Phys. Div. Ann. Prog. Rep. Sept. 1, 1957, ORNL-2389, p. 99.

Table I. Coincidence Circuit Efficiency (Preliminary)

Gamma-Ray Energy Absorbed in the Scintillator (Mev)	Coincidence Circuit Efficiency*
0.01	0.77 ± 0.03
0.015	0.89 ± 0.02
0.025	0.97 ± 0.02
0.035	0.98 ± 0.01
0.050	1.00 ± 0.005
> 0.05	1.000

*Defined as the fraction of pulses from true prompt gamma rays which were accepted as such by the coincidence circuit using a $(7.0 \pm 0.1) \times 10^{-8}$ sec resolving time.

For the very approximate calculations of absolute spectral yield reported below, the spectrometer efficiency was guessed on the basis of measurements for a similar crystal.[5] This approach is poor for continuous spectral distributions because no correction has been made for the compton tails resulting from the spectrometer response to higher-energy gamma rays.

The calculated subtraction of chance background was demonstrated to be correct by delaying the signals from the gamma-ray detector by 0.96 μsec and noting the agreement of the observed spectrum due to random coincidences with the predicted spectrum.

The data points in Fig. 1 show coincidence count rates obtained by delaying the signal from the fission chamber channel. The peak at 1.5×10^{-7} sec corresponds to the prompt-fission gamma rays. Greater times correspond to delayed gamma rays or neutrons. The expected contribution due to gamma rays from short-lived isomers which would penetrate a 1.75-mm-thick lead filter between the fission chamber and flight path is shown by the dashed curve, which was normalized to the prompt peak at 1.5×10^{-7} sec. This contribution was obtained with a time analyzer and a flight path of only a few centimeters. It has been corrected for the resolving time used in the measurement. The expected neutron contribution, indicated by the dotted curve, corresponds to the known prompt-fission neutron spectrum converted to a time scale appropriate to a 342-cm flight path and smeared

5. Mott, W. E., and Sutton, R. B., Handbuch der Physik (ed. by S. Flugge), Vol. XLV, p. 128, Springer-Verlag, Berlin, 1958.

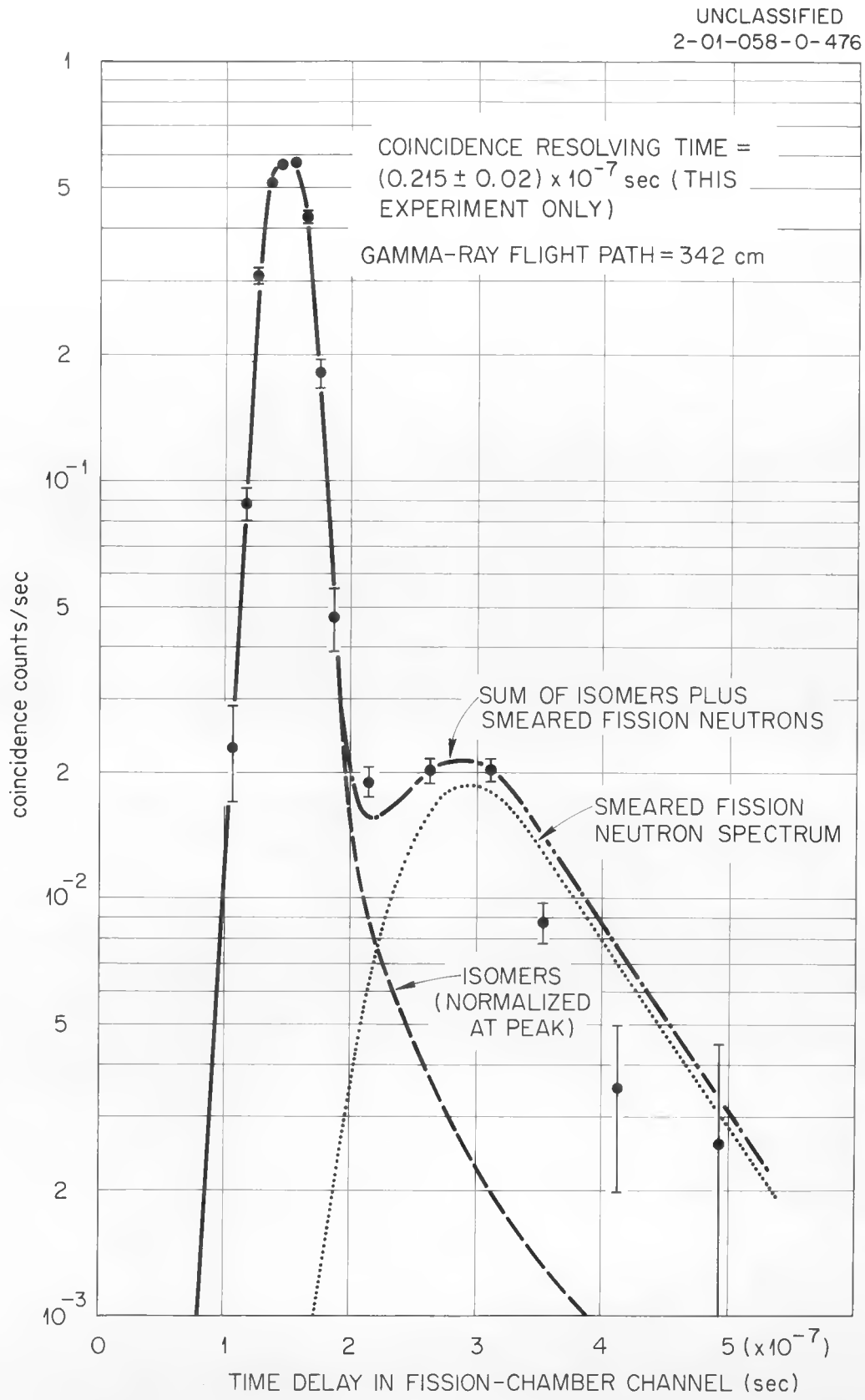

Fig. 1. Coincidence Count Rate as a Function of Time Delay (from an Arbitrary Zero) of the Fission Chamber Signal. Errors shown are statistical only. Gamma-ray channel set to accept pulses corresponding to energies in the range 0.035 Mev $\leq E \leq$ 0.99 Mev. 1.75-mm-thick lead absorber.

to account for jitter in the gamma-ray detector and the coincidence resolving time. Constant efficiency vs energy was assumed to obtain this curve, which is normalized arbitrarily. The dash-dot curve, which is the sum of the plotted isomer and fission-neutron effects, fits the shape of the observed delayed data.

Spectral data (with poor statistics) were obtained at a delay time of 3×10^{-7} sec, corresponding to the maximum fission-neutron effects in the crystal. These spectra showed the most prominent of the usual peaks[4] (at 0.06, 0.21 Mev) due to interaction of neutrons and sodium iodide.

Pulse-height spectra obtained with a time delay corresponding to the gamma-ray peak of Fig. 1 are shown in Fig. 2. The results of three runs at different gains are given. A total of 14 runs were completed at these three gains. The energy scale is approximate with an error of 2% or 2 kev, whichever is greater, an error estimate which will be significantly reduced in the final data analysis. Energies of the apparent peaks in the spectrum are shown on the graph. The corresponding data of Voitovetski[3] are also shown. He used a smaller crystal of sodium iodide and no time-of-flight descrimination against neutrons and therefore a much smaller detector-source separation distance. The curve at the bottom of Fig. 2 shows the results obtained with a 9.0-mm-thick lead sheet placed in the flight path. With this gamma-ray absorber present, any neutron-induced peaks should be greatly enhanced relatively. Similar data, not shown on the figure, were taken for a thicker piece of lead at the lowest gain and the absorption effects of the lead were experimentally checked with monoenergetic sources of gamma rays and compared to good-geometry calculations. As shown by the lead data, any neutron peak at 60 kev is less than 10% as intense as the fission gamma rays and at other energies the neutron-induced pulses are negligible. The very broad peak in the lead data at ~ 60 kev may include the effects of lead x-rays.

The data of Fig. 3 represent the results of applying the approximate spectrometer efficiency values tabulated above to the spectral data of Fig. 2. The logarithmic energy scale makes more apparent the low-energy peaks due to the x-rays emitted by the light and heavy fission fragments. The absolute intensities in this energy region are affected appreciably by the gamma-ray absorption in the fission chamber but no correction has yet been made.

The new data substantiate the existence of a peak at ~ 350 kev as previously indicated by the Compton spectrometer, but the marked discrepancy in yield at energies above 0.4 Mev between these sets of data indicates the magnitude of the errors induced by the use of an assumed spectrometer efficiency and the lack of a correction for the nonunique response of the spectrometer. All of the above data must be regarded as preliminary.

A meaningful comparison of these data with the earlier results for higher energies must await a careful analysis of the data. However, the similarity of the spectral shape to that observed by Voitovetskii is

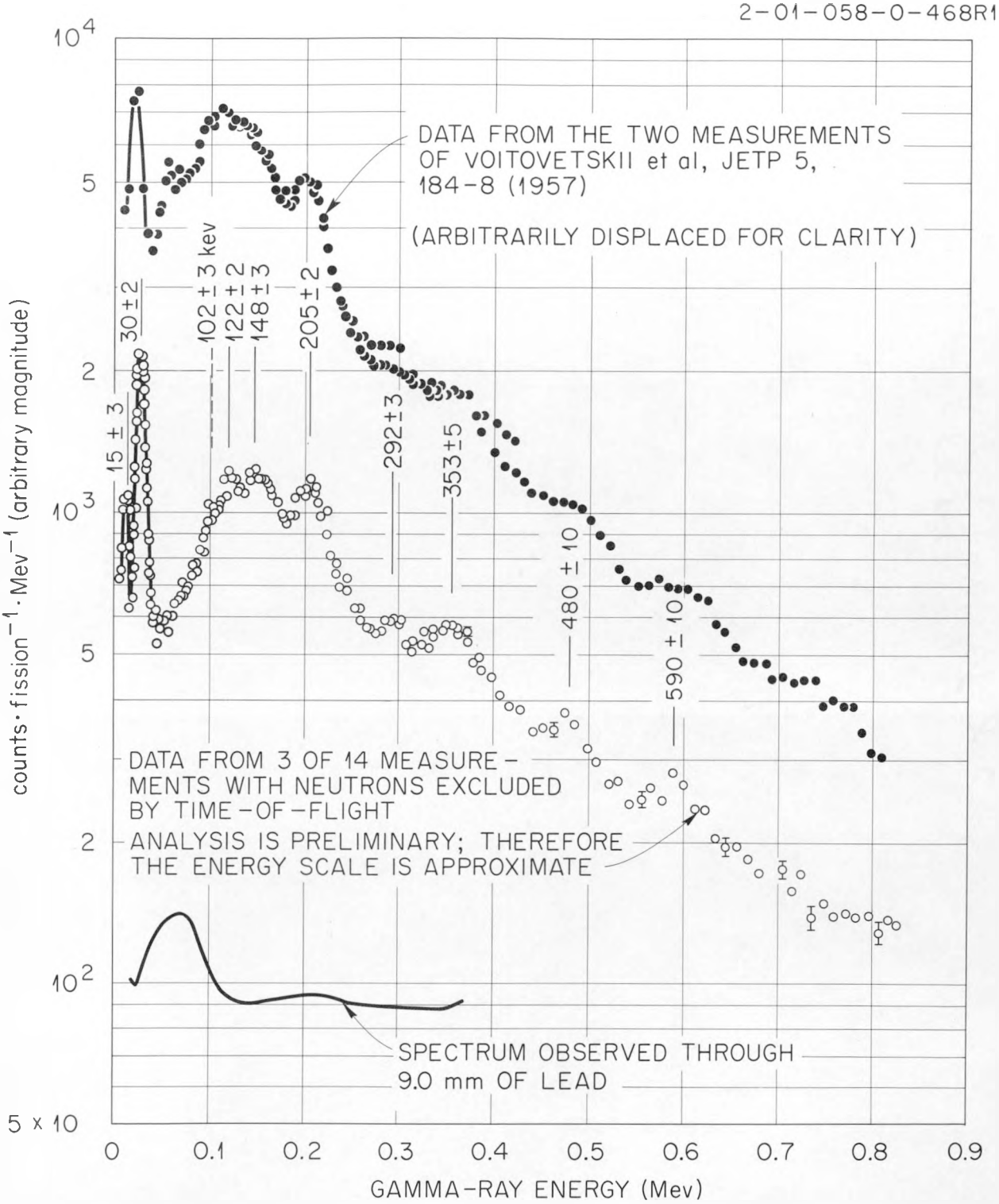

Fig. 2. Pulse-Height Spectra of Prompt Gamma Rays from the Thermal Fission of U^{235}. The top curve is the data of Voitovetski et al., the middle and lower curves are obtained with a coincidence resolving time of $7.0 \pm 0.015 \times 10^{-8}$ sec and a 342-cm flight path. A 9.0-mm-thick lead disk was inserted in the flight path adjacent to the fission chamber to obtain the bottom curve.

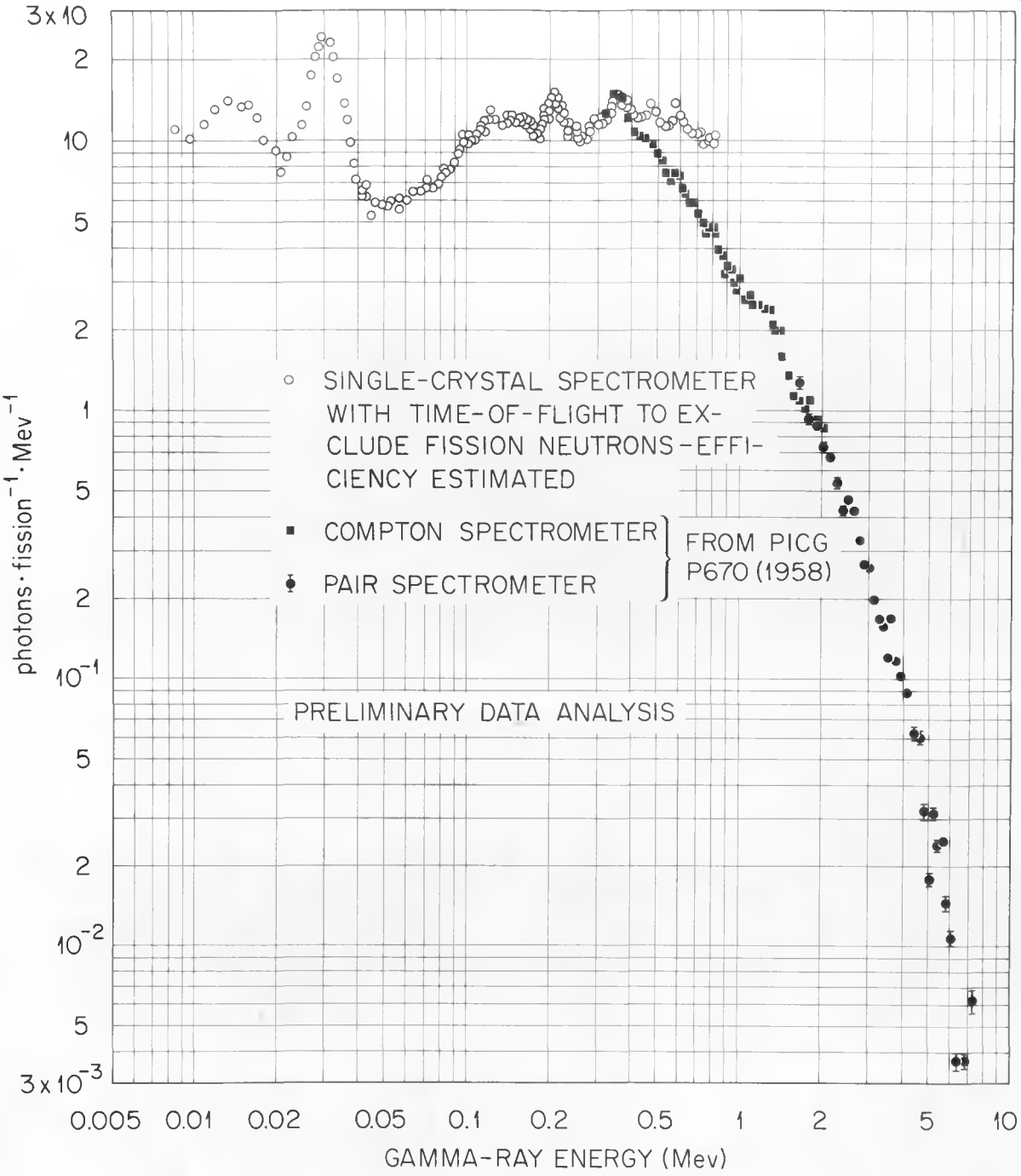

Fig. 3. Preliminary Spectrum of Gamma Rays of Energies from 10 to 800 kev Emitted within ~10^{-7} sec after Fission of U^{235}. Assumed spectrometer efficiency and no correction for nonunique response of spectrometer. Previously obtained higher-energy data is also shown. The peaks due to the x rays from the light and heavy fission fragments show clearly at ~15 and ~30 kev.

striking and indicates that his separation of peaks into neutron and gamma-ray effects was correct. The peak in the data of Voitovetskii at 60 kev is due to neutrons and that at ~75 kev is due to lead x-rays. The more rapid fall-off with energy for his data would be expected since he used a smaller crystal.

Fortunately it was possible in this experiment to measure at sufficiently low energies to separate clearly the x-rays due to the light fragments (at ~15 kev) and those due to the heavy fragments (at ~30 kev). The yield of x-rays from the lighter fragments is less as would be expected since internal conversion is less probable for the lower Z nuclei and since the K x-ray fluorescent yield is lower. The other more-or-less defined peaks with energies as shown in Fig. 2 are presumably superimposed on a continuum of gamma rays from the decay of a statistical ensemble of many of the nuclear levels formed in fission. The number of peaks separated in this measurement is probably limited by the finite resolution of the spectrometer.

It would be instructive to determine whether similar spectral structure is observed in fast fission or in the thermal fission of other nuclei. Studies with Cf^{252}, which are relatively easy because of the low backgrounds associated with spontaneous fission, would display the gamma rays from fission fragments in a higher mass region.

PRELIMINARY MEASUREMENTS OF THE GROSS SPECTRUM OF GAMMA RAYS ASSOCIATED WITH THE INTERACTION OF THERMAL NEUTRONS AND U^{235}

As was pointed out in the preceding discussion, extensive spectral measurements of the prompt gamma rays associated with the thermal fission of U^{235} have been carried out at ORNL. In addition to determining the energy spectrum for prompt gamma rays, the spectrum for fission-product gamma rays has been obtained.[1,2] It has been suggested by H. Goldstein[6] that a spectral measurement of the total gamma-ray production due to the absorption of thermal neutrons in U^{235} would also be desirable for shielding calculations. A preliminary experiment has now been performed to measure the gross spectrum, and the results are reported below. Only the relative shape of the spectrum was obtained since the fission rate was not determined and several sources of error which were recognized could not be corrected for. As explained later in the paper, an adequate refinement of the experiment would be difficult with the existing apparatus.

The pertinent features of the experimental arrangement are shown in Fig. 4. A three-crystal pair spectrometer[2] was used to examine the gamma radiation emitted by a disk of U^{235} positioned over the thermal column adjacent to the Bulk Shielding Reactor. The disk was approximately 0.700 in. in diameter and about 0.042 in. thick. The response of the pair spectrometer

6. Goldstein, H., Fundamental Aspects of Reactor Shielding, p. 63, Addison-Wesley, Reading, 1959.

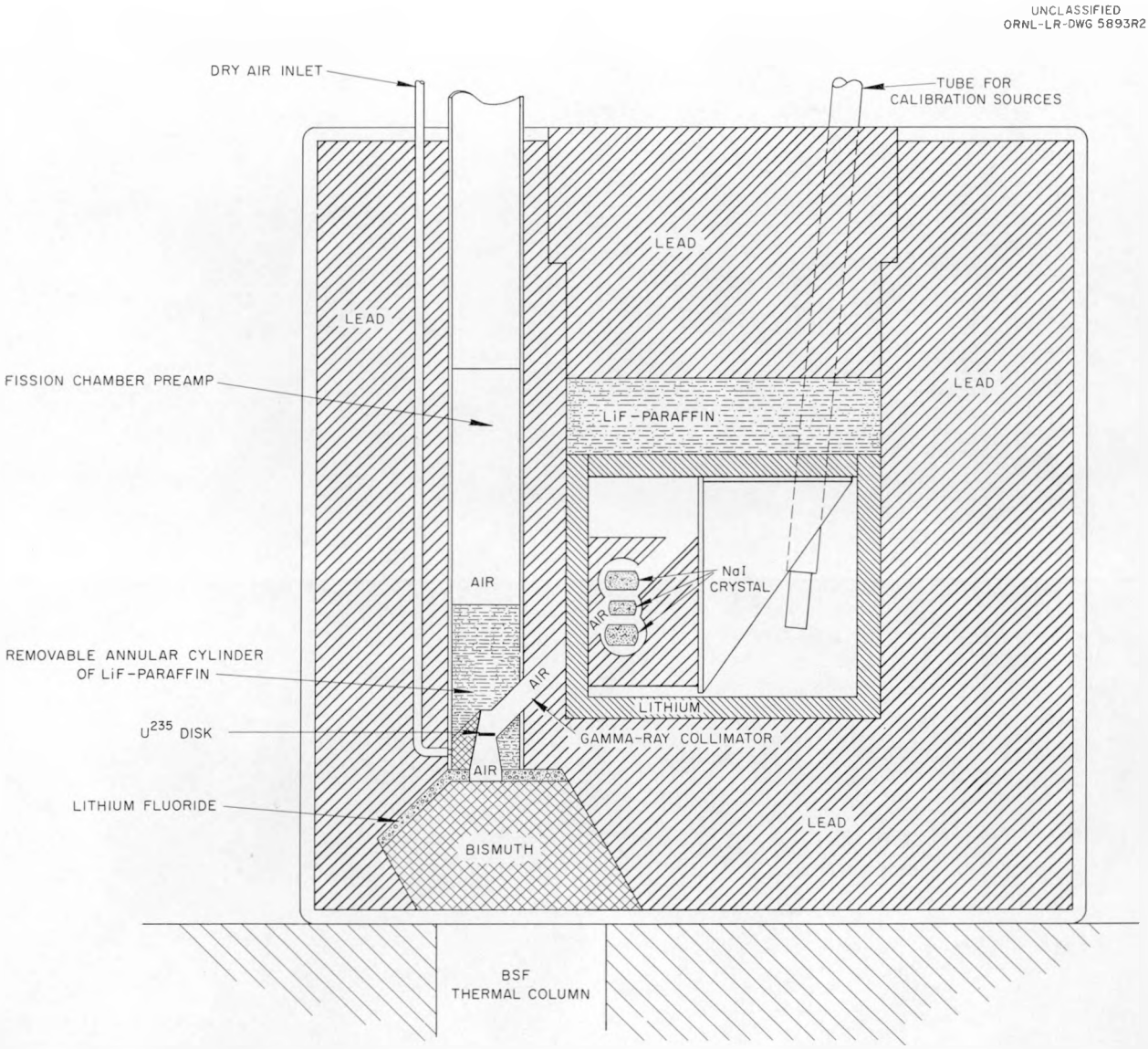

Fig. 4. Arrangement of Apparatus for Determination of Integral Gamma-Ray Spectrum Associated with the Interaction of Thermal Neutrons and U^{235}.

to monoenergetic gamma rays is shown in Fig. 1b of the second paper cited in Ref. 2, and the neutron response was estimated to be small on the basis of investigations described elsewhere.[4] The magnitude of the radiation not associated with the interaction of thermal neutrons with U^{235}, that is, the background radiation, was determined by replacing the U^{235} disk with a U^{238} disk of approximately equal weight.

The experimental data obtained in this experiment were not appreciably affected by the instrumentation errors such as analyzer nonlinearity, count losses, gain drifts, etc. Thermal-neutron interactions in the spectrometer walls and in the NaI(Tl) crystals used in the spectrometer were minimized by the extensive use of lithium shielding, and the short-time response of the spectrometer (about 10^{-7} sec) to fast capture or inelastic scattering of fission neutrons had already been shown to be small for this geometry.[4] Interactions due to partially moderated neutrons in the kev region were not eliminated as a source of appreciable background. Nor was a correction made for the nonunique response of the spectrometer. This latter correction would probably vary from about 10% at the high energies to about 20% at 2 Mev and to a factor of 2 at the lowest energy. No correction was made for the fact that the fission products were not quite saturated in the 9000-sec run. Examination of the fission-product spectrum[1,2] indicates that this would have no appreciable effect on the spectral shape, however.

The spectral data obtained when the U^{235} disk was in position were combined into energy bins and a subtraction was made for the background. (The background caused by random coincidences, which amounted to no more than 2.5% at any energy, was not subtracted.) The results, arbitrarily normalized to give the best over-all fit, are shown in Fig. 5. The background spectrum is also presented. Both sets of data were corrected for the relative spectrometer efficiency and thus represent the relative number of gamma rays as a function of energy. The errors shown are those due to counting statistics only. It may be noted that these errors become appreciable at the higher energies since the background is about an order of magnitude larger than the foreground. An indication of the success of the background subtraction is given by the removal of the gamma-ray peak due to hydrogen capture, which is quite prominent in the background.

The solid curve in Fig. 5 was obtained by adding the prompt-fission and fission-product gamma-ray spectra reported in Refs. 1 and 2. The statistical errors shown there vary from about 20% at 7 Mev to a negligible error at low energies. The summation of these two spectra is completely consistent in shape with the results of the present experiment when the error due to the nonuniqueness of spectrometer response is considered. It is probable that the data of Motz,[7] also shown in Fig. 5 are consistent with the results of the present experiment, but this cannot be verified since no errors are available for the Motz experiment.

It is reassuring to observe the apparent agreement in spectral shapes between the two integral measurements of U^{235} gamma rays and the summation of the prompt-fission and fission-product spectra. However, the errors

7. Motz, J. W., Phys. Rev. 86, 753 (1952).

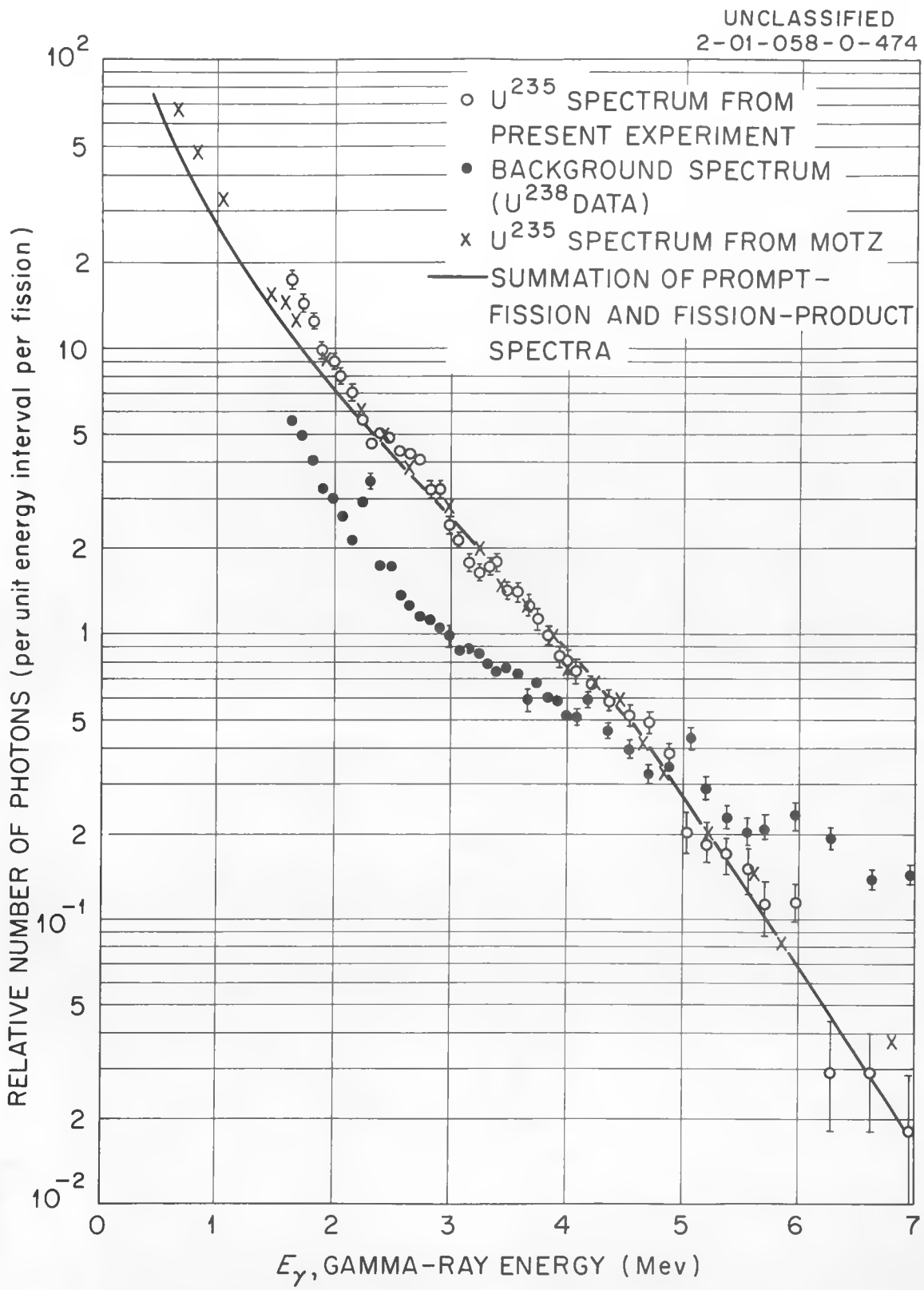

Fig. 5. Energy Spectra for Gamma Rays from the Interaction of Thermal Neutrons and U^{235}. All data normalized to give the best over-all fit.

in the integral measurements are so large that no meaningful conclusions can be drawn concerning the other sources of gamma radiation, primarily gamma rays resulting from neutron capture in U^{235} and very short-lived fission products ($T_{1/2} < 1$ sec). For this purpose a much more accurate measurement would be required and the fission rate should be determined so that the energy yield could be checked on an absolute basis.

A measurement of adequate accuracy would be difficult with the existing apparatus, however. An accurate determination of the fission rate would be made difficult by the variation of the thermal-neutron flux in the region around the U^{235}. In addition, the presence of apparatus around the fission source may lead to the partial moderation of fission neutrons, thus increasing their probability of interaction in the sodium iodide crystals. Partially moderated prompt-fission neutrons would not have been detected in the prompt-fission gamma-ray experiment because of the time-coincidence requirement. Fully moderated (thermal) neutrons are excluded from the crystals by the lithium shield.

It further appears desirable to measure the gamma rays from the U^{235} at a backward angle with respect to the incident thermal-neutron beam since the neutron beam is inevitably contaminated with gamma rays. The scattering of such gamma rays will be much worse at low energies which were not studied in the present preliminary experiment.

Because of the considerations outlined above, it would appear that new experimental apparatus would have to be assembled if a meaningful measurement of the gamma rays due to the interaction of thermal neutrons with U^{235} were to be performed. The requirements for a well-collimated, high-intensity thermal-neutron beam with little contamination and low general background could not easily be met. The interfering effects considered in this section and the other sources of error would also need to be studied carefully. Some of the neutron-induced background problems might be alleviated by the use of a magnetic-deflection Compton spectrometer, but the extremely low efficiency of such devices would aggravate the need for an intense beam and the determination of the fission rate. It is not clear that the effort necessary for an accurate measurement would be warranted.

4. A COMPARISON OF EXPERIMENTAL GAMMA-RAY RESPONSE MEASUREMENTS WITH CALCULATIONS FOR AN 8-IN. RIGHT CYLINDRICAL NaI(Tl) CRYSTAL

G. T. Chapman
T. A. Love

Oak Ridge National Laboratory
Oak Ridge, Tennessee

A COMPARISON OF EXPERIMENTAL GAMMA-RAY RESPONSE MEASUREMENTS WITH CALCULATIONS FOR AN 8-IN. RIGHT CYLINDRICAL NaI(Tl) CRYSTAL

by

G. T. Chapman and T. A. Love

Oak Ridge National Laboratory*
Oak Ridge, Tennessee

A right circular, cylindrical NaI(Tl) crystal 8 in. in diameter and 8 in. long has been tested at the Bulk Shielding Facility. The crystal was formed by optically coupling two smaller crystals, each 8 in. in diameter and 4 in. long, together in such a way that the composite gave results comparable to a single crystal. By mounting a 2-in.-thick crystal containing a 1/2-in.-dia axial hole through it on the end of the large crystal and taking the anticoincidence spectrum from the large crystal, it was shown that the ratio of the peak area to the total area could be improved by the addition of a well in the crystal. The experimental data were compared with a Monte Carlo calculation for a crystal of the same size.

The Bulk Shielding Facility at ORNL has been investigating the possible use of very large NaI(Tl) crystals for total-absorption, gamma-ray spectroscopy. The term "total absorption" will be understood to mean that a major fraction of the monoenergetic gamma rays incident on the crystal will give up all of their energy in the crystal. The ratio of the area under the total absorption peak of the pulse-height distribution to the total area of the distribution curve for such a crystal is very large compared to the same ratio for smaller crystals. This ratio, which is known as the photofraction, is a characteristic parameter of the performance of a given crystal. The large photofraction means that the tail of the distribution is greatly reduced, since such features as the Compton distribution and escape peaks are virtually eliminated. The simpler pulse-height distribution facilitates the "unscrambling" of continuous spectra. The large size of the crystal eliminates the necessity of the coincidence circuits used in multicrystal spectroscopy and reduces the required time for experimental work because of the increased crystal efficiency.

Figure 1 shows the geometry of the large crystals that were available prior to a few months ago. Because of the shape of the ingot in which the crystals were grown, and in order to make the crystals as long as possible, the truncated, conical end was retained on the cylindrical section of the crystal. Experiments indicated[1] that if monoenergetic gamma rays were

---

* Operated by Union Carbide Corporation for the U. S. Atomic Energy Commission

1. Chapman, G. T. and Love, T. A., "Total Absorption Spectroscopy," Appl. Nuc. Phys. Ann. Prog. Rep. Sept. 1, 1957, ORNL-2389, p. 233.

UNCLASSIFIED
2-01-058-0-203

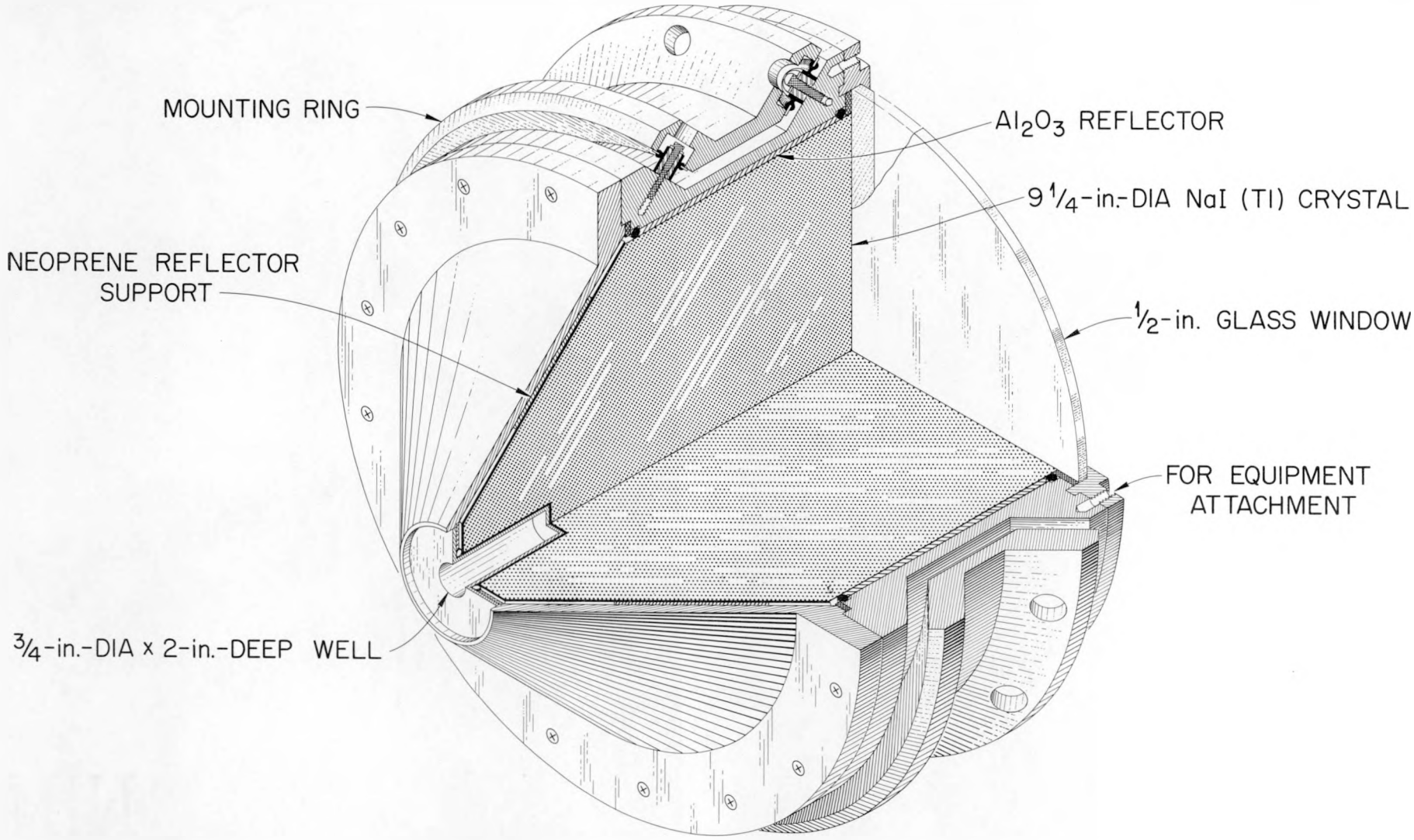

Fig. 1. Sketch of 9-3/8-in.-dia NaI(Tl) Gamma-Ray Spectrometer Crystal Showing 3/6-in.-dia by 2-in.-deep Well in Truncated End

collimated into the conical end along the axis of the crystal, then two partially resolved peaks would occur in the pulse-height distribution. Owing to this and other experimental results, it was concluded, though not yet fully explained, that this double peak effect was a consequence of the difference in the optics of the conical and cylindrical regions.

Recently, one of the suppliers[2] of large NaI(Tl) crystals was able to produce a relatively long right circular, cylindrical crystal by optically coupling two smaller crystals together. The smaller crystals were each 8 in. in diameter and 4 in. long, producing, when coupled, a right circular, cylindrical crystal 8 in. in diameter and 8 in. long. The composite crystal is conventionally canned with the customary aluminum oxide reflector on all surfaces except the end through which the light passes to reach the photomultiplier tubes. This crystal was obtained on a loan basis for test at the Bulk Shielding Facility.

When tested with known-energy gamma rays, using an array of three 3-in.-dia photomultiplier tubes to observe the light pulses in the crystal, the composite crystal responded as one uniform crystal. For gamma rays ranging in energy up through the 2.76-Mev photon from the decay of Na^{24} there was no evidence of the double peaks which were characteristic of the conically ended crystals mentioned previously. The resolution at the Cs^{137} gamma-ray energy of 0.662 Mev was measured to be 11.8% and the ratio of the area under the peak to the total area under the distribution was about 0.75. Since the data were taken without a well in the crystal, there was, of course, a contribution to the tail from the loss of gamma rays scattered back out of the crystal. This was demonstrated by collimating the Cs^{137} gamma rays through a 1/2-in. diameter hole along the axis of an additional 4-in.-diameter by 2-in.-long crystal mounted on the end of the large crystal and observing the anticoincidence spectra from the large crystal. This increased the peak-to-total ratio to 0.83.

As reported elsewhere,[3] a Monte Carlo code has been developed for calculations of the response functions of scintillation detectors to monoenergetic gamma rays. This code was used to calculate the response of an 8-in.-dia by 8-in.-long NaI crystal for five different gamma-ray energies and the results are compared with the experimental data for the composite crystal in Table I. The conditions for the calculations, including crystal dimensions and collimation of the gamma rays along the crystal axis, resembled the experimental conditions as closely as possible. The calculations gave only the peak-to-total ratio and the Compton distribution in the tail. It will be noticed that the peak-to-total ratios for the calculated values are much higher than the measured values. It is probably not possible to

---

2. Harshaw Chemical Co., Cleveland, Ohio.

3. Zerby, C. D., "Monte Carlo Code for the Calculation of Response Functions of Gamma-Ray Scintillation Detectors," Seventh ANP Shielding Information Meeting, October 14-15, 1959, this report; Zerby, C. D., and Moran, H., Neutron Physics Div. Ann. Rep. Sept. 1, 1959, ORNL-2842, Sec. 8.3.

Table I. Comparison of Experimental and Calculated Results for the Response of an 8-in.-dia by 8-in.-long NaI(Tl) Crystal

Photon Energy (Mev)	Measured Resolution (%)	Measured Photofraction[a,b] (%)	Calculated Photofraction[a] (%)
0.662	11.8	83	92.9
0.899	8.8	66	90.0
1.368	8.6	61	84.9
1.840	7.3	60	80.8
2.754	6.3	52	79.2

a. Photofraction is defined as the ratio of the area under the total absorption peak to the total area under the pulse-height distribution curve.

b. Values of the measured photofractions are reproducible to < 3%.

attain the theoretical photofractions in practice because of the unavoidable scattering effects of the material around the detector. For example, owing to the finite size of the gamma-ray source and source container used to make these measurements, it is estimated that as much as a 3% contribution to the distribution in the tail may be due to scattering within the source. In addition, R. W. Peelle at ORNL has pointed out that, based on the work of a group of MIT students at ORNL,[4] there may be as much as a 9% contribution from the effect of the collimator. The measured resolution for this crystal is also shown in Table I as a function of the gamma-ray energy.

Figure 2 shows the pulse-height distribution for Cs^{137} compared to the calculated distribution for the same energy. Since, as mentioned before, the calculations gave only the Compton distribution and the value of the photofraction, a gaussian distribution with the same standard deviation as the experimental data was assumed for the total-absorption peak. The curves shown are (1) the calculated distribution with the distribution in the tail presented in histogram form, (2) the distribution for the single 8-in.-dia by 8-in.-long crystal, and (3) the anticoincidence distribution

4. Carlson, R. W., McGoff, D. J., and Sapir, J. L., Gamma-Ray Scattering and Penetration in a Lead Collimator, EPS-X-393, MIT Practice School, ORGDP (Dec. 1, 1958).

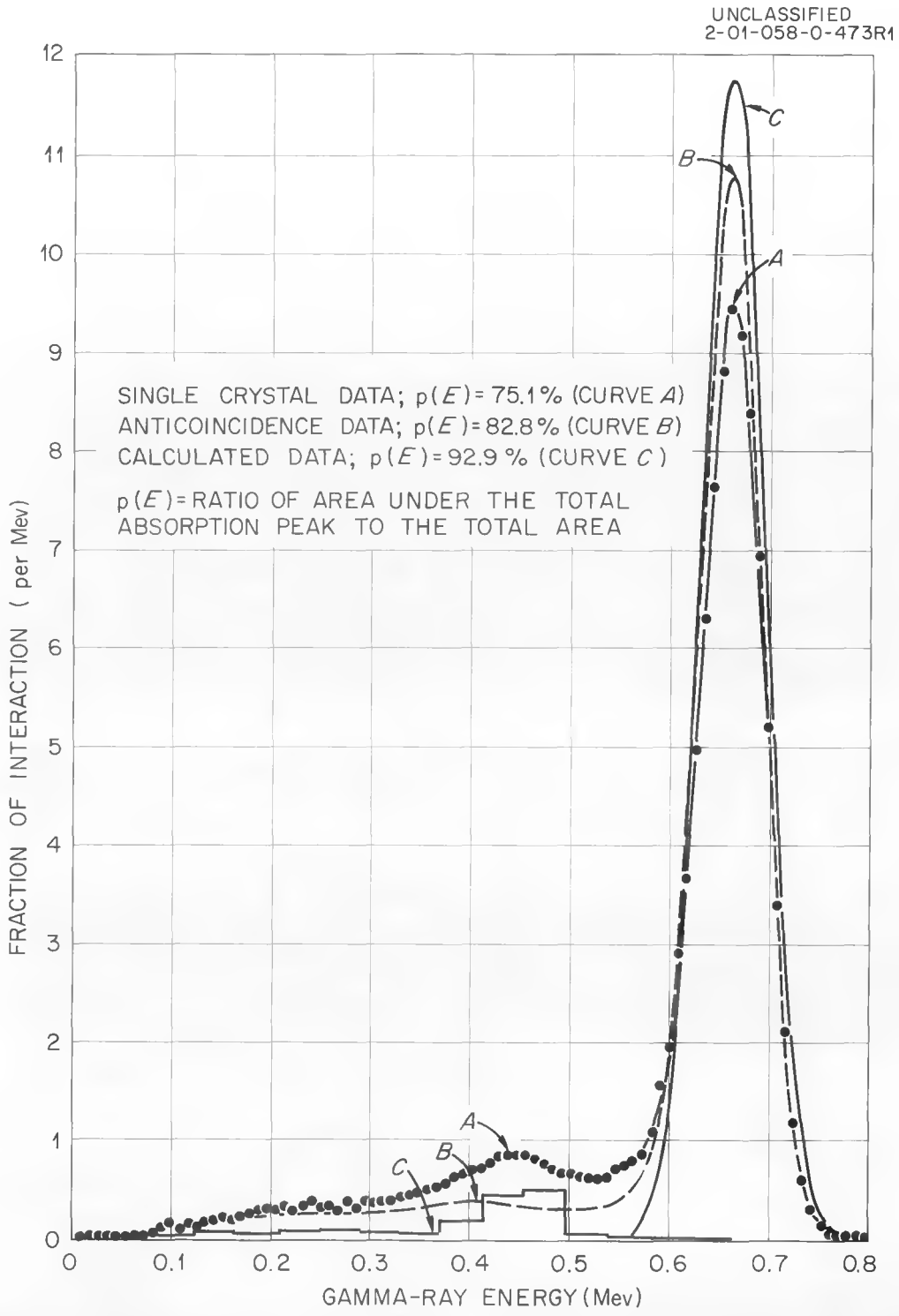

Fig. 2. Calculated and Experimental Response of an 8-in.-dia. by 8-in.-long NaI(Tl) Crystal to the 0.662-Mev Gamma Ray from Cs^{137}

for the large crystal taken with the gamma rays collimated through the small, 2-in.-thick crystal mentioned before. Note that the anticoincidence data almost eliminates the small back-scattered peak found at about 0.45 Mev in the data for the composite crystal alone. This implies that the addition of a well in the end of the composite crystal would increase the peak-to-total ratio. The measured distribution, in general, is reproduced by the calculated distribution except for the region between 0.5 and 0.6 Mev. This region in the experimental data probably is the result of those gamma rays which have been degraded in energy by scattering in the collimator and would not appear in the calculated distribution.

Figure 3 shows the measured distribution compared to the calculated distribution for the 1.368- and 2.754-Mev gamma rays from the decay of Na^{24}. The curve with the data points shows the distribution obtained experimentally with the gamma rays collimated into the crystal along the axis. The other curve is the calculated distribution. The experimental data shows a small peak just below the 2.754-Mev peak which is lower in energy than the peak of the Compton distribution indicated by the calculation. Since at this energy the pair process is important, it is thought that the experimental Compton distribution is smeared out between the first-escape peak and the total-absorption peak. At the lower energy of 1.368 Mev, where the effects of pair production are not so important, it will be noticed that the calculated Compton distribution follows more closely in shape the experimental distribution. The small peak at a little in excess of 0.5 Mev is probably an annihilation radiation peak from the lead of the collimator and shield wall and is not expected to appear in the calculations.

It should be emphasized again that the 8-in.-dia by 8-in.-long crystal reported on here was a composite of two smaller crystals optically coupled together. Although the effects of the interface formed by coupling two crystals together has not yet been studied to any extent, the over-all response of the composite crystal discussed here has been much more satisfactory than that of the conically ended crystals. It thus appears that it is possible to produce large, usable, total-absorption crystals by this method.

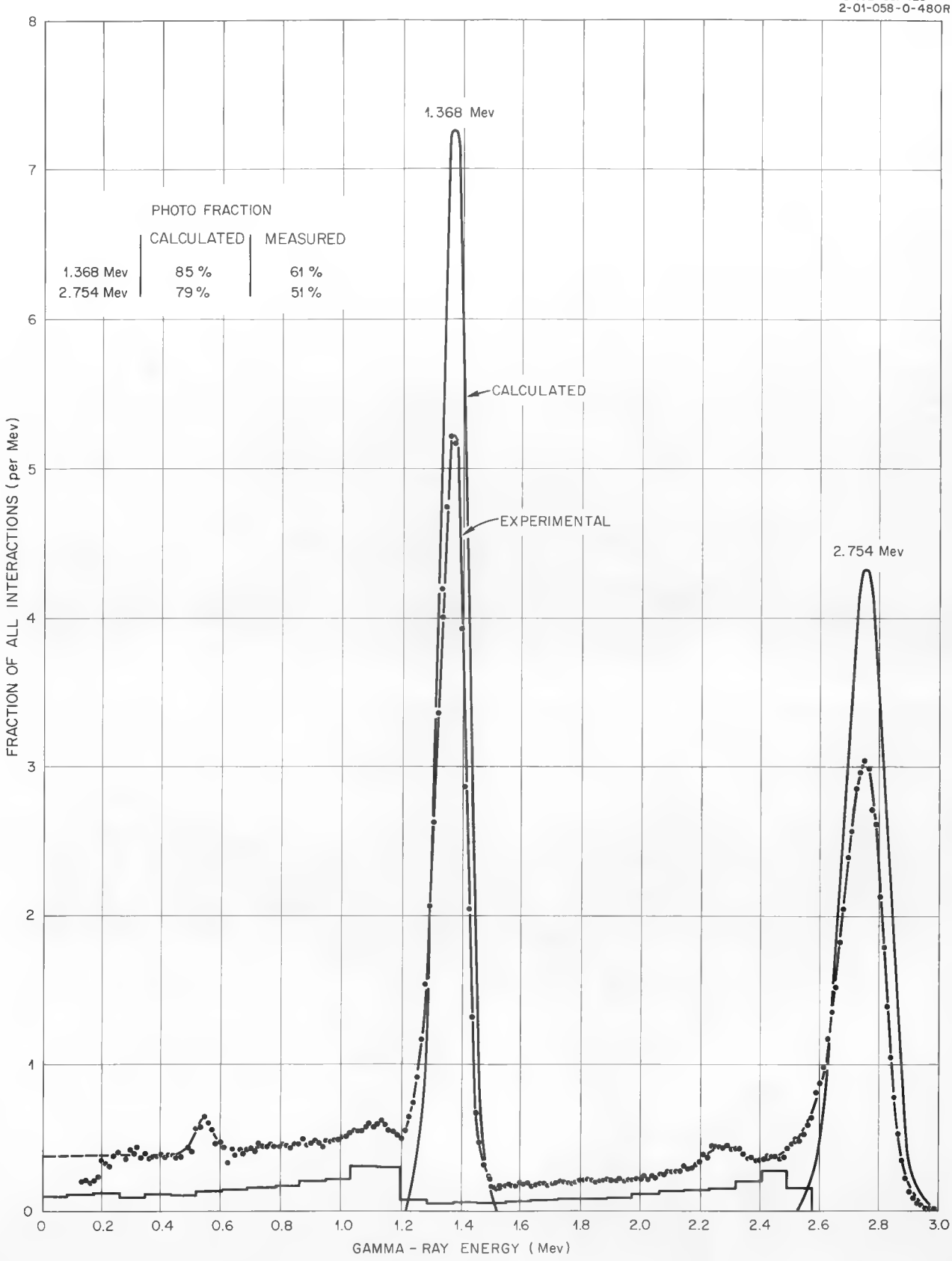

Fig. 3. Comparison of Calculated Response to Measured Response for Collimated Na^{24} Gamma Rays Incident Along the Axis of an 8-in.-dia by 8-in.-long Na(Tl) Crystal

5. EFFECTIVE NEUTRON REMOVAL CROSS SECTION OF ZIRCONIUM

J. M. Miller

Oak Ridge National Laboratory
Oak Ridge, Tennessee

EFFECTIVE NEUTRON REMOVAL CROSS SECTION OF ZIRCONIUM

by

J. M. Miller

Oak Ridge National Laboratory*
Oak Ridge, Tennessee

The effective removal cross section of zirconium has been determined as 2.36 ± 0.12 barns on the basis of thermal-neutron flux measurements made at the LTSF beyond two slabs of zirconium (1.8 wt% hafnium), each 54 by 49 by 2 in. A mass attenuation coefficient (Σ_R/ρ) based upon the removal cross section and a measured density of 6.54 g/cm^3 is (1.56 ± 0.08) x 10^{-2} cm^2/g.

The effective neutron removal cross section, defined as the equivalent absorption cross section which most nearly describes the fast-neutron attenuation of a material added to hydrogeneous shield, has previously been measured for a wide variety of elements.[1] In an attempt to narrow the rather broad region between Z = 29 and Z = 74, for which no cross sections were recorded, a measurement of the effective removal cross section of zirconium (Z = 40) has recently been made at the Lid Tank Shielding Facility.

The zirconium used in the experiment is in the form of two slabs, each 54 by 49 by 2 in. The metal contains 1.8 wt% hafnium as the main impurity and has a density of 6.54 g/cm^3.

The dry sample was placed at the source plate end of the usual steel configuration tank[2] in the Lid Tank, and was followed by an aluminum tank (1/8-in.-thick walls) containing light water. Thermal-neutron flux measurements were made on the axis of the source plate in the water beyond the material, and are compared with measurements made with the zirconium removed in Fig. 1. Standard instrumentation, including a 12-1/2-in. BF_3 counter, a 3-in. fission chamber, and a 1/2-in. fission chamber, was used.

---

* Operated by Union Carbide Corporation for the U. S. Atomic Energy Commission

1. Chapman, G. T. and Storrs, C. L., Effective Neutron Removal Cross Sections for Shielding, ORNL-1843 (1955).
2. This tank has a 3/8-in.-thick aluminum window in the side next to the source plate.

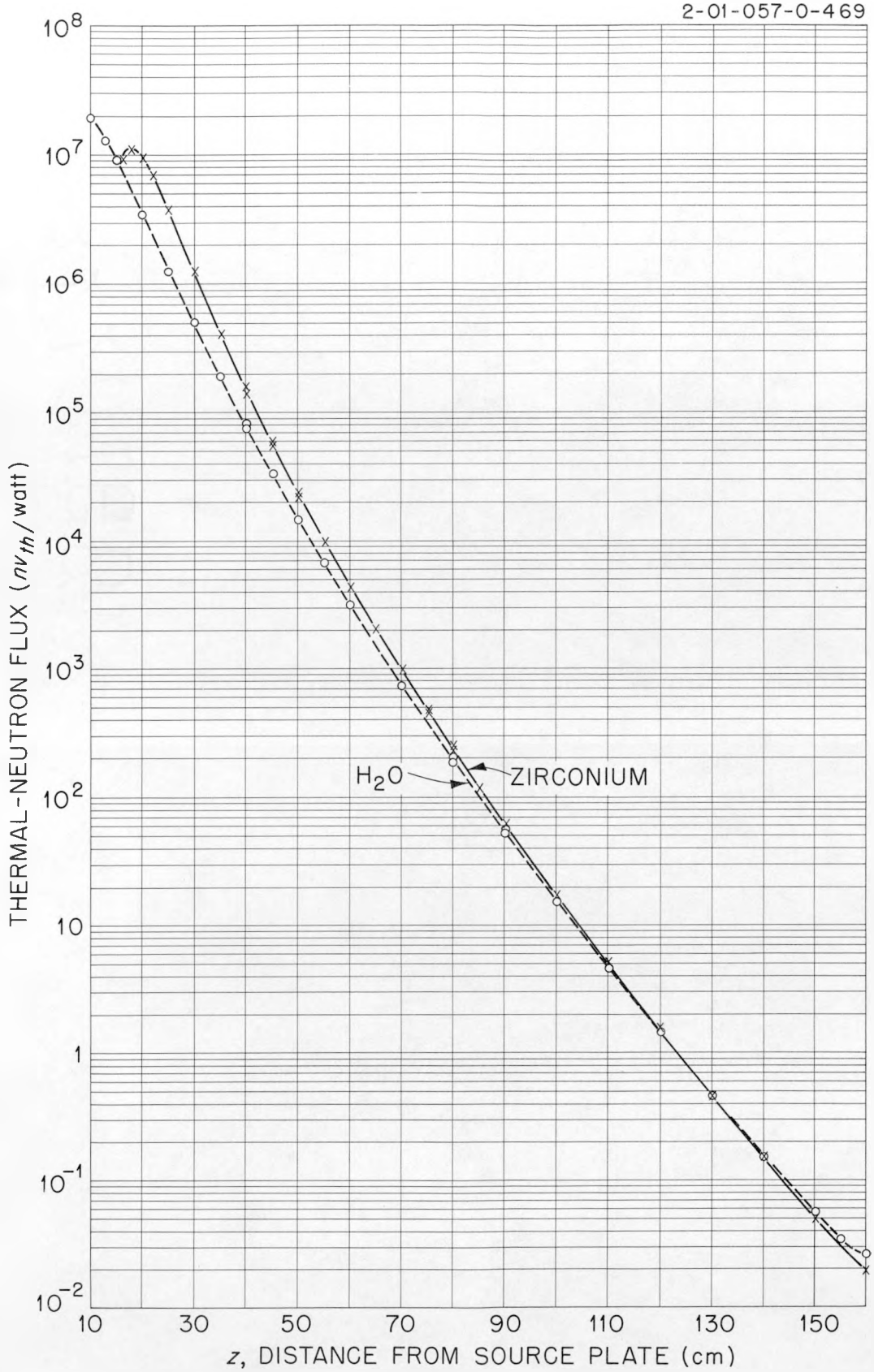

Fig. 1. Thermal-Neutron Flux Measurements in Water Beyond 4 in. of Zirconium

The effective removal cross section of the zirconium was calculated from these measurements by use of a formula due to Blizard.[3] The resulting value was 2.36 ± 0.12 barns. The value of the mass attenuation coefficient of zirconium $[\Sigma_R/\rho = (1.56 \pm 0.08) \times 10^{-2}\ cm^2/g]$ calculated from these data is in excellent agreement with the predicted value deduced from published curves.[4]

---

3. Blizard, E. P., Procedure for Obtaining Effective Removal Cross Sections From Lid Tank Data, ORNL-CF-54-6-164 (1954).

4. Blizard, E. P., Proc. U.N. Intern. Conf. Peaceful Uses Atomic Energy, 2nd, Geneva, 1958, P/2162.

6. PREDICTION OF THERMAL-NEUTRON FLUXES IN THE BSF FROM LTSF DATA

E. P. Blizard
A. D. MacKellar

Oak Ridge National Laboratory
Oak Ridge, Tennessee

PREDICTION OF THERMAL-NEUTRON FLUXES IN THE BSF FROM LTSF DATA

by

E. P. Blizard and A. D. MacKellar
Oak Ridge National Laboratory*
Oak Ridge, Tennessee

Predictions of the thermal-neutron fluxes to be expected near the Bulk Shielding Reactor were made on the basis of Lid Tank Shielding Facility experimental data transformed to the BSR geometry. The predicted fluxes are higher than the measured fluxes by 15 to 25% for distances closer than 60 cm, but they are essentially in agreement for larger distances. At a distance of 125 cm the predicted flux was only 1% too low.

In order to obtain the maximum usefulness from shielding data collected at either the Lid Tank Shielding Facility (LTSF) or the Bulk Shielding Facility (BSF), the power of the experimental source must be accurately known. Furthermore, the data must be correctly converted by geometrical transformations from the experimental source to the reactor for which the shield is being designed. One method for checking the powers quoted for the LTSF source (a disk-shaped uranium plate) and the BSF reactor, as well as a method for checking on the validity of the geometrical transformations, is to perform a calculation predicting the neutron flux in the BSF on the basis of LTSF data transformed first to a point-to-point kernel and then to the geometry of the BSF reactor. A discrepancy between the predicted and the measured fluxes would indicate either that one of the quoted powers was in error or that the geometrical transformations were not properly derived.

A calculation[1] that compared the fast-neutron doses was performed in 1952. Since neither the power of the Bulk Shielding Reactor (BSR) nor the power of the LTSF source plate was accurately known at that time, it was not surprising that the calculated and experimental results were not in agreement. Re-estimates of both the power of the BSR[2] and the power of the LTSF source plate[3] have since become available, however, and a second calculation has been made in which the thermal-neutron fluxes at the two facilities have been compared.

Before a conversion from LTSF data to BSF data could be made it was necessary to obtain information about the self-attenuation of neutrons inside the BSR. This was done by placing an all-aluminum mockup of one layer of fuel elements of the BSR adjacent to the source plate in the LTSF and taking thermal-neutron measurements in the water beyond the mockup. Three configurations

*Operated by Union Carbide Corporation for the U. S. Atomic Energy Commission.

were used: no mockup; a nine-plate mockup (one-half of a layer of elements); and an 18-plate mockup (a full layer of elements). The resulting data for a plane-disk source were converted to a point-source geometry by standard transformations for the three configurations measured. The data were then extrapolated to a reactor loading with a six-element thickness, which was the thickness of the loading for which BSR experimental data were available, and the thermal-neutron flux in the BSF was calculated from the following equation:

$$D(R) = \int_{\text{Reactor volume}} P(R_1)\, G(R_1,R)\, dV$$

where

$D(R)$ = flux in water at a distance R from the face of the reactor,

R_1 = distance from the face of the reactor to a point inside the reactor,

$P(R_1)$ = power distribution in the reactor,

$G(R_1,R)$ = attenuation kernel for a medium made up of an R_1 thickness of reactor material and an R thickness of water.

Since the power distribution through the BSF reactor was irregular, a single mathematical expression could not be obtained for the entire reactor. Therefore, the reactor was divided into 304 volume elements, and the power in each volume element was computed. These calculations were based on mappings of the thermal-neutron fluxes in the reactor that were reported by Johnson.[2]

The results of the calculation are compared with experimental measurements in Table I and Fig. 1. At a distance of 25 cm from the reactor the predicted flux is too high by a factor of 1.21, while for a distance of 125 cm the predicted flux is too low by 1%. The agreement between the measured and calculated fluxes appears to be good for the larger distances, but there is a discrepancy of 15 to 25% for distances closer than 60 cm from the reactor. There is a possibility that the size of volume element used in the approximate integration over the reactor was too large to be accurate for these distances, or that extrapolation errors of the attenuation kernels were greater for closer distances Also, the possibility of the source calibration being in error is not completely discounted. This will be partially answered by a recalibration of the BSR now being planned.

The details of this calculation are presented elsewhere.[4]

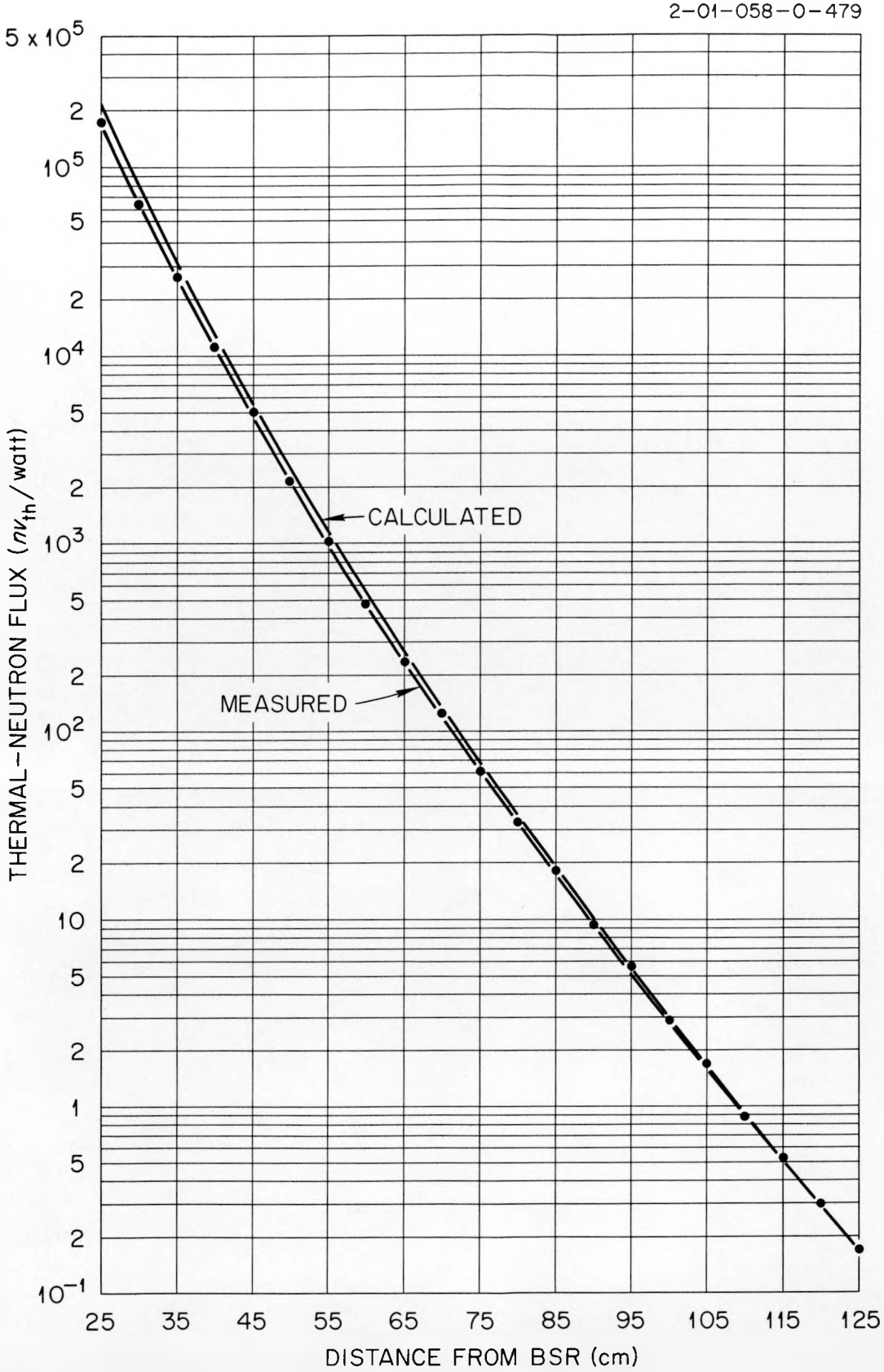

Fig. 1. Comparison of Predicted and Measured Thermal-Neutron Fluxes near the Bulk Shielding Reactor

TABLE I. Predicted and Measured Thermal-Neutron Fluxes in BSF

Distance from BSR (cm)	Thermal-Neutron Flux, (nv_{th}/watt)		Ratio of Calculated Flux to Measured Flux
	Calculated	Measured	
25	2.151×10^{5}	1.78×10^{5}	1.21
30	8.140×10^{4}	6.49×10^{4}	1.25
35	3.235×10^{4}	2.67×10^{4}	1.21
40	1.342×10^{4}	1.13×10^{4}	1.19
45	5.741×10^{3}	5.11×10^{3}	1.12
50	2.558×10^{3}	2.18×10^{3}	1.17
55	1.178×10^{3}	1.06×10^{3}	1.11
60	5.648×10^{2}	4.81×10^{2}	1.17
65	2.701×10^{2}	2.38×10^{2}	1.14
70	1.372×10^{2}	1.25×10^{2}	1.10
75	6.981×10^{1}	6.11×10^{1}	1.14
80	3.616×10^{1}	3.29×10^{1}	1.10
85	1.968×10^{1}	1.82×10^{1}	1.08
90	1.013×10^{1}	9.33×10^{0}	1.09
95	5.466×10^{0}	5.55×10^{0}	0.98
100	3.017×10^{0}	2.85×10^{0}	1.06
105	1.666×10^{0}	1.67×10^{0}	1.00
110	9.282×10^{-1}	8.89×10^{-1}	1.04
115	5.232×10^{-1}	5.233×10^{-1}	1.00
120	2.930×10^{-1}	2.94×10^{-1}	1.00
125	1.664×10^{-1}	1.685×10^{-1}	0.99

REFERENCES

1. T. A. Welton and E. P. Blizard, Reactor Sci. Technol. 2, No. 2, p. 73 (1952) (Classified).

2. E. B. Johnson, Power Calibration for BSR Loading 33, ORNL-CF-57-11-30 (1957).

3. D. R. Otis, Lid Tank Shielding Facility at the Oak Ridge National Laboratory, Part II, Determination of the Fission Rate of the Source Plate, ORNL-2350 (1959).

4. A. D. MacKellar, Prediction of Thermal-Neutron Fluxes Near the Bulk Shielding Reactor from Lid Tank Shielding Facility Data, ORNL-CF-59-1-24 (to be published).

7. MONTE CARLO CODE FOR THE CALCULATION OF RESPONSE FUNCTIONS OF GAMMA-RAY SCINTILLATION DETECTORS

C. D. Zerby

Oak Ridge National Laboratory
Oak Ridge, Tennessee

MONTE CARLO CODE FOR THE CALCULATION OF RESPONSE FUNCTIONS OF GAMMA-RAY SCINTILLATION DETECTORS

by

C. D. Zerby

Oak Ridge National Laboratory*
Oak Ridge, Tennessee

A Monte Carlo code has been written for the IBM-704 computer for calculations of the gamma-ray response functions of NaI and xylene scintillation counters. The counter geometry can be either a right cylinder or a right cylinder with one conical end. The source is restricted to a monoenergetic source of arbitrarily chosen energy in the range from 0.005 to 10.0 Mev. The treatment of the primary incident radiation takes into account Compton scattering, pair production, and the photoelectric effect. The secondary Bremsstrahlung and annihilation radiation are also taken into account in the case of a NaI crystal. The particular Monte Carlo method used is designed for minimum statistical error in the so-called "Compton tail" of the spectrum.

This paper describes a Monte Carlo code for the IBM-704 which has been developed at Oak Ridge National Laboratory to calculate the response functions of gamma-ray scintillation detectors.

This computation is not unique in many respects as other installations have carried out similar calculations. Notable among these is the work of Berger and Doggett[1] at the National Bureau of Standards and the recent work of Miller and Snow[2] at Argonne National Laboratory. However, the calculation described here has several features that make it sufficiently different to warrant a general description.

In order to encompass a variety of detector shapes which seem to be of interest to those working with the detectors, the geometry shown in Fig. 1 has been adopted. It can be seen from the figure that it is possible to investigate the large, so-called "total absorption" NaI crystals with truncated conical ends and a hole in the incident face. The letters shown in Fig. 1 designate certain unrestricted input parameters to the code. Thus, for instance, one could investigate cylindrical detectors by setting the parameters D, F, and E equal to zero.

---

*Operated by Union Carbide Corporation for the U.S. Atomic Energy Commission.

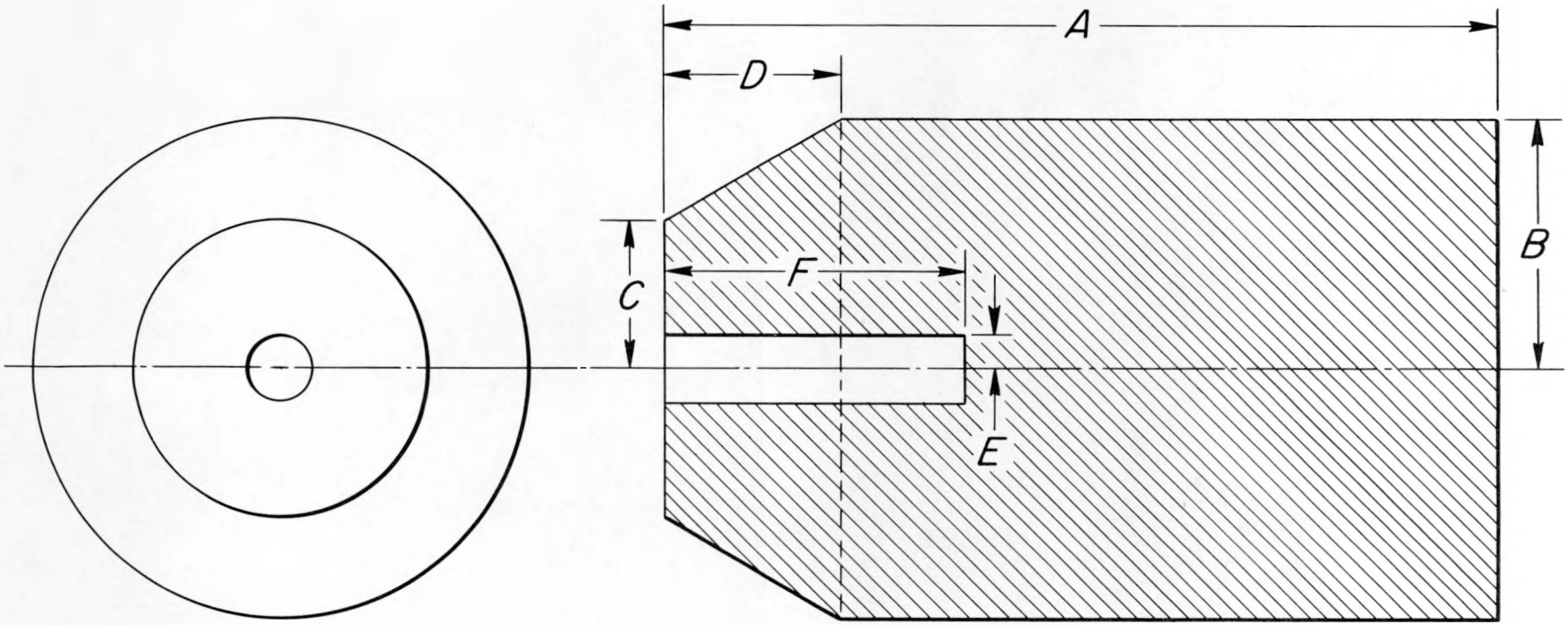

Fig. 1. Assumed Counter Geometry for Calculations of Scintillation Counter Gamma-Ray Response Functions

Figure 2 shows the three possible source configurations allowed by the code. In each case the source radiation is assumed to be monoenergetic in the range from 5 Kev to 10 Mev.

At present there are two versions of the calculation. The first one which is a production code does not include the energy losses from the detector resulting from secondary Bremsstrahlung or annihilation radiation and is therefore restricted to source energies below approximately 2 Mev. The primary, or source, radiation is treated as completely as possible taking into account the Compton scattering, pair production and photoelectric effect. The latter two effects are treated as total absorption processes. Two materials for the detector are at the option of the user of the code. These are Xylene and NaI.

The second version of the code which is within a few days of becoming a production code takes into account the secondary annihilation radiation and Bremsstrahlung losses. In this connection the very fine work of Williams and Snow[2] who have just recently completed a similar calculation for cylindrical NaI crystals should be noted.

The second version of the code, in its final form, will consist of three packages to compute the response from either NaI, Xylene, or CsI.

It is not necessary to go into detail on the Monte Carlo techniques used in this calculation as there is nothing unusual in the technique except for its application to the type of detector problem considered here. In essence, it is a statistical estimation method which was designed to minimize the variance of the response function in the so-called Compton tail.

The results obtained from the calculation include the intrinsic efficiency, the photofraction (also called the peak-to-total ratio) and the shape of the Compton tail in histogram form. The histogram is given in two forms, the first is for an ideal instrument-detector combination and the second is the response function broadened by a gaussian weighting factor which should correspond to the actual response observed during an experiment.

In Fig. 3 the photofraction obtained from this calculation for the case of a right cylindrical NaI crystal are compared with published results from two calculations and an experiment. No comparisons of the intrinsic efficiency are given as it is calculated analytically in the present calculation and is as accurate as the known cross sections will permit.

Figures 4, 5, and 6 show some results obtained from the calculation using a NaI crystal with a hole in the incident face. The object here was to investigate the effect of the depth of hole, length, and diameter on the resulting response function.

In Fig. 4 the main body of the crystal was kept constant and cylindrical sections containing 1.5-cm-dia holes along their axes were added to the incident face. Since the incident radiation was monodirectional and confined to a 1.0-cm diameter, the incident radiation always hit the same surface.

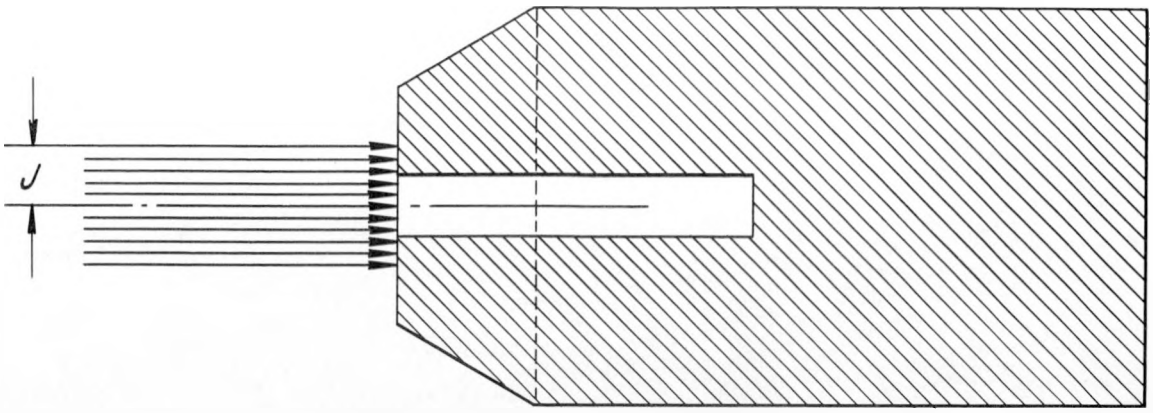

(a) MONODIRECTIONAL SOURCE

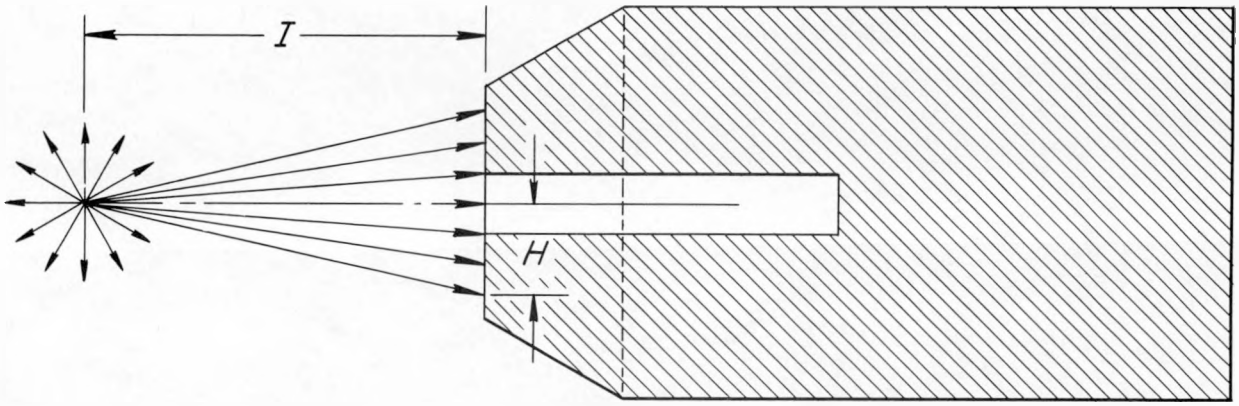

(b) CONICAL EXTERIOR SOURCE

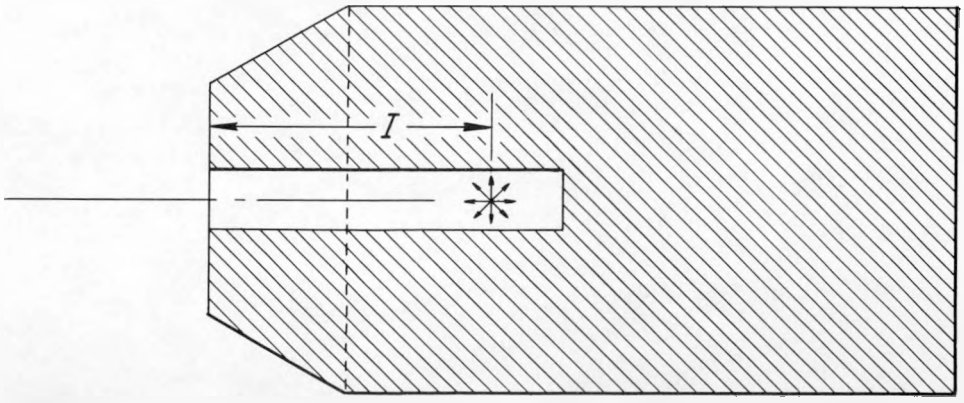

(c) POINT ISOTROPIC INTERIOR SOURCE

Fig. 2. Assumed Source-Counter Geometries for Calculations of Scintillation Counter Gamma-Ray Response Functions

Comparison of Experimental and Calculated Photofractions for a 4-in.-dia by 4-in.-long Cylindrical NaI Crystal with Monoenergetic Point Isotropic Source 30 in. from End of Crystal[a]

Author(s)	Photofraction	
	1.33-Mev Source	0.661-Mev Source
Kreger[b] (exp)	0.54	0.725
Miller et al.[c] (calc)	0.599	0.777
Berger and Doggett[d] (calc)	0.58	0.74
Present calculation	0.582	0.784

a. That is, conical exterior source geometry; 0.625-in. beam radius at crystal face.

b. E. W. Kreger, Phys. Rev. 96, 1554 (1954).

c. W. F. Miller, J. Reynolds, and W. J. Snow, Efficiencies and Photofractions for Gamma Radiation in Sodium Iodide (Thallium Activated) Crystals, ANL-5902 (1958).

d. M. J. Berger and J. Doggett, Rev. Sci. Instr. 27, 269 (1956).

Fig. 3

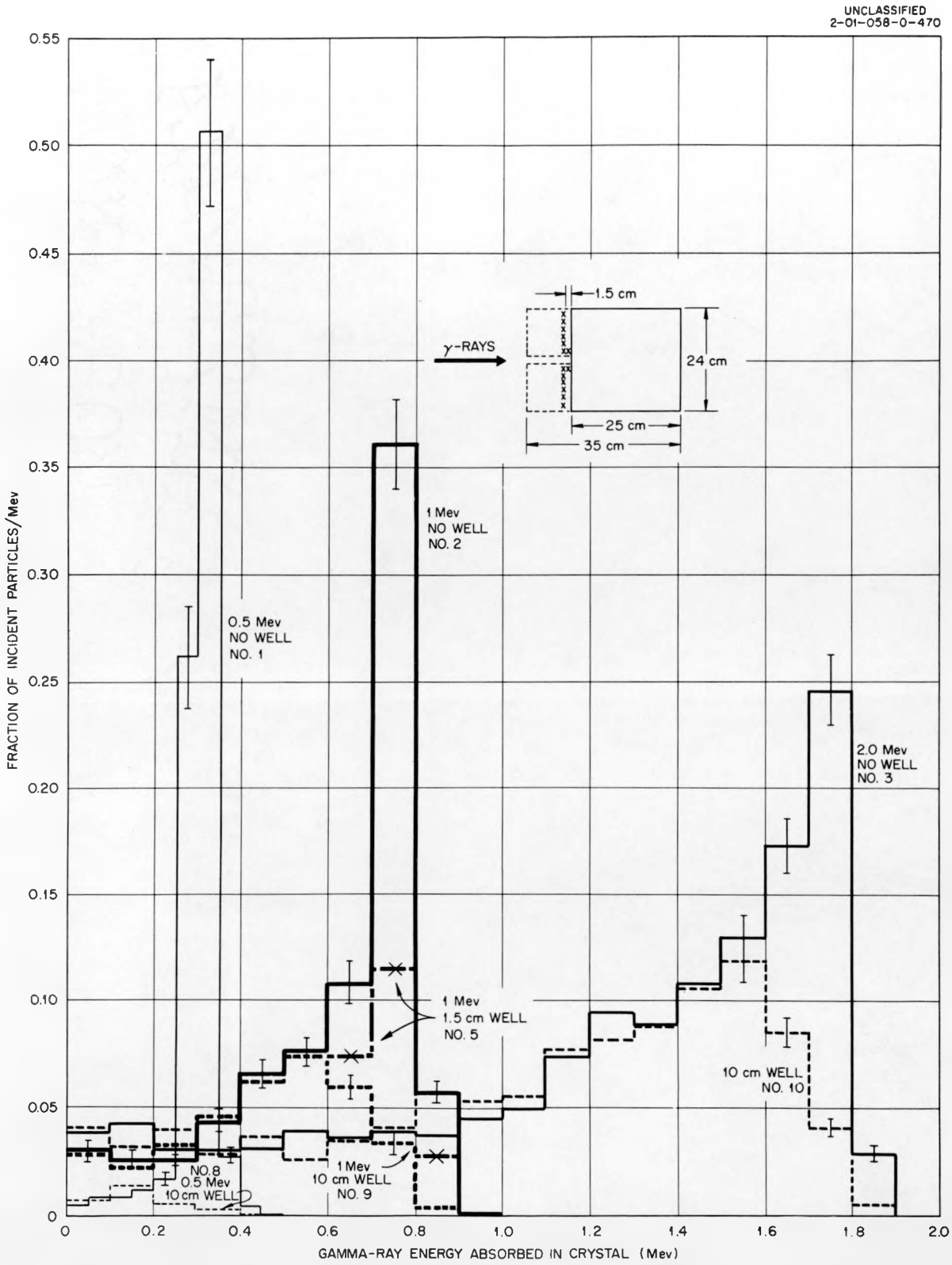

Fig. 4. Absorption of 0.5-, 1.0-, and 2.0-Mev Gamma Rays in a 24-cm-dia by 25-cm-long NaI(Tl) Crystal: Effect of Well on Predicted Tail Spectra

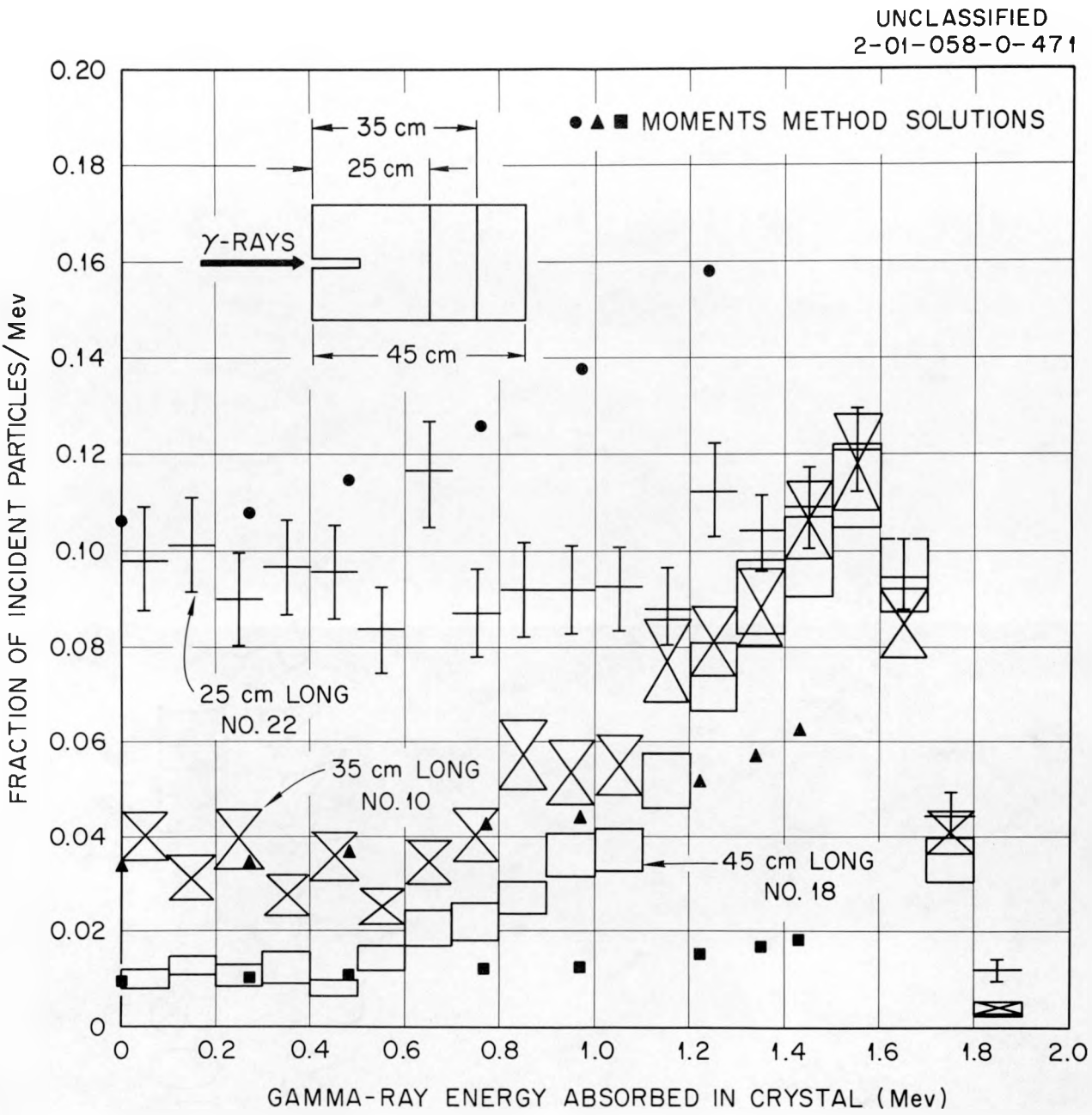

Fig. 5. Absorption of 2-Mev Gamma Rays in 24-cm-dia NaI(Tl) Crystals with 10-cm-deep Wells: Effect of Crystal Length on Predicted Tail Spectra

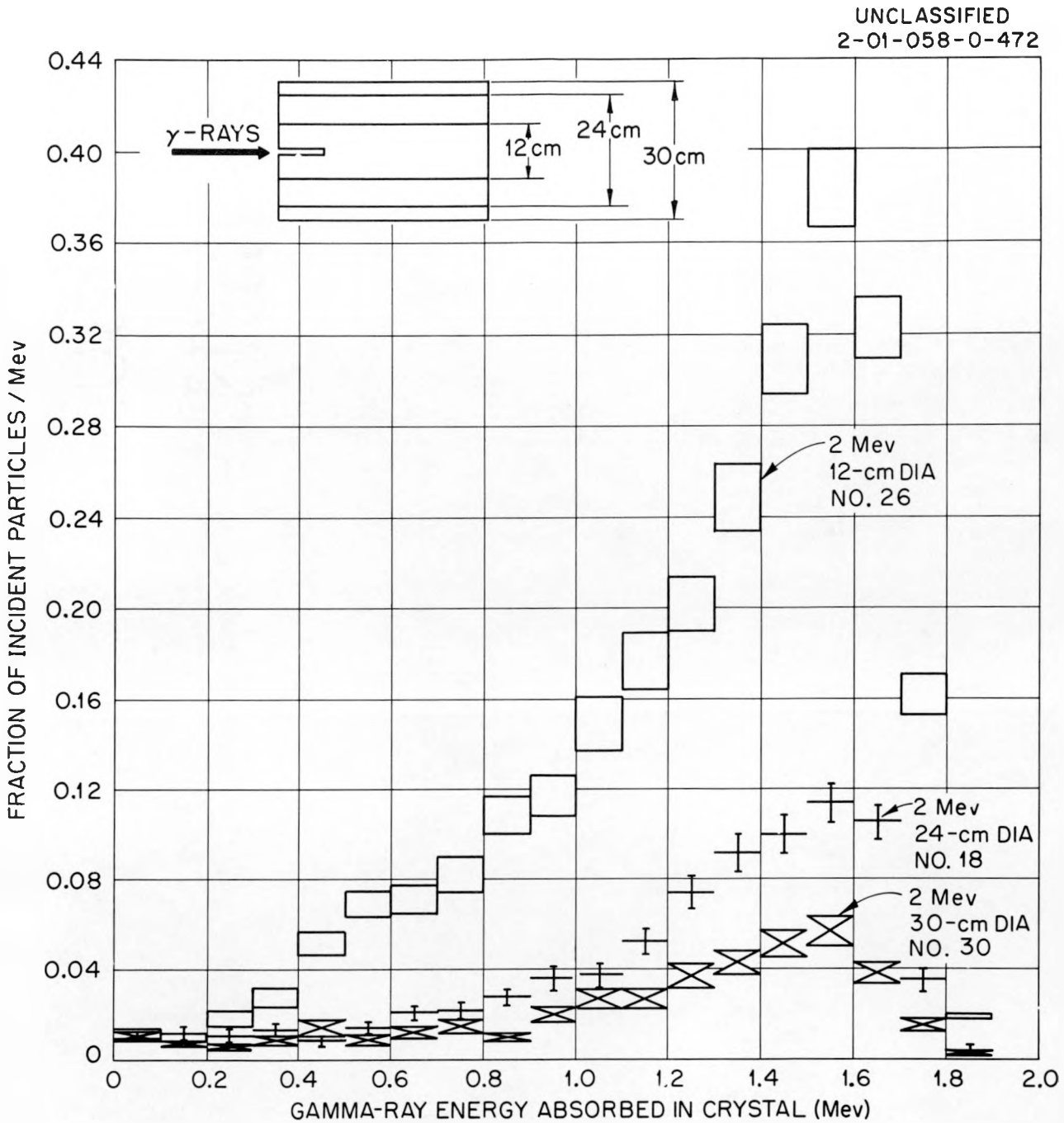

Fig. 6. Absorption of 2-Mev Gamma Rays in 45-cm-long NaI(Tl) Crystals with 10-cm-deep Wells: Effect of Crystal Diameter on Predicted Tail Spectra

At each of the three source energies shown in Fig. 4 one can see the reduction of the response function at the high-energy end as the hole depth is increased. This reduction corresponds to a reduction of losses of back-scattered radiation.

Figure 5 shows the effect of the length on the response function. As the length is increased the low-energy end of the response function is reduced, corresponding to a reduction in losses of forward-scattered gamma rays.

Figure 6 shows the effect of the diameter on the response function. As the diameter is increased the intermediate-energy gamma-ray loss is reduced and the sections of the response function curves affected by these gamma rays are correspondingly reduced.

REFERENCES

1. M. J. Berger and J. Doggett, J. Natl. Bureau Standards 56 (1956).

2. W. F. Miller and W. J. Snow, to be published.

8. DETERMINATION OF NEUTRON AND SECONDARY PHOTON SPECTRA FROM A THICK LAMINATED SHIELD WITH SPHERICAL SYMMETRY

U. S. Naval Air Development Center
Johnsville, Pennsylvania

U. S. NAVAL AIR DEVELOPMENT CENTER
JOHNSVILLE, PENNSYLVANIA

AC-31
2 October 1959

ACLTN NO. 59-55-06

Subj: Summary of Aeronautical Computer Laboratory Methods for the Determination of the Neutron and Photon Spectra Emerging from a Thick Laminated Shield with Spherical Symmetry

Ref: (a) WADC TR 58-80 of Apr 58
(b) ACLTN No. 59-55-04
(c) AEC Rpt. LA-1891 of Feb 55
(d) ACLTN No. 59-55-05

1. This note gives in rather general terms, an account of the Aeronautical Computer Laboratory's (ACL) methods which are being or which are expected be used in the determination of the neutron and secondary photon spectra (with respect to energy and direction) emerging from a thick laminated (lead-water) shield with spherical symmetry. Neutron source spectra are given at the surface of the core, assumed to be those existing in the presence of the shield. This work has been carried out under an ANP shielding program sponsored by the Bureau of Aeronautics.

2. The problem falls naturally into two parts, the neutron problem and the secondary photon problem. In order to determine the emergent secondary photon spectrum, it is necessary first to find the neutron fluxes throughout the shield, which may be done as part of the neutron problem. These neutron fluxes are used to provide secondary photon source data.

3. As used here, the term "thick" means that the neutron problem qualifies as a deep penetration case (the attenuation is $>>10^4$) and that the emergent primary photon density is probably negligible compared to the emergent secondary photon density. The primary photons will not be dealt with in this paper.

4. It was determined that procedures which were available at the time the program was started, over a year ago, were not adequate to solve the neutron problem, using the equipment at hand in ACL. On the other hand, it appeared that the photon problem could be solved on the available IBM 650 RAMAC computer, using a properly designed Monte Carlo program. Such a program has been evolved. In order to test out this program and to obtain initial estimates of the emergent secondary photon spectrum, the Monte Carlo program is being applied by using photon source data obtained from neutron fluxes calculated by a combination of age and diffusion theory. These fluxes were calculated so as to provide a fit to measurements made outside a mockup of the shield. (Actually, the particular shield configuration used was chosen because measurements existed for it.)

5. The secondary photon Monte Carlo program makes considerable use of the techniques developed by Technical Research Group (TRG), reference (a), which in this case were applied only to a slab geometry. The ACL method was developed for the extreme complications encountered when solving the finite media--spherical shield case. Photon histories are taken in groups according to the layer of material in which the photon originates and the initial energy of the photon. Location of the photon within the layer is determined by random sampling from a source density distribution which is approximated linearly within the layer. The initial direction of motion and the length of first path is obtained by a combination of systematic and importance sampling. The photon is never allowed to be absorbed, to produce pairs, to escape, or to penetrate the core; i.e., all collisions are scattering collisions and the photon always undergoes collision. Escape probabilities are taken care of by tabulating emergent photon of appropriate weight, direction, and energy. Absorption is accounted for by adjusting the weight of the scattered photon, while pair production is taken care of by tabulating a photon of the appropriate weight and location. Importance sampling is used in determining the direction of scattering in order to favor scattering radially outwards while it is also used in determining path lengths between collisions so as to favor longer paths when travelling outwards and shorter paths when travelling inwards. Histories may be terminated when the energy or weight of the photon falls below predetermined amounts. In the first case (energy) the history ends; in the second (weight) Russian roulette is applied to the weight. A detailed description of the entire procedure is given in reference (b), (ACLTN No. 59-55-04).

6. Up to the present, results of the Monte Carlo program have been, on the whole, encouraging. On the average, the history of each initial photon lasts about 15 to 25 seconds of machine time, with a collision occurring about every three to five seconds, accompanied by output. It is not yet clear how many histories will be required in order to reduce the variance within acceptable limits, as sufficient data has not yet been accumulated. At this point, the length of machine time which will be required for the program may be estimated as about five weeks.

7. After an earlier study of more or less straightforward applications of Monte Carlo method to the neutron problem, the conclusion was reached that such a procedure is not likely to be successful with the techniques available at that time using the basic IBM 650. Attention was focussed on a direct attack upon the transport equation. The transport equation for this problem is an integro-differential equation involving simultaneous integration of two variables. Two approaches have been considered, use of a modification of the Carlson S_n method and a direct analytical solution.

8. Basically standard DC analog computers integrate with respect to time. Certain techniques are available to permit integration with respect to a variable which can be expressed as a function of time. This is done at the cost of additional equipment and complexity. Integration in two directions simultaneously where the integrations are not completely independent would require such large complexes of equipment for this size problem that it would never be undertaken. Therefore, only by the development of new specialized techniques can this type problem be handled on analog equipment. ACL has for some time believed that this can best be done by the marriage of analog and digital equipment and techniques. Toward this end ACL has designed equipments and techniques based on this philosophy. Their use in this problem as described below gives promise of success.

9. The Carlson S_n method is described in reference (c), (AEC Rpt. LA-1891 of Feb 55) and outlined in several texts. Where scattering is assumed to be isotropic in the laboratory system (or where an approximation which integrates out the effect of direction may be used) the method results in a series of first order equations, one set for each energy group into which the energy domain is divided. The dependent variables are the neutron densities along n directions, as functions of radius. It is assumed that the neutron densities vary linearly with direction between the values along the n directions chosen. If an initial set of neutron densities is assumed, an iterative procedure generates new sets. One of the convenient features of the method is that the solution of each set of equations proceeds successively instead of simultaneously. Incidentally, anisotropy can be taken into consideration at the cost of some additional complexity in the equations.

10. Carlson's method is normally carried through on digital computers and appears to require fairly high speed and large memory equipment. However, the set of equations occurring in Carlson's method is of a type which can be conveniently handled on analog equipment. It is true that some complications arise. First, since a set of equations occurs for each energy group, it is necessary to set up an analog for all sets at the same time or to have some means of storing and applying the results from one energy group to the next. Second, the nature of the boundary conditions requires that integration be in the direction of decreasing radius for certain directions of neutron motion and in the direction of increasing radius for the rest. Finally, a scale problem may arise, since an analog computer operates over a much smaller range of values than most digital machines.

11. To set up a simultaneous analog for all of the sets of equations would require a very large amount of equipment. On the other hand, the amount of equipment required for an analog of the equations for one

energy group is modest. The output obtained in the solution of the equations for one energy group is used in solving the equations for all lower en groups. Thus, in this case, it would be necessary to store and play back all such output. Equipment capable of this performance has been designed by ACL and will be available for use in the near future. It consists of analog-digital and digital-analog conversion units and digital tape record-playback equipment. In operation, the voltages coming out of the analog computer are digitized and recorded. Playback is made through a digital-analog converter. The tape equipment is capable of recording or playing back as many as 15,000 quantities per second, distributed over as many as 50 variables. Accuracy is at least equal to that of the analog computer itself.

12. In order to handle the Carlson equations, it will be necessary to make use of the linearity of the equations. Some form of superposition procedure will probably be used. At worst, an iterative process may be set up, involving successive integrations in opposite directions.

13. It is expected that the neutron densities will decrease exponentially with radius. This behavior poses a scaling problem on an analog computer, since neutron densities at the outside surface of the shield in which we are mainly interested, would be below the noise level. In order to meet this difficulty, it has been suggested that an exponential transformation be applied to the neutron density. Such a transformation produces a minor modification in the equations (the total cross-section is changed by an amount proportional to the constant in the exponent). Experimentation would be required during the course of the runs on the analog computer in order to determine optimum values for these constants.

14. It will not be necessary to adhere strictly to the Carlson method in carrying out this procedure. For example, different equations from Carlson's may be obtained by making assumptions different from Carlson's as to the variation of neutron density with direction. In addition, the analog procedure may be applied directly to the transport equation, divided into energy groups. In this case, a much smaller analog could be used and the directional domain could be given a finer subdivision. The integration would proceed radially over successive strips located between suitably chosen values of the directional variable. Directional derivatives would, as before, be represented by finite difference ratios. Although a much larger number of integrations would be required than by the straightforward Carlson scheme, the difficulties previously mentioned involving direction of integration would not arise. Also the scale problem would be easier to handle. However, one added difficulty would arise. In the spherical case, the directional variable would be μ, the cosine of the angle between the radius and the direction at the point considered. The μ domain would extend from -1 to +1. The first

integration would start at the outside radius over a strip in μ lying between -1 and a suitable higher value. If the value $\mu = -1$ were used in the equation, the directional derivative would vanish and there would be no way to continue the process after the first integration. An average μ should be used in order to avoid this, but the result of the integration will still be strongly dependent on the value chosen. This point has yet to be investigated.

15. Aside from its availability, the use of the equipment described previously has the advantage of providing greater speed than conventional digital equipment, but with the disadvantage of lower accuracy. It is clear that error studies will be required.

16. An analytical attack on the transport equation for the conditions of this problem has been made by ACL. This work has been carried out by Dr. Emil Grosswaldwho is a consultant to ACL. He has succeeded in developing a solution for the case of isotropic scattering in the laboratory system (use of the transport approximation is equally feasible). Reference (d) describes this development.

17. The problem treated by this analysis may be stated as follows: The shield consists of concentric spherical shells, each of a given material, bounded by a minimum (core) radius r_o and a maximum (shield surface) radius R. Two functions $\Sigma(r, v)$ and $\uparrow(r, v, w)$ are given, which are step functions in r for constant v and w. Here, r is the radius coordinate, v is the speed of the neutron, and w is the neutron speed prior to an interaction which results in a speed v. The quantity $\Sigma(r, v)$ is the total macroscopic cross section for neutrons of speed v while $\uparrow(r, v, w) = w\, c(w) \Sigma(r, w)\, f(r, v, w)/v$. Here, c(w) is the fraction of interacting neutrons of speed w which are scattered and f(r, v, w) is the fraction of neutrons of speeds between w and w + dw which, when scattered, attain speeds between v and v + dv. The step function behavior in r of $\Sigma(r, v)$ and $\uparrow(r, v, w)$ means simply that, within a layer, Σ and $\uparrow$ may be written as $\Sigma(v)$ and $\uparrow(v, w)$; i.e., for a given material, these properties are functions of energy only. It is desired to find a function $N(r, \mu, v)$ which is defined, continuous, and non-negative in the region given by $r_o \leq r \leq R$, $-1 \leq \mu \leq +1$, (μ has been defined above) and $0 \leq v \leq V$, where V is the maximum neutron speed considered. In addition the first and second partial derivatives of N with respect to r and μ exist in the same region except possibly at the shell interfaces. The boundary

conditions to be satisfied by $N(r, \mu, v)$ are:

$$\lim_{r \to r_o} N(r, \mu, v) = \phi(\mu, v) \qquad (17.1)$$

for $\mu > 0$, and

$$\lim_{r \to R} N(r, \mu, v) = 0 \qquad (17.2)$$

for $\mu \leq 0$

where $\phi(\mu, v)$ is the given neutron spectrum emerging from the core. It can be seen that (17.2) places the shield in a vacuum; i.e., no back scattering occurs. Finally, $N(r, \mu, v)$ satisfies the transport equation.

$$\mu (\partial N/\partial r) + (1 - \mu^2)(\partial N/\partial \mu) / r + \Sigma(r, v)N = 1/2 \int_o^{-V} \left\{ \int_{-1}^{+1} N(r, v, w)dv \right\} \tau(r, v, w)\, dw \qquad (17.3)$$

except possibly at the shell interfaces. Equation (17.3) is the transport equation for the case of scattering which is isotropic in the laboratory system; this is the single limitation, although in some respects an important one.

18. It turns out that, as stated, the problem has in general no solution; the condition of continuity of N with μ cannot be met. If all the other given conditions are retained, N will have at most one finite discontinuity for some $\mu = \mu_o$. On the other hand, if the boundary condition at $r = r_o$ be supplemented by

$$\lim_{r \to r_o} \lim_{\mu \to 0-} N(r, \mu, v) = \lim_{\mu \to 0+} \phi(\mu, v) \qquad (18.1)$$

the condition of continuity on N is met.

19. The solution incorporating the possible discontinuity at $\mu = \mu_o$ falls into three parts, one for each of three regions in μ. For $-1 \leq \mu \leq 0$,

$$N(r, \mu, v) = \exp\left[-\mu r \Sigma(r, v)\right] \int_r^R t(t^2 - r^2 + r^2\mu^2)^{-1/2} \left[\exp\left\{-(t^2 - r^2 + r^2\mu^2)^{1/2} \Sigma(t, v)\right\}\right] \Psi(t, v)\,dt \quad (19.1)$$

For $0 < \mu < \mu_o$,

$$N(r, \mu, v) = \exp\left[-\mu r \Sigma(r, v)\right] \int_{r(1-\mu^2)^{1/2}}^{r} t(t^2 - r^2 + r^2\mu^2)^{-1/2} \left[\exp\left\{-(t^2 - r^2 + r^2\mu^2)^{1/2} \Sigma(t, v)\right\}\right] \Psi(t, v)\,dt$$

$$+ \int_{r(1-\mu^2)^{1/2}}^{R} t(t^2 - r^2 + r^2\mu^2)^{-1/2} \left[\exp\left\{-(t^2 - r^2 + r^2\mu^2)^{1/2} \Sigma(t, v)\right\}\right] \Psi(t, v)\,dt \quad (19.2)$$

For $\mu_o < \mu \leq +1$,

$$N(r, \mu, v) = \exp\left[-\mu r \Sigma(r, v)\right] \left\{ \int_{r_o}^{r} t(t^2 - r^2 + r^2\mu^2)^{-1/2} \Psi(t, v) \exp\left\{(t^2 - r^2 + r^2\mu^2)^{1/2} \Sigma(t, v)\right\} dt + \phi(r^{-1}(r_o^2 - r^2 + r^2\mu^2)^{1/2}, v) \exp\left\{(r_o^2 - r^2 + r^2\mu^2)^{1/2} \Sigma(r_o, v)\right\} \right\} \quad (18.3)$$

In equations (19.1), (19.2), and (19.3), $\Psi(t, v)$ is a bounded, non-negative function, integrable with respect to t, continuous in v, and satisfying the integral equation:

$$\int_v^V \left\{ \int_{r_o}^R \Psi(t, w) G(t, w; r, v)\,dt \right\} dw + F(r, v) = \Psi(r, v) \quad (19.4)$$

where

$$F(r, v) = \int_v^V \Phi(r, w)\, \tau(r, v, w)\, dw \qquad (19.5)$$

$$G(t, w; r, v) = \tau(r, v, w)\, t\, K(t, r, v) \qquad (19.6)$$

In equation (19.5), $\Phi(r, w)$ is given by

$$\Phi(r, v) = 1/2 \int_{\mu_o}^{1} \phi(r_o^{-1}(r_o^2 - r^2 + r^2\mu^2)^{1/2}, v) \exp\left\{-r\mu\, \Sigma(r,v) + (r_o^2 - r^2 + r^2\mu^2)\, \Sigma(r_o, v)\right\} d\mu \qquad (19.7)$$

and in equation (19.6), K (t, r, v) is given by

$$K(t, r, v) = (2r)^{-1} \left\{E\left(-\Sigma(r, v)\left[(r^2 - r_o^2)^{1/2} + (t^2 - r_o^2)^{1/2}\right]\right) - E(-\Sigma(r, v)\,|r - t|)\right. \qquad (19.8)$$

The function E(x) is defined as

$$E(x) = \log x + \sum_{n=0}^{\infty} x^n / n!\, n \qquad (19.9)$$

Note that F(r, v) and G(t, w; r, v) are completely determined by the conditions of the problem.

20. The term $\Psi(t, v)$ has a relationship to N(r, -1, v), the density of inward bound neutrons. Let $N(r, \mu, v) = \exp\{-\Sigma(r, v)\mu r\}$ $N_1(r, \mu, v)$. Then $N_1(r, -1, v) = \exp\{-r\,\Sigma(r, v)\}\ N(r, -1, v)$. Replace r and μ by the variables ρ and u, defined by

$$\rho = r; \qquad u = r^2(1 - \mu^2) \qquad (20.1)$$

Then $N_1(\rho, 0, v) = \exp\{-\rho\,\Sigma(\rho, v)\}\ N(\rho, 0, v)$ (20.2)

Differentiating (20.2) with respect to ρ :

$$(\partial N_1/\partial\rho) = \left[(\partial N/\partial\rho) - \Sigma(\rho, v)\, N\right] \exp\{-\rho\,\Sigma(\rho, v)\} \qquad (20.3)$$

2 October 1959

ACLTN NO. 59-55-06

The quantity in square brackets in (20.3) is defined as $\Psi(\rho, v)$.

21. The integral equation (19.4) possesses a unique solution which can be found by standard means, involving some form of infinite expansion, except for the case where $\lambda = 1$ happens to be an eigenvalue of

$$\lambda \int_{v}^{V} \int_{r_o}^{R} \Psi \, G \, dtdw + F(r, v) = \Psi(r, v) \qquad (21.1)$$

It has not yet been determined how much of a program would be required on the digital computer to carry out the indicated solution. For the present, it appears best to use this solution as a check on some conveniently chosen case which will be solved by the use of our analog computer-digital tape unit combination. The latter scheme can be employed without the restriction of laboratory system isotropy required in Dr. Grosswald's solution. Since our primary interest in the solution of the neutron problem is as a means of obtaining secondary photon sources, it appears that errors would be incurred by making the assumption of isotropy. However, there is no reason why a check could not be had by solving a case in which the isotropy assumption has been made by both methods.

HGT

E. Toll

EUGENE TOLL

9. APPLICATION OF THE CARLSON S_n-METHOD TO SHIELD CALCULATIONS

N. Edmonson, Jr.
J. J. Henrick
T. A. Moss

Convair
A Division of General Dynamics Corporation
Fort Worth, Texas

APPLICATION OF THE CARLSON S_n-METHOD TO SHIELD CALCULATIONS

by

N. Edmonson, Jr., J. J. Henrick, and T.A. Moss

Convair
A Division of General Dynamics Corporation
Fort Worth, Texas

The Carlson S_n-Method is being adapted at Convair-Fort Worth to the calculation of angular and total flux distributions in shielding configurations. Accordingly, computational procedure for spherically symmetric shields has been developed which fully accounts for the anisotropy of elastic scattering of neutrons. Preliminary calculations for a water shield have given flux distributions that compare favorably with the results of moments method and Monte Carlo calculations.

INTRODUCTION

The adaptation of the Carlson S_n-Method[1] to the calculation of neutron distributions, both angular and total, is being studied at Convair-Fort Worth. The objective of these studies is to develop an efficient program for use in work ranging from research and development to shield-design engineering. To date work has been done on spherically symmetric shield configurations of finite radius, with neutron sources distributed uniformly in small spheres concentric with the shield. This paper briefly describes some of the work that has been done.

THEORETICAL DEVELOPMENT OF THE BASIC EQUATION

A total neutron energy range

$$E_o \leq E \leq E_N \tag{1}$$

with E_o greater than thermal energy is assumed. This range is divided into subintervals

$$E_{g-1} \leq E \leq E_g \tag{2}$$

of lengths indicated by the smoothness of the nuclear cross-section data, by inserting intermediate values of the energy

$$E_o < E_1 < E_2 - - - < E_{g-1} < E_g < - - - < E_N \tag{3}$$

The basic equation is the Boltzmann linear transport equation for a spherically symmetric system:

$$\left[\mu D_r + \frac{1-\mu^2}{r} D_\mu\right] N(r,\mu,E) + \sigma_T(E)\, N(r,\mu,E)$$

$$= \int_{\vec{\Omega}'} d\emptyset'\, d\mu' \int_E^{\left(\frac{M+1}{M-1}\right)^2 E} N(r,\mu',E')\, \sigma_{es}(\bar{\mu},E',E)\, dE' \tag{4}$$

$$+ \int_{\vec{\Omega}'} d\emptyset'\, d\mu' \int_{E'} N(r,\mu',E')\, \sigma_{is}(E' \rightarrow E)\, dE' + S(r,\mu,E)$$

The terms used in Equation 4 are illustrated by the geometry in Figure 1 and are defined as follows:

$\vec{r}$ = position vector from center of shield,

r = $|\vec{r}|$;

Θ = angle between direction of neutron motion and $\vec{r}$ at $\vec{r}$;

$\emptyset$ = azimuthal angle of neutron direction with respect to an arbitrary plane containing $\vec{r}$.

μ = $\cos \Theta$;

$\bar{\Theta}$ = angle between the pre-collision and post-collision directions of the neutron motion.

$\bar{\mu}$ = $\cos \bar{\Theta}$;

E = neutron energy;

ELASTIC SCATTERING PROCESS GEOMETRY

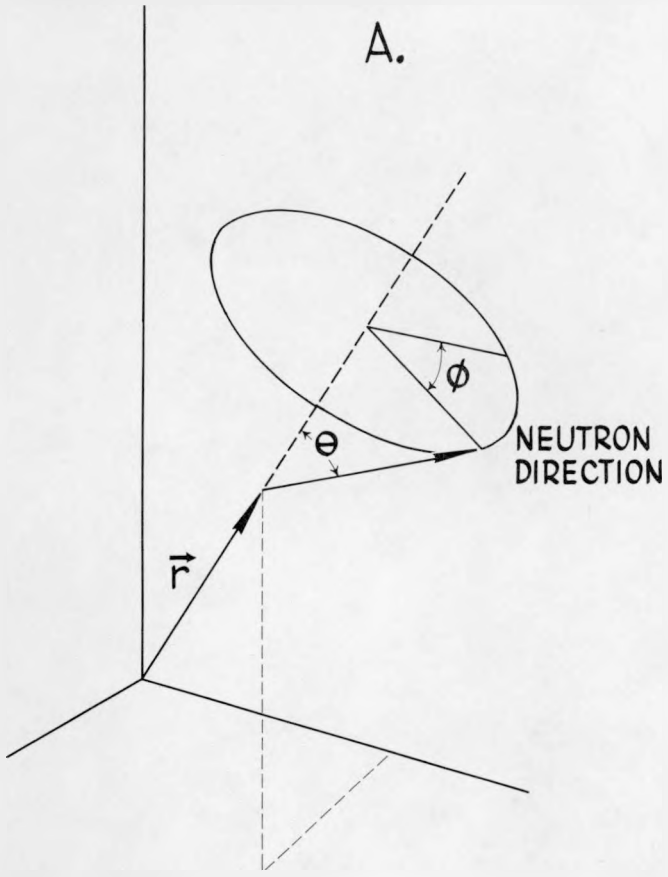

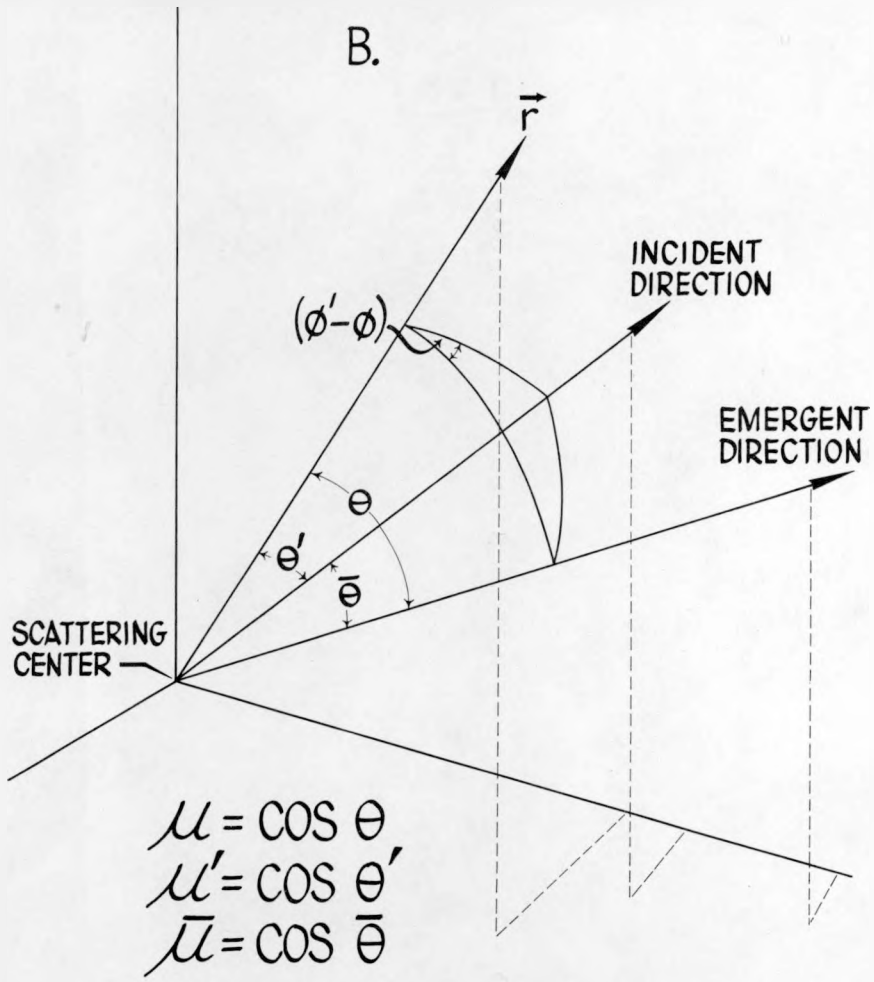

NPC 10,288

FIGURE 1

From energy considerations connected with elastic collisions, it follows that

$$\left.\begin{aligned} \bar{\mu}(E',E) &= \frac{(M+1)E-(M-1)E'}{2\sqrt{E}\ \sqrt{E'}} \\ \text{for}\quad E'\left(\frac{M-1}{M+1}\right)^2 &\leq E \leq E' \\ \text{or}\quad E \leq E' &\leq \left(\frac{M+1}{M-1}\right)^2 E \end{aligned}\right\} \qquad (9)$$

Thus, Equation 8 is restricted by Equation 9.

Treating $\bar{\mu}$ from Equation 8 and $\bar{\mu}(E',E)$ from Equation 9 as independent variables is analytically convenient. This is accomplished by writing

$$\sigma_{es}(\bar{\mu},E',E) = \sigma(\bar{\mu},E')\ \delta\left[\bar{\mu}(E',E)-\bar{\mu}\right]\ \frac{d\bar{\mu}(E',E)}{dE}\ . \qquad (10)$$

In Equation 10 the δ function has the effect of giving to $\sigma_{es}(\bar{\mu},E',E)$ the value 0 if the values for $\bar{\mu}$ given by Equations 8 and 9 are not equal. The presence of $d\bar{\mu}(E',E)/dE$ is due to the fact that $\sigma(\bar{\mu},E',E)$ is a differential angular cross section. The quantity $\sigma(\bar{\mu},E')$ is the differential angular cross section for $\bar{\mu}$, E', and E as connected by Equation 9. The form of Equation 10 for $\sigma(\bar{\mu},E',E)$ is chosen since the independent variables are E' and E; thus, multiplying by dE yields the neutrons scattered into the solid angle

$$2\pi d\bar{\mu}(E',E) = 2\pi\ \frac{d\bar{\mu}(E',E)}{dE}\ dE.$$

Equation 10 is expanded into a series of Legendre polynomials relative to $\bar{\mu}$:

$$\sigma(\bar{\mu},E',E) = \sum_{L=0}^{\infty} \frac{2L+1}{4\pi}\ B_L(E',E)P_L(\bar{\mu})$$

$N(r,\mu,E)$ = neutron flux at $\vec{r}$ in direction ($\Theta = \cos^{-1}\mu$), with energy E;

$\sigma_{es}(\bar{\mu},E',E)$ = differential angular cross section or transfer coefficient from the energy E' to the energy E through the angle $\cos^{-1}\bar{\mu}$ for elastic scattering in the laboratory system (L-system);

$\sigma_{is}(E' \longrightarrow E)$ = cross section for inelastic scattering of a neutron from energy E' to energy E, inelastic scattering assumed to be isotropic in the L-system of coordinates;

$\sigma_T(E)$ = total cross section of nuclei for neutrons of energy E;

$S(r,\mu,E)$ = independent source of neutrons.

All quantities are assumed to be measured in the L-system of coordinates. Primes indicate pre-collision values.

The Carlson S_n-approximation for the neutron flux is assumed. The range

$$-1 \leq \mu \leq 1 \tag{5}$$

is divided into n-subintervals

$$-1 = \mu_o < \mu_1 < \mu_2 \ . \ . \ . < \mu_{j-1} < \mu_j < \ . \ . \ . < \mu_n = 1 \tag{6}$$

which, for convenience, are chosen of equal length, with one subdivision point falling on $\mu = 0$. Then in the $j^{\underline{th}}$ subinterval it is assumed that

$$N(r,\mu,E) = N(r,\mu_j,E)\ \frac{\mu-\mu_{j-1}}{\mu_j-\mu_{j-1}} + N(r,\mu_{j-1},E)\ \frac{\mu_j-\mu}{\mu_j-\mu_{j-1}}\ . \tag{7}$$

$\bar{\mu}$ is determined geometrically by the formula

$$\bar{\mu} = \mu\mu' + \sqrt{(1-\mu^2)(1-\mu'^2)}\ \cos(\phi'-\phi)\ . \tag{8}$$

$$B_L(E',E) = 2\pi \int_{-1}^{1} \sigma(\bar{\mu},E',E) P_L(\bar{\mu}) d\bar{\mu}$$

$$= 2\pi \int_{-1}^{1} \sigma(\bar{\mu},E') \, \delta\left[\bar{\mu}(E',E)-\bar{\mu}\right] \frac{d\bar{\mu}(E',E)}{dE} P_L(\bar{\mu}) d\bar{\mu} \qquad (11)$$

$$= 2\pi\sigma\left[\bar{\mu}(E',E),E'\right] \; P_L\left[\bar{\mu}(E',E)\right] \frac{d\bar{\mu}(E',E)}{dE} \; .$$

Also

$$\left.\begin{aligned} \sigma\left[\bar{\mu}(E',E),E'\right] &= \sum_{L=0}^{\infty} \frac{2L+1}{4\pi} B_L(E') \; P_L\left[\bar{\mu}(E',E)\right] \\ B_L(E') &= 2\pi \int_{-1}^{1} \sigma(\bar{\mu},E') P_L(\bar{\mu}) d\bar{\mu} \end{aligned}\right\} \qquad (12)$$

The neutron flux $N(r,\mu,E)$ is expanded in a series of Legendre polynomials:

$$\left.\begin{aligned} N(r,\mu,E) &= \sum_{L=0}^{\infty} \frac{2L+1}{4\pi} N_L(r,E) P_L(\mu) \\ N_L(r,E) &= 2\pi \int_{-1}^{1} N(r,\mu,E) P_L(\mu) d\mu \end{aligned}\right\} \qquad (13)$$

In Equation 13 the integration relative to μ is carried out using the Carlson linear approximation of Equation 7 in each subinterval (μ_{j-1}, μ_j) of the cosine range (Eq. 5).

The expansions from Equations 11 and 13 are substituted into the elastic scattering integral of Equation 4, and each side of the resulting equation is integrated over the energy interval $E_{g-1} \leq E \leq E_g$. This equation is then expressed in terms of the average values of $N(r,\mu,E)$ and $\sigma_T(E)$ in the interval $E_{g-1} \leq E \leq E_g$. This equation is then integrated over each one of the μ intervals $\mu_{j-1} \leq \mu \leq \mu_j$ by using the Carlson approximation (Eq. 7) for the neutron flux. The result of these operations is a system of n ordinary differential equations relative to the variable r for the n+1 quantities $N_{gj}(r)$:

$$\left[a_j D_r + \frac{b_j}{r} + \overline{\sigma_{Tg}}\right] N_{gj}(r) + \left[\bar{a}_j D_r - \frac{b_j}{r} + \overline{\sigma_{Tg}}\right] N_{g,j-1}(r) \tag{14}$$

$$= \sum_{g'=g}^{k+1} \sum_{k=0}^{n} \sigma_{g'gkj} N_{g'k}(r) + S_{gj}(r) \quad (j = 1,2, - - - n)$$

In Equation 14, the quantities a_j, $\bar{a}_j$, and b_j are defined as follows:

$$a_j = (2\mu_j + \mu_{j-1})/3 \qquad \bar{a}_j = (\mu_j + 2\mu_{j-1})/3$$

$$b_j = \frac{2}{3}\left(\frac{3 - \mu_j^2 - \mu_j\mu_{j-1} - \mu_{j-1}^2}{\mu_j - \mu_{j-1}}\right)$$

An additional equation is needed to complete the system of Equation 14, since n+1 quantities $N_{g'j}(r)$ for $j = 0,1 \ldots n$ must be determined. This additional equation is obtained from Equation 4 by setting $\mu = -1$ and then performing a set of operations corresponding to those used in obtaining Equation 14.

In Equation 14, the inelastic scattering effects are included in the transfer coefficients $\sigma_{g'gkj}$. The structure of the transfer coefficients due to anisotropic elastic scattering is complex. For example, a typical coefficient $\sigma_{g'gkj}$ has, for its part due to elastic scattering, the following:

$$\sum_{L=0}^{\infty}\sum_{L'=0}^{\infty}\frac{2L+1}{2}\frac{2L'+1}{2}\left[\int_{\mu_{j-1}}^{\mu_j}P_L(\mu)\,d\mu\right]B_{Lg'}\left[\int_{\mu_{k-1}}^{\mu_k}\frac{\mu-\mu_{k-1}}{\mu_k-\mu_{k-1}}P_L(\mu)\,d\mu\right.$$

$$\left.+\int_{\mu_k}^{\mu_{k+1}}\frac{\mu_{k+1}-\mu}{\mu_{k+1}-\mu_k}P_L(\mu)\,d\mu\right]. \qquad (15)$$

$$\cdot\int_{E'_{g'-1}}^{E'_{g'}}\int_{E_1(E')}^{E_2(E')}P_L\left[\bar{\mu}(E',E)\right]\;P_{L'}\left[\bar{\mu}(E',E)\right]\frac{d\bar{\mu}(E',E)}{dE}\,dE\,dE'$$

The calculation of transfer coefficients has been studied extensively at Convair–Fort Worth during the course of these investigations. As a result of these studies, an alternative procedure has been derived which avoids the use of the delta function. This procedure is straightforward and numerically more convenient than the delta-function expansion and will be described in detail in a report[2] soon to be published.

The quantity $B_{Lg'}$ is an average value over the energy interval $E'_{g'-1} \le E' \le E'_{g'}$. This number must be determined from cross-section data usually given in the center-of-mass (CM) coordinate system. Thus, the value of $B_{Lg'}$ depends on transferring numerical data from the CM system to the L-system.

A remark should be made about the range of E' involved in the determination of the transfer coefficients $\sigma_{g'gkj}$. If hydrogen (M = 1) is not involved, then in general all energies E' satisfying

$$E_{g-1} \le E' \le E_g\left(\frac{M+1}{M-1}\right)^2$$

will contribute to the neutron flux in the interval $E_{g-1} \le E \le E_g$. If

$$E_g\left(\frac{M+1}{M-1}\right)^2 \le E_N\,,$$

the integration in E' is from E_{g-1} to $E_g \left(\frac{M+1}{M-1}\right)^2$. In general $E_g \left(\frac{M+1}{M-1}\right)^2$ is not one of the subdivision points of Equation 3.

If $E_N < E_g \left(\frac{M+1}{M-1}\right)^2$

the upper limit for the integration relative to E' is E_N. For hydrogen, E_N is the upper limit of integration.

The source term S_{gj} in Equation 14 comes from the source term of Equation 4 by the double integration and averaging process

$$\int_{E_{g-1}}^{E_g} \int_{\mu_{j-1}}^{\mu_j} S(r,\mu,E)\,d\mu\,dE = (E_g - E_{g-1}) \int_{\mu_{j-1}}^{\mu_j} S(r,\mu,\overline{E_g})\,d\mu \tag{16}$$

$$= (E_g - E_{g-1})\ S_{gj}(r)$$

The resulting set of n+1 ordinary differential equations is then solved by iterated numerical integration after the formulation of boundary conditions suitable to the shield configuration. If the shield is assumed to be surrounded by a perfectly absorbing medium, all fluxes for which $\mu \leqq 0$ are taken to be zero at the boundary. The set of boundary conditions is completed by assuming flux angular symmetry at the origin.

The numerical iteration process is then started at the highest energy group by assuming arbitrary initial values for the fluxes. The process then cascades downward through the lower energy group since no energy can be gained by the neutron on scattering. The integration is always in the direction of neutron flow to avoid cumulative errors.

SOME NUMERICAL RESULTS

The numerical results here presented are to be considered as preliminary in nature.

The angular and total neutron fluxes were calculated for two spherically symmetric water shields. One was 80 cm in radius with a uniformly distributed source 0.1 cm in radius; the other a 120-cm sphere with a uniformly distributed source

2 cm in radius. These sources were used to approximate point sources, since point sources cannot be used in this integration scheme. The source spectrum in each case was a Watt[3] fission spectrum normalized to one neutron per second emitted isotropically. To avoid boundary considerations, the remaining nuclear properties of the source volume were assumed to be the same as for water. The energy range was taken from

$$E_N = 14 \text{ Mev to } E_o = 0.5 \text{ Mev, with } N = 14.$$

The directional flux was divided into four angular segments, and the resulting equations solved by numerical methods.

These computed results were compared with those obtained by the moments method[4] for a point isotropic fission source having an upper energy $E_N = 18$ Mev in an infinite water medium.

In Figure 2, dose rate as a function of distance from the origin as calculated with the S_4 approximation is compared with results of the moments method calculations. Results of S_4 calculations are shown for both the 0.1-cm- and 2-cm-sources. The boundary effects at 80 cm and 120 cm are visible in the S_4 calculations.

In Figure 3, the values of the differential number spectra at r = 10 cm and at r = 92 cm are compared with those computed by the moments method. The points of the S_4 curve are plotted at the midpoints of the intervals of their respective energy groups. As expected, some general agreement can be seen near the source. However, at deep penetrations, the S_4 spectrum is softer than the moments-method spectrum. This could possibly be due, in part, to the fact that the oxygen cross sections used in the S_4 calculation were not exactly the same as those used in the moments method, and the energy ranges of the two calculations are not identical. Also, the moments method computations were for an infinite water medium.

The angular flux distribution is shown in Figure 4 at a distance of 100 cm for a few energy groups to illustrate its extremely directional characteristics at large distances from the source. Higher order S_n approximations should be used for a more accurate determination of this distribution.

DOSE RATE COMPARISON

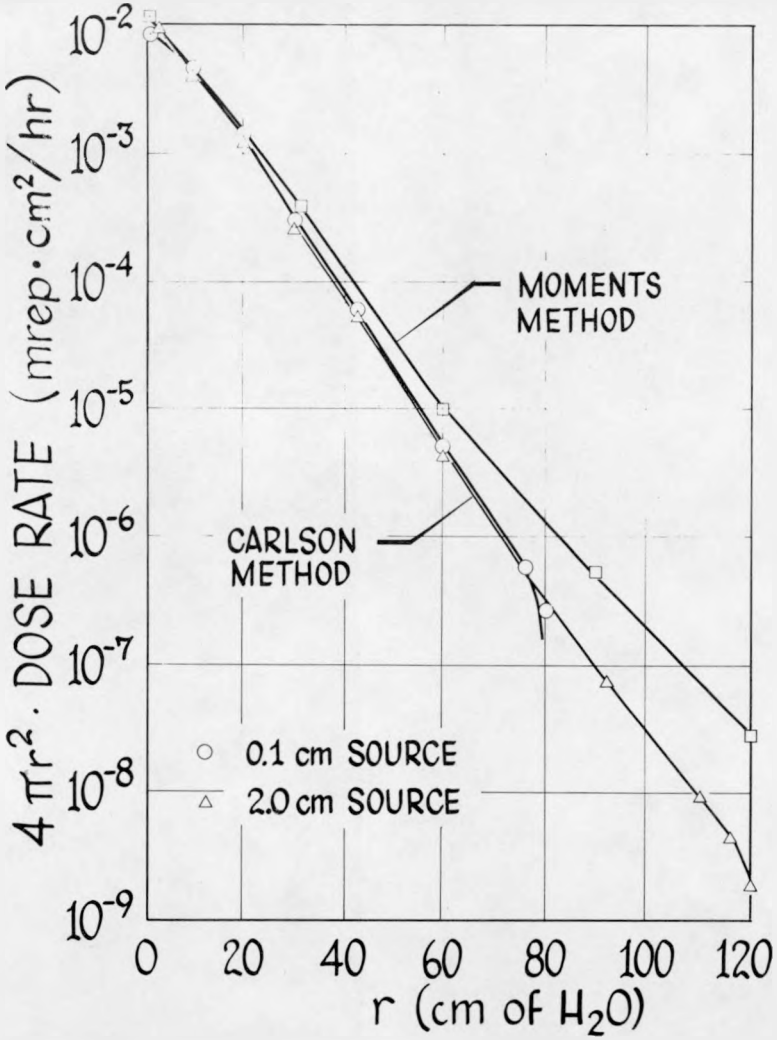

NPC 10,290

FIGURE 2

DIFFERENTIAL NUMBER SPECTRUM

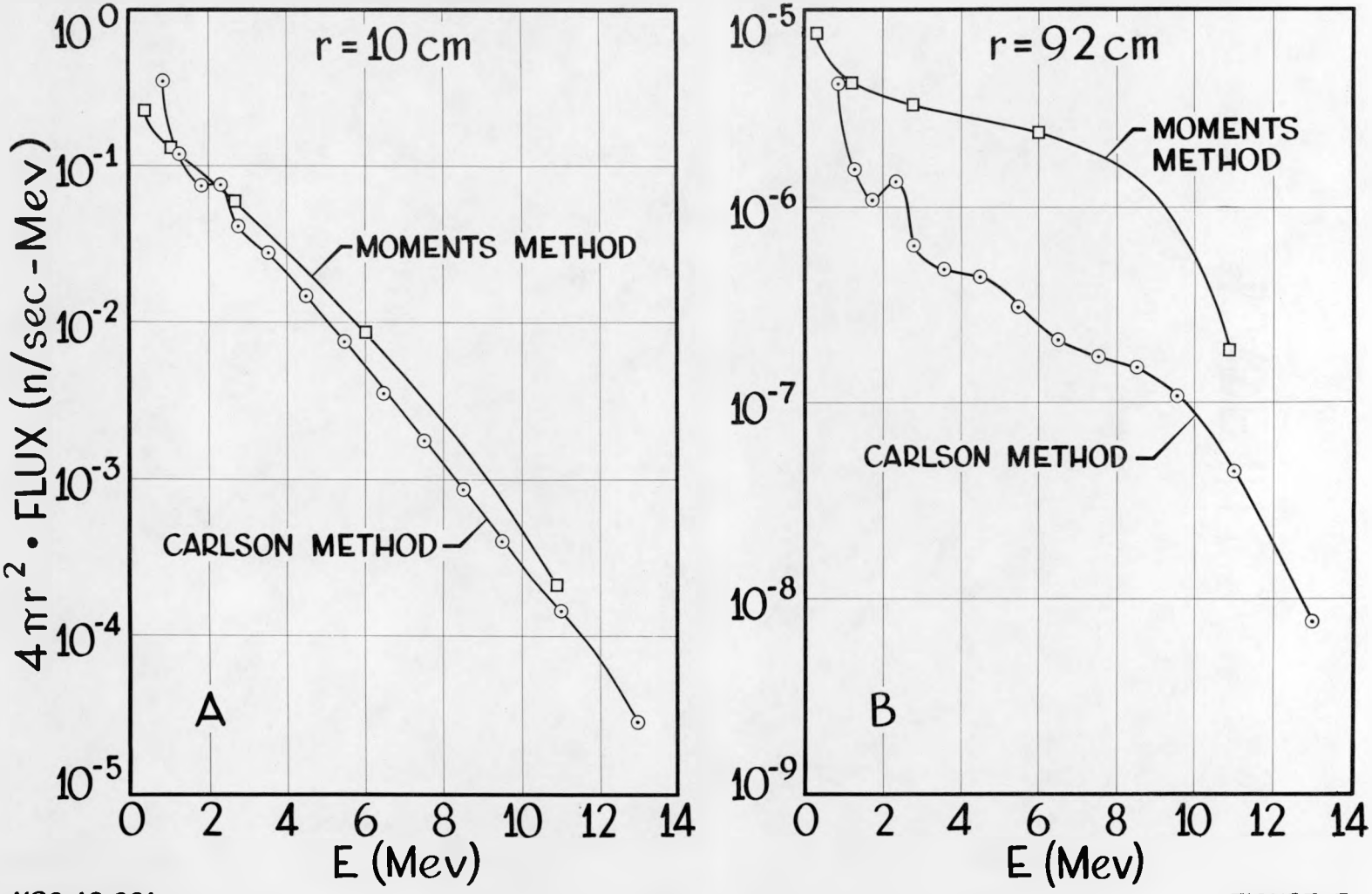

NPC 10,291

FIGURE 3

ANGULAR FLUX DISTRIBUTION AT 100 cm

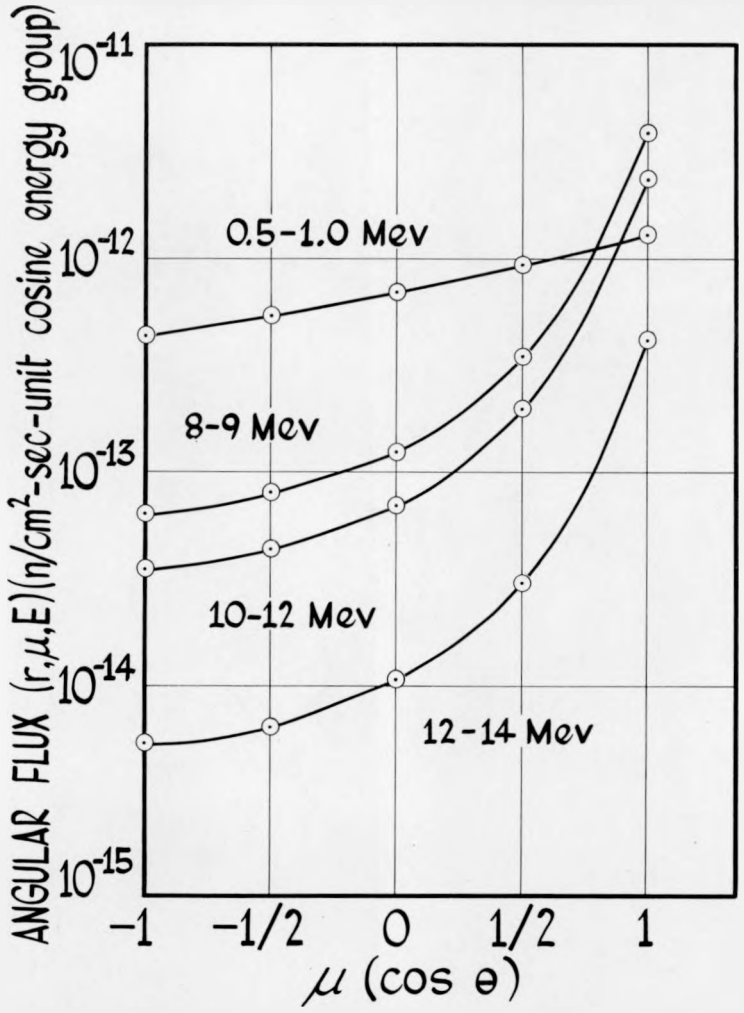

NPC 10,293

FIGURE 4

FURTHER WORK

The results so far obtained from the S_n-Method have given strong support to its further development. It will next be developed for multi-layered, multi-material spherical shields, in conjunction with more complex neutron sources. Cylindrical configurations will be studied.

REFERENCES

1. Carlson, B., Solution of the Transport Equation by S_n Approximations. Los Alamos Scientific Laboratory Report LA-1891 (February 1955).

2. Edmonson, N. Jr., Henrick, J. J., and Moss, T. A., The Application of the Carlson S_n-Method to Calculation of Neutron Angular and Total Flux Distribution in a Spherically Symmetric Shield (Convair-Fort Worth Report in preparation).

3. Watt, B. E., "Energy Spectrum of Neutrons from Thermal Fission of U^{235}," Physical Review 87, 1037 (1952).

4. Aronson, R., Certaine, J., Goldstein, H., and Preiser, S., Neutrons from a Point Isotropic Source Fission Source in Water. Nuclear Development Associates, Inc. Report NYO-6267 (September 1954).

10. RESULTS OF AN OPTIMIZATION PROCEDURE

W. Cranford
R. A. Miller

Convair
A Division of General Dynamics Corporation
Fort Worth, Texas

RESULTS OF AN OPTIMIZATION PROCEDURE

by

W. Cranford and R. A. Miller

Convair
A Division of General Dynamics Corporation
Fort Worth, Texas

Some results are reported on reactor and crew-compartment shields minimized by an optimization procedure called GYPSY. For a fast-neutron shield, the adequacy of using a representative point source appears to be settled affirmatively. The effect of optimization of a crew shield for different point detector positions has been investigated.

INTRODUCTION

The problem of an optimal shield weight for an airborne reactor and crew compartment is of major importance in the design of a nuclear-powered aircraft. One concept for weight reduction is a divided shield in which each of these two components is shielded separately. Further consideration is given to the simultaneous shaping of both reactor and crew compartment shields so that the shield system will be optimum. This idea contrasts with attempts to shape the shield of one component while leaving a fixe shield on the other. The radiation level to which a crew may be safely exposed determines the crew compartment dose-rate constraint. The radiation tolerance of equipment outside the crew compartment fixes reactor-leakage constraints for neutrons and gamma rays. Engineering structural design places a maximum radius-bound on shielding thicknesses. A particular idealization of the problem permits expressions for weight, dose rate, and constraints as functions of the shielding thicknesses.

MATHEMATICAL MODEL

The basic theoretical foundation is the gradient nonlinear programming procedure which was described by Sheffield and Miller at the Third and Fourth Semi-Annual ANP Shielding meetings. The complete theory has been published by Convair-Fort Worth in MR-N-186 (NARF 57-62T, December 1957) and MR-N-207 (NARF 58-24T, June 1958). Underlying assumptions are the following:

1. The source is adequately represented by a point source for air scattering computations.

2. The weight and dose-rate functions and constraints are expressed in terms of thicknesses of shielding materials.

3. The reactor and crew compartment are subdivided into r and s sectors, respectively, with t_i different layers of shielding materials on the ith sector.

4. The probability that radiation emerges from sector i of the reactor and enters sector j of the crew compartment is known.

5. Radiation leakage is calculated by exponential attenuation.

The weight of shielding materials for a cylindrical reactor and crew compartment is represented by a cubic polynominal in n variables with non-negative coefficients determined by geometrical parameters and densities of materials. The dose-rate expression is assumed to be an analytic function which is the sum of several negative exponential terms. A typical term is of the form

$$\exp - \left(\sum_{k=1}^{3} \mu_{ki} \; x_{ki} + \sum_{k=4}^{5} \nu_{kj} \; x_{kj} \right) ,$$

where x_{ki} and x_{kj} are the shielding thicknesses for the kth layer and ith sector of the reactor shield and the kth layer and jth sector of the crew compartment shield. The μ_{ki} and ν_{kj} are absorption coefficients which are linear or quadratic functions of the shielding-material thickness.

The problem may be formally stated in this manner:

Determine $X^{(o)} = (x_1^o, \text{-----}, x_n^o)$ which minimizes the weigh

function $W(X) = W(x_1, \text{------}, x_n)$ (1)

of $n = 3r + 2s$ variables, subject to a nonlinear dose rate constraint

$$D(X) = D_o \; , \qquad (2)$$

and 2r reactor-leakage constraints

$$\begin{aligned} a_{1i}\, x_{1i} + a_{2i}\, x_{2i} + a_{3i}\, x_{3i} &\geq G_i \\ b_{1i}\, x_{1i} + b_{2i}\, x_{2i} + b_{3i}\, x_{3i} &\geq N_i \end{aligned} \qquad (i = 1,--,r) \qquad (3)$$

and r + s maximum-radius constraints

$$\begin{aligned} x_{1i} + x_{2i} + x_{3i} &\leq M_i \qquad (i = 1,--,r) \\ x_{4j} + x_{5j} &\leq M_j \qquad (j = 1,--,s) \end{aligned} \qquad (4)$$

and bounded-variable constraints

$$0 \leq c_i^* \leq x_i \leq c_i \qquad (i = 1,--,n) \qquad (5)$$

SOLUTION METHOD

The procedure for solving the minimum problem consists of the following steps:

1. Constraint-set consistency test.
2. Dose-rate reduction (Phase I)
3. Weight reduction for constant dose rate (Phase II)
4. Constraint-set check.
5. Convergence test.

An optimization procedure, GYPSY, has been used with success in shaping reactor and crew compartment shields. In general terms the procedure adds shielding judiciously to achieve the dose rate level, and then shifts material to reduce weight while maintaining the constant dose rate and also satisfying the other constraints. An iterative process continues until the convergence criterion is satisfied.

In Phase I, from an initial set of feasible thicknesses $X^{(1)} = (x_1^1, \ldots, x_n^1)$, a sequence $\left(X^{(j)}\right)$ is determined by the relations

$$x_k^{(j+1)} = x_k^{(j)} + \frac{\Delta D}{\left|\overrightarrow{\text{grad } D}\right|^2_{X(j)}} \left(\frac{\partial D}{\partial x_k}\right)_{X(j)} \quad (k = 1, ---, n) \quad (6)$$

where $x_k^{(j)}$ is the thickness of kth material of the jth iteration, and ΔD is the desired change in $D(X)$. To hasten convergence, the arithmetic mean $\bar{E}$ of the ratios

$$E_k = \frac{\partial W}{\partial x_k} \Big/ \frac{\partial D}{\partial x_k}$$

is determined. An arbitrary interval length 2ϵ about $\bar{E}$ is selected so that shielding is added if $E_k < \bar{E} - \epsilon$ and is decreased if $E_k > \bar{E} + \epsilon$. This procedure continues until a set $X^{(m)}$ is found such that $D(X^{(m)}) = D_o$.

In Phase II, in order to maintain a constant $D(X)$ and to reduce $W(X)$ in a stepwise linear manner, we require the analytical conditions

$$\overrightarrow{\text{grad } D} \cdot \overrightarrow{dX} = 0 \quad (7)$$

$$\overrightarrow{\text{grad } W} \cdot \overrightarrow{dX} < 0 \quad (8)$$

until $W(X)$ is a minimum, then

$$\overrightarrow{\text{grad } (W + \lambda D)} = 0 \quad (9)$$

A new sequence $\left\{X^{(t)}\right\}$ is found through the recursion formula

$$x_k^{(t+1)} = x_k^{(t)} + \frac{\Delta W}{Q} \sum_{j=1}^{n} C_j A_{jk} \quad (k = 1, ---, n) \quad (10)$$

where

$$\left.\begin{aligned} C_j &= \frac{\partial D}{\partial x_j}, \quad B_j = \frac{\partial W}{\partial x_j} \\ A_{jk} &= B_j C_k - B_k C_j = C_k C_j (E_j - E_k) \end{aligned}\right\} \quad (11)$$

and

$$Q = \sum_{\substack{i,j=1 \\ i<j}}^{n} A_{ij}^2$$

A short, albeit cumbersome, computation shows that the vector change of Equation 10 will satisfy Equations 7, 8, and 9. It may be noted from Equations 10 and 11 that all variables x_j will be increased for which $E_j < E_k$. Furthermore a decrease in W(X) is possible unless $A_{jk} = 0$ for all j and k. In this case, since $C_j > 0$ for all j, $E_j = E_k$ and the convergence criterion of Equation 9 is satisfied.

It should be pointed out that the equality of the E_j's can be attained in case the constraints are not violated. In order to recover a feasible set of variables when the constraints are violated, orthogonal projections are made upon the appropriate plane defined by the Equations 3 and 4. In this case, if the solution $X^{(0)}$ lies on a plane, or if some variables are zero, the E_i's cannot attain a common value. For such constrained variables, equality is sought for an alternate quantity F_i which is defined as

$$F_i = \frac{C_i(E_i - \bar{E})}{\mu_{ki}} \qquad (12)$$

The equalization of F_i on each constrained sector gives an optimal interchange of heavy and light shielding materials. This assertion is supported by the results obtained by optimizing a reactor shield; that is, the shield weight (32,000 lb) was reduce by 1500 pounds with the E_i's for unconstrained variables converging to 7.192(8), and the F_i's for constrained variables converging to 1.375(5).

COMPUTATIONAL RESULTS

As indicated previously, one basic assumption in the mathematical model used in the GYPSY optimization procedure is the representation of a distributed source by a point source. The question of the adequacy of this simplified model for optimization purposes appears to be settled affirmatively in the case of a shield for multiple air-scattered fast neutrons. With an optimized shield for a 3-Mw reactor, dose rates at 50 feet as computed by a distributed source reactor shield penetration procedur were compared with those computed by GYPSY. In making this comparison, the same geometry, relaxation lengths, and other parameters were maintained in the two programs. The only difference in the calculations was an assumed representative point source at the core center in GYPSY and a distributed source of 104 sourc points in the other procedure.

A profile of the reactor geometry, as seen by GYPSY, is indi cated in Figure 1. This geometry was utilized in the distributed

OPTIMIZED REACTOR SHIELD GEOMETRY

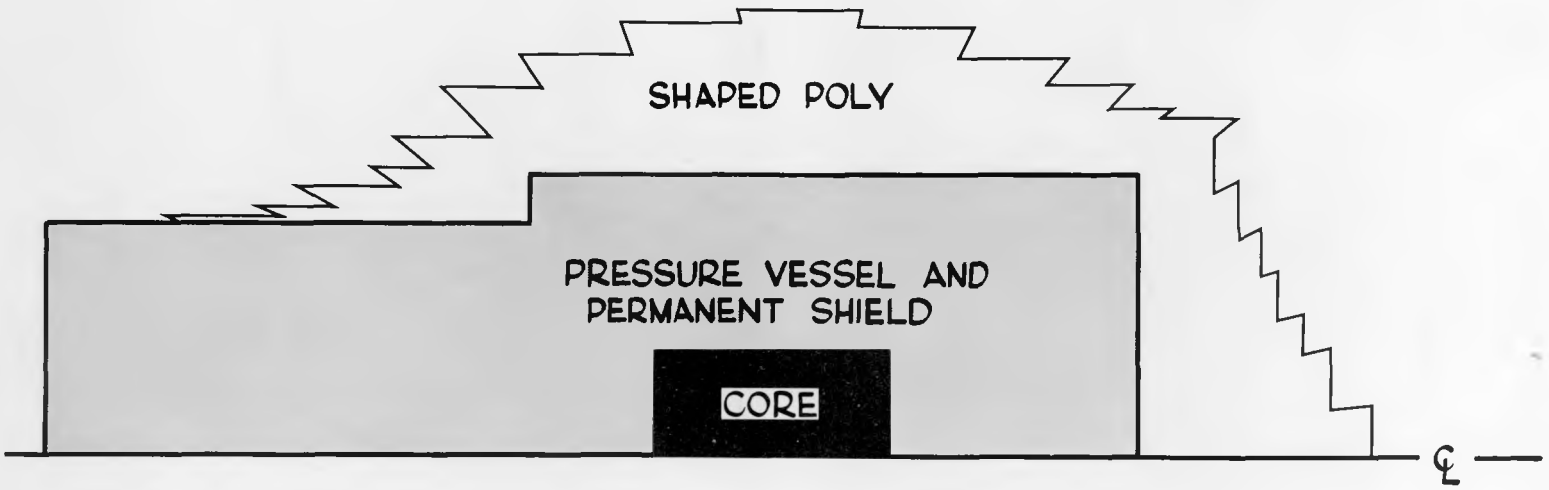

NPC 10,284

FIGURE 1

source penetration calculations for 18 detector points. A comparison of the fast-neutron dose rates through the borated polyethylene shield at 50 feet is given in Figure 2. The smooth curve through the circles represents the dose rate calculated by GYPSY techniques as a function of emission angle. The distributed source computations, as indicated by squares, agree remarkably well, except at corners. These results present a plausible argument for utilization of a point source under similar conditions.

In the GYPSY model, the reactor and crew compartment shields are shaped for a point detector and a point source along the center line. The effect of three different pre-selected position for the detector are reported for a one-layer neutron shield. Th reactor and crew compartment shield configurations were shaped fo a target neutron dose rate of 0.15 mrem/hr at the midpoint C of the crew compartment. For this shield, the dose rates at point A, 132.4 cm toward the rear from C, and at B, 132.4 cm toward the front, were 1.34 mrem/hr and 2.27 mrem/hr, respectively. With this evidence of variation, by a factor of from 9 to 15, of the neutron dose rate at C, it was decided to reshape the configurations relative to the points A and B.

The results of the shaping for the three detector points are indicated by the profiles of Figures 3a and 3b. Although essenti ally no change in shape is noted for the reactor shield, the shape of the crew compartment shield is altered radically with the greatest side thickness directly above the detector. One may conjecture that to maintain a maximum dose rate for all points along the crew compartment axis, a neutron shield of uniform thickness should be used along the sides of the crew compartment.

The results of a calculation to optimize the reactor and crew compartment shield with a uniform side thickness and front and rear plugs are indicated by dotted lines D in Figures 3 and 3(b). The additional side thickness on the reactor may be attributed to the uniform side of the crew compartment. The total weight is 11,895 pounds, of which the reactor weighs 6,355 pounds and the crew compartment weighs 5,540 pounds. Thus a weight penalty of about 20 percent was incurred by using a slab side on the crew compartment. The rear, side, and front thickness for the crew compartment were 36.2, 28.4, and 19.4 cm, respective

Efforts to shape the front and rear of the crew compartment with a uniform side shield are in progress. It is anticipated that results from Convair's neutron shield shaping experiment will be beneficial toward the solution of this problem.

NEUTRON DOSE RATE AT 50 FEET

3 MW REACTOR SHIELD

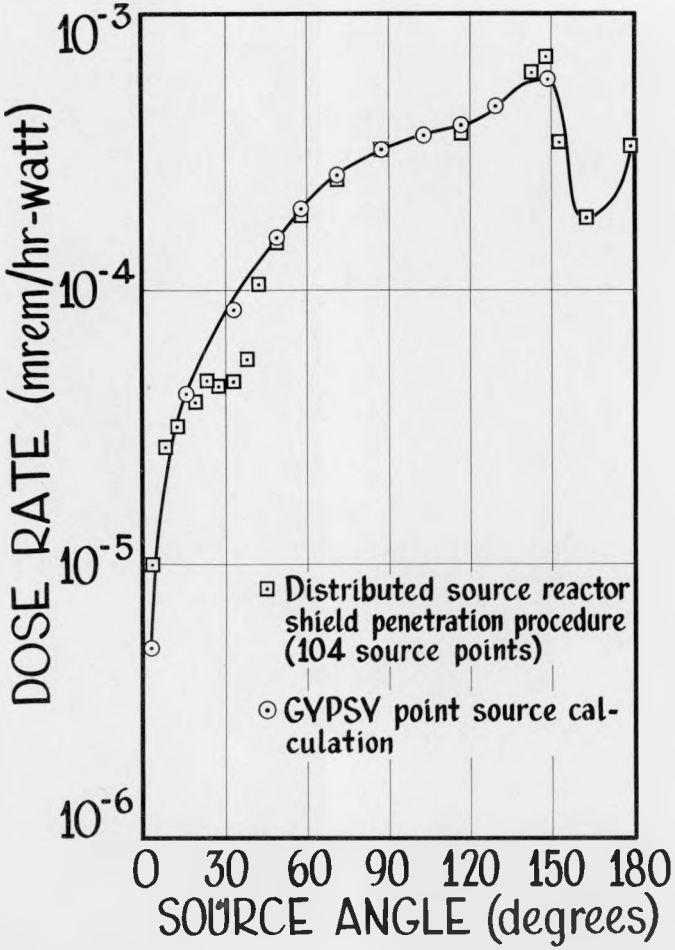

NPC 10,285

FIGURE 2

FAST NEUTRON SHIELD

THREE DETECTORS AND SLAB SIDE

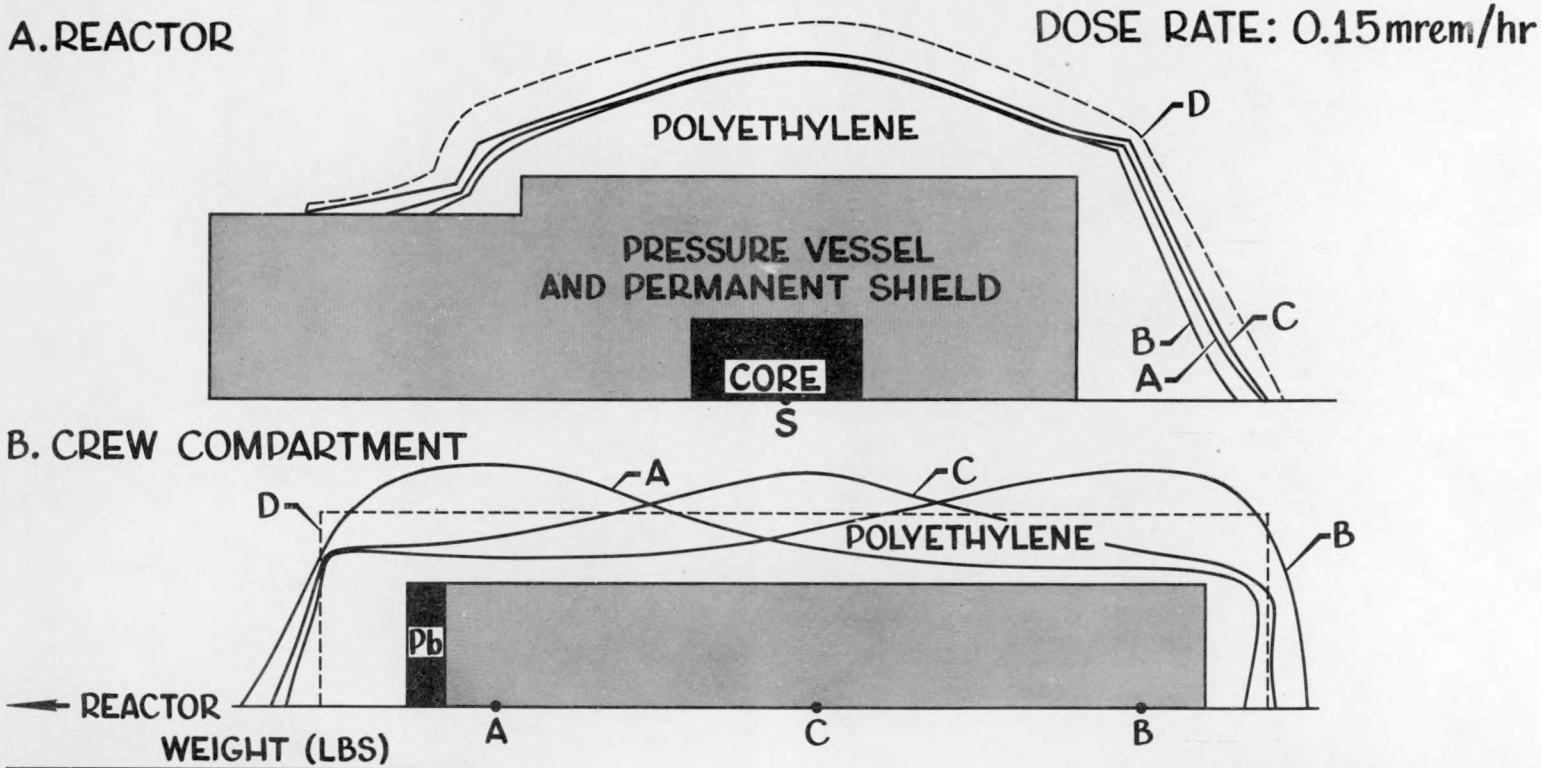

WEIGHT (LBS)

SHIELD	CREW COMP.	REACTOR
A	4490	3570
B	5400	3650
C	5400	4320
D	5540	6355

SHIELD C

DETECTOR	DOSE RATE (mrem/hr)
A	1.34
B	2.27
C	0.15

NPC 10,287

FIGURE 3

11. MONTE CARLO CALCULATIONS OF FAST-NEUTRON ENERGY SPECTRA IN AIR

M. B. Wells

Convair
A Division of General Dynamics Corporation
Fort Worth, Texas

MONTE CARLO CALCULATIONS OF FAST-NEUTRON ENERGY SPECTRA IN AIR

by

M. B. Wells

Convair
A Division of General Dynamics Corporation
Fort Worth, Texas

This paper presents the results of Monte Carlo air-scattering calculations for source-neutron energies above the threshold energy of inelastic scattering. Energy and angular distributions of the scattered neutron flux and angular distributions of the scattered dose rate are given for point isotropic monoenergetic sources at source-detector separation distances of up to 200 feet. The results of this study are compared with other calculations made by Holland and Richards and by Zerby in order to evaluate the effect of inelastic scattering on the scattered energy spectrum.

INTRODUCTION

This paper presents the results of some recent Monte Carlo calculations for the angular distribution and energy spectrum of air-scattered fast neutrons as a function of source-detector separation distance and source energy. The Monte Carlo code from which these calculations were obtained has been previously described.[1] The results of these calculations differ from other Monte Carlo neutron air-scattering results[2,3] in that inelastic scattering was included in the calculations.

The energy spectrum of air-scattered neutrons has previously been computed by Holland and Richards.[4] Their results were obtained from a moments-method solution of the Boltzmann transport equation; but lack of accurate cross-section data for inelastic scattering and the use of the elastic differential scattering cross sections of nitrogen for those of air cast some doubt on the reliability of their results at energies above 3 Mev.

Zerby,[3] utilizing the Monte Carlo method, has also computed the energy spectrum for air-scattered fast neutrons; but neglect of inelastic scattering and absorption at energies above 3 Mev and assumption of isotropic scattering in the center-of-mass system for energies above 0.5 Mev are not realistic.

CROSS SECTIONS FOR AIR

The microscopic neutron cross sections for nitrogen and oxygen were taken from the data given by Lustig, Goldstein, and Kalos in References 5 and 6. The elastic differential scattering cross sections were obtained from the Legendre expansions given in the reports cited. At neutron energies below 0.25 Mev, the elastic scattering probabilities for nitrogen and oxygen were assumed to be isotropic in the center-of-mass system.

Lustig et al. have computed the inelastic scattering cross sections for excitation of the 2.31-, 3.95-, 4.91- and the 5.10-Mev levels in nitrogen at neutron energies between 3 and 6 Mev. An extrapolation of their calculations to neutron energies above 6.0 Mev was made by substracting the sum of the first four levels from the total inelastic cross section. This extrapolation allows one to obtain an approximation of the inelastic cross section for the 5.69-Mev level. By extrapolating the cross sections for the first five levels to higher energies, it is then possible to obtain an approximation of the inelastic cross section for excitation of levels above 6.0 Mev. The inelastic cross sections of nitrogen that were used in the Monte Carlo calculations are shown in Figure 1. Whenever the excitation level of the collision nucleus was chosen at random to be greater than 6.0 Mev, the excitation level actually used in the calculations was the highest excitation level above 6 Mev that could be excited by the neutron. The method used to obtain the inelastic cross sections for each level in nitrogen is similar to that described by Keller and Merrill in Reference 7.

Although Lustig et al. give the total inelastic cross section for oxygen, no cross sections are given for the excitation of any particular level. Cross sections for the excitation of the 6.1-, 6.91-, and 7.12-Mev levels are given in BNL-325[8] from the threshold energy of the 6.1-Mev level to about 9.6 Mev. Conner[9] has measured the inelastic cross section of oxygen at 14.1 Mev and reports a value of 0.5 barn. Thompson and Risser[10] report that the emission of a 6.1-Mev photon is four times as probable as the emission of either a 6.9- or a 7.1-Mev photon. The data from BNL-325 were extended from 9.6 Mev so as to pass through the

NITROGEN INELASTIC CROSS SECTIONS

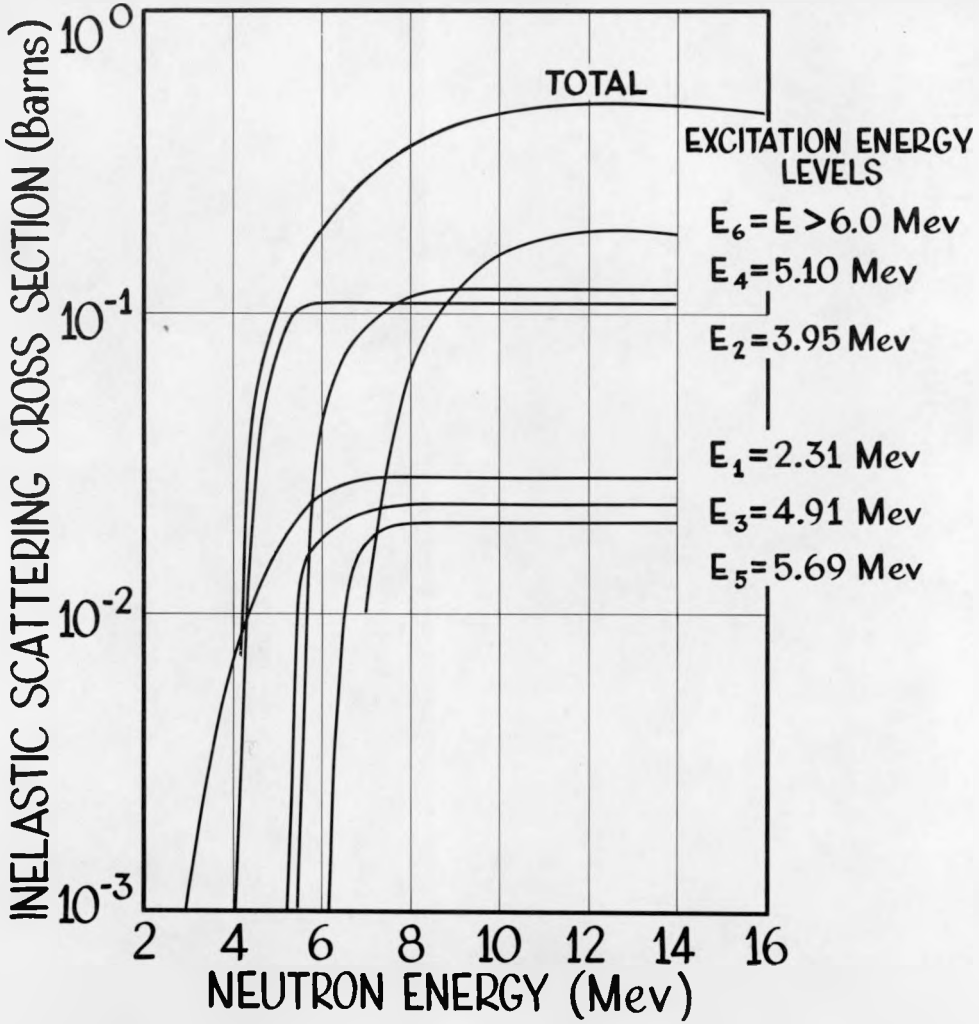

NPC 10,264

FIGURE 1

value reported by Conner at 14.1 Mev. Since the total inelastic cross section given in Reference 6 did not agree exactly with the measurements given in BNL-325, it was decided to use the total inelastic cross section as given by Lustig et al. in the Monte Carlo calculations and to use the measured values only to obtain the probability of exciting the various levels. We have assumed that the excitation of the 6.9-Mev and the 7.1-Mev levels are equally probable, and that these levels may be represented by one level of 7.0 Mev. The inelastic cross sections used for oxygen and the cross sections for exciting the 6.1- or 7-Mev level are shown in Figure 2.

The macroscopic total and scattering cross sections for air were computed from the data in References 5 and 6 by assuming that the number of atoms in one cubic centimeter of air is 5.37×10^{19} at an air density of 0.1293×10^{-2} gm/cm^3. The nitrogen atoms were assumed to make up 78% of this amount and the oxygen atoms the remaining 22%. The total cross section for air is shown in Figure 3.

The flux-to-dose conversion factors used were obtained from calculations of Hurst and Ritchie.[11]

RESULTS

Monte Carlo calculations have been made to determine the air-scattered neutron flux and dose rate for separation distances of up to 200 feet at sea-level air density and for source energies of 6, 10, and 14 Mev. The data presented in this section were obtained for point isotropic sources in an infinite medium of air.

The Monte Carlo results were obtained from sample sizes of 1000 neutron histories with 10 collisions per history. Neutron histories were terminated when the neutron had either undergone 10 collisions or when the neutron energy had been reduced below 1 Mev.

The variation of the air-scattered neutron flux and dose rate with separation distance is shown in Figure 4 for source energies of 6, 10, and 14 Mev. At separation distances between 20 and 40 feet, both the scattered flux and the dose rate for the 6-Mev source are greater than that computed for the 10- and 14-Mev sources. The scattered dose rate is seen to fall off faster with distance for the 6-Mev source than for either of the other sources. The larger cross section at low neutron energies

OXYGEN INELASTIC CROSS SECTIONS

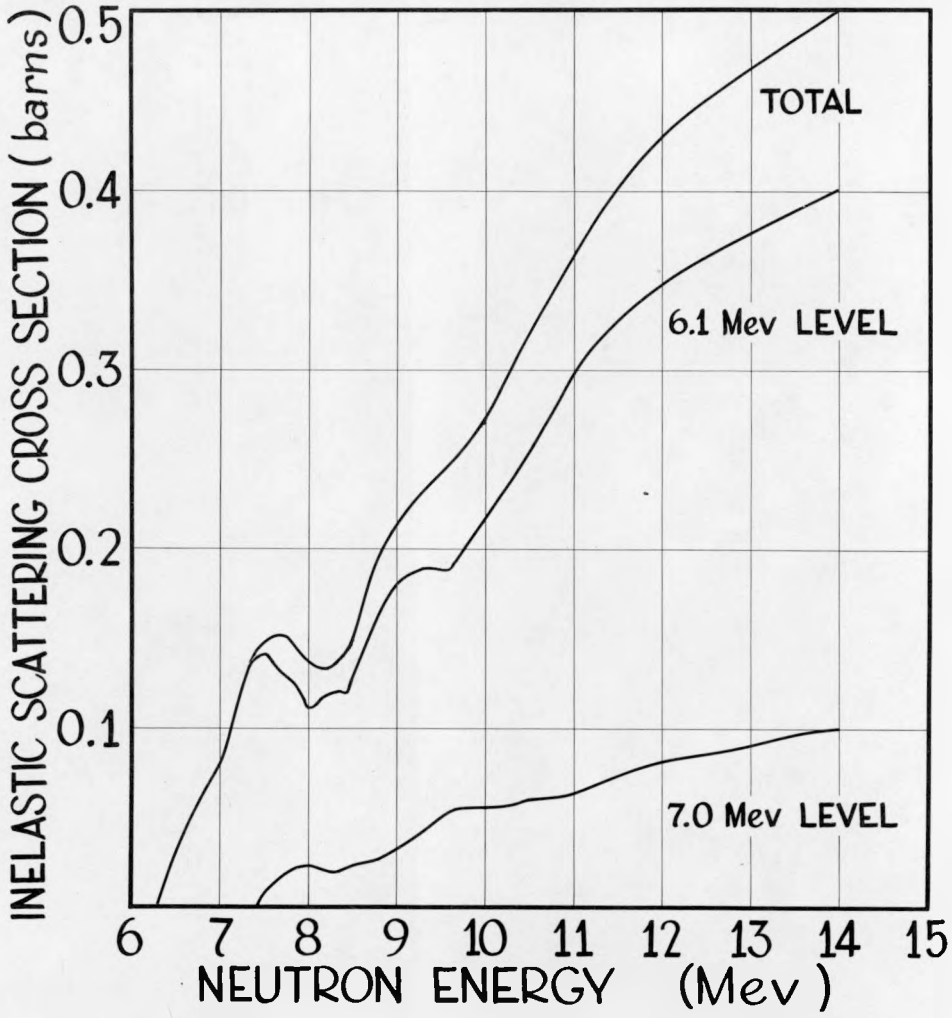

NPC 10,265

FIGURE 2

TOTAL CROSS SECTION FOR AIR

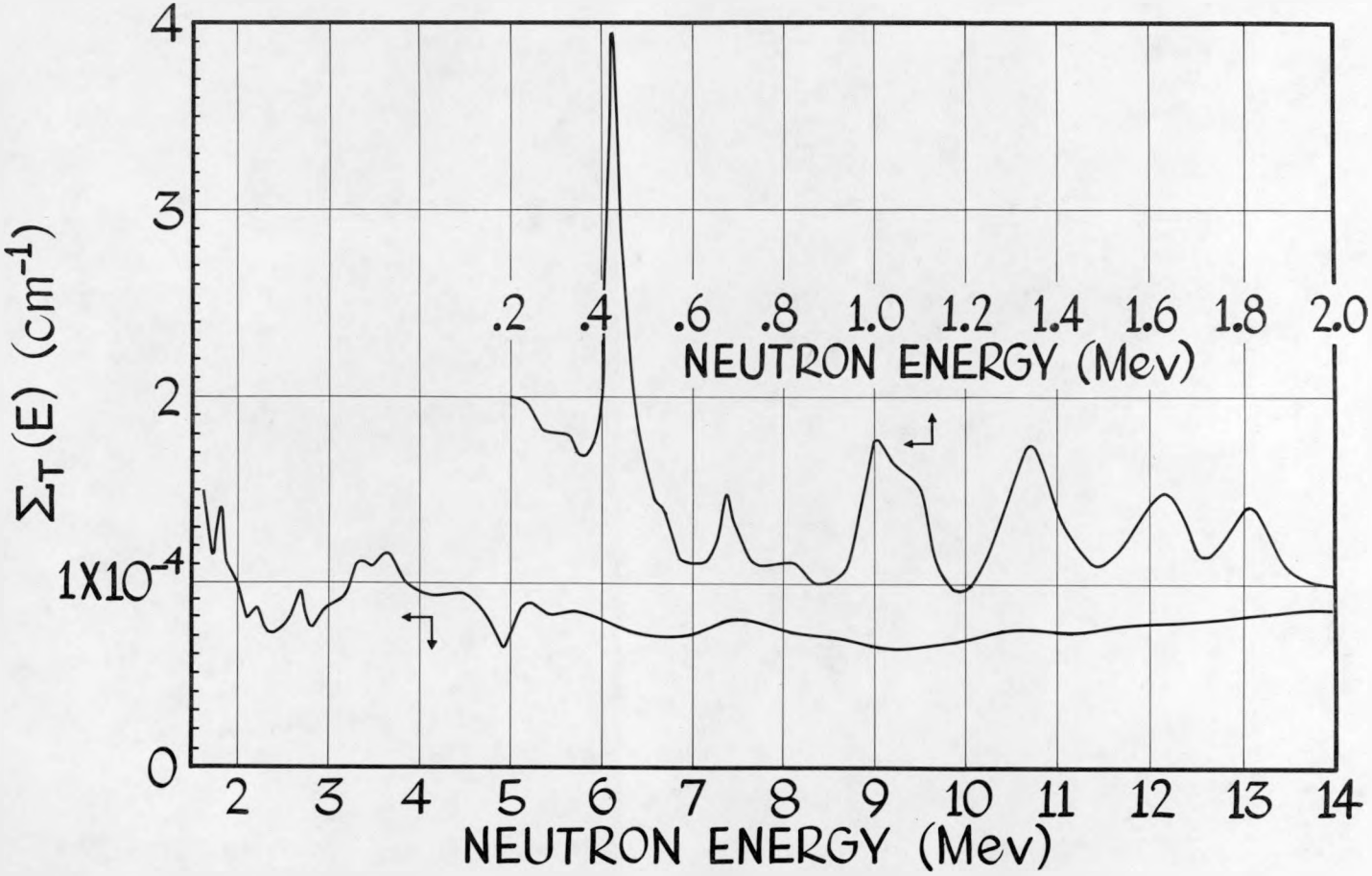

NPC 10,266

FIGURE 3

AIR-SCATTERED NEUTRON FLUX AND DOSE RATE

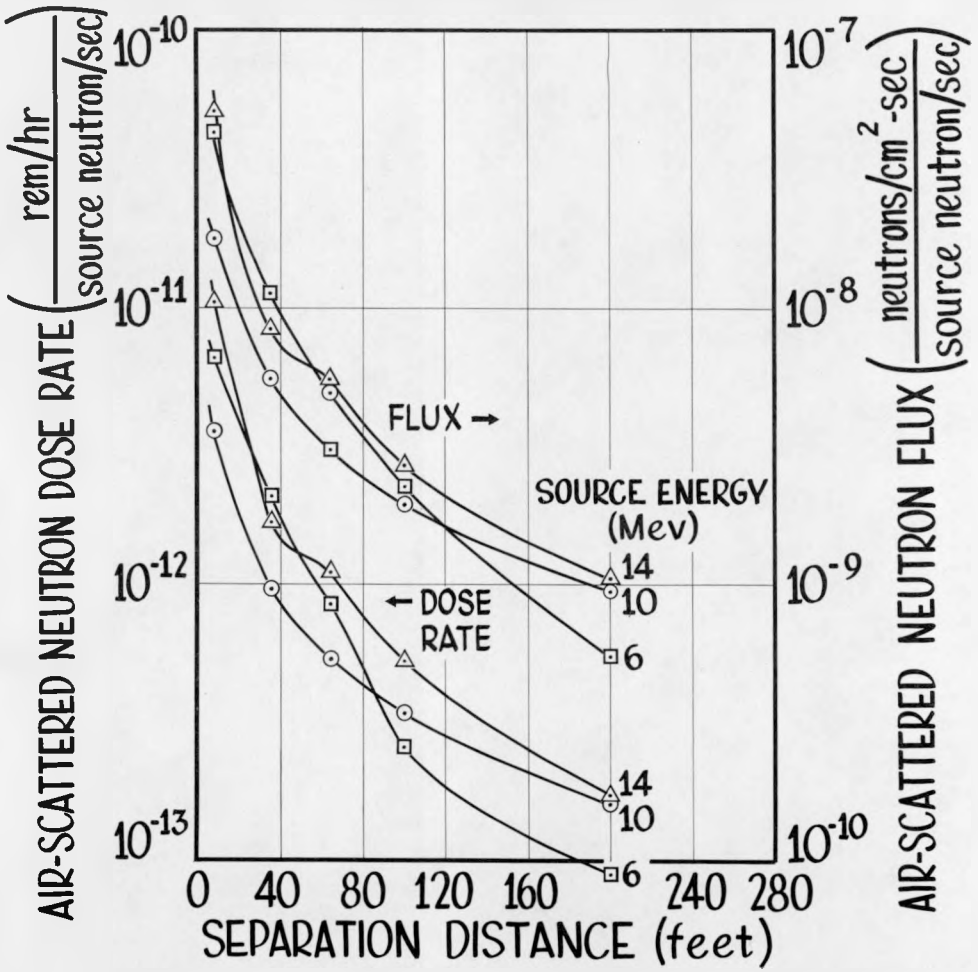

NPC 10,267

FIGURE 4

causes the 6-Mev-source neutrons to undergo most of their scattering in a region near the source, and thus creates a large scattered-flux component at small separation distances. As the separation distance increases, these same high neutron cross sections at low energies result in a more rapid attenuation of the scattered flux from the 6-Mev source. The dose rate from the 14-Mev source is seen to fall off faster with distance than the dose rate from the 10-Mev source. This difference in fall-off with distance probably results from the fact that the 14-Mev neutrons can undergo more inelastic collisions than the 10-Mev neutrons in slowing-down to an energy of 1 Mev.

The variation of the detected scattered dose rate with detector angle is shown in Figure 5 for source energies of 6, 10, and 14 Mev and separation distances of 64 and 100 feet. At 64 feet, a shadow shield in front of the detector with an effective half-angle of 30^{o} would reduce the detected scattered dose rate by 40% for all source energies shown. At 100 feet, the angular distribution for source energies greater than 6 Mev is peaked even more forward than it is at 64 feet. A reduction of 50% in the scattered dose rate can be achieved at 100 feet by shielding out the scattered dose rate entering the detector in the first 30^{o}. This rapid decrease in dose rate with detector angle indicates that most of the high-energy scattered neutrons are entering the detector through small detector angles. That this is so is seen from the energy spectra shown in Figure 6. This figure shows the variation of the energy spectrum with detector angle for a source energy of 14 Mev and a separation distance of 100 feet. The number of neutrons per Mev at the high-energy end of the spectrum decreases much more rapidly with shadow-shield angle than does the low-energy portion of the spectrum.

The differential energy spectra for source energies of 6 and 10 Mev at separation distances of 64, 100, and 200 feet are shown in Figures 7 and 8. The differential energy spectra for these energies exhibit a steep drop near the source energy. This drop results from highly forward elastic scattering which tends to conserve neutrons. The initial drop in the spectra is interrupted by a rise resulting from first-collison excitation of the 2.31-Mev level in nitrogen and a buildup near the energy corresponding to the limit of single scattering for elastic collisions. The spectra have peaks that occur near the energies expected from single-collision excitation of both oxygen and nitrogen. Although these peaks are fairly broad, the rapid drop in the 10-Mev spectra at energies below the threshold energy for nitrogen inelastic scattering indicates that very few of the neutrons undergo more than one inelastic collision in slowing down to 1 Mev.

AIR-SCATTERED DOSE RATE VS. DETECTOR ANGLE

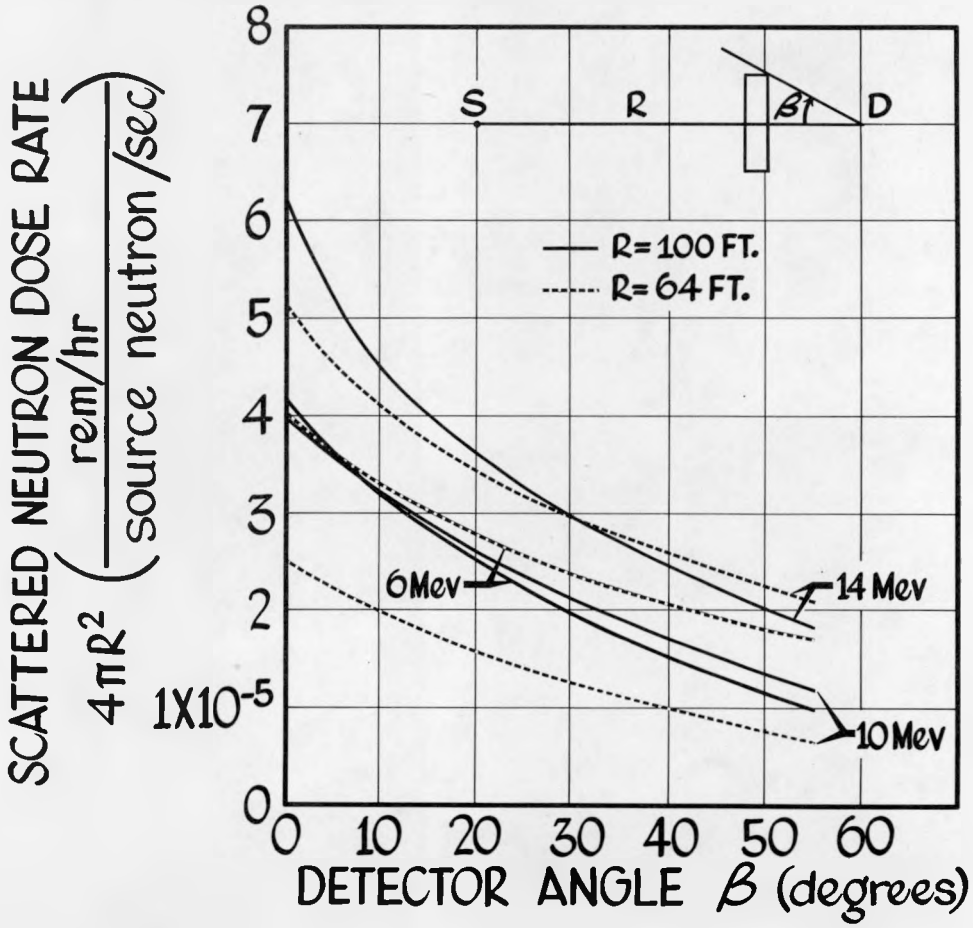

NPC 10,268

FIGURE 5

ENERGY AND ANGULAR DISTRIBUTION OF THE SCATTERED FLUX

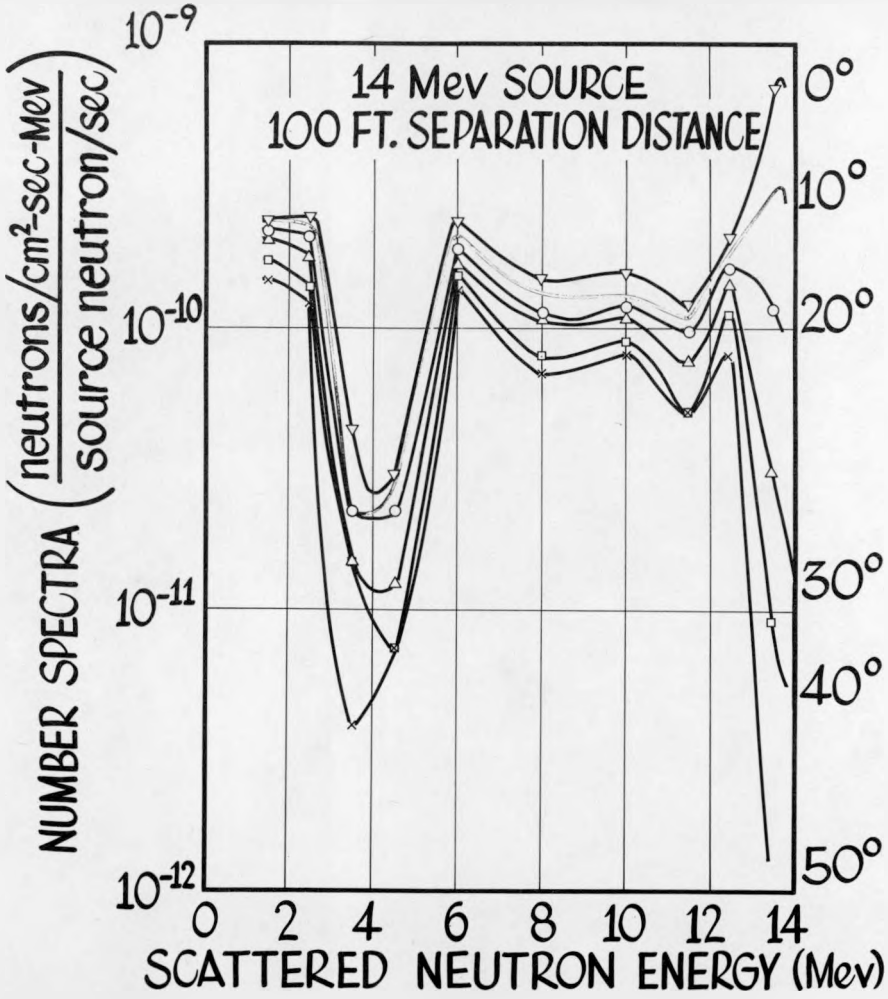

NPC 10,269

FIGURE 6

DIFFERENTIAL ENERGY SPECTRA

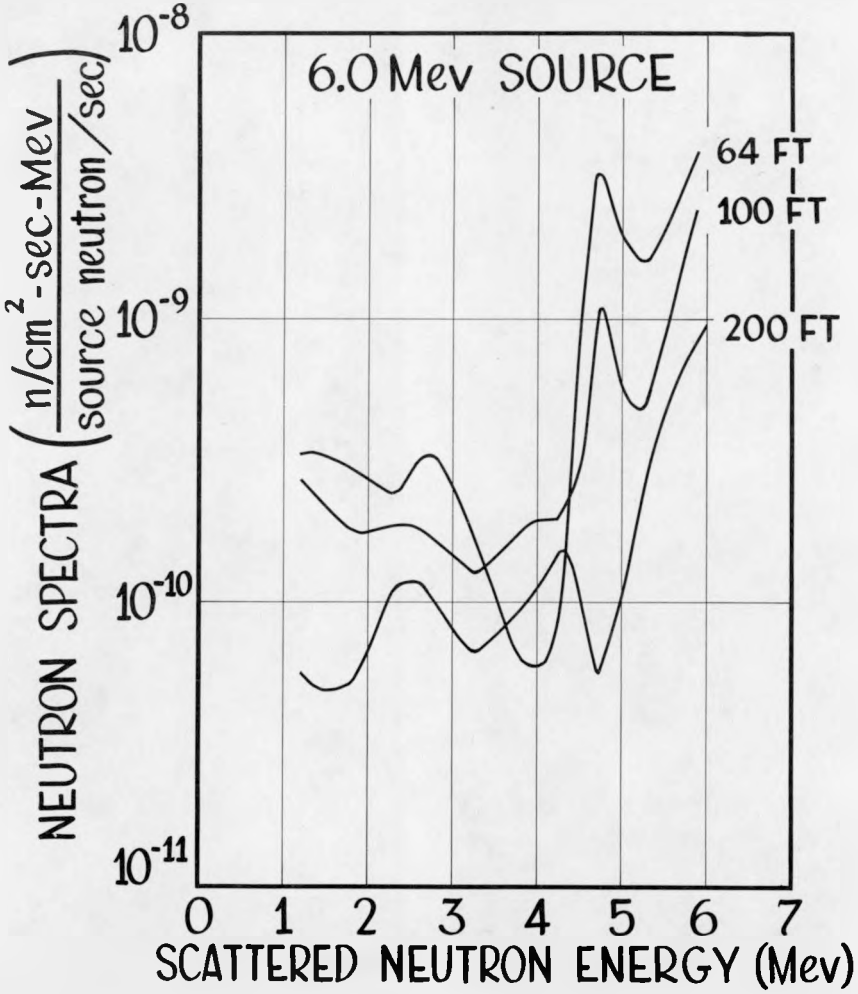

NPC 10,270

FIGURE 7

DIFFERENTIAL ENERGY SPECTRA

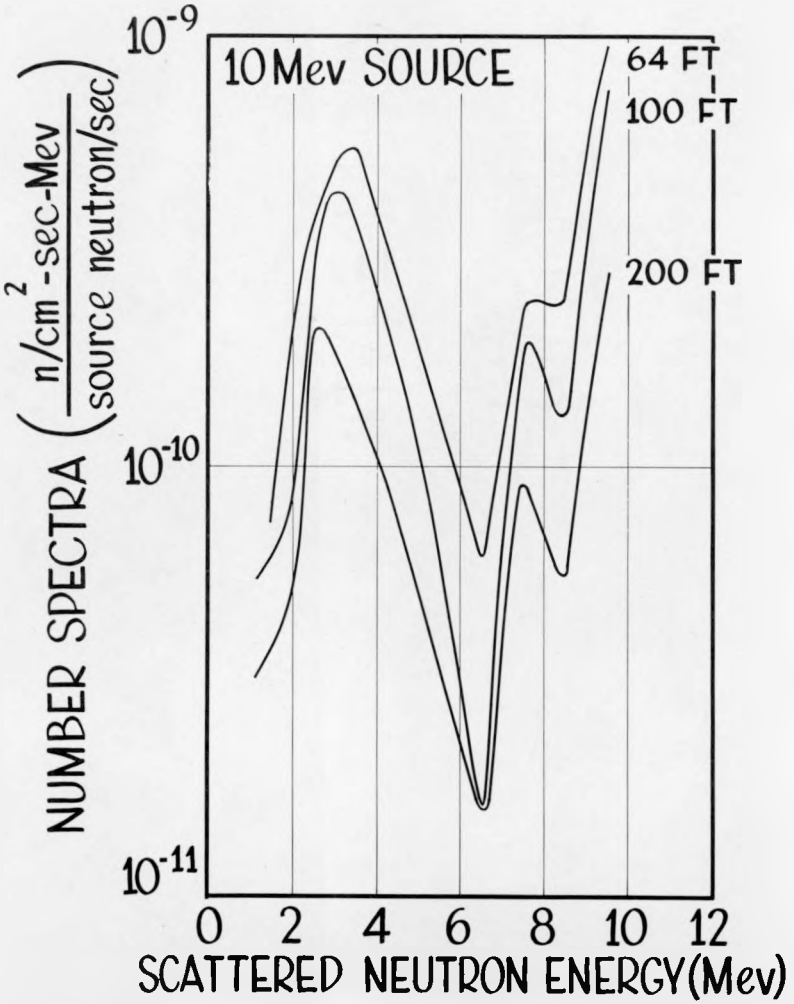

NPC 10,271

FIGURE 8

The energy spectra for a 14-Mev point isotropic source is compared in Figure 9 with the Holland and Richards moments-method results[4] and the Monte Carlo results obtained by Zerby[3] for a separation distance of 190.3 feet. The differences between the Holland and Richards and the Convair calculated spectra are largely due to the inelastic scattering cross sections used in the calculations. The assumption by Holland and Richards that there is a continuous distribution of available excited levels in air and that all these levels are equally probable, combined with a scanty knowledge of the inelastic cross section, is probably responsible for the differences between the two calculations. The energy spectra computed by Zerby shows a steady decrease with decreasing energy for energies below 11 Mev. The assumption that the total cross section is identical with the elastic scattering cross section produces a spectrum that is typical of that obtained by neglecting inelastic scattering.

Recently, some Monte Carlo neutron air scattering calculations were made at Convair-Fort Worth for a point isotropic fission source in air at separation distances of up to 1500 yards at sea-level air density. These calculations, transformed to the air density of the Nevada weapons testing site, have been used to predict the spatial, energy, and angular distributions of the neutrons from a nuclear weapon. Ground effects and self-attenuation of the neutrons in the nuclear device were neglected in the calculations. The calculated neutron dose is compared in Figure 10 with dose measurements recently reported by Ritchie and Hurst in Health Physics.[12] The slope of the calculated neutron dose is in good agreement with the measured data over most of the five-decade range of attenuation. However, at distances greater than 1500 yards, the calculated dose has started to diverge from the measured dose. The neutron spectrum, also compared in Figure 10 with the measured spectrum, is essentially constant, as indicated by approximately parallel flux curves. The calculations are lower than the measurements at large distances because they do not reflect the increased statistical importance of the more penetrating high-energy neutrons. The rather good agreement between the calculations and measurements for distances less than 1500 yards is gratifying, as this agreement is an indication of the accuracy of the inelastic cross sections used in the calculations. For the calculations shown in Figure 10, the neutron histories were terminated only after the neutron energy dropped below 0.2 Mev.

DIFFERENTIAL ENERGY SPECTRA

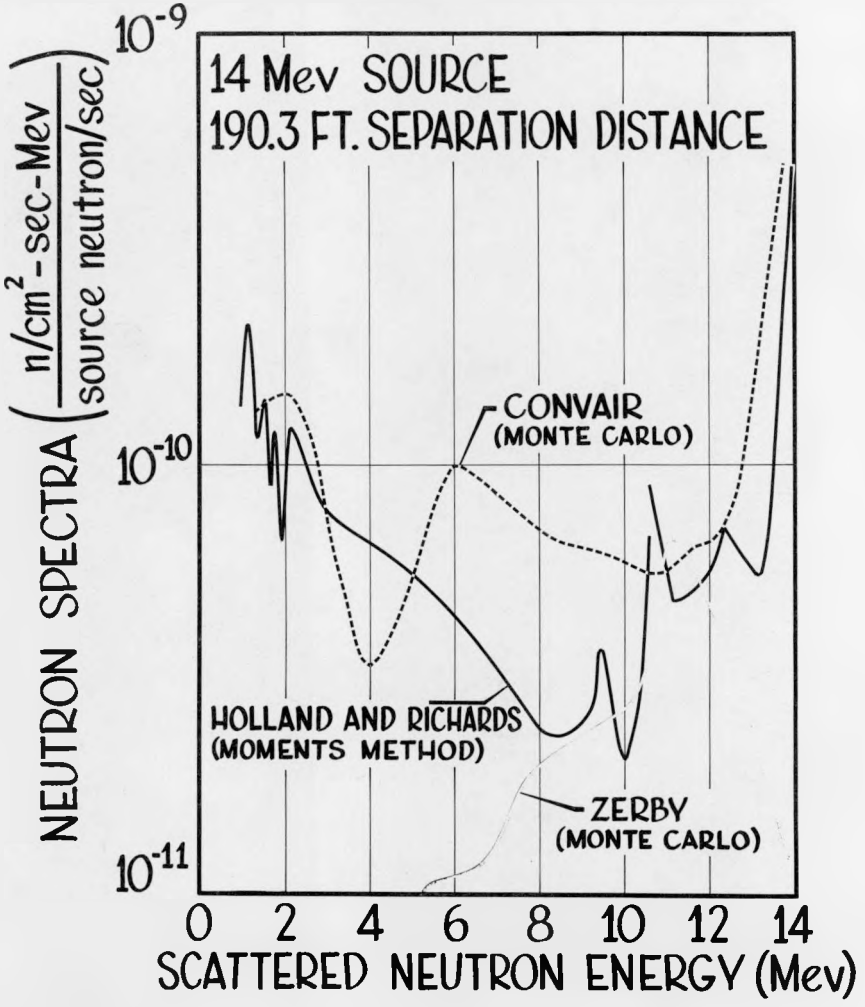

NPC 10,272

FIGURE 9

NEUTRON DOSE AND FLUX VERSUS SLANT RANGE

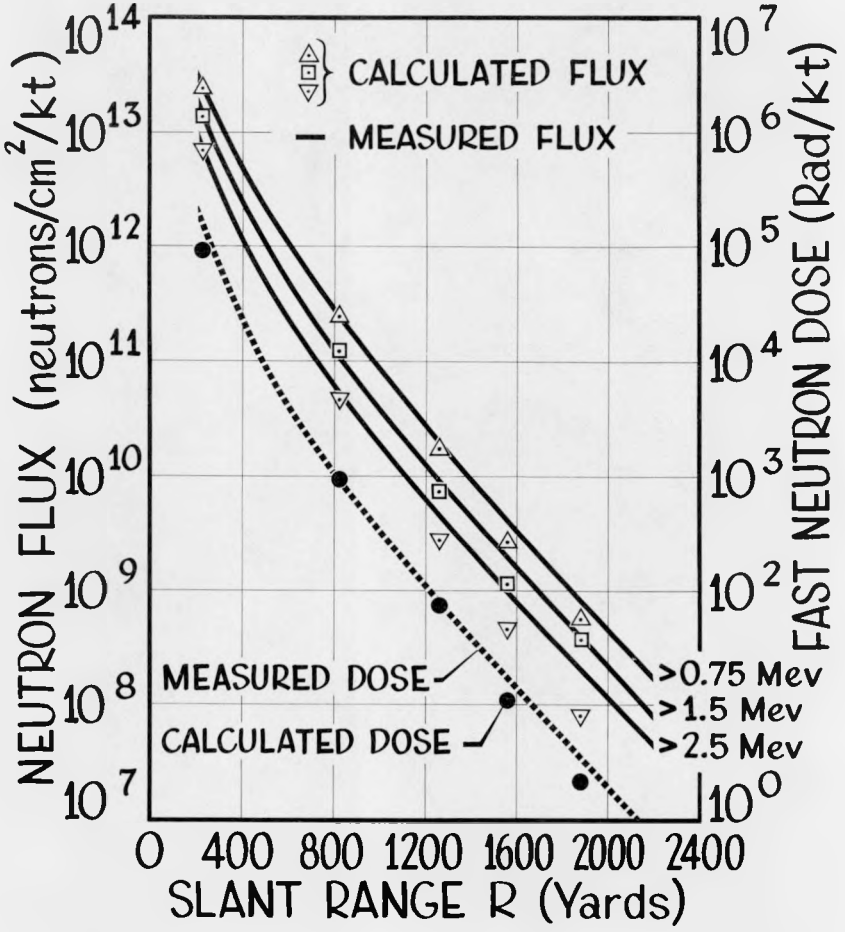

NPC 10,273

FIGURE 10

CONCLUSIONS

The results of the Monte Carlo air-scattering calculations show conclusively that inelastic scattering plays a predominate role in determining the shape of the scattered neutron energy spectrum in air, even for distances less than 200 feet. Monte Carlo calculations are now under way at Convair-Fort Worth to determine the air-scattered neutron flux from monoenergetic line-beam sources; source energies above 3.0 Mev and separation distances of up to 100 feet are being considered. The calculations now under way will utilize the inelastic scattering cross sections described in this paper.

REFERENCES

1. Wells, M. B., Monte Carlo Calculations of Fast Neutron Energy Spectra. Convair-Fort Worth Report FZM-1267 (December 1958). Paper presented at the Sixth ANP Shielding Information Meeting, 2-3 December 1958.

2. Wells, M. B., Studies in Shielding-III. Convair-Fort Worth Report FZK-9-120A (December 1957).

3. Zerby, C. D., A Monte Carlo Calculation of Air-Scattered Neutrons. Oak Ridge National Laboratory Report ORNL-2277 (May 1957).

4. Holland, S. S., and Richards, P. I., Penetration of Neutrons in Air. Technical Operations, Inc. Report AFSWC-TR-55-27 (Sept. 1955).

5. Lustig, H., Goldstein, H., and Kalos, M. H., The Neutron Cross Sections of Nitrogen. Nuclear Development Corporation of America Report NDA 86-1 (June 1957).

6. Lustig, H., Goldstein, H., and Kalos, M. H., An Interim Report on the Neutron Cross Sections of Oxygen. Nuclear Development Corporation of America Report NDA-086-2 (Jan. 1958).

7. Keller, F. L., and Merrill, O. S., Analysis of the Recent T.S.F. Secondary Gamma-Ray Experiment. Oak Ridge National Laboratory Report ORNL-2586 (Sept. 1958).

8. Hughes, D. J., and Schwartz, R. B., Neutron Cross Sections. Brookhaven National Laboratory Report BNL-325, Second Edition (July 1958).

9. Conner, J. P., "A Cloud-Chamber Study of The Scattering of Fast Neutrons in Oxygen." Physical Review 89, 712 (Feb. 1953).

10. Thompson, L. C., and Risser, J. R., "Gamma Rays from Inelastic Scattering of 14-Mev Neutrons in C^{12} and O^{16}." Physical Review 94, 941 (May 1954).

11. Hurst, G. S., and Ritchie, R. H., A Count-Rate Method of Measuring Fast Neutron Tissue Dose. Oak Ridge National Laboratory Report ORNL-930 (Jan. 1951).

12. Ritchie, R. H., and Hurst, G. S., "Penetration of Weapons Radiation: Application to The Hiroshima-Nagasaki Studies." Health Physics Vol. 1, No. 4, (Mar. 1959).

12. CREW SHIELD SHAPING

K. M. Simpson
C. C. Douglass
H. E. Stern

Lockheed Aircraft Corporation
Georgia Division
Marietta, Georgia

CREW SHIELD SHAPING

by

K. M. Simpson, C. C. Douglass, and H. E. Stern

Lockheed Aircraft Corporation
Georgia Division
Marietta, Georgia

A method for shaping the shielding on the sides of a cylindrical crew compartment is being developed. The shield is designed to achieve minimum weight subject to the requirement of a specified weighted average dose rate along the compartment center line. A machine program has been written for a single component of radiation in which attenuation through a single shield material and angular distribution inside are incorporated in the form of general subroutines.

The weighted average dose, $\phi_{av}(\text{℄})$, due to one type of radiation, along the axis of a cylindrical crew shield may be expressed in the form:

$$\phi_{av}(\text{℄}) = \int_o^L \int_o^L \frac{2\pi\,\phi_o(y)\,A(t)\,G(t,\theta)\,u(x)}{\left[1+(y-x)^2\right]^{3/2}}\,dxdy \qquad (1)$$

L is the length of the shield; y is measured along the outside surface parallel to the central axis; x is measured along the central axis; θ is the angle determined by a straight line from a point at y to a point at x and the central axis.

$\phi_o(y)$ expresses the flux at y on the outside surface. $A(t)$ expresses the attenuation of the radiation due to the thickness t. $G(t,\theta)$ expresses the fraction of flux per steradian at y in the direction θ; $u(x)$ is a weighting function expressed along the central axis.

$\left[1+(y-x)^2\right]^{-3/2}$ is due to the inverse square law and an apparent area correction factor.

All distances have been made dimensionless by dividing by R, the inside radius. The weight, W, of the crew shield may be expressed in the form:

$$W = \int_o^L F(t,y)\,dy, \qquad (2)$$

where F is some known function of t, the thickness, and t is a function of y to be determined.

A function, t(y) is required such that the weight, equation (2), is a minimum, and a predetermined weighted average dose is obtained, as expressed in equation (1).

To minimize

$$W = \int_o^L F(t,y)\, dy$$

subject to the constraint

$$\phi_{av}(\mathfrak{L}) = \int_o^L \int_o^L \frac{2\pi \phi_o(y) A(t) G(t,\theta) u(x)}{\left[1 + (y-x)^2\right]^{3/2}} dxdy$$

the integral

$$I = \int_o^L \left[F(t,y) + \lambda \int_o^L \frac{2\pi \phi_o(y) A(t) G(t,\theta) u(x)}{\left[1 + (y-x)^2\right]^{3/2}} dx \right] dy \tag{3}$$

may be written *. Here λ is the Lagrange multiplier.

The integral I, equation (3), may now be minimized subject to no constraint.

The variation on I

$$\delta I = \int_o^L \left[F_t(t,y) + \lambda \int_o^L \frac{2\pi \phi_o(y) \left[A(t) G_t(t,\theta) + A_t(t) G(t,\theta)\right]}{\left[1 + (y-x)^2\right]^{3/2}} u(x)\, dx \right] \delta t dy \tag{4}$$

implies a minimum if t(y) satisfies:

$$F_t(t,y) + \lambda \int_o^L \frac{2\pi \phi_o(y) \left[A(t) G_t(t,\theta) + A_t(t) G(t,\theta)\right]}{\left[1 + (y-x)^2\right]^{3/2}} u(x)\, dx = 0 \tag{5}$$

In general, equation (5) will not be soluble analytically, because of transcendental elements; however, an iterative method has proved successful. To this end, the attenuation function is written

$$A(t) = e^{-\mu R \left(1 - \epsilon(t)\right) t^*}; \tag{6}$$

where the t* merely indicates the t to be determined in the iterative process.

* Hildebrand, F. B., Methods of Applied Mathematics, p. 143.

From (6) $A_t(t) = (-\mu R) A(t) \left[1 - \epsilon(t) - t\,\epsilon_t(t)\right]$.

Let $f(t) = (-\mu R) \left[1 - \epsilon(t) - t\,\epsilon_t(t)\right]$.

Then equation (5) becomes:

$$F_t(t,y) + \lambda\, 2\pi \phi_o(y) A(t) \int_o^L \frac{\left[G_t(t,\theta) + f(t)\, G(t,\theta)\right]}{\left[1 + (y-x)^2\right]^{3/2}} u(x)\, dx = 0 \tag{7}$$

Solving for A (t),

$$A(t) = \frac{-F_t(t,y)}{\lambda\, 2\pi \phi_o(y) \int_o^L \frac{\left[G_t(t,\theta) + f(t)\, G(t,\theta)\right]}{\left[1 + (y-x)^2\right]^{3/2}} u(x)\, dx} \tag{8}$$

Using the expression for A (t) in equation (6) and solving for t*:

$$t^* = \frac{1}{\mu R \left(1 - \epsilon(t)\right)} \ln \left[\frac{\lambda\, 2\pi \phi_o(y) \int_o^L \frac{\left[G_t(t,\theta) + f(t)\, G(t,\theta)\right]}{\left[1 + (y-x)^2\right]^{3/2}} u(x)\, dx}{-F_t(t,y)} \right] \tag{9}$$

To determine the unknown constant, λ , substitute the expression for A(t), equation (8), into the constraining condition, equation (1), and solve for λ ;

$$\lambda = \frac{-1}{\phi_{av}(\mathcal{L})} \int_o^L \int_o^L \frac{G(t,\theta)\, F_t(t,y)\, u(x)}{\left[1 + (y-x)^2\right]^{3/2} \int_o^L \frac{\left[G_t(t,\theta) + f(t)\, G(t,\theta)\right]}{\left[1 + (y-x)^2\right]^{3/2}} u(x)\, dx} dx\,dy \tag{10}$$

Equations (9) and (10) may now be used in an iterative process to determine the shield thicknesses, t; the convergence of equation (9) and the satisfaction of equation (5) will indicate the minimizing thicknesses which fulfill the constraining requirements.

A program has been written for the IBM-704 to compute weight-minimizing thicknesses for the case of the single-layer crew shield.

Six fictitious test cases have been submitted to the IBM-704 program; three cases use constant functions as subroutines, and three use variable functions. These cases should not be interpreted as representing actual design specifications. In all six cases, the following definitions apply:

LENGTH	=	true length/radius
RADIUS	=	true radius (36 inches)
RHO	=	density of shielding material
MU	=	absorption coefficient
PHI(AB)	=	relative unshielded weighted average dose along the center line
PHI(AVE)	=	relative weighted average dose along the center line
B	=	reduction factor (i.e., PHI(AVE) = PHI(AB)/B)
P	=	standard deviation of $(\lambda_i / \lambda_{av})$
Q	=	relative tolerance of the reduction factor
PHI(X)	=	relative dose at x on the center line
T(Y)·R	=	true thickness at y
D(Y)	=	the ratio $\frac{\partial W}{\partial t_i} \Big/ \frac{\partial \phi_{av}}{\partial t_i} = \lambda_i$

In Table I, the constant cases (B = 10, 100, 1000) incorporated the following functions:

$G(t, \theta)$	=	$\frac{1}{2\pi}$
$\epsilon(t)$	=	0
$u(x)$	=	1/L
$\phi_o(y)$	=	1

In Table II, the variable cases (B = 10, 100, 1000) incorporated these functions:

$$G(t, \theta) = 1/2\pi \cdot e^{-\mu Rt} + \frac{1}{\pi} (1 - e^{-\mu Rt}) \sin \theta$$

$$\epsilon(t) = \frac{1}{\pi} \text{Arctan} \left(\frac{\mu Rt}{5}\right)$$

$$u(x) = \frac{1}{L} \left(1 + 1/2 \sin \left(\frac{\pi x}{L} - \frac{\pi}{2}\right)\right)$$

$$\phi_o(y) = 1$$

SHIELD SHAPING — PROBLEM 1102

LENGTH	RADIUS	RHO	MU	PHI (AB)	PHI (AVE)	ERROR LIMITS AND CONVERGENCE CRITERIA	CALCULATED ERRORS
5.00	36.00	1.00	0.500	1.64E 00	1.64E-01	B = 1.00E 01 P = 10.00E-05 Q = 10.00E-03	BE = 1.07E-06 DO = 2.48E-05

** CONVERGED IN 4 ITERATIONS.

X	PHI(X)	Y	T(Y)*R	D(Y)	X	PHI(X)	Y	T(Y)*R	D(Y)
0.	1.14E-01	0.	3.62E 00	5.60E 05	0.25	1.38E-01	0.25	4.04E 00	5.60E 05
0.50	1.56E-01	0.50	4.33E 00	5.60E 05	0.75	1.66E-01	0.75	4.53E 00	5.60E 05
1.00	1.71E-01	1.00	4.65E 00	5.60E 05	1.25	1.73E-01	1.25	4.72E 00	5.60E 05
1.50	1.73E-01	1.50	4.77E 00	5.60E 05	1.75	1.73E-01	1.75	4.81E 00	5.60E 05
2.00	1.72E-01	2.00	4.83E 00	5.60E 05	2.25	1.72E-01	2.25	4.84E 00	5.60E 05
2.50	1.72E-01	2.50	4.84E 00	5.60E 05	2.75	1.72E-01	2.75	4.84E 00	5.60E 05
3.00	1.72E-01	3.00	4.83E 00	5.60E 05	3.25	1.73E-01	3.25	4.81E 00	5.60E 05
3.50	1.73E-01	3.50	4.77E 00	5.60E 05	3.75	1.73E-01	3.75	4.72E 00	5.60E 05
4.00	1.71E-01	4.00	4.65E 00	5.60E 05	4.25	1.66E-01	4.25	4.53E 00	5.60E 05
4.50	1.56E-01	4.50	4.33E 00	5.60E 05	4.75	1.38E-01	4.75	4.04E 00	5.60E 05
5.00	1.14E-01	5.00	3.62E 00	5.60E 05					

SHIELD SHAPING — PROBLEM 1103

LENGTH	RADIUS	RHO	MU	PHI (AB)	PHI (AVE)	ERROR LIMITS AND CONVERGENCE CRITERIA	CALCULATED ERRORS
5.00	36.00	1.00	0.500	1.64E 00	1.64E-02	B = 1.00E 02 P = 10.00E-05 Q = 10.00E-02	BE = 1.91E-05 DO = 1.79E-05

** CONVERGED IN 4 ITERATIONS.

X	PHI(X)	Y	T(Y)*R	D(Y)	X	PHI(X)	Y	T(Y)*R	D(Y)
0.	1.14E-02	0.	8.22E 00	6.23E 06	0.25	1.38E-02	0.25	8.65E 00	6.23E 06
0.50	1.56E-02	0.50	8.94E 00	6.23E 06	0.75	1.66E-02	0.75	9.13E 00	6.23E 06
1.00	1.71E-02	1.00	9.25E 00	6.23E 06	1.25	1.73E-02	1.25	9.33E 00	6.23E 06
1.50	1.73E-02	1.50	9.38E 00	6.23E 06	1.75	1.73E-02	1.75	9.41E 00	6.23E 06
2.00	1.72E-02	2.00	9.43E 00	6.23E 06	2.25	1.72E-02	2.25	9.44E 00	6.23E 06
2.50	1.72E-02	2.50	9.45E 00	6.23E 06	2.75	1.72E-02	2.75	9.44E 00	6.23E 06
3.00	1.72E-02	3.00	9.43E 00	6.23E 06	3.25	1.73E-02	3.25	9.41E 00	6.23E 06
3.50	1.73E-02	3.50	9.38E 00	6.23E 06	3.75	1.73E-02	3.75	9.33E 00	6.23E 06
4.00	1.71E-02	4.00	9.25E 00	6.23E 06	4.25	1.66E-02	4.25	9.13E 00	6.23E 06
4.50	1.56E-02	4.50	8.94E 00	6.23E 06	4.75	1.38E-02	4.75	8.65E 00	6.23E 06
5.00	1.14E-02	5.00	8.22E 00	6.23E 06					

SHIELD SHAPING — PROBLEM 1104

LENGTH	RADIUS	RHO	MU	PHI (AB)	PHI (AVE)	ERROR LIMITS AND CONVERGENCE CRITERIA	CALCULATED ERRORS
5.00	36.00	1.00	0.500	1.64E 00	1.64E-03	B = 1.00E 03 P = 10.00E-05 Q = 10.00E-01	BE = 1.60E-04 DO = 1.33E-05

** CONVERGED IN 4 ITERATIONS.

X	PHI(X)	Y	T(Y)*R	D(Y)	X	PHI(X)	Y	T(Y)*R	D(Y)
0.	1.14E-03	0.	1.28E 01	6.87E 07	0.25	1.38E-03	0.25	1.32E 01	6.87E 07
0.50	1.56E-03	0.50	1.35E 01	6.87E 07	0.75	1.66E-03	0.75	1.37E 01	6.87E 07
1.00	1.71E-03	1.00	1.39E 01	6.87E 07	1.25	1.73E-03	1.25	1.39E 01	6.87E 07
1.50	1.73E-03	1.50	1.40E 01	6.87E 07	1.75	1.73E-03	1.75	1.40E 01	6.87E 07
2.00	1.72E-03	2.00	1.40E 01	6.87E 07	2.25	1.72E-03	2.25	1.41E 01	6.87E 07
2.50	1.72E-03	2.50	1.41E 01	6.87E 07	2.75	1.72E-03	2.75	1.41E 01	6.87E 07
3.00	1.72E-03	3.00	1.40E 01	6.87E 07	3.25	1.73E-03	3.25	1.40E 01	6.87E 07
3.50	1.73E-03	3.50	1.40E 01	6.87E 07	3.75	1.73E-03	3.75	1.39E 01	6.87E 07
4.00	1.71E-03	4.00	1.39E 01	6.87E 07	4.25	1.66E-03	4.25	1.37E 01	6.87E 07
4.50	1.56E-03	4.50	1.35E 01	6.87E 07	4.75	1.38E-03	4.75	1.32E 01	6.87E 07
5.00	1.14E-03	5.00	1.28E 01	6.87E 07					

TABLE I CONSTANT CASES

SHIELD SHAPING PROBLEM 1102

LENGTH	RADIUS	RHO	MU	PHI (AB)	PHI (AVE)	ERROR LIMITS AND CONVERGENCE CRITERIA	CALCULATED ERRORS
5.00	36.00	1.00	0.500	1.64E 00	1.64E-01	B = 1.00E 01 P = 10.00E-05 Q = 10.00E-03	BE = 2.68E-03 DO = 1.50E-05

** CONVERGED IN 7 ITERATIONS.

X	PHI(X)	Y	T(Y)*R	D(Y)	X	PHI(X)	Y	T(Y)*R	D(Y)
0.	1.69E-01	0.	4.13E 00	9.10E 05	0.25	2.11E-01	0.25	4.80E 00	9.10E 05
0.50	2.37E-01	0.50	5.28E 00	9.10E 05	0.75	2.44E-01	0.75	5.64E 00	9.10E 05
1.00	2.41E-01	1.00	5.93E 00	9.10E 05	1.25	2.32E-01	1.25	6.18E 00	9.10E 05
1.50	2.20E-01	1.50	6.41E 00	9.10E 05	1.75	2.08E-01	1.75	6.63E 00	9.10E 05
2.00	1.97E-01	2.00	6.84E 00	9.10E 05	2.25	1.86E-01	2.25	7.04E 00	9.10E 05
2.50	1.76E-01	2.50	7.23E 00	9.10E 05	2.75	1.68E-01	2.75	7.40E 00	9.10E 05
3.00	1.60E-01	3.00	7.55E 00	9.10E 05	3.25	1.54E-01	3.25	7.67E 00	9.10E 05
3.50	1.49E-01	3.50	7.77E 00	9.10E 05	3.75	1.44E-01	3.75	7.82E 00	9.10E 05
4.00	1.40E-01	4.00	7.82E 00	9.10E 05	4.25	1.34E-01	4.25	7.73E 00	9.10E 05
4.50	1.24E-01	4.50	7.51E 00	9.10E 05	4.75	1.08E-01	4.75	7.09E 00	9.10E 05
5.00	8.49E-02	5.00	6.41E 00	9.10E 05					

SHIELD SHAPING PROBLEM 1103

LENGTH	RADIUS	RHO	MU	PHI (AB)	PHI (AVE)	ERROR LIMITS AND CONVERGENCE CRITERIA	CALCULATED ERRORS
5.00	36.00	1.00	0.500	1.64E 00	1.64E-02	B = 1.00E 02 P = 10.00E-05 Q = 10.00E-02	BE = 8.67E-02 DO = 5.73E-05

** CONVERGED IN 7 ITERATIONS.

X	PHI(X)	Y	T(Y)*R	D(Y)	X	PHI(X)	Y	T(Y)*R	D(Y)
0.	1.75E-02	0.	1.12E 01	1.29E 07	0.25	2.19E-02	0.25	1.21E 01	1.29E 07
0.50	2.45E-02	0.50	1.27E 01	1.29E 07	0.75	2.51E-02	0.75	1.32E 01	1.29E 07
1.00	2.47E-02	1.00	1.36E 01	1.29E 07	1.25	2.36E-02	1.25	1.39E 01	1.29E 07
1.50	2.23E-02	1.50	1.42E 01	1.29E 07	1.75	2.10E-02	1.75	1.45E 01	1.29E 07
2.00	1.98E-02	2.00	1.47E 01	1.29E 07	2.25	1.86E-02	2.25	1.50E 01	1.29E 07
2.50	1.76E-02	2.50	1.52E 01	1.29E 07	2.75	1.67E-02	2.75	1.54E 01	1.29E 07
3.00	1.59E-02	3.00	1.56E 01	1.29E 07	3.25	1.52E-02	3.25	1.58E 01	1.29E 07
3.50	1.47E-02	3.50	1.59E 01	1.29E 07	3.75	1.42E-02	3.75	1.60E 01	1.29E 07
4.00	1.38E-02	4.00	1.60E 01	1.29E 07	4.25	1.32E-02	4.25	1.59E 01	1.29E 07
4.50	1.23E-02	4.50	1.56E 01	1.29E 07	4.75	1.07E-02	4.75	1.51E 01	1.29E 07
5.00	8.42E-03	5.00	1.42E 01	1.29E 07					

SHIELD SHAPING PROBLEM 1104

LENGTH	RADIUS	RHO	MU	PHI (AB)	PHI (AVE)	ERROR LIMITS AND CONVERGENCE CRITERIA	CALCULATED ERRORS
5.00	36.00	1.00	0.500	1.64E 00	1.64E-03	B = 1.00E 03 P = 10.00E-05 Q = 10.00E-01	BE = 7.50E-01 DO = 1.57E-05

** CONVERGED IN 7 ITERATIONS.

X	PHI(X)	Y	T(Y)*R	D(Y)	X	PHI(X)	Y	T(Y)*R	D(Y)
0.	1.80E-03	0.	1.96E 01	1.59E 08	0.25	2.24E-03	0.25	2.06E 01	1.59E 08
0.50	2.50E-03	0.50	2.13E 01	1.59E 08	0.75	2.56E-03	0.75	2.18E 01	1.59E 08
1.00	2.50E-03	1.00	2.22E 01	1.59E 08	1.25	2.38E-03	1.25	2.26E 01	1.59E 08
1.50	2.25E-03	1.50	2.29E 01	1.59E 08	1.75	2.11E-03	1.75	2.32E 01	1.59E 08
2.00	1.98E-03	2.00	2.35E 01	1.59E 08	2.25	1.86E-03	2.25	2.38E 01	1.59E 08
2.50	1.75E-03	2.50	2.41E 01	1.59E 08	2.75	1.66E-03	2.75	2.43E 01	1.59E 08
3.00	1.58E-03	3.00	2.45E 01	1.59E 08	3.25	1.51E-03	3.25	2.47E 01	1.59E 08
3.50	1.45E-03	3.50	2.48E 01	1.59E 08	3.75	1.41E-03	3.75	2.49E 01	1.59E 08
4.00	1.36E-03	4.00	2.49E 01	1.59E 08	4.25	1.31E-03	4.25	2.47E 01	1.59E 08
4.50	1.22E-03	4.50	2.44E 01	1.59E 08	4.75	1.06E-03	4.75	2.39E 01	1.59E 08
5.00	8.37E-04	5.00	2.29E 01	1.59E 08					

TABLE II VARIABLE CASES

13. A MONTE CARLO CALCULATION OF THE TRANSPORT OF NEUTRONS THROUGH IRON SLABS

M. O. Burrell
D. L. Cribbs

Lockheed Aircraft Corporation
Georgia Division
Marietta, Georgia

A MONTE CARLO CALCULATION OF THE TRANSPORT OF NEUTRONS THROUGH IRON SLABS

by

M. O. Burrell and D. L. Cribbs

Lockheed Aircraft Corporation
Georgia Division
Marietta, Georgia

A Monte Carlo sampling is used to calculate the transmitted number current, number flux, dose, and the dose albedos of neutrons incident on an iron slab. A plane parallel source of monoenergetic neutrons with a number current density of 1 neutron/cm^2-sec is incident from a vacuum upon an iron slab of finite thickness. Transmission factors and linear buildup factors are computed for the above quantities. The dose transmission and the dose albedo are also calculated for each of 120 equal solid angles. Gamma rays from inelastic scattering are recorded as a function of energy and penetration depth.

In the past, the use of a stochastic method to calculate the transmission of neutrons in relatively dense media has been seriously hampered by the lack of basic data, including differential scattering cross sections and the gamma-ray spectra resulting from inelastic scattering; the latter is still uncertain above a few Mev. The present calculation utilizes the most recent compilations of cross section data in a Monte Carlo 704-Computer program to determine several parameters and distributions that should be of use in shielding calculations.

The computer program solves the slab transmission problem, using random sampling techniques. A plane parallel beam of monoenergetic neutrons with a scalar number current density, J_o, of 1 neutron/cm^2-sec is incident, at an angle Θ_o with the normal, upon a slab of finite thickness, Z_t, but infinite extent. The neutron number current, number flux, and dose transmitted through the slab are determined. It is assumed that the slab material is such that, within the energy range of 18 Mev to the 50 ev region, neutron capture is negligible. Elastic and inelastic scattering are assumed to be the only mechanisms that alter neutron energy and direction. This assumption is valid up to about 10 Mev for iron, while inelastic scattering is not possible for neutron energies below the minimum excitation level of 0.85 Mev.

Since the uncollided fraction of the transmitted neutrons is given by

$$U = \exp\left[-\Sigma_T(E_o)\, Z_T/\cos\Theta_o\right],$$

it is necessary to consider in the Monte Carlo program only those neutrons which suffer a collision. Consequently, the fraction of the scattered neutrons transmitted, S, is calculated by random sampling; this, when combined with the uncollided fraction U, yields a buildup factor, $(U + S)/U$. A transmission factor is determined from the expression $T = (U + S)$. A similar set of expressions is used for flux and dose.

In the present slab problem, the points of first collision are biased to occur inside the slab and are computed systematically rather than by random sampling. After the first collision, the only way a history can be terminated is for the neutron to escape the slab or to be degraded in energy below a preassigned level. At each point of collision, a statistical estimation of the number current transmitted through the slab in a sampled direction is expressed by

$$s_i = J_o W \times \exp\left[-\Sigma_T(E_i)\, Z_i/\cos\Theta_i\right]$$

where W is a weight correction for biasing on the first scatter. The s_i's are summed for all scatters of the i^{th} neutron. If there are N histories, the value

$$S = \frac{1}{N}\sum_{j=1}^{N}\sum_{i=1}^{X} s_{ji}$$

is an estimate of the scattered number current crossing the slab boundary. The scattered number flux is determined from

$$F = \frac{1}{N}\sum_{j=1}^{N}\sum_{i=1}^{X}\left(s_{ji}/\cos\Theta_i\right)$$

and the dose is given by the expression

$$D\,(\text{mrem/hr}) = \frac{1}{N}\sum_{j=1}^{N}\sum_{i=1}^{X}\left(\frac{s_{ji} \times f_i(E)}{\cos\Theta_i}\right)$$

where the quantity $f_i(E)$ is the flux to dose conversion factor determined at each scatter point. The albedo is computed in a like manner but tabulated separately. An estimate of the standard error in C is computed from the expression

$$\sigma_c = \frac{1}{N}\sqrt{\sum_{j=1}^{N}\sum_{i=1}^{X} s_{ji}^{2} - NS^2}$$

A similar error estimate is determined for the flux and dose.

It is also desirable in the present program to compute the dose scattered from the slab face into an increment of solid angle. The following procedure is used to determine the scattered dose transmission per steridian. The polar angle Θ_i, and azimuthal angle ϕ_i at which

the scattered dose component $s_i f_i / \cos \Theta_i$ crosses the slab boundary are determined for each scatter. The dose components are tabulated in intervals of $\Delta \cos \Theta = 0.1$ and $\Delta \phi = 30°$. Because of the azimuthal symmetry of scattering, it is necessary to tabulate data for ϕ only in the range (0°, 180°); the range (180°, 360°) is superimposed on the first range. After N histories are run, with each neutron's scattered components recorded in the appropriate solid angle, the summed dose in each solid angle is multiplied by the factor

$$\frac{\cos \Theta_o}{2f(E_o)\,\Delta \cos \Theta\, \Delta \phi},$$

where $\Delta \cos \Theta \Delta \phi = 0.05236$ for each solid angle. The resulting matrix elements, $d(\Theta, \phi)$, are designated scattered dose transmission factors per steradian, and when summed

$$\frac{2\pi}{60} \sum_{j=1}^{6} \sum_{i=1}^{10} d(\Theta_i, \phi_j) + \left(\frac{\text{uncollided dose}}{\text{source dose}} \right) = (\text{total dose transmission factor}).$$

The quantities $d(\Theta_i, \phi_j)$ have the useful property that the scattered dose r cm away, in the solid angle (Θ_i, ϕ_j) is given by

$$D_s(r, \Theta_i, \phi_j) = D_o \frac{d(\Theta_i, \phi_j)}{r^2} \left(\frac{\text{m rem}}{\text{hr}} \right)$$

where D_o is the source dose incident on the slab. An albedo matrix is also computed with elements that are a function of solid angle.

Since neutrons, when elastically scattered from iron nuclei, lose only a small portion of their energy, it was felt that an average energy of the scattered neutrons for each solid angle would describe with sufficient accuracy the energy spectrum in each solid angle -- except, perhaps, for relatively high energy neutrons (> 3 Mev), where inelastic scattering can result in a rather large energy loss. However, even for source energies as high as 18 Mev, an average scattered energy would be justified, since the neutron flux to dose conversion factors are fairly insensitive in the energy range of 1 to 18 Mev. For these reasons, a weighted average neutron energy as a function of each solid angle was determined.

To account for inelastic scattering, the present program uses total, elastic, and differential elastic cross section data taken from NDA 2111-1 and NDA 2111-2.[1] The excitation levels and the energy losses of inelastically scattered neutrons with energies between 0.85 and 4 Mev are taken from CWR-4040.[2] The energy loss spectrum of the scattered neutron, between 4 and 10 Mev, is estimated from relative probability curves in APEX 467.[3] The inelastic scattering energy loss spectra above 10 Mev are estimated from NDA 2111-1. For computing purposes, the energy loss spectrum of neutrons suffering inelastic scattering is written as a discrete probability function of thirteen energy values which typify the energy spreads for 0.85 Mev to 18 Mev incident neutrons.

A sampling technique is used at each collision to decide whether an elastic or inelastic scatter occurs. If the choice, which depends on neutron energy, is an inelastic

scatter, then the neutron's energy loss is taken from one of thirteen discrete values by using a partial summation technique to approximate the upper limit of the integral,

$$\int_0^S N(E)\,dE = R$$

where R is a pseudo-random number. The energy value thus selected is subtracted from the neutron's original energy and a scattering angle is then determined from the expression

$$\cos \Theta_L = 2R-1.$$

However, instead of choosing a single gamma-ray equal in energy to the neutrons's energy loss, relative probabilities have been adapted for the excitation of the various energy levels in iron, depending on the neutron's incident energy. These probabilities are associated with the appropriate geometric region in the slab where the neutron incident took place and thus became origins for gamma rays due to inelastic scattering.

Some of the preliminary results obtained for number transmissions are presented in Figures 1, 2 and 3. Figure 4 shows a plot of probable gamma rays from inelastic scatter as a function of depth in the slab for two different excitation groups. The source consisted of 3 Mev neutrons with the possible excitation levels in iron being 0.85, 2.10, 2.6, and 2.9 Mev. A typical energy of 2.5 Mev is substituted for the three levels between 2 and 3 Mev. Table I is an example of the output from the computer where the upper left matrix depicts the scattered dose transmission per steradian in the indicated solid angles. The upper right matrix presents the average energy per steradian for each element of the scattered dose transmission matrix. The lower two matrices represent similar values for the albedos. The bottom array of numbers gives the volume distribution of gammas from inelastic scattering as a function of gamma energy.

REFERENCES

1. Troubetzkoy, E. S., Fast Neutron Cross Sections of Iron, Silicon, Aluminum, and Oxygen, NDA 2111-1 and NDA 2111-2, April and July 1959.

2. Kavanagh, D. L., and Mandeville, C. E., Elastic and Inelastic Neutron Cross Sections, CWR-4040, June 1958.

3. Tralli, N., et al, Some Neutron Cross Sections for Multigroup Calculations, APEX-467, June 1958.

4. Kahn, Herman, Applications of Monte Carlo, RM-1237 AEC, April 1954.

Number Current Transmission

of 1 Mev Neutrons Incident

at Angle Θ_o on Iron Slab

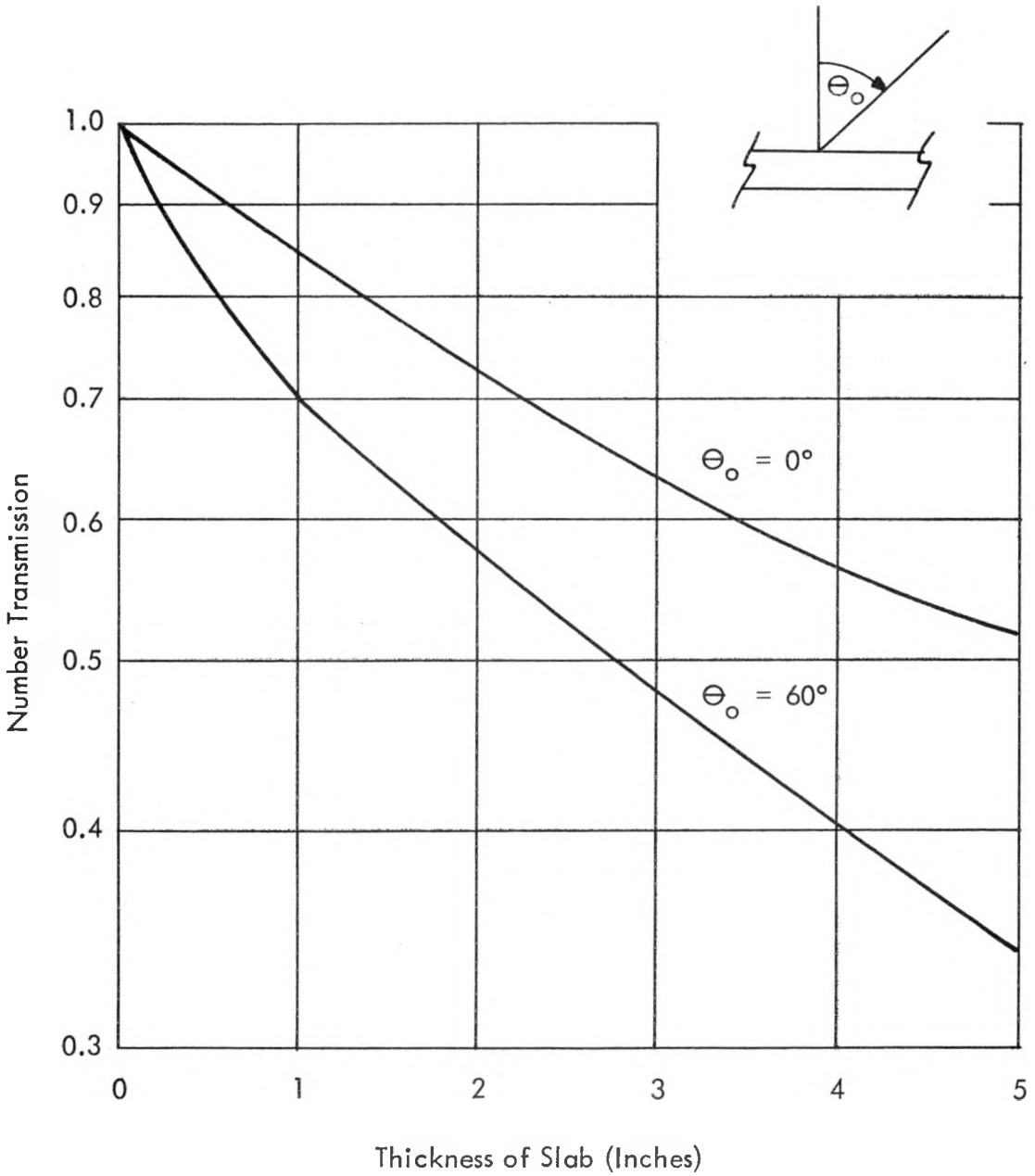

FIGURE 1

Number Current Transmission

of 3 Mev Neutrons Incident

at Angle Θ_o on Iron Slab

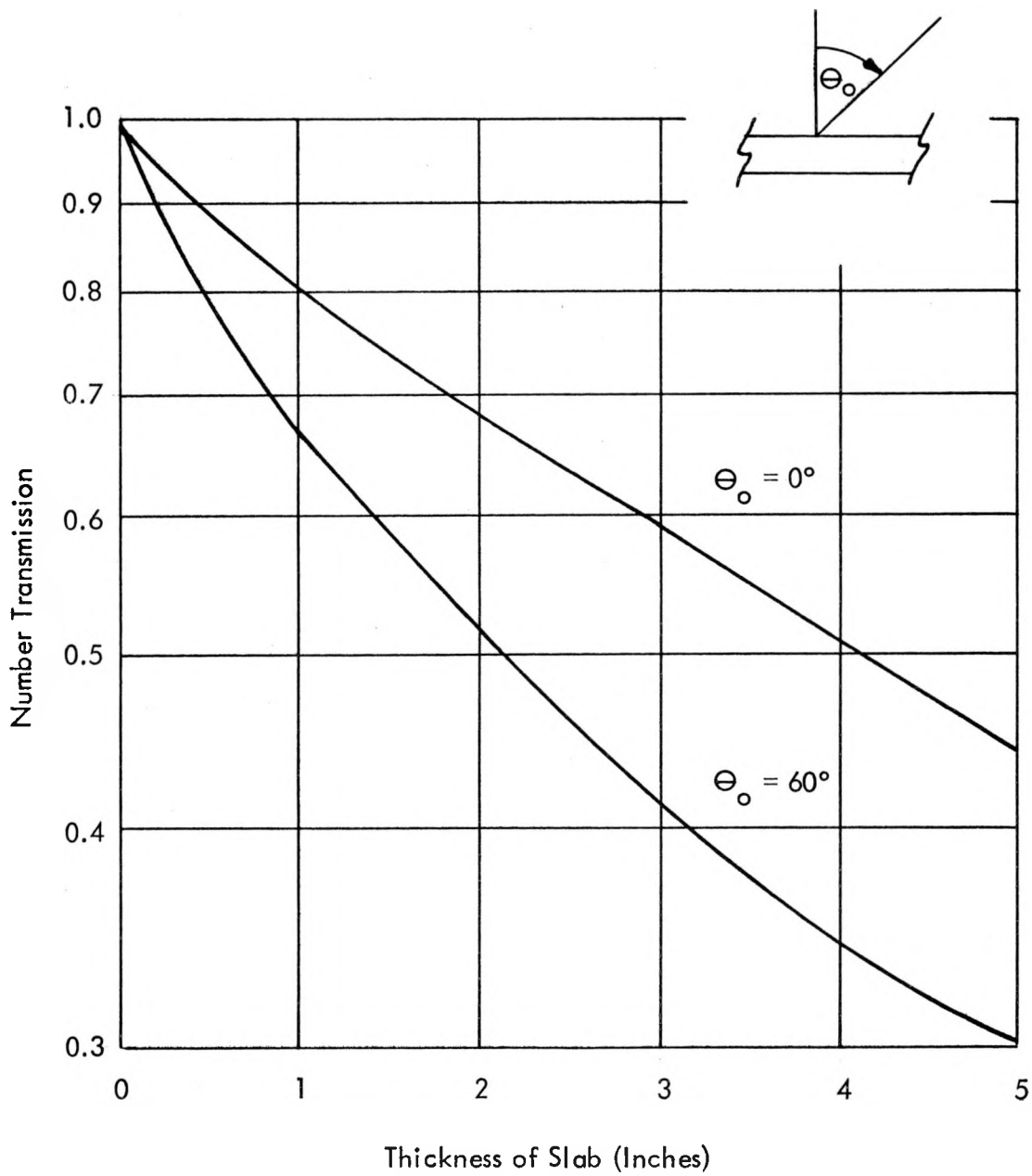

FIGURE 2

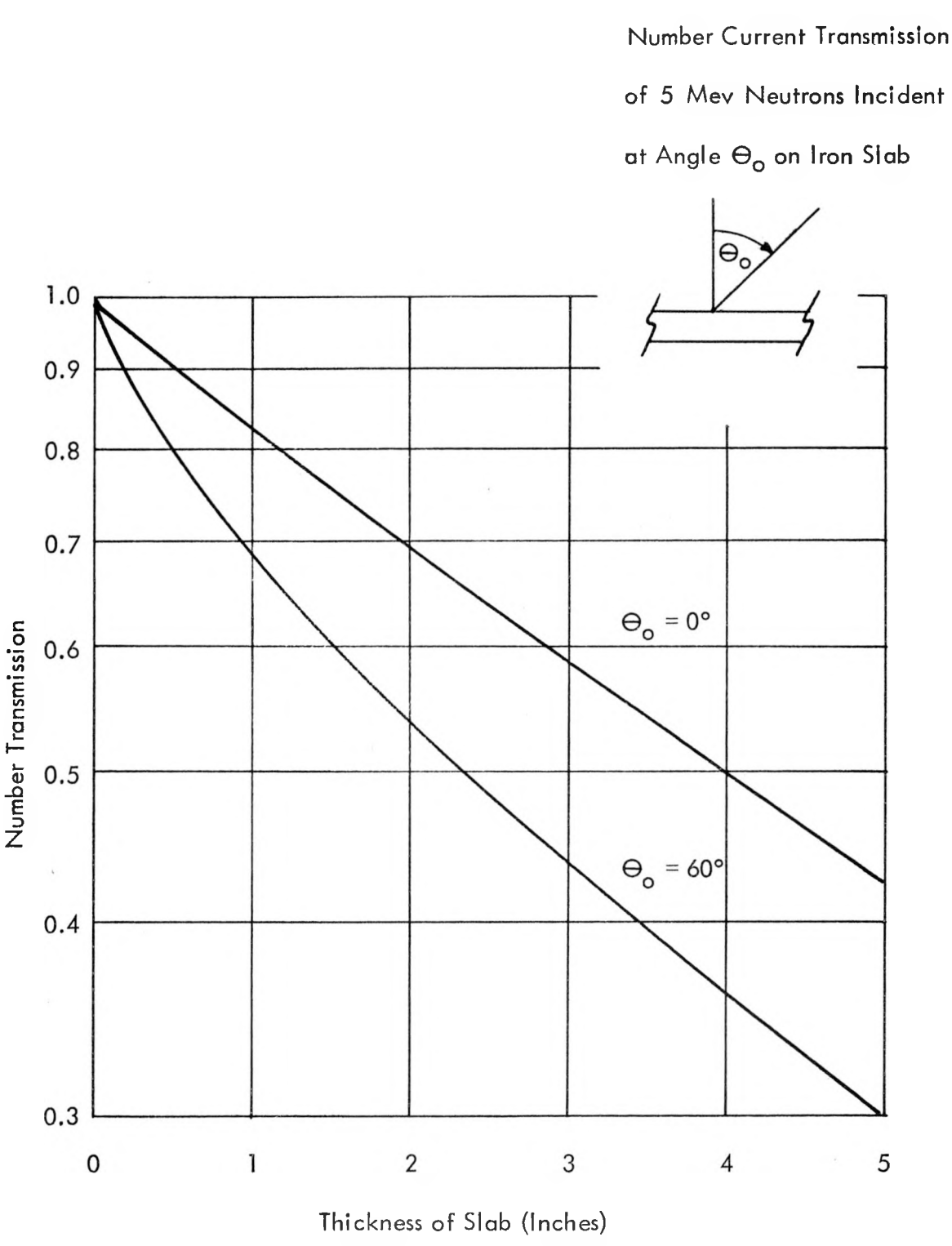
Number Current Transmission
of 5 Mev Neutrons Incident
at Angle Θ_o on Iron Slab
Θ_o
1.0
0.9
0.8
0.7
0.6
0.5
0.4
0.3
Number Transmission
Θ_o = 0°
Θ_o = 60°
0
1
2
3
4
5
Thickness of Slab (Inches)

FIGURE 3

Volume Distribution of Inelastic Gammas in Iron From 3 Mev Neutrons Normally Incident on a 5 Inch Slab. Current Density of Source is $\frac{1 \text{ Neutron}}{\text{Cm}^2 \text{ Sec}}$; Sample Size is 1000 Histories.

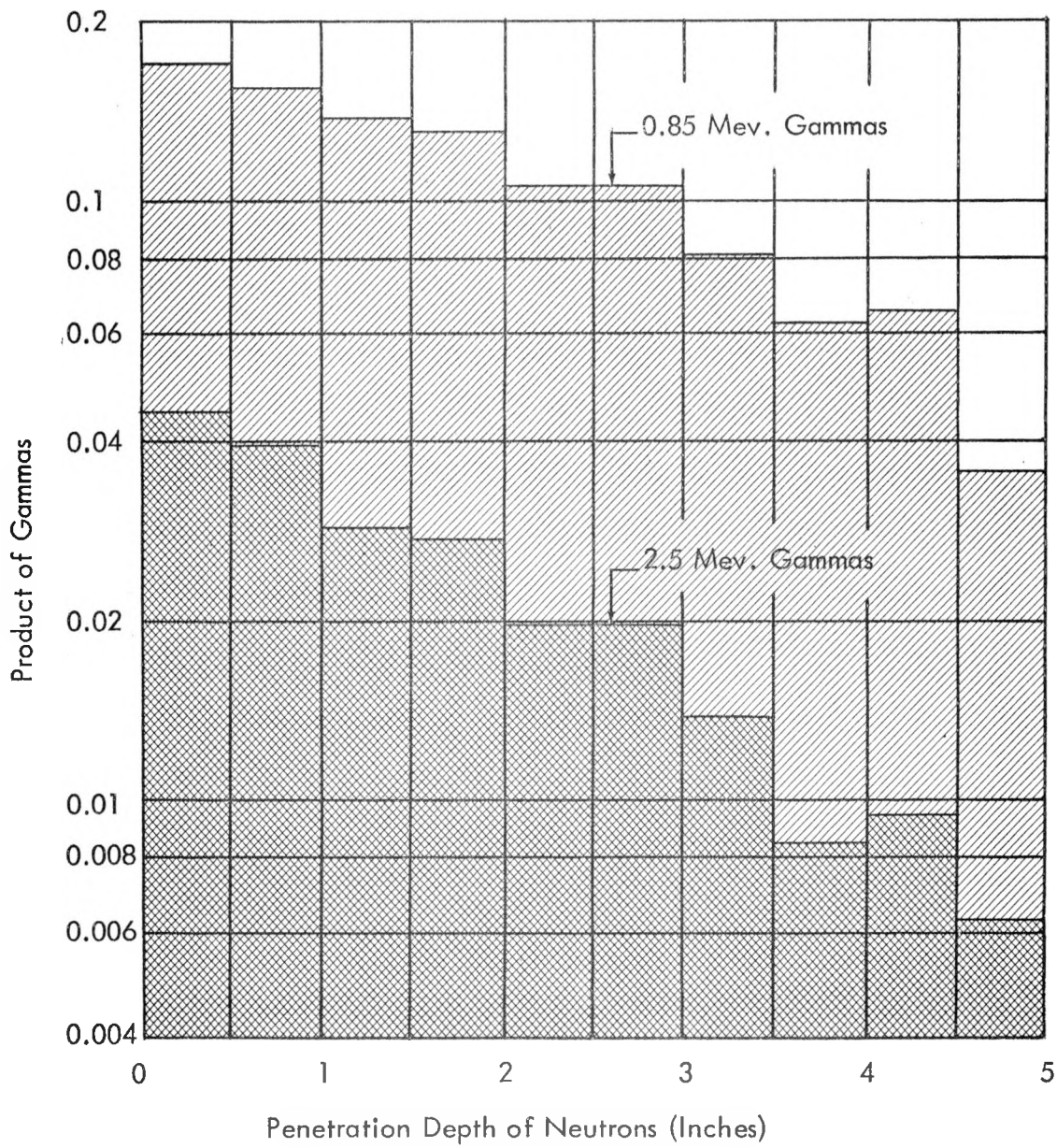

FIGURE 4

COS THETA 0	COS PHI 0	EO	(CM) ZB	K	ETEST
9.9999E-01	9.9999E-01	4.0000E 00	1.2700E 01	1000	10.0000E-04

	SOURCE	U	S	SIGMA	BUILD-UP	SIGMA/U	A	SIGMA	A/(S+U)
CURRENT	1.0000E 00	1.9324E-02	4.1576E-01	1.8133E-02	2.2514E 01	9.3835E-01	5.6204E-01	1.8557E-02	1.2918E 00
FLUX	1.0000E 00	1.9325E-02	7.0380E-01	3.6739E-02	3.7420E 01	1.9012E 00	1.1494E 00	5.6805E-02	1.6331E 00
DOSE(MR/HR)	1.3160E-01	2.5431E-03	7.5673E-02	4.0224E-03	3.0756E 01	1.5817E 00	1.2636E-01	6.8449E-03	1.6698E 00

DOSE TRANS= 5.9434E-01 SIGMA = 3.0565E-02 MUT = 3.9464E 00 DOSE REF = 9.6016E-01 SIGMA = 5.2012E-02

RANDOM NO. 118 778 273 RANDOM NO. 15741844753

ΔCOS Θ	Φ = 180-150	150-120	120-90	90-60	60-30	30-0	AVG. ENERGY 180-150	150-120	120-90	90-60	60-30	30-0
0.1	9.84E-03	4.58E-03	1.33E-01	2.88E-02	3.13E-02	8.91E-03	8.22E-01	5.04E-01	2.67E 00	1.74E 00	5.74E-01	2.09E-01
0.2	7.10E-02	3.99E-02	2.80E-02	8.76E-02	7.04E-02	3.55E-02	2.02E 00	8.69E-01	4.60E-01	2.43E 00	7.07E-01	4.54E-01
0.3	4.51E-02	7.96E-02	1.15E-01	5.74E-02	7.24E-02	1.18E-01	1.60E 00	1.48E 00	1.32E 00	1.54E 00	2.18E 00	1.03E 00
0.4	8.97E-02	4.02E-02	2.83E-02	4.87E-02	6.03E-02	7.06E-02	1.12E 00	1.50E 00	1.38E 00	1.06E 00	1.23E 00	2.07E 00
0.5	1.05E-01	1.15E-01	7.55E-02	1.17E-01	1.15E-01	9.95E-02	1.33E 00	2.17E 00	1.63E 00	1.92E 00	1.56E 00	2.16E 00
0.6	9.89E-02	7.11E-02	6.58E-02	7.49E-02	9.78E-02	6.82E-02	2.27E 00	1.58E 00	1.44E 00	1.64E 00	1.32E 00	1.92E 00
0.7	1.17E-01	1.20E-01	1.14E-01	7.92E-02	1.37E-01	1.24E-01	2.13E 00	1.76E 00	1.56E 00	1.70E 00	1.62E 00	1.66E 00
0.8	1.58E-01	1.30E-01	1.15E-01	1.08E-01	1.21E-01	1.05E-01	1.91E 00	2.00E 00	2.05E 00	2.03E 00	2.28E 00	2.08E 00
0.9	1.86E-01	1.32E-01	8.49E-02	1.33E-01	9.47E-02	1.10E-01	2.13E 00	2.54E 00	2.04E 00	1.95E 00	2.44E 00	2.07E 00
1.0	1.51E-01	1.16E-01	1.80E-01	1.40E-01	1.28E-01	1.29E-01	2.57E 00	2.19E 00	2.66E 00	2.65E 00	2.29E 00	2.39E 00
	Φ = 180-150	150-120	120-90	90-60	60-30	30-0	180-150	150-120	120-90	90-60	60-30	30-0
-0.1	3.00E-01	3.03E-01	1.34E-02	2.43E-01	7.23E-02	3.21E-04	3.47E 00	1.60E 00	8.28E-01	1.80E 00	1.03E 00	1.70E 00
-0.2	2.89E-01	1.37E-01	2.96E-01	2.10E-01	9.57E-02	1.76E-01	1.94E 00	2.25E 00	2.83E 00	2.11E 00	2.48E 00	1.73E 00
-0.3	1.31E-01	1.87E-01	9.50E-02	1.20E-01	1.01E-01	1.28E-01	1.64E 00	2.36E 00	2.20E 00	1.29E 00	2.63E 00	8.18E-01
-0.4	1.94E-01	1.79E-01	1.97E-01	1.36E-01	1.52E-01	1.20E-01	1.61E 00	2.25E 00	2.17E 00	1.94E 00	1.74E 00	1.44E 00
-0.5	1.22E-01	1.83E-01	1.20E-01	1.43E-01	8.97E-02	1.58E-01	1.32E 00	2.07E 00	1.95E 00	1.52E 00	1.39E 00	1.62E 00
-0.6	2.20E-01	1.49E-01	1.88E-01	2.27E-01	1.75E-01	1.77E-01	1.64E 00	1.70E 00	1.84E 00	1.91E 00	2.19E 00	1.80E 00
-0.7	1.31E-01	1.51E-01	1.26E-01	1.88E-01	1.76E-01	1.15E-01	1.76E 00	1.83E 00	1.97E 00	1.57E 00	2.01E 00	1.73E 00
-0.8	1.30E-01	1.70E-01	1.79E-01	1.66E-01	1.17E-01	1.21E-01	1.32E 00	1.63E 00	1.61E 00	1.87E 00	1.65E 00	1.75E 00
-0.9	1.25E-01	1.91E-01	1.19E-01	1.46E-01	1.23E-01	1.05E-01	1.43E 00	1.62E 00	1.59E 00	1.64E 00	2.13E 00	1.51E 00
-1.0	1.14E-01	1.21E-01	1.36E-01	1.17E-01	1.27E-01	1.48E-01	1.75E 00	1.76E 00	1.42E 00	1.60E 00	1.56E 00	1.55E 00

CM. TO BOUND	MEV ENERGY .85	2.5	3.5	4.5	5.5	6.5	7.5	8.5	9.5	11.0	13.0	15.0
1.27	4.20E-02	1.84E-02	3.38E-03-0.	-0.	-0.	-0.	-0.	-0.	0.	0.	0.	
2.54	4.88E-02	1.49E-02	3.02E-03-0.	-0.	-0.	-0.	-0.	-0.	0.	0.	0.	
3.81	5.98E-02	2.38E-02	4.63E-03-0.	-0.	-0.	-0.	-0.	-0.	0.	0.	0.	
5.08	7.12E-02	2.88E-02	5.85E-03-0.	-0.	-0.	-0.	-0.	-0.	0.	0.	0.	
6.35	1.04E-01	3.65E-02	7.45E-03-0.	-0.	-0.	-0.	-0.	-0.	0.	0.	0.	
7.62	1.10E-01	5.15E-02	1.00E-02 0.	0.	0.	0.	0.	0.	0.	0.	0.	
8.89	1.34E-01	6.23E-02	1.25E-02-0.	-0.	-0.	-0.	-0.	-0.	0.	0.	0.	
10.16	1.39E-01	6.60E-02	1.29E-02 0.	0.	0.	0.	0.	0.	0.	0.	0.	
11.43	1.08E-01	6.27E-02	1.34E-02 0.	0.	0.	0.	0.	0.	0.	0.	0.	
12.70	1.23E-01	8.45E-02	1.90E-02-0.	-0.	-0.	-0.	-0.	-0.	0.	0.	0.	

TABLE I

Computer Output Example

14. CYLINDRICAL SHIELD MONTE CARLO

C. W. Hill

Lockheed Aircraft Corporation
Georgia Division
Marietta, Georgia

Normally the incident photon would impinge on the surface and be transmitted to a fixed detector; instead, the point of incidence is now fixed and the detector is allowed to range along the axis. Accordingly, the dose due to transmissions from the fixed point on the surface are found at equi-distance points on the axis. These doses are finally summed to give the approximate total dose at the center point of the axis.

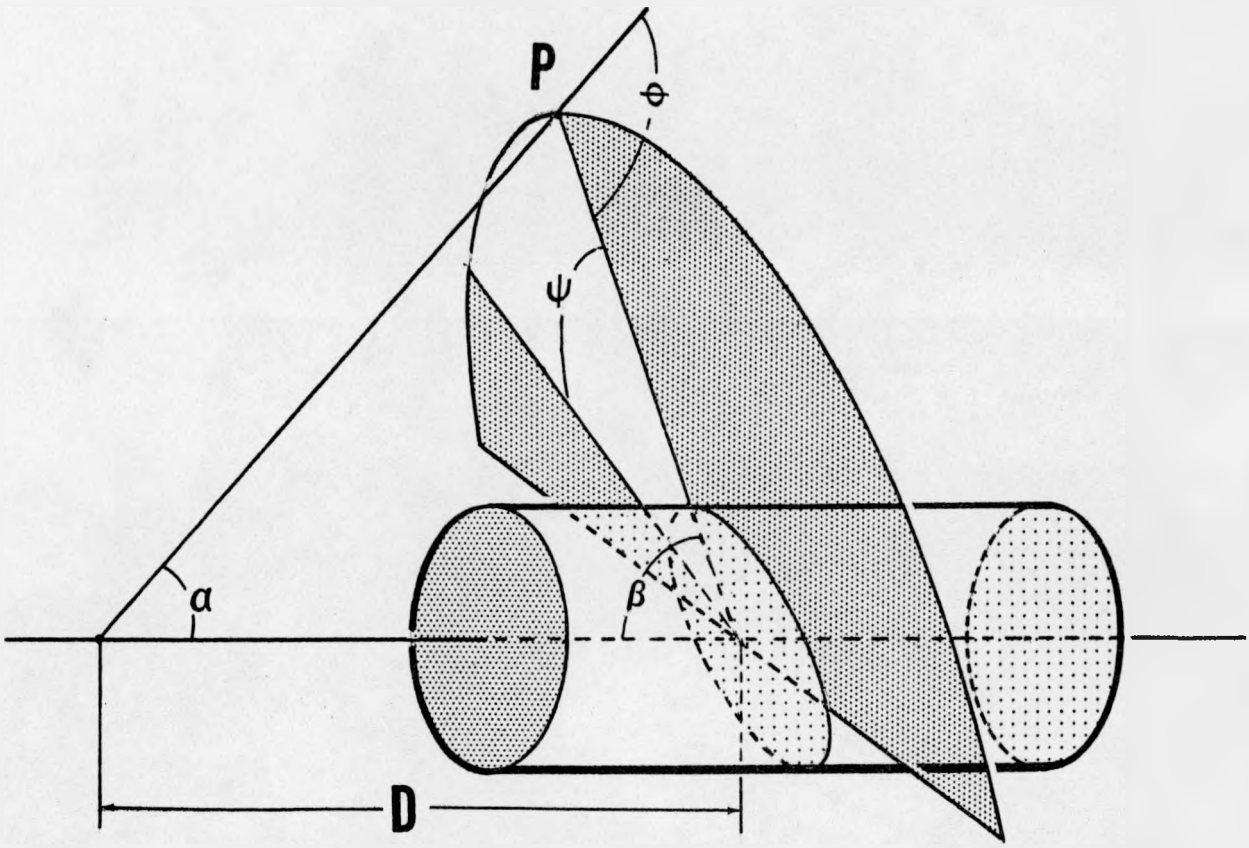

FIGURE 1 AIR SCATTER GEOMETRY

CYLINDRICAL SHIELD MONTE CARLO

by

C. W. Hill

Lockheed Aircraft Corporation
Georgia Division
Marietta, Georgia

Monte Carlo calculations of single air scattered gamma transfer functions have been performed using a cylindrical geometry. Center line dose has been calculated for a typical case. An estimate of the variation of dose along the axis is shown. End effects were approximated by a simple cutoff.

This program calculates the gamma dose rate at the center axis of a shielded crew compartment arising from single scatters in air. A number of similar calculations have been made in the past, notably those of Goldstein[1] in 1953 and Perkins[2], et al., in 1958. The present effort differs from earlier calculations primarily in two ways. First, the gammas are traced through a cylindrical shield rather than an equivalent slab. Secondly, the centerline dose, rather than the wall dose, is found. In addition, this program can calculate the variation of dose along the centerline, although this has not yet been done.

The reactor is represented as a point source on the prolongation of the axis of the crew compartment (see Figure 1). The source has azimuthal symmetry, and three Mev is used as a representative energy. The crew compartment, with black ends, is composed of a cylinder of lead surrounded by a cylinder of plastic.

In any rigorous calculation, the scatters from a point P in the air would be followed to the surface of the crew compartment and the dose contribution to a detector on the axis would be found. This would require following an inordinate number of histories by Monte Carlo from the surface to the detector. This is simplified by finding the number of photons incident on a point at the intersection of the mid-plane with the surface. For small values of α , the angles of incident of the scattered photon with the surface are somewhat distorted, but for larger α 's, this simplification is a reasonable approximation.

$\mu(E)$ = total cross section for air

$C(E_o, d, \alpha, \Theta, \Psi)$ = C (uncollided) + C (collided)

where

C (Uncollided) = $\mathrm{Exp}\left[-(\mu_1(E)t_1 + \mu_2(E)t_2)\ \csc\beta\right]$

μ_i = total cross section of i-th shell,

and t_i = thickness of i-th shell

(Collided) = $2R_1 \int_{\text{LENGTH}} dL \int_o^{\frac{\pi}{2}} \cos\textcircled{H}\, \frac{1}{N} \sum_{i=1}^{N} I_{ij}(\alpha, \beta, \Psi)\, d\Psi$

R_1 = outer radius of crew compartment

$\textcircled{H}$ = angle between incoming ray and the outward pointing normal

N = number of histories followed

$I_{ij}(\alpha, \beta, \Psi)$ = dose from i-th scattered particle at α, β, Ψ to j-th detector

I_{ij} is estimated by a Monte Carlo calculation which follows the particles through the cylindrical shield. At each scatter point, the contributions to all detectors are calculated, the weight of the particle is reduced by $\frac{\mu_A}{\mu_T}$ and a new direction and path length are chosen. The particle is "killed" when the energy falls below an arbitrary cutoff point, or the dose contributions become very small and a Russian Roulette game fails.

The path lengths available to the particle are truncated to imprison the particle in the shield. Also path lengths are biased toward long traverses when headed in a favorable direction and shortened in other directions. At each scatter, the polar angle is sampled from the Klein-Nishina distribution.[3] The azimuthal angle is sampled from a distribution which biases scatters toward a favorable direction.

The dose rate to the center of the crew compartment is calculated as follows:

$$\text{Dose Rate } (E_o, D) = \int_o^{\pi} S(E_o, \alpha)\, f(E_o, \alpha, d, D)\, d\alpha$$

Where E_o = initial energy gamma

D = reactor to crew compartment center distance

$\frac{S(E_o, \alpha)}{4\pi}$ = (energy) / (unit time) (unit energy interval at E_o) (unit solid angle at α)

d = shield parameters

$\frac{2}{\sin \alpha} f(E_o, \alpha, d, D)$ = single scattered dose from unit source at α through shield with parameters d.

$$f(E_o, \alpha, d, D) = \int_{r_o}^{\infty} \frac{\sin \alpha}{2} \frac{E}{E_o} \frac{N}{F} \left(\frac{d\sigma}{d\Omega}\right)_{\theta} \Delta\Omega A(E_o, D, \alpha, \theta)\, C(E_o, d, \alpha, \theta, \Psi)\, dr$$

which reduces to

$$f(E_o, \alpha, d, D) = \frac{N}{2DFE_o} \int_{\alpha}^{\pi} E\, A(E_o, D, \alpha, \theta)\, C(E_o, d, \alpha, \theta, \Psi) \left(\frac{d\sigma}{d\Omega}\right)_{\theta} d\theta$$

where

where N = air electron density

F = flux to dose conversion factor

$\left(\frac{d\sigma}{d\Omega}\right)_{\theta}$ = Klein-Nishina differential scattering cross section at θ

$A(E_o, D, \alpha, \theta)$ = air attenuation

$C(E_o, d, \alpha, \theta, \Psi)$ = shield attenuation

$$A(E_o D, \alpha, \theta) = \text{Exp}\left[-\frac{D}{\sin \theta} (\mu(E_o) \sin \beta + \mu(E) \sin \alpha)\right]$$

Some difficulties with statistical variation have been encountered with this program. A variance comparable to that of Perkins, et al.,[2] is achieved by running 10 to 20 times longer on the IBM-704. There are two reasons for this poor behavior. First, cylindrical geometry is more troublesome than slab geometry. Secondly, the doses to eleven detector stations on the axis are computed rather than the dose emerging from a slab.

Figure 2 compares the results of this program to those of Perkins, et al., for two cases. The cause of the discrepancy has not yet been determined, though cross sections[4] used are slightly different. In addition, the centerline dose is expected to run higher than the wall dose. The results are correct within 10 - 20%. At any rate, enough information is obtained to estimate the variation of dose along the axis.

For a given choice of source, shield and reactor-crew compartment distance, two factors affect the dose profile along the axis. The dose calculated at the axis center contains a $\frac{1}{D}$ dependence. This dependence may be used to obtain a first approximation to dose profile. The second factor combines the effects of the black ends and the anisotropy of the scattered gammas.

The second factor may be understood as follows: The axis center receives radiation from the entire length of the cylinder. A point near one end also receives radiation from the entire length, but part of the cylinder is further away and subtends a smaller solid angle. If the radiation were isotropic, the dose profile could be calculated analytically and would be symmetrical in this factor. However, the radiation is peaked in the forward direction so that the dose near the rear will be lower than the dose near the front.

The anisotropy of the radiation is shown in Figures 3 and 4. These graphs show the relative contributions to the dose along the axis from radiation striking the central part of the cylinder for several values of α. Since the program is not set up to calculate the dose profile at present, the result of a hand calculation is shown in Figure 5. The dose slope for $\alpha = 20^{o}$ is used in this calculation. This single angle approximation may be valid for the divided shield since:

a. Most of the single scatter gamma contribution is due to angles α smaller than 60^{o}.

b. Figures 3 and 4 show that the relative contribution along the axis is not a rapidly varying function of α at small angles. This calculation does not handle the uncollided dose properly near the back of the crew compartment. The thin plastic case is about 10% high and the thick plastic case about 2% high in this region. Thus, the dose profiles are not sensitive to variations in the plastic thickness for a half inch lead inner shell.

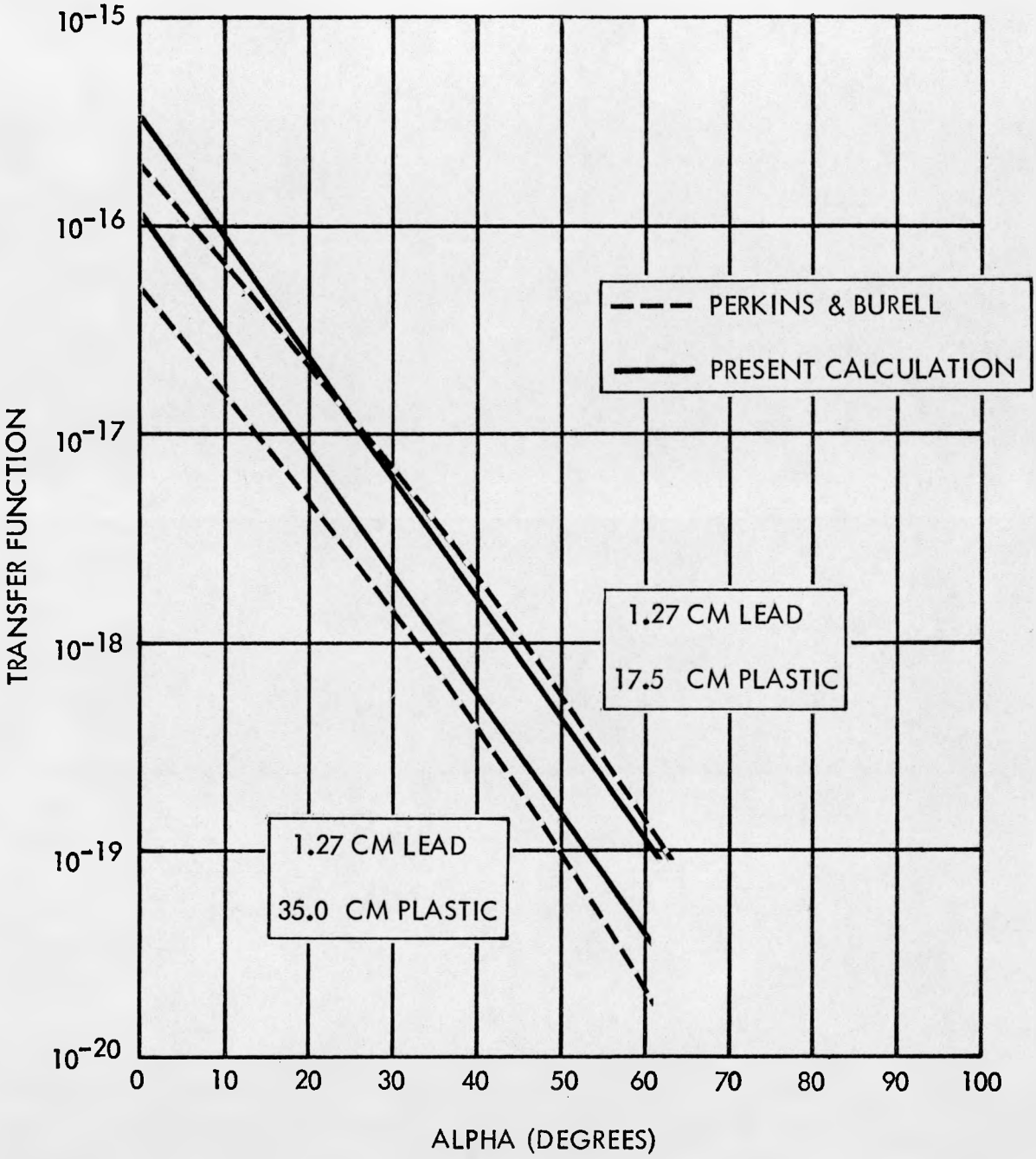

FIGURE 2 TRANSFER FUNCTION VS ALPHA

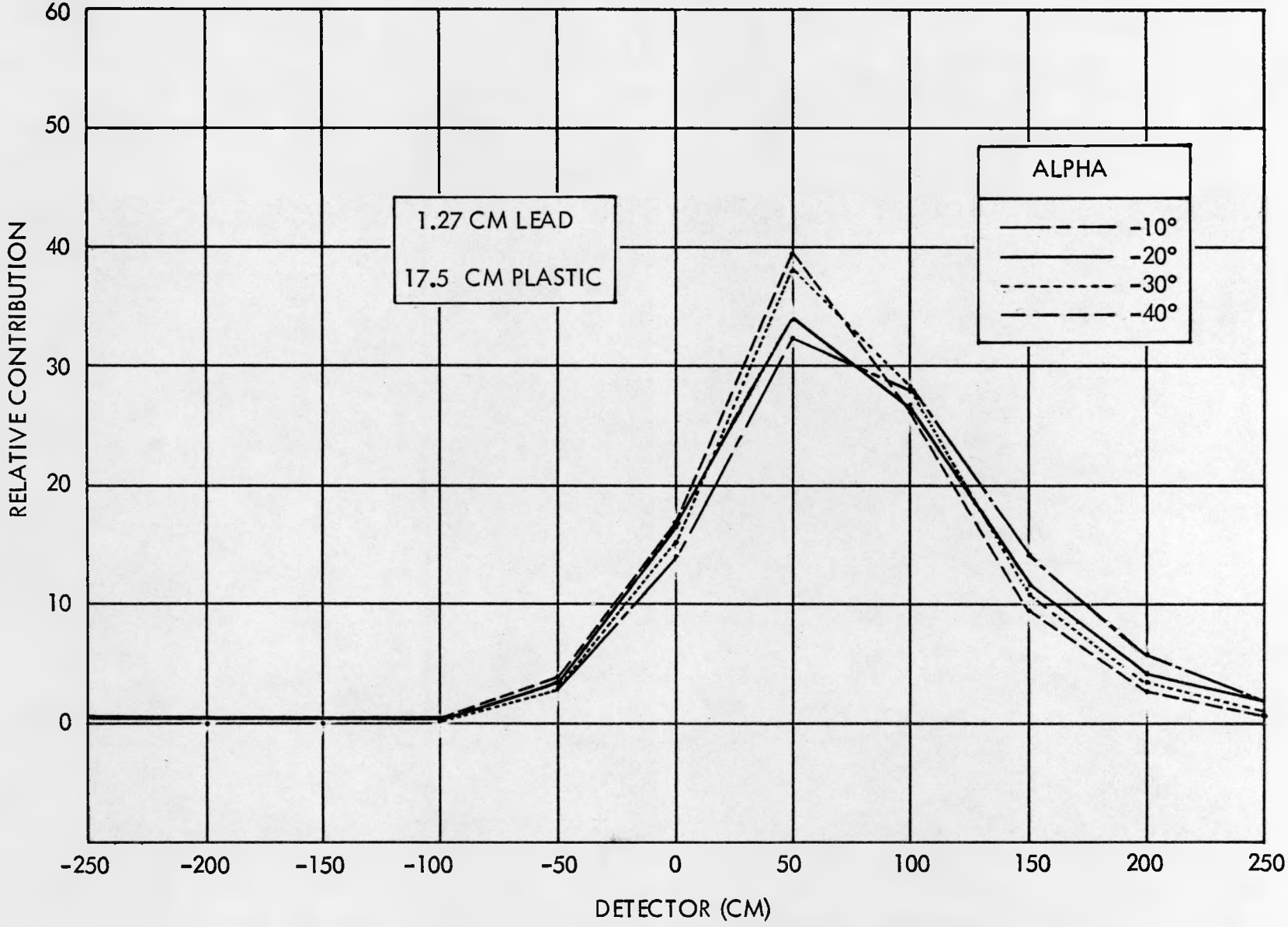

FIGURE 3 RELATIVE CONTRIBUTION ALONG AXIS FROM CENTER RING

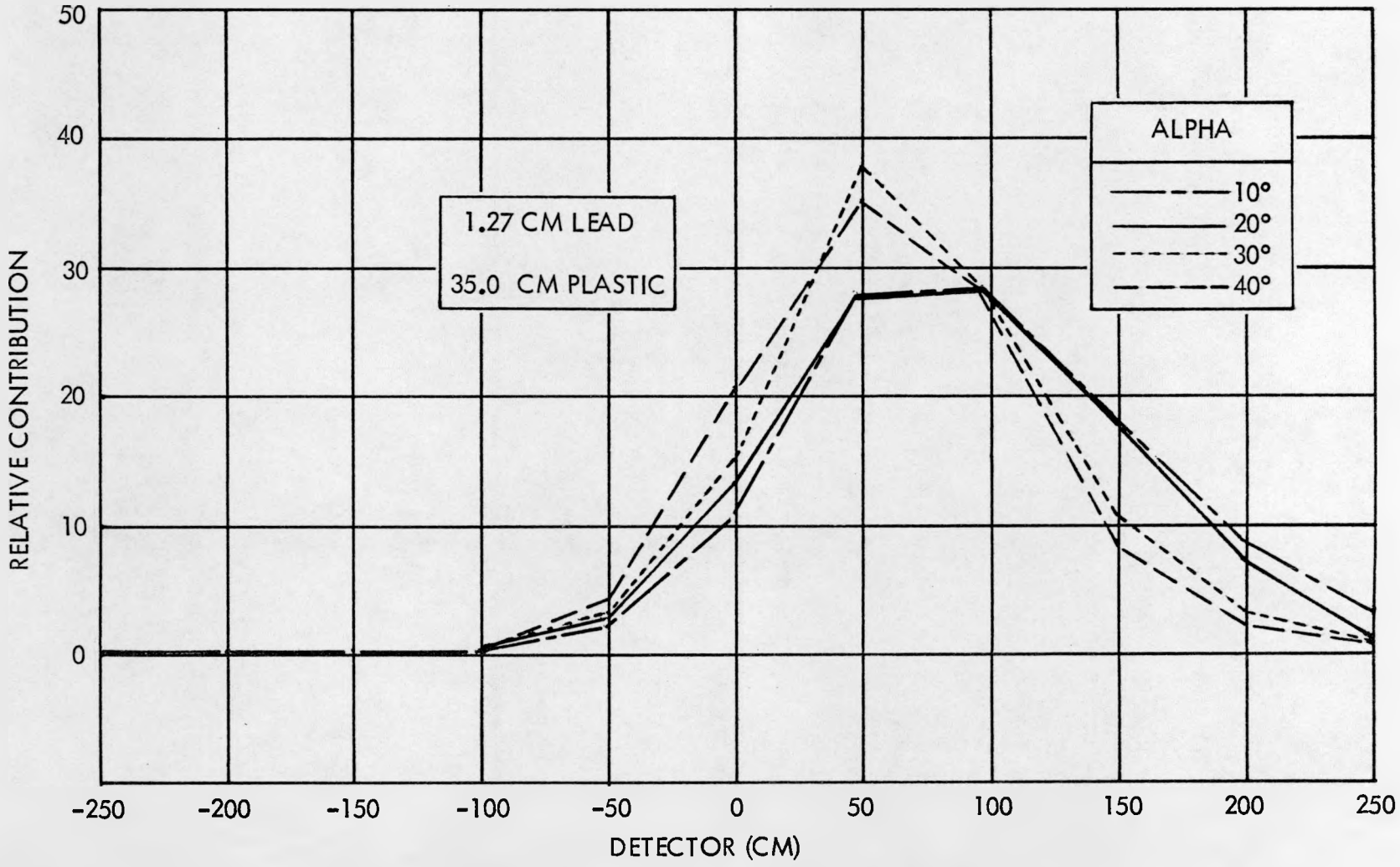

FIGURE 4 RELATIVE CONTRIBUTION ALONG AXIS FROM CENTER RING

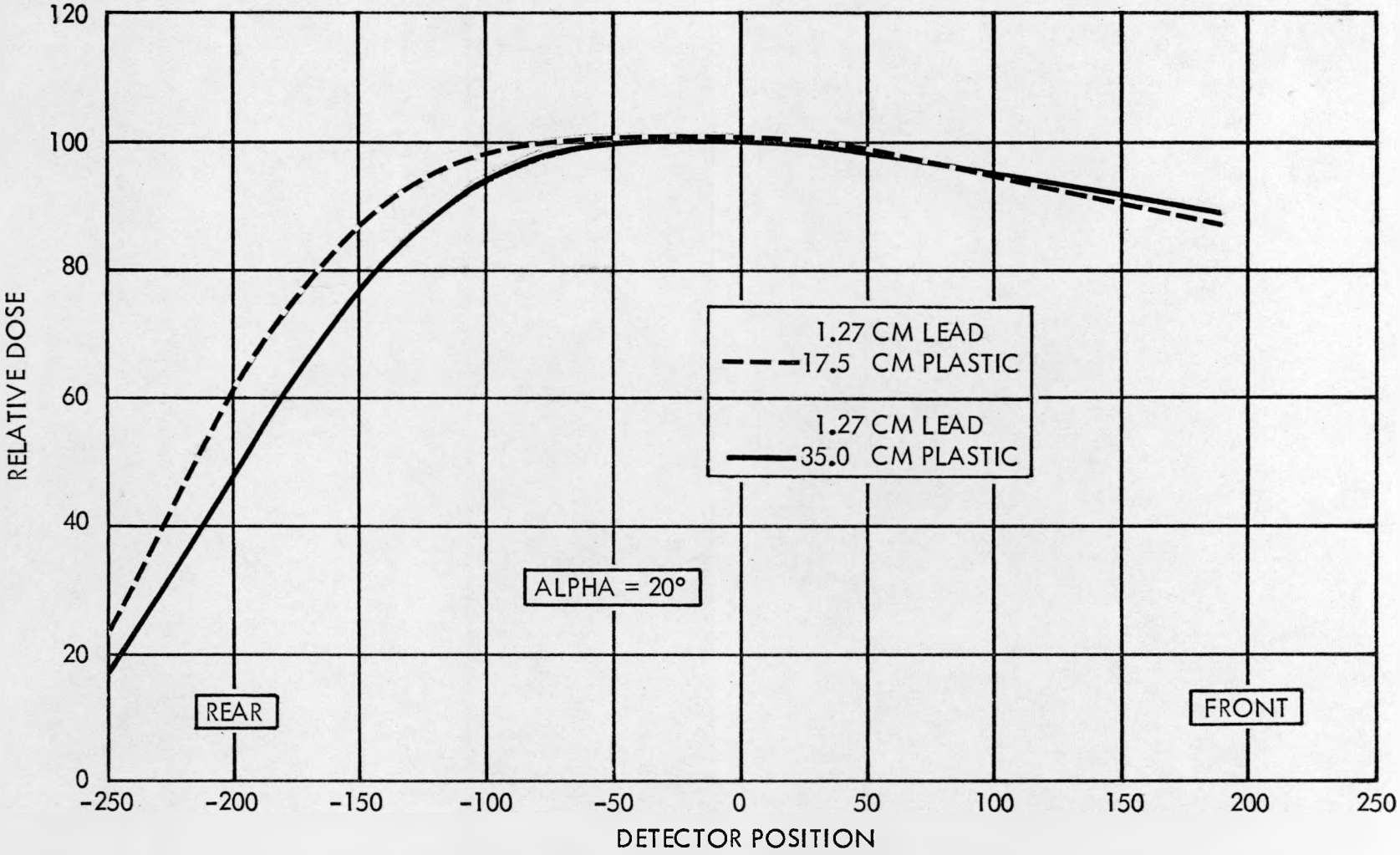

FIGURE 5 RELATIVE DOSE ALONG CREW COMPARTMENT AXIS

REFERENCES

1. Goldstein, H. "Air, Ground, and Structure Scattering for the Divided Shield," Reactor Handbook, Volume 1, Chapter 2.9, (1953)
(Secret)

2. J. F. Perkins, C. W. Hill, and M. O. Burrell, Crew Compartment Dose Rates Due to Single Air Scattering of Gamma Rays. A paper presented at the Sixth Semi-Annual ANP Shielding Meeting, December 2-3, 1958.

3. Kahn, H., Applications of Monte Carlo, RM-1237 AEC, 20, April 19, 1954.

4. Grodstein, Gladys White X-Ray Attenuation Coefficients from 10 Kev to 100 Mev. National Bureau of Standards Report 103 (1952).

15. NUCLEAR SHIELDING FOR SPACE ENVIRONMENT - THE SCATTERING SHIELD

Carl N. Klahr
Kalman Held

TRG, Incorporated
Syosset, New York

NUCLEAR SHIELDING FOR SPACE ENVIRONMENT-THE SCATTERING SHIELD

by

Carl N. Klahr and Kalman Held

TRG, Incorporated
Syosset, New York

Shielding of a nuclear reactor in a space vehicle should be designed to eliminate radiation predominantly by scattering it into space rather than by absorption. This can eliminate much of the multiply scattered radiation (buildup) which would normally contribute to the dose. The following general rules for nuclear shadow shielding in space environment constitute what we call the space scattering principles.

(1) Multiple splitting of the shadow shield to increase the probability of scattering into space.
(2) Shaping of each shadow disc to increase scattering into space.
(3) Reliance on good scatterers with more isotropic cross section.
(4) Possibility of using low density materials without weight penalty because of the one dimensional geometry

Some schematic calculation results will be presented.

We would like to present a new approach to shield design for space vehicles - the multiply split shadow shield, or the scattering shield.

This shielding concept takes advantage of the space environment of the vehicle. The important characteristic of space for our purposes is that there is no backscattering from space. Hence we wish to eliminate neutrons and gammas primarily by scattering them into space. It is possible to eliminate much of the multiply scattered radiation - the buildup - which would normally contribute to the dose.

This is therefore a scattering shield as compared with the usual shield which one can call an absorbing shield. Shielding of a nuclear reactor in a space vehicle can be designed to eliminate radiation predominantly by scattering into space rather than by absorption.

Let us examine shielding requirements for various space vehicles by looking at Figure 1.

From Figure 1 we can consider the shield weight in terms of attenuation lengths and potential shield weight savings. Figure 1 assumes a weight savings of 30% by elimination of the buildup. More realistic numbers may be larger or smaller, depending on whether neutrons or gammas constitute the main dose, and depending on the number of attenuation lengths required.

Now we consider the principles of the multiply split shadow shield. We refer to Figure 2. This compares elimination of radiation by absorption and by scattering. Multiple splitting of the shield permits scattered radiation to escape readily into space. The effect of scattering is to eliminate all or a part of the buildup when the shield is multiply split. This is shown in Figure 3.

The usefulness of multiple splitting the shadow shield will depend on the relative sizes of source and crew. We have investigated primarily the situation when these sizes are about the same.

The usefulness of multiple splitting will also depend on the importance of structure scattering.

The following general rules for nuclear shadow shielding in space environment constitute what we call the space scattering principles:

(1) Multiple splitting of the shadow shield to increase the probability of scattering into space.

(2) Shaping of each shadow disc to increase scattering into space.

(3) Reliance on good scattering materials with cross sections that tend to be isotropic, rather than on good absorbers

(4) Possibility of using low density materials without weight penalty because of the one dimensional geometry.

The disc shaping principle is illustrated in Figure 4, by the convex shaped disc and by the doughnut and plug disc. Both shapes can increase scattering into space.

Hydrogen is the best gamma scatterer, having more electrons per unit weight than any other material. Reliance on elimination of gammas by scattering rather than by absorption would require use of low Z materials, primarily hydrogen, rather than high Z materials for absorbing gammas.

Figure 5 is a rough guide to the maximum weight savings acheivable by elimination of gamma buildup with a scattering shield. The weight savings in one dimensional geometry is proportional to the logarithm of the buildup. It is clear that the largest percentage weight savings will come for thin shields. The material considered is water and a plane monodirectional source is assumed.

If low Z materials are used to eliminate gammas the neutrons will be eliminated more easily and the gamma elimination problem will dictate shield design. For situations in which neutron elimination is critical, we consider what materials to use for neutron scattering. Again low Z materials are best because the neutron cross section is more isotropic for low Z materials.

We have made a schematic calculation of the effectiveness of shield splitting for a simple case. We compare a split disc with a single disc. See Figure 6. The discs are each assumed λ mean free paths thick and the mass is assumed concentrated in the plane of each disc. Isotropic scattering is assumed. A point source is assumed and the receiver is a small sphere. Figure 6 shows the integral giving the contribution of neutrons scattered in each disc and reaching the receiver.

Figure 7 gives formulas for three types of contributions the unscattered neutrons reaching the receiver, the once-scattered and the multiply scattered. The unscattered and once-scattered contributions are unaffected by the splitting of the discs. The multiply scattered contribution is strongly affected by the splitting through the integral $I(\alpha)$. α is the ratio of disc radius to the spacing between discs.

A table of values of I (α) for two discs of the same radius is given in Figure 8. It is seen that the probability of escape between discs is considerable even when the discs are fairly close. When $\alpha = 2$ the probability of escape is still about 39%. Multiply splitting the discs cascades this probability.

A numerical example is worked out for the case of two discs in Figure 9. One can see that for a shield thickness of ten attenuation lengths the dose has been reduced by a factor of 20, corresponding to three attenuation lengths. This means a shield weight reduction of about 30% in slab geometry.

FIGURE 1. SHIELDING REQUIREMENTS

Application	Reactor Power Megawatts	Time at Power Seconds	Energy Megawatt Seconds	Required Attenuation	Required Attenuation Lengths	30% Shield Saving in Attenuation Lengths*
ANP	400	10^5	4×10^7	10^8	19	
Hydrogen-Propelled Interplanetary Rocket	1000	300	3×10^5	10^6	14	4.2
Ion-Propelled Interplanetary Rocket	10	3×10^7	3×10^8	10^9	21	6.3
SNAP (unmanned)	0.03	3×10^7	9×10^5	240	5.6	1.7

If buildup is eliminated by scattering into space. Assumed reactor to payload distance 20 meters for cases 1, 2, 3; 1 meter for case 4.

sumed reactor to payload distance 20 meters for cases 1, 2, 3; 1 meter for case 4.

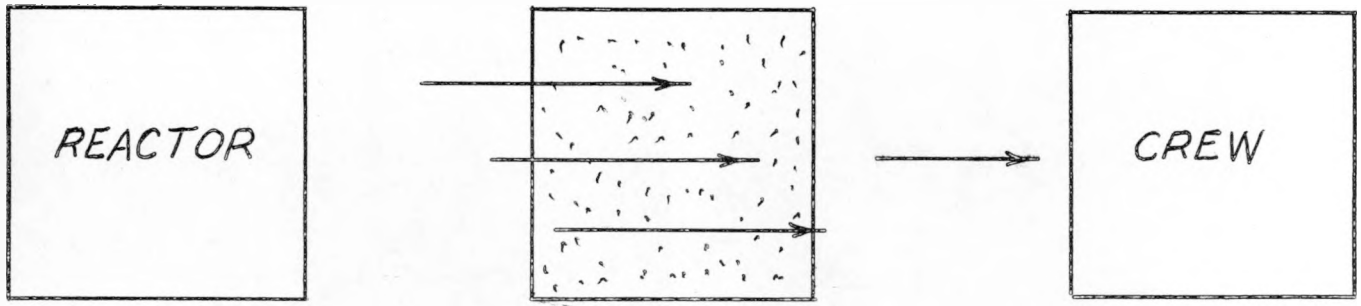

RADIATION ABSORBING SHIELD

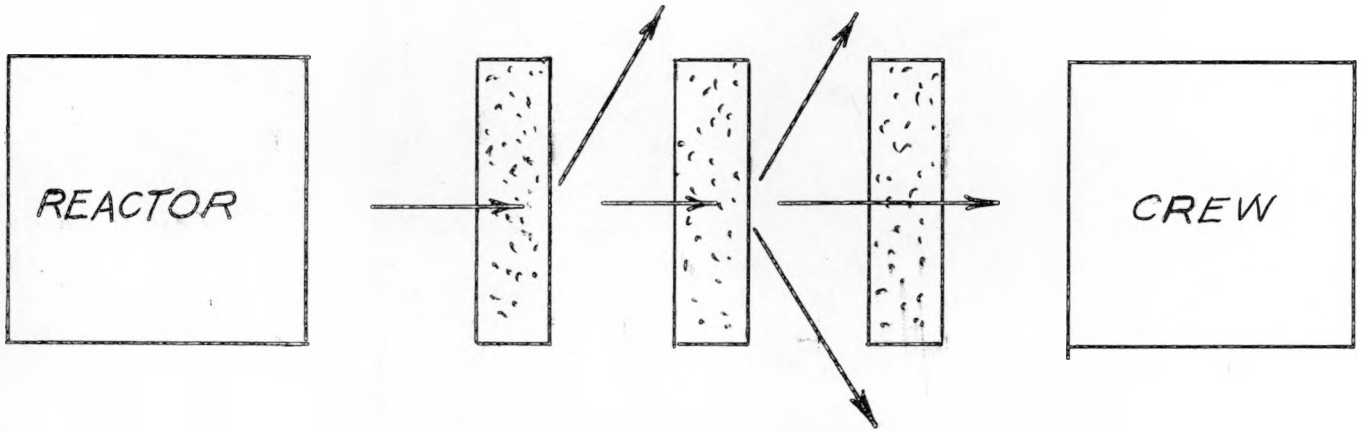

RADIATION SCATTERING SHIELD

FIGURE NO. 2

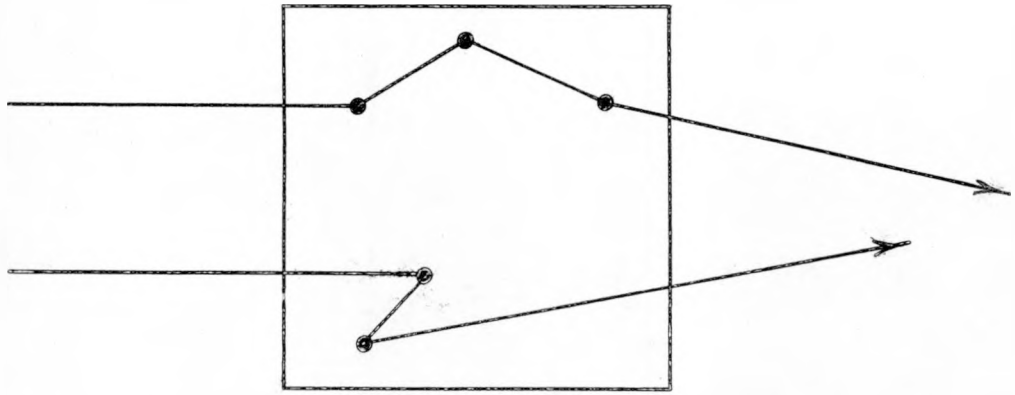

ABSORBING SHIELD - BUILDUP CONTRIBUTES TO DOSE

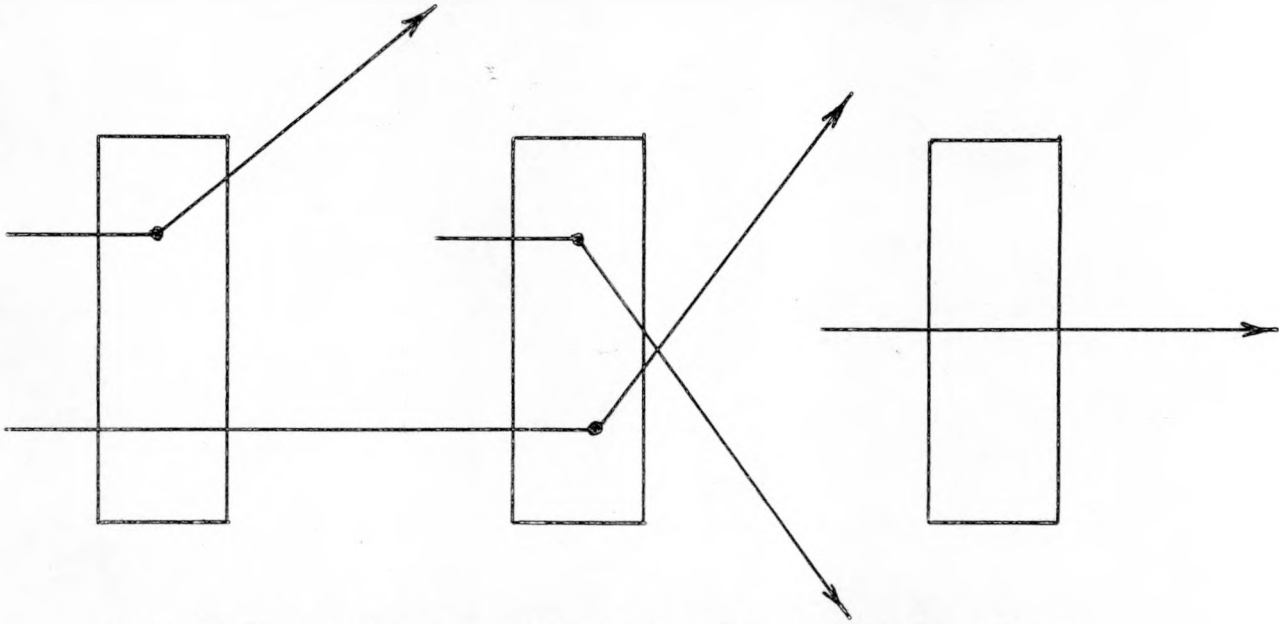

SCATTERING SHIELD - BUILDUP SCATTERED INTO SPACE

FIGURE NO. 3

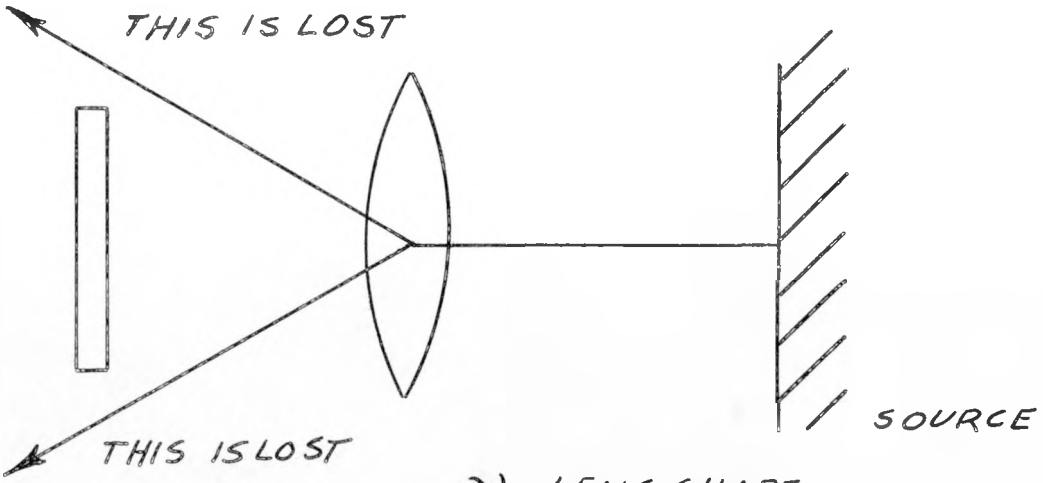

a) LENS-SHAPE

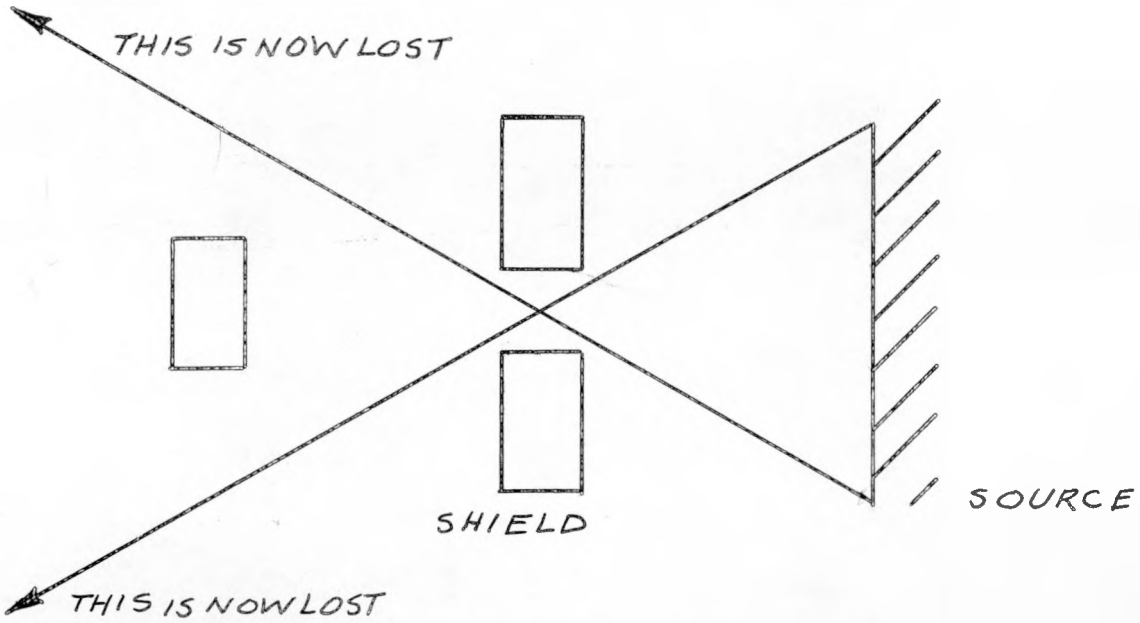

DOUGHNUT-SHAPE

FIG. 4 THE DISC SHAPING PRINCIPLE

Maximum Weight Savings by Buildup Elimination of Gamma Rays in Water

, x	W(2Mev)	W(3Mev)	W(6Mev)
	0.550	0.458	0.308
	0.443	0.358	0.263
	0.335	0.290	0.212
	0.260	0.225	0.169
	0.217	0.186	0.143
>	0.170	0.148	0.116

PLANE MONODIRECTIONAL SOURCE

$$W(\mu_0 x) = \frac{\ln B(\mu_0 x)}{\mu_0 x}$$

Fig. 5

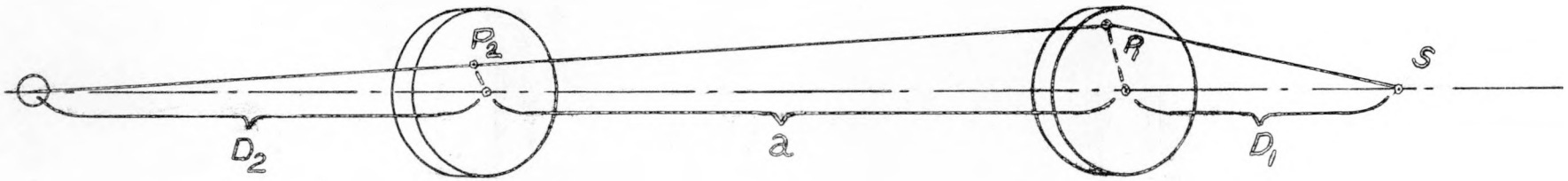

GEOMETRY OF DISC SPLITTING

$$J_2(a) = J_2(a=0) \cdot I\left(\frac{R_1}{a}, \frac{R_2}{a}\right)$$

$$I = \int dx_2 dy_2 \frac{2}{\pi R_1^2} \int \frac{dx_1 dy_1 \cos\theta}{4\pi\left[a^2 + (x_2-x_1)^2 + (y_2-y_1)^2\right]}$$

FIGURE NO. 6

UNSCATTERED

$$J_o = \frac{e^{-2\lambda}}{4\pi (D_1 + D_2 + a)^2}$$

ONCE SCATTERED

$$J_1 \leq e^{-\lambda} \left[\frac{\pi R_1^2}{4\pi D_1^2 \cdot 4\pi (D_2 + a)^2} + \frac{\pi R_2^2}{4\pi D_2^2 \cdot 4\pi (D_1 + a)^2} \right]$$

MULTIPLY SCATTERED

$$J_2 (a) = \frac{\pi R_1^2}{4\pi D_1^2} \quad \frac{(1 - e^{-\lambda})^2}{2} \quad \frac{1}{4\pi D_2^2} \cdot I (\alpha_1, \alpha_2)$$

$$I (\alpha_1, \alpha_2) = \frac{1}{2} \left\{ \left(1 + \frac{\alpha_2^2}{\alpha_1^2} + \frac{1}{\alpha_1^2}\right) - \sqrt{\left(1 + \frac{\alpha_2^2}{\alpha_1^2} + \frac{1}{\alpha_1^2}\right)^2 - 4 \frac{\alpha_2^2}{\alpha_1^2}} \right\}$$

FIG. 7

NON-ESCAPE PROBABILITY BETWEEN DISCS

$\alpha = \frac{\text{radius}}{\text{spacing}}$	$I(\alpha)$
0.0	0
0.2	0.037
0.5	0.172
0.7	0.267
1.0	0.382
1.4	0.477
2.0	0.610
3.0	0.723
5.0	0.820

Fig. 8

NUMERICAL EXAMPLE

$\alpha = 0.2$ $\qquad \lambda = 5$ $\qquad \frac{R}{D} = 0.1$

$$\frac{J_1}{J_0} \approx 1 \qquad \frac{J_2}{J_0} = 100\ I(\alpha)$$

$$\text{DOSE REDUCTION FACTOR} = \frac{J_0 + J_1 + J_2\ I(\alpha)}{J_0 + J_1 + J_2}$$

$$= \frac{1 + 1 + 100 \cdot (.037)}{1 + 1 + 100} \approx \frac{1}{20}$$

FIG. 9

16. HIGH EFFICIENCY MONTE CARLO CALCULATION OF Na^{24} AND BREMSSTRAHLUNG GAMMA PENETRATION

R. Steinberg
R. Aronson

TRG, Incorporated
Syosset, New York

HIGH EFFICIENCY MONTE CARLO CALCULATION OF Na^{24} AND BREMSSTRAHLUNG GAMMA PENETRATION

by

H. Steinberg and R. Aronson

TRG, Incorporated
Syosset, New York

TRG's slab gamma ray code, TRIGR-P, has been modified to give improved results for low energies above the cross section minimum in heavy materials. A series of calculations for transmission of Na^{24} radiation (2.75 and 1.38 Mev photons) through aluminum, iron, and lead was run for five to six thicknesses of from 2-12 mean free paths at the higher energy, for six incident angles varying from normal to 75° with the normal. There were 192 problems in all. Both doses and spectra were obtained.

The standard deviations for the doses were about 5% for 0°, 15°, and 30° incidence and about 10% for the larger angles. A few problems gave 15% deviations, or more for 60°-75° on Al.

The total running time of the IBM 704 was about 4-1/2 hours for all the problems. The Morton similarity transformation was used to make it possible to obtain results for several thicknesses at once.

Spectra from 8 and 10 Mev bremsstrahlung radiation transmitted through 4 and 6 inches of lead were computed and compared with the experimental results of Hubbell, Hayward and Titus.

Calculations of the attenuation of Na^{24} radiation in iron, aluminum and lead, and of 8 and 10 Mev bremsstrahlung radiation in lead have been performed with TRIGR-P, a slab Monte Carlo gamma ray code.

The main features of the code and some results have been reported at previous ANP Shielding Meetings. Very briefly, the code can be used to compute transmission through laminated slabs. Biased sampling and statistical estimation are used. The sampling is such that escape and absorption are forbidden, both being taken into account by a weight adjustment. At every collision, position, wavelength, and azimuthal angle of scattering are all sampled from exponential distributions. Each exponential constant depends on the state (that is, the position, wavelength, and direction of the photon) at that point in its history.

Output consists of the total dose, the energy flux, and either the energy current or the number flux. Flux and current spectra are also obtained. Fractional standard deviations for all the output quantities are printed as well.

The sampling procedure is not entirely random, but in part systematic. The systematic sampling is described in another paper at this meeting. (1)

Several shield thicknesses can be treated at once by the Morton or similarity transformation, which has been extensively described. (2) In the problems reported on in this paper, a fundamental thickness was assumed and the transformation was used to compute transmissions for shields from 0.2 to 1.2 times as thick.

The computations described here, which were carried out under a contract with the Aeronautical Research Laboratory of Wright Air Development Center, gave the transmission of Na^{24} radiation through 2-12 mean free paths of lead and through 2-10 mean free paths of iron and aluminum all measured at 2.75 Mev. Calculations were done for incident angles of 0°, 15°, 30°, 45°, 60°, and 75° with the normal.

Figure 1 shows percent transmission as measured by an ionization meter plotted against slant thickness, for lead. One notes the expected features, that at small penetrations the transmission is independent of angle, but that a larger slant thicknesses the larger angles give increasingly larger buildup. The fractional standard deviations vary from 2-3 percent for normal incidence to about 15-20 percent at 75°. When the observed standard deviation becomes greater than 10-15 percent, the actual error is probably somewhat larger.

Figure 2 shows the same results for iron. The observed fractional deviations were about the same as for lead, but the sensitivity of the results to the sampling scheme was somewhat greater. The basic sampling was appropriate to 10 mean free paths according to the scheme used, but results for 2,4,6,8, and 12 mean free paths were obtained simultaneousl with the similarity transformation. In some of the more oblique cases the results for the large penetrations were poor while those for the smaller penetrations were good. It was assumed that in these cases the transmission was determined largely by photons which penetrate more or less normally after the initial scattering, and the sampling was modified accordingly. In many cases, the results were improved. Where one sampling scheme or another gave clearly smaller deviations, of the order of five percent or less, we believe the results are reliable. The 75° curve in iron did not give such clearcut results, and the 60° or 75° curves in aluminum were quite inconsistent.

In some cases the range of thicknesses was too great for the Morton transformation to give acceptable results at the smaller thicknesses. In these cases, the problem for 2 and 4 mean free paths was redone with the sampling appropriate to 4 mean free paths, in all cases with good results, that is, very small deviations.

Figure 3 gives the results for aluminum. The 60° and 75° curves are not shown. It appears that by doing the thinner (2 and 4 mean free paths) shields in a separate run, with 4 as the base distance using the Morton transformation, one car obtain good results. This has not been done yet in all cases.

The time required for the 192 separate Na^{24} problems (3 materials, 2 energies, 6 angles, 5 or 6 thicknesses) was about 5 hours on the IBM-704 - 3 hours for the first run and about 2 hours for the reruns with the changed sampling.

Monte Carlo calculations of gamma ray transmission through lead have also been performed to compare with experiments carried out at the National Bureau of Standards by Hubbell, Hayward, and Titus.(3) In these experiments bremsstrahlung radiation from 10 Mev electrons was incident upon 4 and 6 inch lead slabs and bremsstrahlung from 8 Mev electrons on 4-inch le slabs. The scattered radiation transmission number flux spectrum was measured and presented in histogram form.

Since the bremsstrahlung radiation is a distributed source in energy and TRIGR-P is designed for monoenergetic sources, several monoenergetic sources were combined to approximate the 8 and 10 Mev bremsstrahlung spectra. Results were obtained for both thicknesses (4 and 6 inches) simultaneously.

The data obtained have estimated errors of about 15% for each histogram entry and about 2-3% in the total scattered radiation. The total radiation obtained by the calculation is about 10% lower than the experimental results. The authors of the experiment noticed a similar discrepancy in comparison with moment method data and concluded that the discrepancy was due to the neglect of certain secondary reactions in the moments calculation, especially bremsstrahlung radiation of Compton scattered electrons. Since TRIGR-P considers the same reactions as the moments calculation, the discrepancy can presumably be accounted for by the same mechanism. Figures 4-6 show the comparisons.

References

1. H. Steinberg, Monte Carlo Calculations of Neutron Penetration through Cylindrical Crew Shield by Importance Sampling
2. K.W. Morton, Scaling Tracks in Monte Carlo Shielding Calculations, Journal of Nuclear Energy, Vol. 5, Nos 3-4 (1957)
3. Hubbell, Hayward, and Titus, Phys. Rev. 106, 1361 (1957)

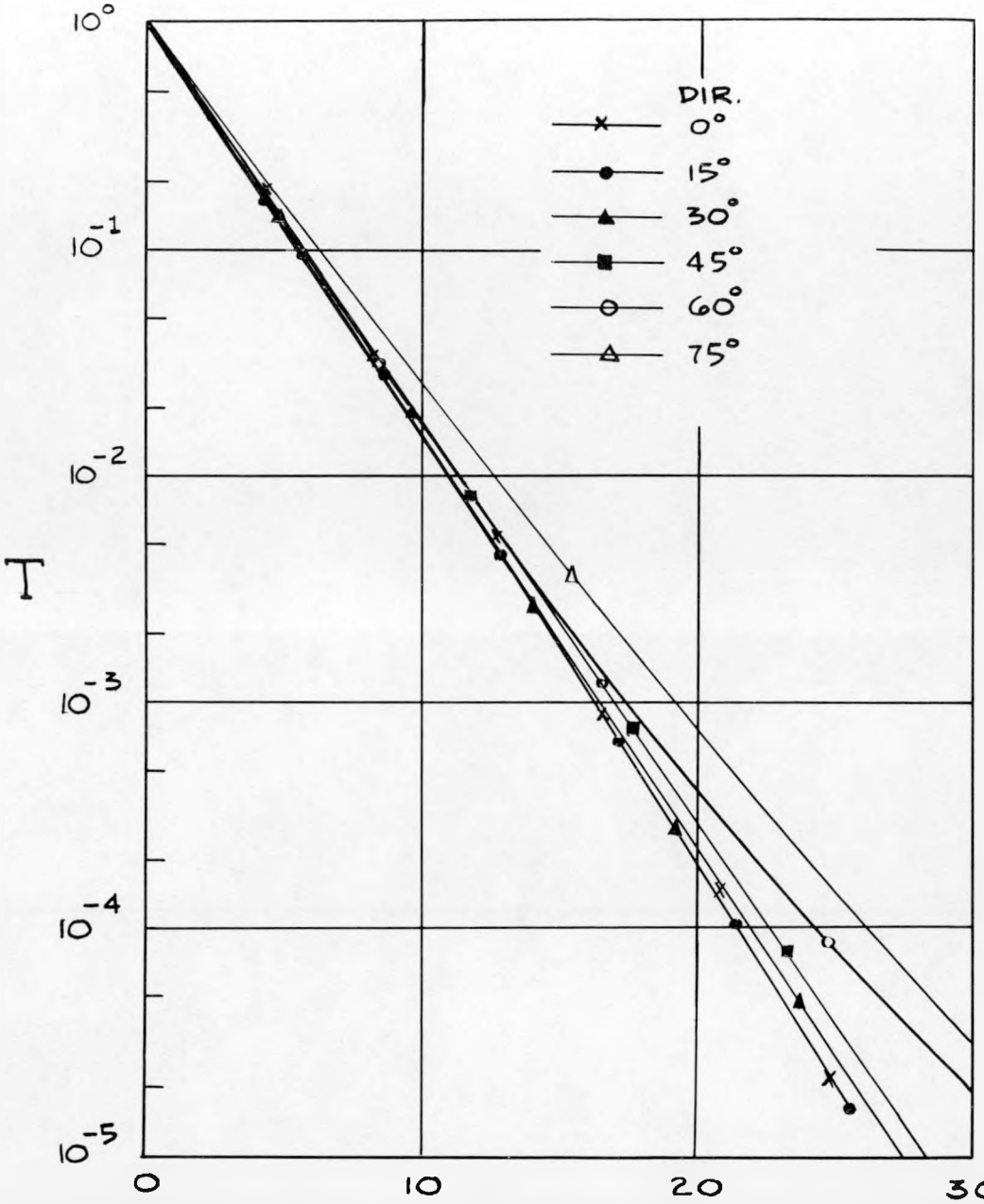

TRANSMISSION vs SLANT THICKNESS FOR Pb.

FIG. 1

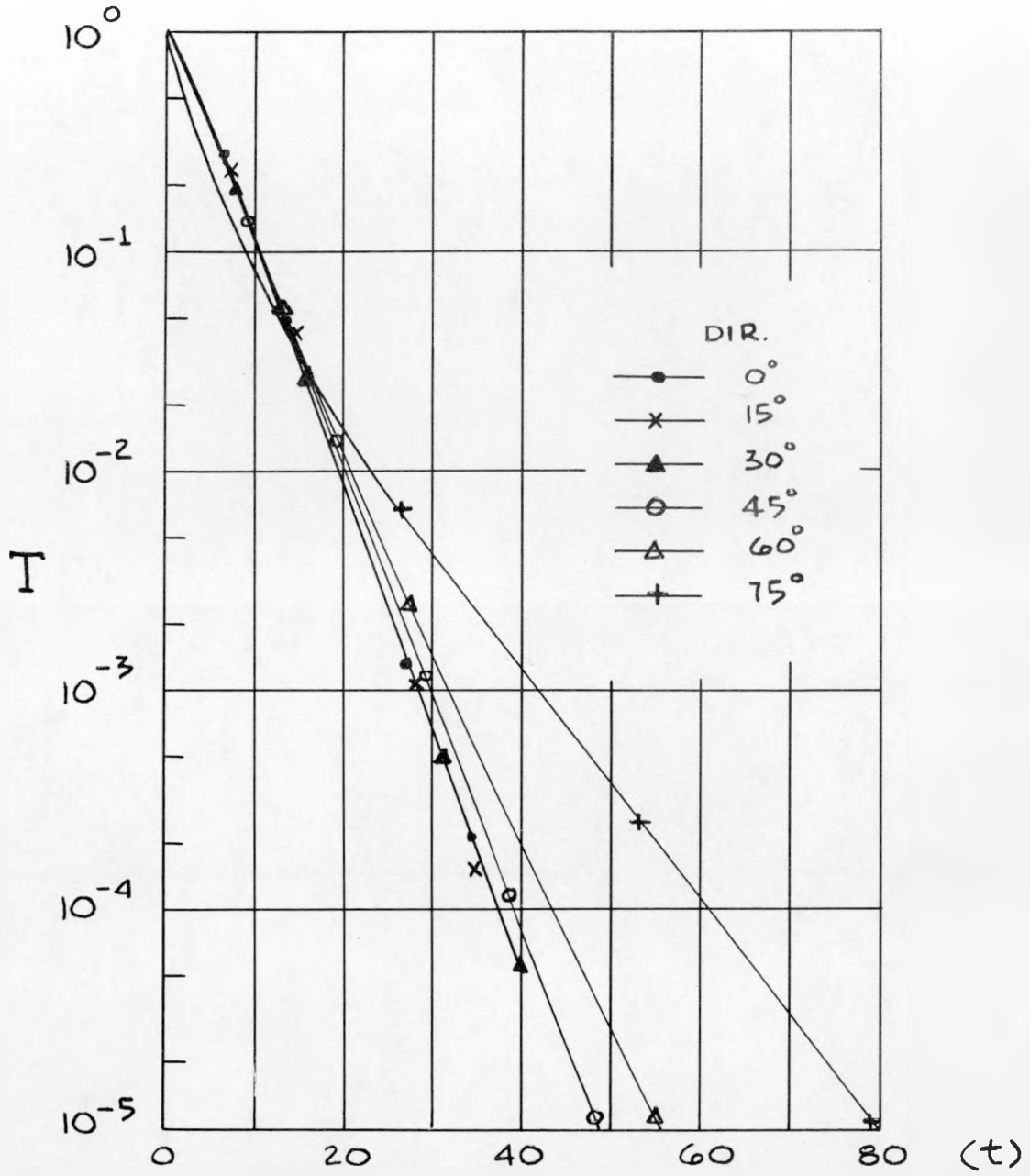

TRANSMISSION vs SLANT THICKNESS FOR Fe.

FIG. 2

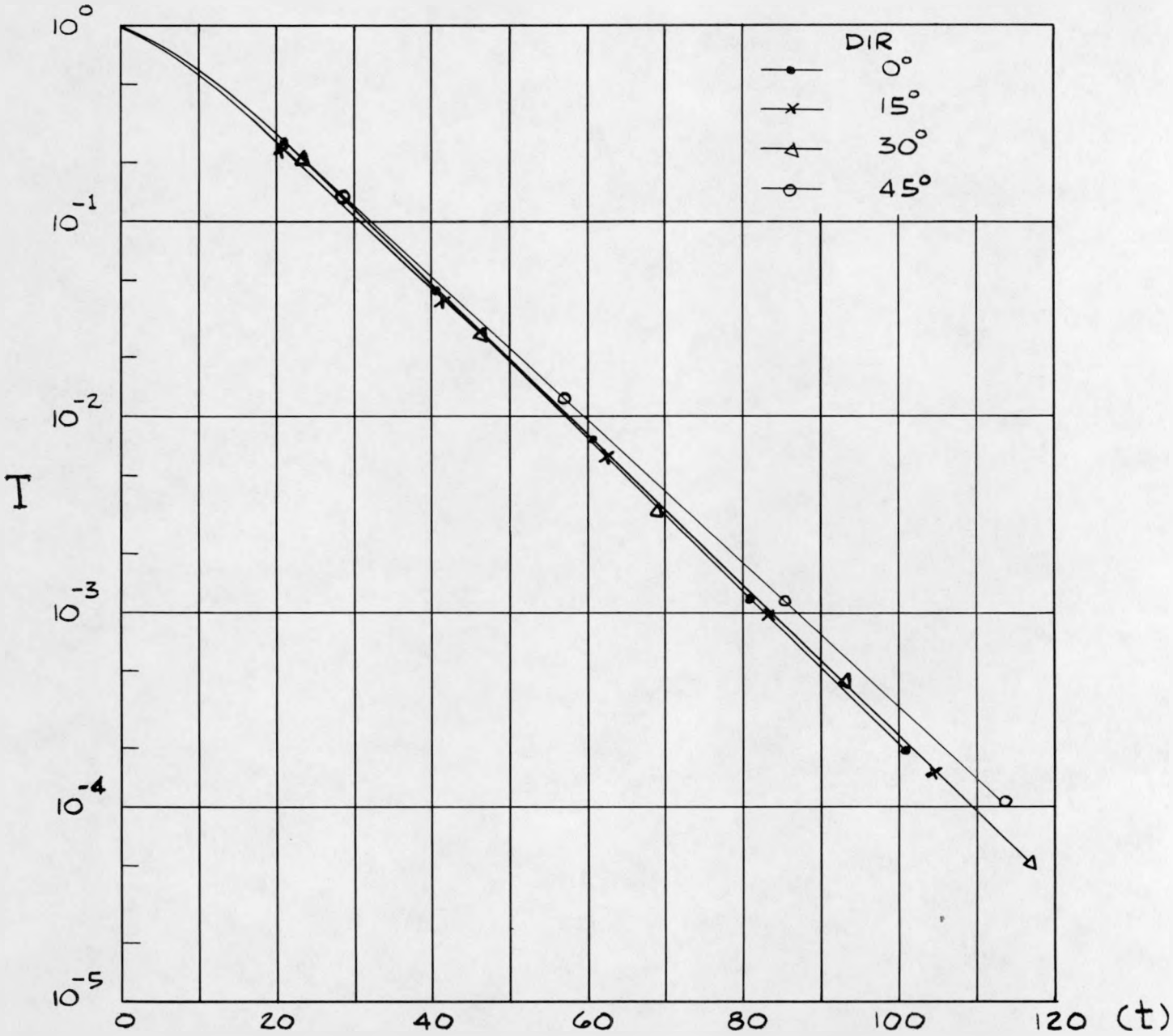

TRANSMISSION vs SLANT THICKNESS FOR Al.

FIG. 3

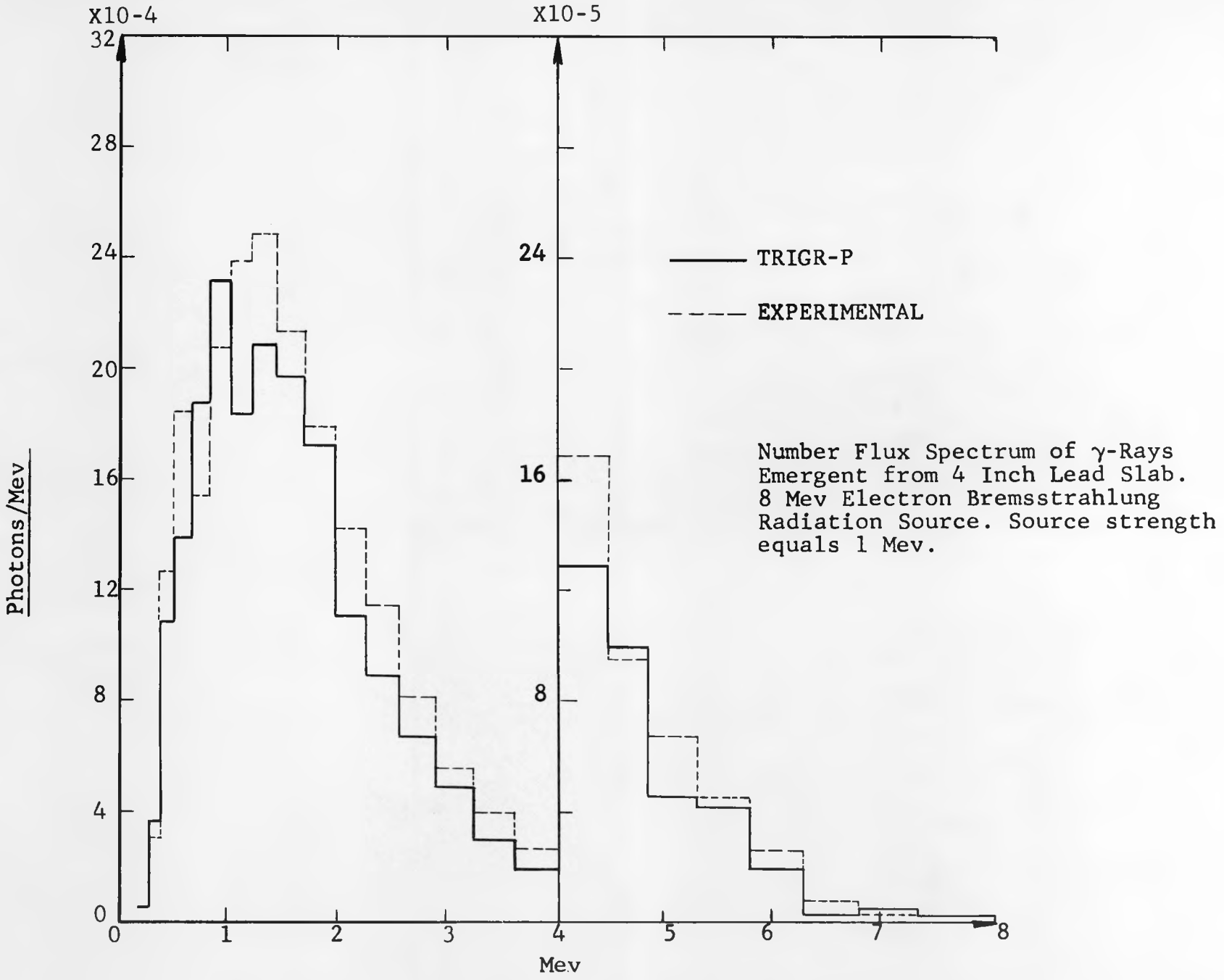
X10-4
X10-5
32
28
24
20
16
12
8
4
0
24
16
8
0
1
2
3
4
5
6
7
8
Mev
Photons/Mev
TRIGR-P
EXPERIMENTAL
Number Flux Spectrum of γ-Rays Emergent from 4 Inch Lead Slab. 8 Mev Electron Bremsstrahlung Radiation Source. Source strength equals 1 Mev.

FIG. 4

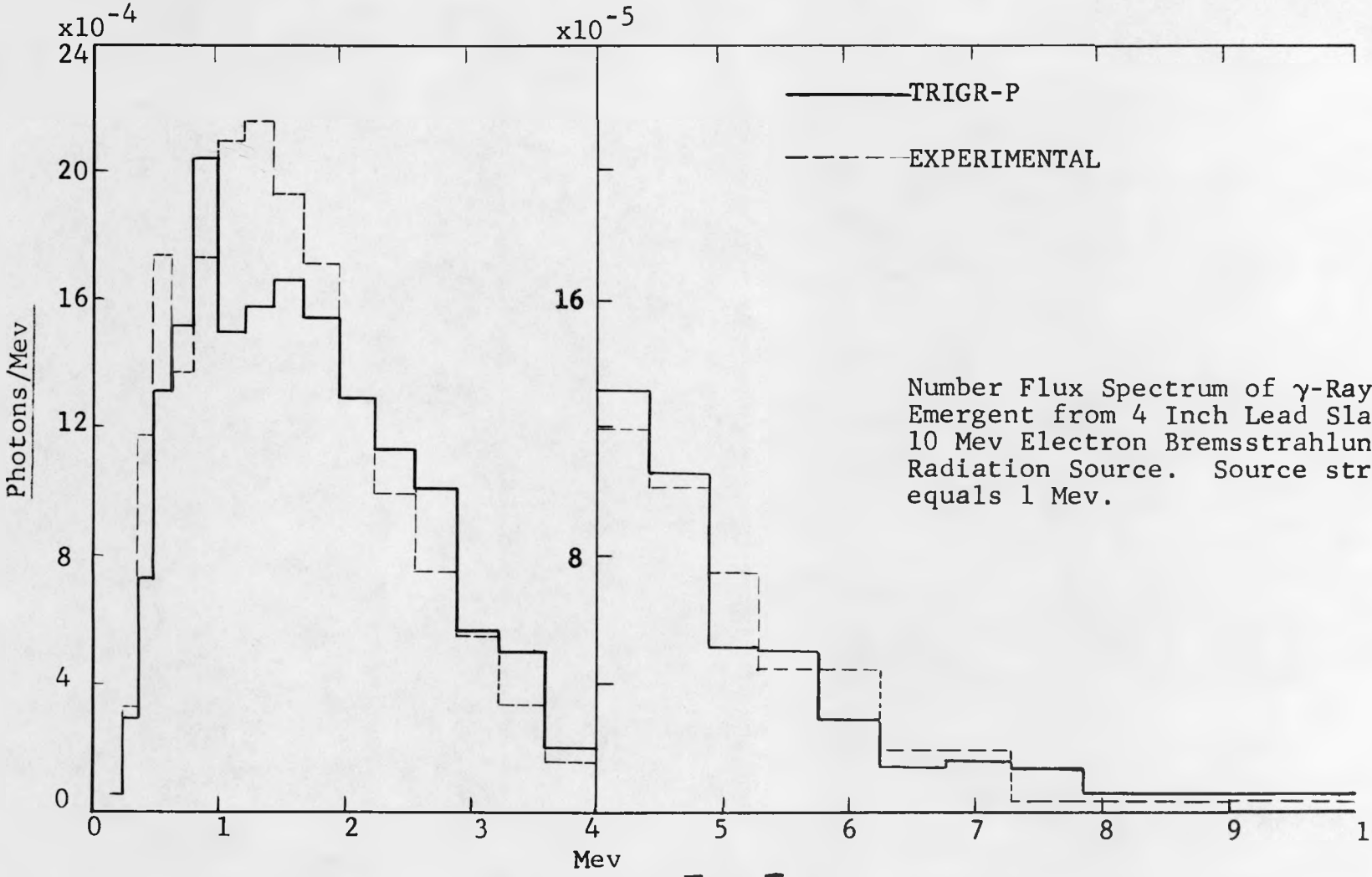
x10^-4
x10^-5
24
20
16
12
8
4
0
16
8
Photons/Mev
TRIGR-P
EXPERIMENTAL
Number Flux Spectrum of γ-Rays
Emergent from 4 Inch Lead Slab.
10 Mev Electron Bremsstrahlung
Radiation Source. Source strength
equals 1 Mev.
0
1
2
3
4
5
6
7
8
9
10
Mev

FIG. 5

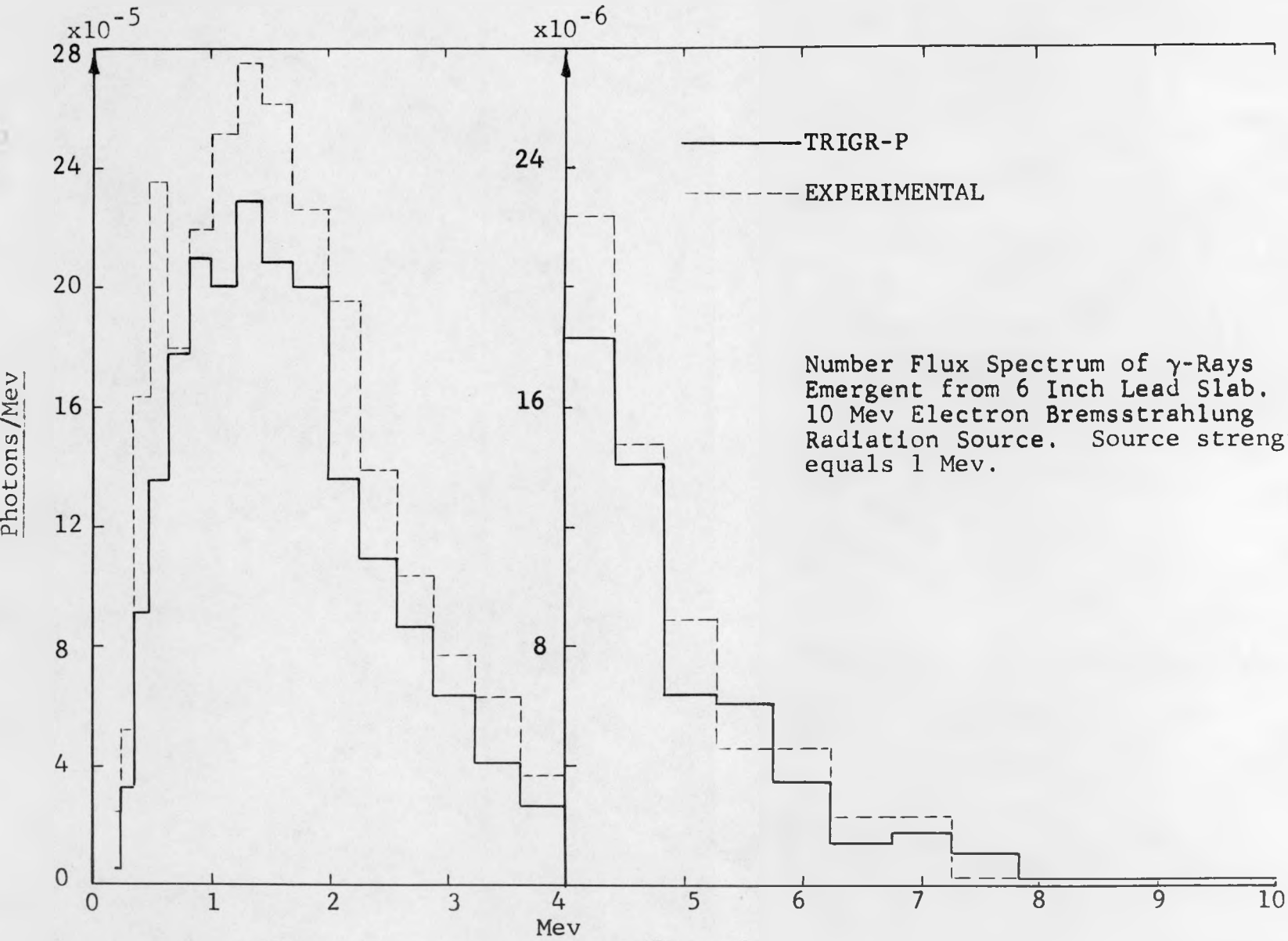
x10^-5
x10^-6
28
24
20
16
12
8
4
0
24
16
8
0
1
2
3
4
5
6
7
8
9
10
Mev
Photons/Mev
TRIGR-P
EXPERIMENTAL
Number Flux Spectrum of γ-Rays
Emergent from 6 Inch Lead Slab.
10 Mev Electron Bremsstrahlung
Radiation Source. Source strength
equals 1 Mev.

FIG. 6

17. GAMMA PENETRATION BY TRANSMISSION MATRIX METHOD

D. Yarmush

TRG, Incorporated
Syosset, New York

GAMMA PENETRATION BY TRANSMISSION MATRIX METHOD

by

D. Yarmush

TRG, Incorporated
Syosset, New York

A code for computing transmission and reflection matrices for gamma rays on slabs has been written and debugged. The code first computes an auxiliary matrix giving the properties of infinitely thin slabs by using empirical cross sections and the Klein-Nishina formula. The flux is represented by dividing the energy range into intervals and by using cosine powers for separate expansions in angle over the forward and backward hemispheres. An option allows for other methods of angular representation, e.g., the half-range Legendre polynomials. Preliminary numerical results are given.

At a previous shielding meeting, I discussed a possible method of computing gamma-ray transmission and reflection through laminated slab shields by means of what was called an H-matrix.* The elements of H are certain simple algebraic combinations of a transmission operator T and a reflection operator R. T can be described in mathematical terms as a linear integral operator which acts on any given incident distribution to produce the corresponding emergent distribution. R acts on an incident distribution to produce the reflected distribution.

For homogeneous slabs, H can be written in the form:

$$H = \begin{pmatrix} U & -UR \\ RU & T-RUR \end{pmatrix}$$

where U is the inverse of T:

$$U = T^{-1}$$

RU means the result of first applying the operator U to a distribution and then the operator R.

* See also WADC Technical Report 58-383 (AD 209063), pp.15-20

It can be shown that the H-matrices for a set of slabs, all of the same material but of different thicknesses t, are given in the form

$$H(t) = \exp Wt = 1 + Wt + \frac{W^2 t^2}{2} + \ldots$$

where W is a certain 2 x 2 matrix of operators:

$$W = \begin{pmatrix} \alpha & -\beta \\ \beta & -\alpha \end{pmatrix}$$

Here α and β describe the transmission and reflection properties respectively of infinitely thin slabs. Thus they can be determined from a knowledge of the collision and differential cross-sections at all energies.

A set of 704 codes which embodies these formulas has been written and debugged by H.J. Zell at TRG. Neutron shielding problems might also be handled, after some changes in the codes. This work was done under contract with the Aeronautical Research Laboratory of WADC. We have been analyzing the preliminary results for gamma rays. Some of these are discussed later. But first we mention the problems that arise in reducing the abstract general formulation just given to a set of algebraic equations which can be used for coding. The continuous range of energies must be finitized or discretized in some way. We have used a division into energy groups, although other approaches are also possible. It seems practical to use between 3 and 20 energy groups.

Within each group, the angular dependence is given by an expansion as a linear sum of basis functions. Our code has an option which permits a free choice of these functions, but probably the most useful will be either the powers of cos θ, where θ is the angle with the normal, or the Legendre polynomials, shifted so that the range of interest is cos θ = θ to cos θ = 1, rather than the usual range from -1 to +1.

In common with all multi-group methods, it is necessary to compute weighted averages of the collision and scattering cross-sections within each group. To do this, one has to assume a distribution function f(E) within a group. This is a well-known problem in neutron calculations. The proper form of f(E) for gamma rays is not very clear. We have experimented with two reasonable choices for f:

1. a distribution which is flat within each group when E is considered as independent variable.

2. a distribution which is flat when wavelength is considered as independent variable. This gives

$$f = \text{const.}/E^2$$

Of course, if the intervals are small enough and the cross-sections do not vary rapidly, the form of the distribution f does not matter. But for energy groups of the size that are practical, the differences in the two weighted averages may be a few percent in some cases. We are investigating this problem.

The decision about the form of f is essentially the only point where we make an approximation in the physics, rather than a mathematical approximation, such as arises in a numerical integration, or in taking only a finite number of terms of an infinite expansion. It may be worthwhile to use an initial guess for f, and then improve it by a recursive process.

Our calculations up to date have assumed a distribution flat in energy (that is, the first form we mentioned for f), and have considered only homogeneous slabs.

Tables 1,2 and 3 compare a selection of our preliminary results with a Monte Carlo Calculation using the code TRIGR-P. The Monte Carlo results are described in detail in the paper by Steinberg and Aronson. Separate calculations were made for monoangular incident distributions, at various angles to the normal. We combined these results to get the effect of an isotropic incident distribution. The fractional deviatio associated with the upper four scattered groups are about 10-15%. The error in the last scattered group is 5-10%. The unscattered flux is exact.

The Monte Carlo calculations used a monoenergetic source at 2.75 Mev, and computed the transmitted flux. The transmission-matrix method works with sources that are distributed in energy. In order to match as well as possible the energy division points used in the Monte Carlo, we took our source to be distributed between 2.50 and 2.75 Mev. Thus the two methods of calculation do not deal with exactly the same physical problem. The Monte Carlo results for unscattered flux, and for the scattering into the uppermost group, have been adjusted to take account of this, as is explained below.

The same total cross-section table was used in all calculations.

Several exploratory calculations were first made using different integration schemes for α and β, and varying certain convergence constants which are needed in computing the eigenvectors of the H-matrix.

From these investigations we are assured that the minor adjustable parameters can be varied over a wide range without affecting the first few significant figures in the calculated transmission. The tables indicate the effect of changing more important parameters, namely the number of angle terms or of energy groups.

First we examine what happens when an energy group is subdivided. (Table 1). The first and third columns of results were both obtained by using 3 terms for the angular representation. The middle energy group for the first calculation was split into 3 groups in the later calculation. We see that the fluxes in the first row are equal, and the sum of the second, 3rd and 4th rows in column 3 equals the second number in column 1. The numbers in the last row are apparently equal, but they actually disagree in the less significant digits which are not shown here. Actually we would not expect them to be exactly equal, because we are calculating energy degradation using a finer mesh here for column 3 than for column 1.

We can also note the effect of increasing the number of angle terms. But it should be first pointed out that our results on angular distributions are actually much more extensive than what is given here. One calculation gives information about how a set of incident distributions, which are isotropic, or distributed like $\cos\theta$ or $\cos^2\theta$, produce transmitted and reflected flux, transmitted and reflected current, and so on. But since only the transmitted flux was available from the Monte Carlo calculations, we have only given our results on the flux produced by an isotropic incident beam. Columns 1 and 2 show the results using 3 energy groups, but 3 angle terms in the first case and 7 in the second. The results for 7 terms are very slightly higher.

For 20 cm. of aluminum, the differences between the third and fourth (Monte Carlo) columns are apparently all within the fractional deviations attached to the Monte Carlo numbers.

The differences increase somewhat with increasing thickness. At 60 cm. (Table 2) they are about 20%, with the Monte Carlo results all higher. The fact that the differences are all in the same direction shows that the inherent random error of the Monte Carlo is not responsible.

We made two matrix calculations for 100 cm. (Table 3), one with 3 energy groups and 7 angle terms, the other with 5 energy groups and 3 angle terms. Thus it is possible to get information about increasing the number of angle terms, if we can disentangle the effect of the subdivision of the middle energy group. But we expect the latter effect to be small. The numbers in the first column are 3-8% higher than those in the second. The fact that they are higher can be justified theoretically. From certain intermediate results, not shown here, we conclude that using more angle terms would not produce any appreciable increase in the calculated transmission. Thus it is best to compare Column 1 here with the Monte Carlo column.

The adjustments in the Monte Carlo transmitted flux in the uppermost group in order to take account of the initial distribution in energy were made as follows:

First we estimate the unscattered flux by an analytic formula using the cross-section for the energy exactly half-way between 2.75 and 2.50 Mev.

To approximate the scattered radiation between 2.75 an 2.50 from a distributed source, we note that incident radiation just a little bit above 2.50 Mev will contribute almost nothing to this scattered term. Since the cross-sections do not vary rapidly, the contribution from an energy $2.50+\Delta$ is roughly proportional to Δ. Thus the average proportion of scattered radiation from a source distributed between 2.5 and 2.75 Mev. is roughly half the proportion scattered from the upper limit, 2.75 Mev, into the range 2.50 to 2.75 Mev. The number given here is therefore half the Monte Carlo result for the 2.75 Mev source.

Clearly to get a stricter comparison between the two methods, it will be necessary either to actually do a Monte Carlo with a distributed source, or else, perform a matrix calculation in which the uppermost group is very narrow.

In summary, we emphasize that the values presented her are a selection from the first significant output of the code. We also have data on reflection for the same thicknesses of aluminum, and for certain problems, we have the coefficients of a Legendre expansion of the transmitted flux up to the term in P_6. We have not had time to study all the data that have been obtained.

A problem of the size we have been discussing takes less than 2 minutes of IBM 704 time for the computation of the α and β matrices, and then one to three minutes to compute transmission and reflection for each thickness. These times will increase rapidly if more energy groups or more angle terms are used.

The code will be speeded up considerably when it is rewritten for a 32,000 - word machine. At present, a memory capacity of 16,000 words is assumed, and it's necessary therefore to write some intermediate results on tape and feed them back in at a later stage in the calculations. This is a comparatively slow process.

One section of the code allows the calculation of transmission through laminated shields, and yields the angular distribution of transmitted radiation for each energy group. The calculations for a great many incident distributions are done at the same time. Thus there is justification for expecting that the transmission matrix method will be economical of computing time, and will produce results which are very difficult to obtain by other methods.

TABLE I

TRANSMISSION THROUGH 20CM. OF ALUMINUM
ISOTROPIC INCIDENCE. NUMBER FLUX.
UNIT IS 10^{-2} x INCIDENT FLUX

Energy Groups Angle Terms	TRANSMISSION MATRIX 3 3 3	3 3 7	5 3		ADJUSTED MONTE CARLO	
Unscattered	3.809	3.833		3.809	3.75	4.04
2.75 - 2.50					.29	
2.50 - 2.25			.639		.63	
2.25 - 2.00	1.970	1.971	.651	1.966	.78	2.11
2.00 - 1.75			.676		.70	
1.75 - 1.00	2.456	2.464		2.456		2.49

TABLE II

TRANSMISSION THROUGH 60CM. OF ALUMINUM
UNIT IS 10^{-4} x INCIDENT FLUX

Energy Groups Angle Terms	TRANSMISSION MATRIX 5 3	ADJUSTED MONTE CARLO	
Unscattered	3.419	3.18	3.92
2.75 - 2.50		.74	
2.50 - 2.25	1.342		1.57
2.25 - 2.00	1.409		1.75
2.00 - 1.75	1.509		1.76
1.75 - 1.00	5.936		7.34

TABLE III

TRANSMISSION THROUGH 100 CM. OF ALUMINUM
UNIT IS 10^{-6} x INCIDENT FLUX

Energy Groups Angle Terms	TRANSMISSION MATRIX 3 7	5 3		ADJUSTED MONTE CARLO	
Unscattered	4.169		3.864	3.83	5.31
2.75 - 2.50				1.48	
2.50 - 2.25		2.263		3.10	
2.25 - 2.00	7.818	2.431	7.348	3.29	9.75
2.00 - 1.75		2.654		3.36	
1.75 - 1.00	11.116		10.798		16.88

18. GAMMA-RAY PENETRATION INTO THE COMPARTMENTS OF A LIGHT AIRCRAFT CARRIER

S. Tomoeda
W. E. Kreger
M. B. Hastings
W. G. Miller

U. S. Naval Radiological Defense Laboratory
San Francisco 24, California

GAMMA-RAY PENETRATION INTO THE COMPARTMENTS OF A LIGHT AIRCRAFT CARRIER

by

S. Tomoeda, W. E. Kreger, M. B. Hastings and W. G. Miller

U. S. Naval Radiological Defense Laboratory
San Francisco 24, California

The penetration of gamma rays into compartments of an aircraft carrier from three different radioisotopes has been measured. Co^{60} (1.25 Mev), Cs^{137} (.66 Mev) and Ir^{192} (.38 Mev) sources were exposed at numerous points on the Flight Deck and Landsverk air-wall equivalent dosimeters were used to measure dose in two general areas of the ship and at three different deck levels. Average dose rates and transmission factors have been calculated by integration of the data to represent the case of uniform contamination of 1 curie per square foot. Point source data have been compared with data taken using a uniformly distributed source. Effective shielding thicknesses of a ship's structure have been determined from the experimental data and compared with known structural thicknesses. Energy dependence of the shielding effectiveness can be adequately accounted for using attenuation coefficients and build-up factors for the particular energies involved.

INTRODUCTION

In order to evaluate the potential hazard to naval personnel due to radiation from a nuclear weapon, it is necessary to determine the shielding effectiveness of the structural components of naval vessels. Determining this effectiveness experimentally for all naval vessels would present an insurmountable task. However, a combination of selected experiments on complex structures such as ships, together with simple geometry experiments and theoretical methods should permit the development of calculational procedures which could handle many combinations of complex structures and radiation fields. The experiment described here is one such experiment designed to provide information on the modification of a radiation field by a complex structure. Shielding factors in selected areas of an aircraft carrier are measured for simple monoenergetic sources distributed on the Flight Deck.

A number of experiments on structure shielding effects

have been carried out in the past several years.[1-18] Several of these[1-5] have actually involved ships. The sources and source geometries used in these experiments were different in each case from the experiment described here except the one described in reference 3. However, that experiment was carried out with Co^{60} gamma radiation only and the detailed data necessary for the type of interpretation attempted in the experiment described here is not available.

The experiment described in this report was directed toward providing information concerning shielding effectiveness of the ship's structure for three different monoenergetic gamma-ray sources placed successively at a large number of positions on the Flight Deck of an aircraft carrier. Many compartments in two markedly different areas of the ship were instrumented in some detail with integrating dosimeters. The two areas chosen had a wide variation in compartment size so as to determine the effects of compartmentation on penetration of radiation from isotropic sources. Use of the data for individual source and dosimeter locations permitted the determination of shielding factors for many different penetration paths and directions. Integration over all source and dosimeter locations yielded an estimate of the shielding effectiveness against uniform contamination.

EXPERIMENTAL PROCEDURE

The sources used in this experiment were 54 curies of Co^{60} with an effective gamma-ray energy of 1.25 Mev, 150 curies of Cs^{137} with an effective energy of .662 Mev, and 261 curies of Ir^{192} which has about 61.5 percent gamma-ray emission at .30 Mev and 24.5 percent at .48 Mev for an effective unattenuated energy of .38 Mev. The sources were in the form of small capsules which could be lowered from shielded containers to selected points on the Flight Deck. The source strengths were calibrated using the dosimeters which were used in the ship. These dosimeters had been calibrated against a standard Co^{60} source.

The dosimeters used in the experiment were made by Landsverk Electrometer Co. and were the 200 mr, 2000 mr and 5000 mr models of that company. The different models made it possible to instrument several decks for a given length of exposure to source radiation and obtain as nearly as possible full discharge on the dosimeters. The integral dose obtained during the exposure was read on Landsverk Model L-62 charger-reader units. Temperature-pressure corrections to the dosimeter readings were made after each run, as well as a calibration correction.

In an experimental run or exposure, charged dosimeters were placed on stands 3.5' above each deck for three

different decks below the Flight Deck. The source was lowered to the Flight Deck and an exposure made, usually for about one hour. After the exposure was completed the source was placed back in its shield and the dosimeters were collected and read. Measurements were made in two different sections of the ship. "A" Section covered the forward portion of the ship between frame 0 and 45 (frame spacing, approximately 4 ft.). "B" Section covered the area in the central portion of the ship between frame 45 and 145. Data were taken in an area which extended only for about 40 ft. within the area described above. Instrumented compartments in "A" Section were small and approximately equal size with the exception of the Main Deck wardroom mess. "B" Section compartments were relatively large and of different sizes. Deck separations are 8 ft. on the average except that the Hangar Deck is 21 ft. below the Flight Deck.

Figure 1 shows the locations on the Flight Deck of the Co^{60} source for the different exposures in the "B" Section of the ship. The source array was chosen to average out major structural components of the ship. Figure 2 shows a similar source array for the Co^{60} and Cs^{137} sources on the Flight Deck in the "A" Section. The decks instrumented in "B" Section in order from the Flight Deck were the Hangar Deck, the 2nd Deck and the 3rd Deck. In "B" Section, the decks instrumented were the Gallery Deck, the Forecastle Deck and the Main Deck.

Figure 3 indicates the Gallery Deck locations of the dosimeters for a representative source exposure in the "A" Section. The Co^{60} source was placed directly above station 24. The dosimeter readings are given next to the station position for a one-hour exposure to the Co^{60} source. The variation in readings is due to the different source to detector distances and the differences in attenuating material along the various gamma-ray penetration paths. Figure 4 shows similar results for the Main Deck in "A" Section, which is two decks deeper in the ship than the previous data. At this level most of the dosimeters are about the same distance from the source so that differences in dose values are mostly due to variations in attenuation in structural material.

TREATMENT OF THE DATA

Each dosimeter reading was recorded on an IBM card together with the information on the length of the exposure, the effective source strength at the time of exposure, the coordinates of the dosimeter station, the source position, source type, and dosimeter type. A program was set up for the Datatron computer to process all the dosimeter readings. For each exposure the dosimeter readings were corrected to absolute dose rates in roentgens per hour and normalized to

one effective source strength. Then for each deck the computer went through the following averaging procedure. The instrumented area was divided into 30 concentric annular areas with the perpendicular projection of the source point as center. The incremental radius for each ring was 2 ft. The dosimeter readings for all the dosimeters falling in a particular annular area were averaged and printed out along with the corresponding zone or ring number, the number of readings within the zone, and the mean deviation of the values about the average. These results were later averaged by zones over all the positions of a given source for each deck and plotted as a function of zone. Figures 5, 6, and 7 give the plots of these averaged results on the three different decks for the Co^{60} source in "A" Section. The small numbers next to the data points are the number of dosimeter readings contributing.

The values at each ring were multiplied by the ring area to give effective dose contribution from concentric rings on the Flight Deck contaminated to one curie per square foot of the particular source (also corrected to one photon per disintegration). In this procedure, the contour of the Flight Deck was adhered to. Since the maximum width of the Flight Deck is about 70 ft., the zones beyond zone 16 were not complete rings. Data were used up to zone 30 which gives results out to 60-ft. ring radius. Although a completely contaminated Flight Deck would involve much greater ring radii (out to 300 ft. radius), it was determined that rings beyond 60-foot radius contributed less than 5 percent of the total dose at the highest deck and less at the other decks.

Table I shows the results of the procedure described above. The top set of numbers, labeled A, gives the calculated dose in air at the indicated (left-hand column) distance from a contaminated plane having one curie/sq. ft. contamination. No air attenuation was included. The numbers labeled B are the results of the same kind of calculation as A except that a $B_r e^{-\mu x}$ factor is included for each path of direct gamma-ray penetration from the source to the detector point. The build-up factor (B_r) used was the point isotropic infinite medium dose build-up factor in iron, the μ is the total attenuation coefficient for iron at the source energy involved, and the x is the thickness of known deck plating material (iron) along the particular penetration paths under consideration. The numbers designated C are the experimental results. Figures 8 and 9 show this same data plotted as a function of energy for the "A" Section data and "B" Section data respectively.

These data have been turned into transmission factors by dividing the numbers of row C in each case by the numbers of row A. These transmission factors are tabulated in Table II together with a transmission factor in which

TABLE I

Gamma-Ray Dose Rate

"A" Section

Gamma-Ray Energy		1.25 Mev	0.66 Mev	0.38 Mev
Gallery Deck 6.5' Below Flight Deck	A	91.4 r/hr	49.2 r/hr	28.4 r/hr
	B	53.2 "	27.6 "	11.4 "
	C	30 "	13 "	4.7 "
Forecastle Deck 13.5' Below Flight Deck	A	62.2 r/hr	33.5 r/hr	19.3 r/hr
	B	35.6 "	17.9 "	6.91 "
	C	11 "	5.5 "	1.3 "
Main Deck 21.5' Below Flight Deck	A	46.5 r/hr	22.4 r/hr	12.9 r/hr
	B	22.5 "	11.2 "	4.0 "
	C	5.4 "	2.1 "	0.37 "

"B" Section

Hangar Deck 17.5' Below Flight Deck	A	49.3 r/hr	26.5 r/hr	15.3 r/hr
	B	37.5 "	20.5 "	9.17 "
	C	24 "	8.6 "	4.2 "
2nd Deck 29.5' Below Flight Deck	A	30.4 r/hr	16.4 r/hr	9.45 r/hr
	B	11.6 "	5.44 "	1.46 "
	C	4.1 "	0.74 "	0.23 "
3rd Deck 38.0' Below Flight Deck	A	22.7 r/hr	12.2 r/hr	7.05 r/hr
	B	7.6 "	3.42 "	0.847 "
	C	0.99 "	0.21 "	0.064 "

A = Calculated dose rate in air from a 60 foot radius area contoured to the Flight Deck contaminated to 1 curie per square foot and attenuated by inverse square only to distances indicated.

B = Calculated dose rate from 60 foot radius area contaminated to 1 curie per square foot and attenuated by the average thickness plating of the various decks.

C = Dose rate found by integrating 60 foot radius circle contoured to the Flight Deck contaminated to 1 curie per square foot and using experimental curves shown in Figs. 5, 6, 7.

TABLE II

Transmission Factors

"A" Section

Gamma-Ray Energy		1.25 Mev	0.66 Mev	0.38 Me
llery Deck 5' from Flight Deck	Transmission Factor 3.5 Transmission Factor d=6.5	0.260 0.328	0.209 0.264	0.131 0.165
recastle Deck .5' from Flight Deck	$T_{3.5}$ T_d=13.5	0.095 0.177	0.088 0.164	0.036 0.067
in Deck .5' from Flight Deck	$T_{3.5}$ T_d=21.5	0.047 0.116	0.044 0.094	0.010 0.029

"B" Section

Gamma-Ray Energy		1.25 Mev	0.66 Mev	0.38 Me
ngar Deck .5' from Flight Deck	$T_{3.5}$ T_d=17.5	0.208 0.487	0.138 0.324	0.117 0.274
d Deck .5' from Flight Deck	$T_{3.5}$ T_d=29.5	0.035 0.135	0.012 0.045	0.006 0.024
d Deck .0' from Flight Deck	$T_{3.5}$ T_d=38.0	0.009 0.044	0.003 0.017	0.002 0.009

$T_{3.5}$ = Ratio of average dose rate on given deck to the theoretically calculated dose rate 3.5' off the Flight Deck. Theoretical dose rates at 3.5' above Flight Deck are 1.25 Mev ~ 115.6 r/hr, 0.66 Mev ~ 62.3 r/hr, and 0.34 Mev ~ 35.9 r/hr.

T_d = Ratio of average dose rate at the given deck to the theoretically calculated dose rate in air at that deck.

the denominator is the dose at 3.5 ft. above the Flight Deck rather than at the deck under consideration.

In Table I it is apparent that simple calculations taking into account inverse square effects and exponential attenuation in deck plating only are grossly inadequate for predicting dose rates. This conclusion is not very surprising in view of the fact that there is so much material distributed between the various decks that is not deck plating. This factor will be discussed later in this paper.

ADDITIONAL RESULTS

In order to determine whether the averaging and integration procedure used with point sources was a correct one, an additional experiment was undertaken using a source which could be pumped through plastic tubing distributed around the Flight Deck of the carrier. This source was developed by Technical Operations, Inc., of Burlington, Mass., and used a Co^{60} capsule of approximately 200 curie strength. Figure 10 shows the schematic diagram of the experimental setup. Dosimeters were distributed in a manner similar to that of the previous experiment and integrated dose readings determined for an exposure where the source was pumped at uniform speed through the entire tubing length. Table III shows a comparison of the results determined from the data taken using the two methods. There seems to be reasonable agreement except in the case of the Gallery Deck in the "A" Section. It is not surprising, in view of the complexity of the structure in the ship, that the limited number of point source positions do not adequately average out all the complexities.

In order to get a more reasonable thickness of material from which to calculate attenuation, the structural weights of the ship were determined from the design drawings. Table IV shows the results of this determination. The "Fixed Structure" weights are the weights of fixed structure from the Flight Deck down to the dosimeter plane at the deck in question divided by the area involved. "Equipment" represents removable items including machinery and "Systems" represents electrical, plumbing, and ventilation systems, etc. Deck plating weights are those used in the calculations described above and presented as a factor in the row B data of Table I. The last column labeled Experimental was obtained from the data using point sources in the following manner. Curves were plotted of $B_r e^{-\mu x}$ for steel and the three source energies involved. The values of the transmission factors for individual source rings or zones and source energies were considered to be equivalent to $B_r e^{-\mu x}$ so that one could use the experimental

TABLE III

Comparison of Distributed Source Experiment with Point Source Results

Dose Rate for One Curie/Square Foot of Co^{60}		
Decks	Distributed Source	Integrated Point Source
Gallery	47.6 r/hr	60 r/hr
Forecastle	20.5 r/hr	22 r/hr
Main	10.0 r/hr	10.8 r/hr
Hangar	40.3 r/hr	48.0 r/hr
Second	9.0 r/hr	8.1 r/hr
Third	2.7 r/hr	2.0 r/hr

TABLE IV

Effective Shielding Weights and Tabulated Ship Weights

A Section	Ship Weights - lb./sq. ft.				Plating in Decks - lb./ sq. ft.	Experimental lb./sq. ft.
	Fixed Structure	Equipment	Systems	Total		
Gallery Deck	52.5	20.9	2.9	76.3	15.8	28 - 36 32.1
Forecastle Deck	68.9	25.7	4.5	99.1	23.9	40 - 72 64.2
Main Deck	91.7	32.0	6.9	130.6	31.9	56 - 96.2 88.0

B Section	Ship Weights - lb./sq. ft.				Plating in Decks - lb./ sq. ft.	Experimental lb./sq. ft
	Fixed Structure	Equipment	Systems	Total		
Hangar Deck	58.7	7.1	6.7	72.5	15.8	32 - 52 48.2
2nd Deck	122.0	19.9	10.2	152.1	51.5	112 - 132 120
3rd Deck	170.1	22.4	25.9	218.4	62.5	148 - 168 160

value and the curves to obtain effective material thickness values. The slant angle of penetration for each zone's source to detector path was taken out of the value to give effective normal (vertical) thickness. The top numbers in each block of the last column represent the range of effective thickness values for the different zones and source energies, while the bottom is the average value. It can be seen that these numbers agree quite well with the fixed structure thickness values except at the highest deck level. This would seem to indicate that in order to get average dose levels at various decks, structural material, including beams and vertical bulkheads, can be smeared out as if it constituted a uniform horizontal layer of material.

It is planned to attempt to get a better fit between experiment and theory by using a more realistic build-up factor than the point isotropic infinite medium one. Possibilities include actual slab build-up factors which have been measured at NRDL, infinite medium build-up factors corrected for finite bounded medium situations, etc. There have been some proposals that no build-up factor should be necessary due to elimination of most of the scattered radiation by the vertical bulkheads.

A major fraction of the work reported here has appeared in a technical report.[19] In addition to this experiment, data are presently being analyzed for source locations along the side of the ship, and for source locations at points in space at some distance from the ship and at various orientations relative to the ship's axis. In addition, experiments of a similar nature have been carried out using a destroyer as the target vessel. These results together with the more detailed results of the experiment described here will be presented as forthcoming USNRDL technical reports.

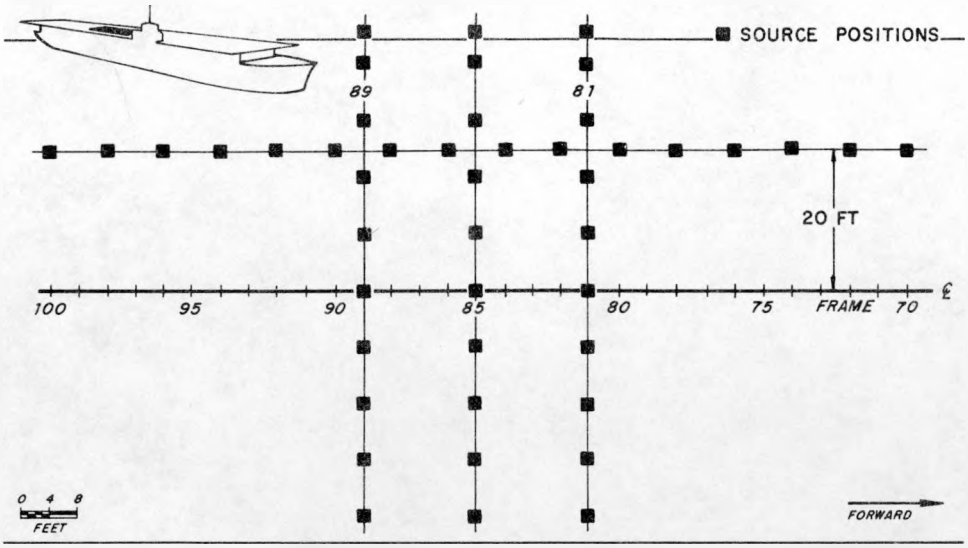

Fig. 1 Co^{60} source positions on the Flight Deck in the "B" section.

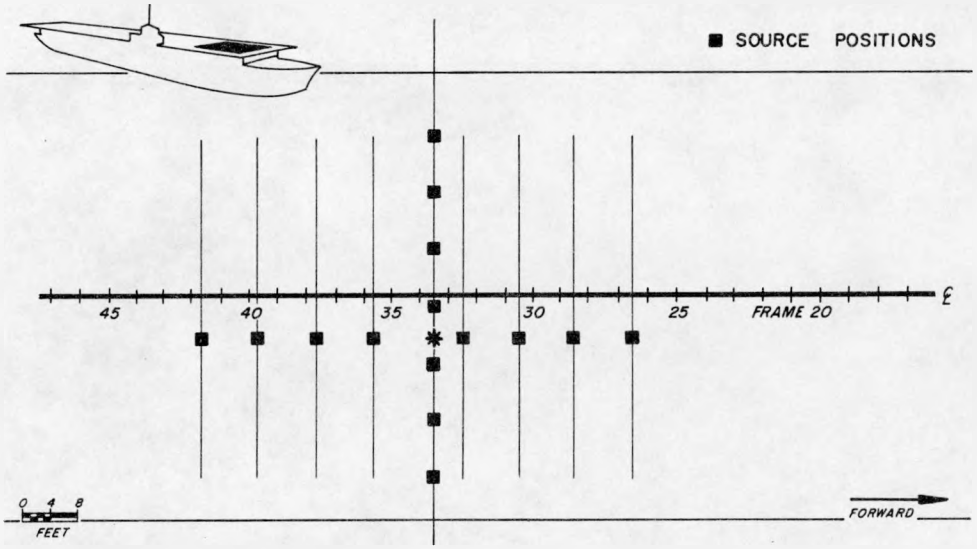

Fig. 2 Co^{60} and Cs^{137} source positions on the Flight Deck in the "A" section.

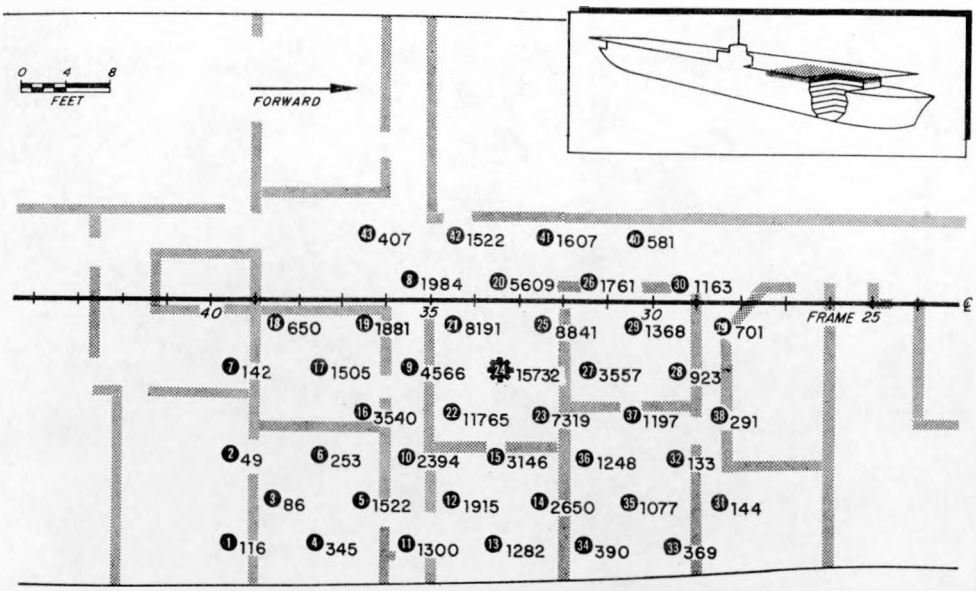

Fig. 3 Sample data obtained on Gallery Deck with the cobalt source exposed on the Flight Deck at a position perpendicularly above the point marked with the star. The source strength was 53 curies and the dose rate is in mr/hr.

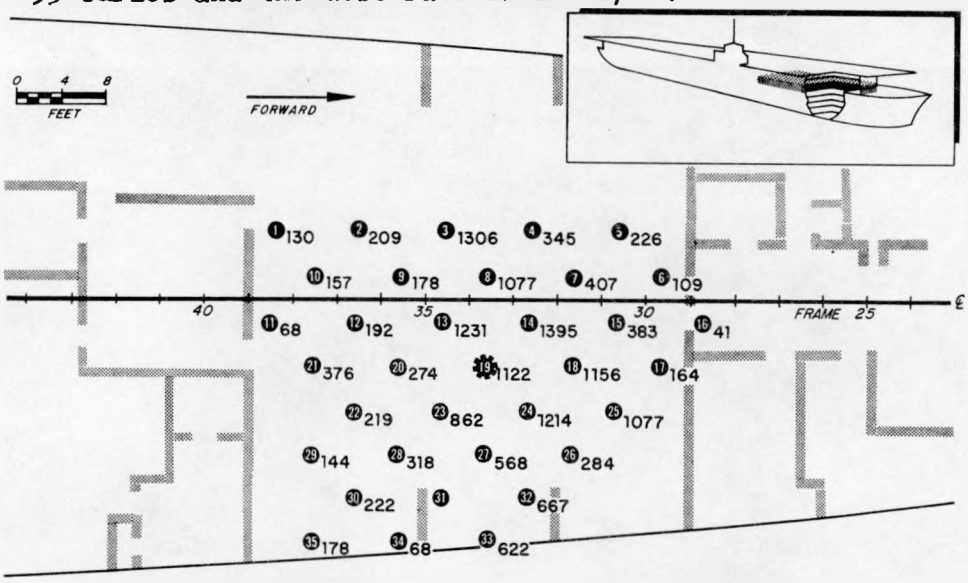

Fig. 4 Sample data obtained on the Main Deck with the cobalt source exposed on the Flight Deck at a position perpendicularly above the point marked with the star. The source strength was 53 curies and the dose rate is in mr/hr.

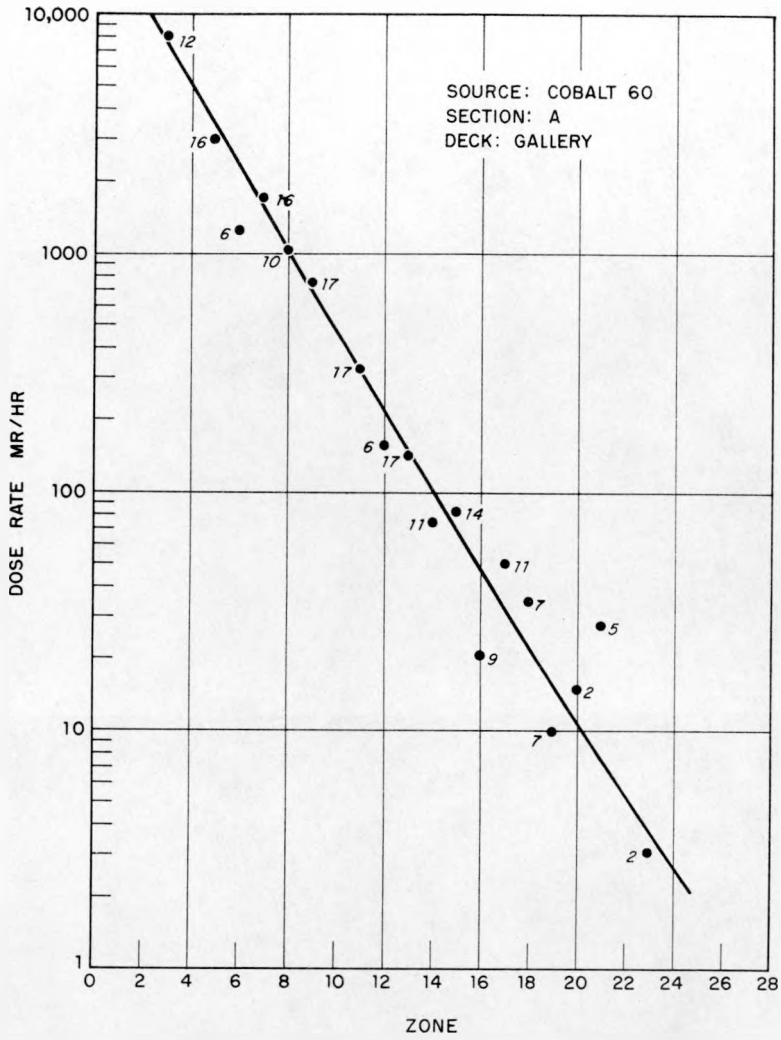

Fig. 5 Typical response curve of dose rate versus zone number for the Gallery Deck obtained from computer averaging of the data obtained from all source positions (Fig. 2) and associated dosimeter positions. The Co^{60} source strength was 53 curies for all exposure conditions. The numbers accompanying the points of the curve give the number of dosimeter readings used in finding the average dose rate for any particular zone.

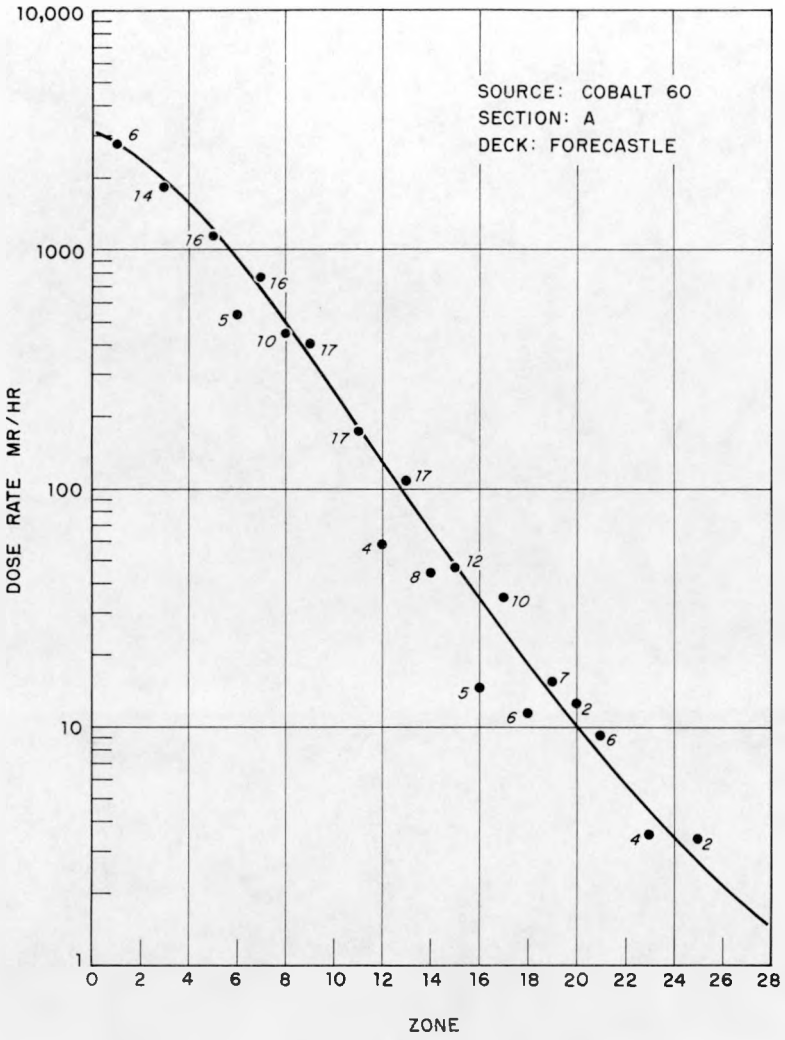

Fig. 6 Typical response curve of dose rate versus zone number for the Forecastle Deck obtained from computer averaging of the data obtained from all source positions (Fig. 2) and associated dosimeter positions. The Co^{60} source strength was 53 curies for all exposure conditions. The numbers accompanying the points of the curve give the number of dosimeter readings used in finding the average dose rate for any particular zone.

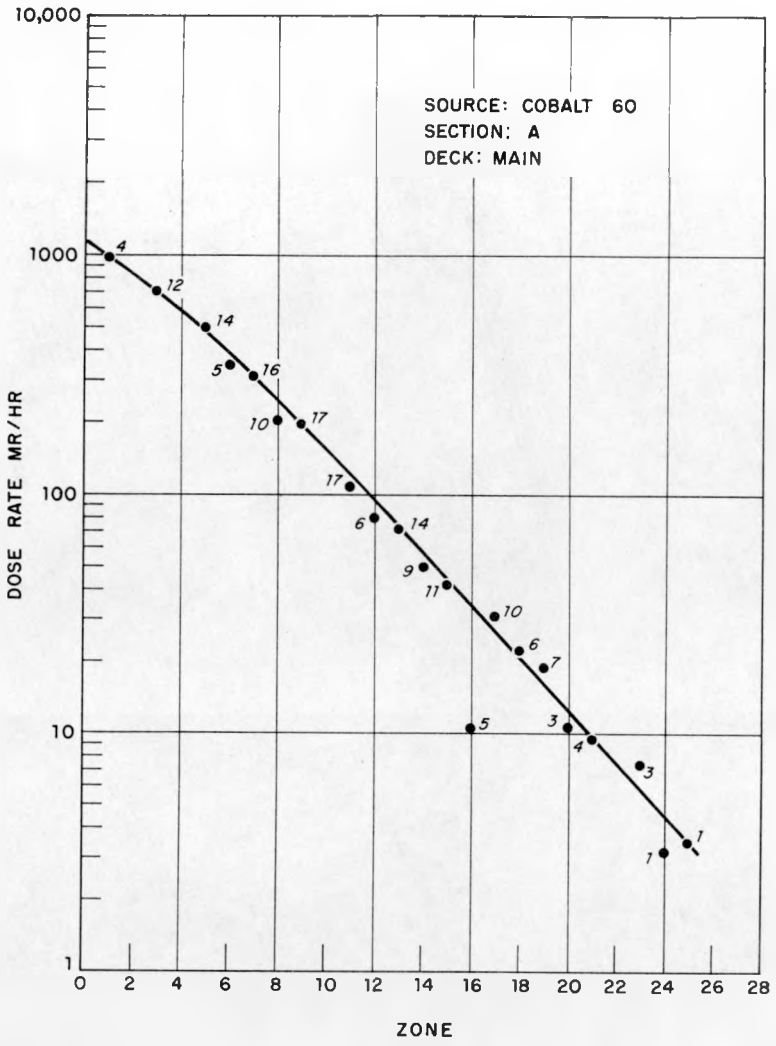

Fig. 7 Typical response curve of dose rate versus zone number for the Main Deck obtained from computer averaging of the data of all source positions (Fig. 2) and associated dosimeter positions. The Co^{60} source strength was 53 curies for all exposure conditions. The numbers accompanying the points of the curve give the number of dosimeter readings used in finding the average dose rate for any particular zone.

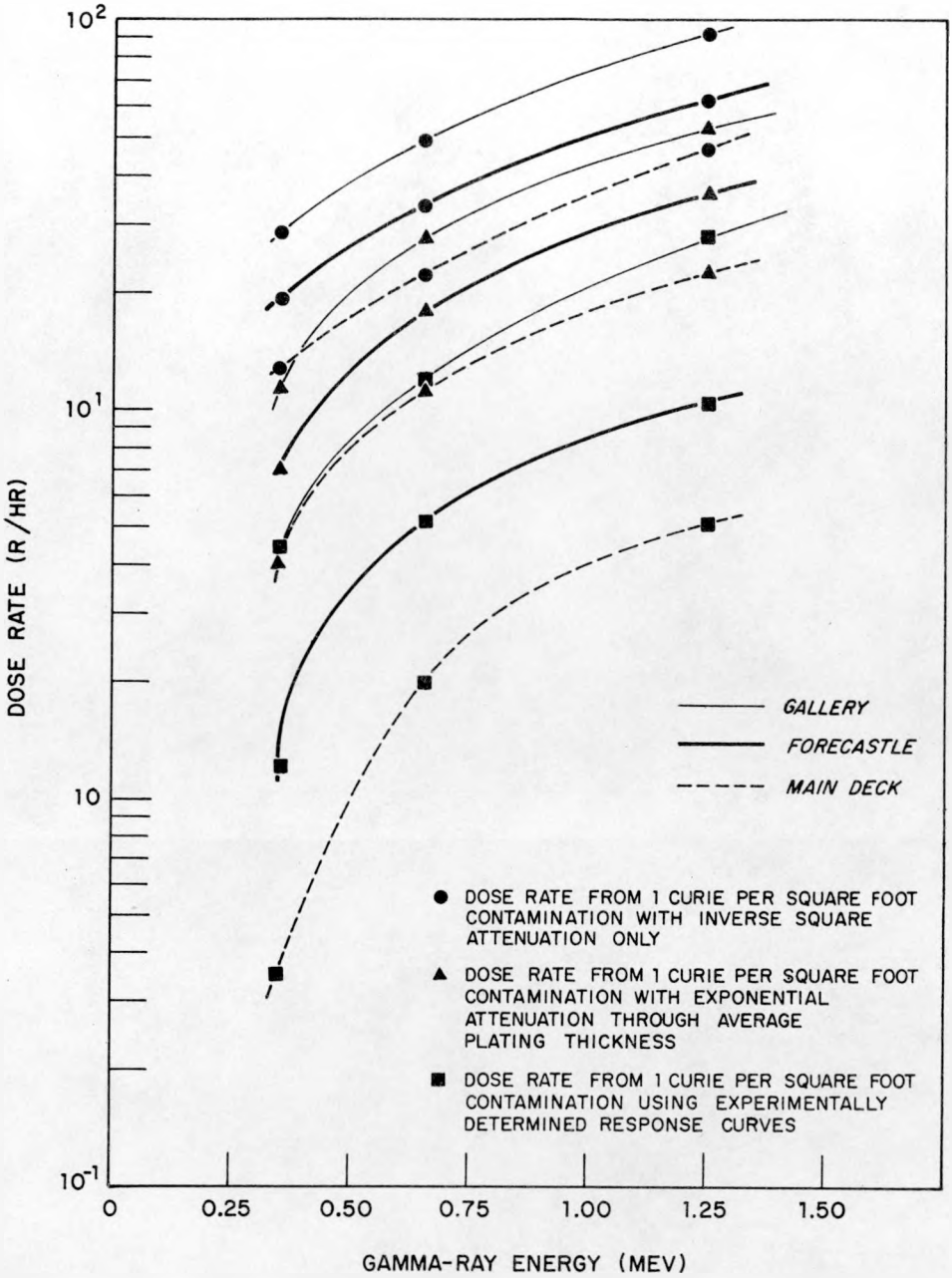

Fig. 8 Comparison curves of theoretical and experimental dose rates for three gamma-ray energies. These results are for the three decks under consideration in the "A" section.

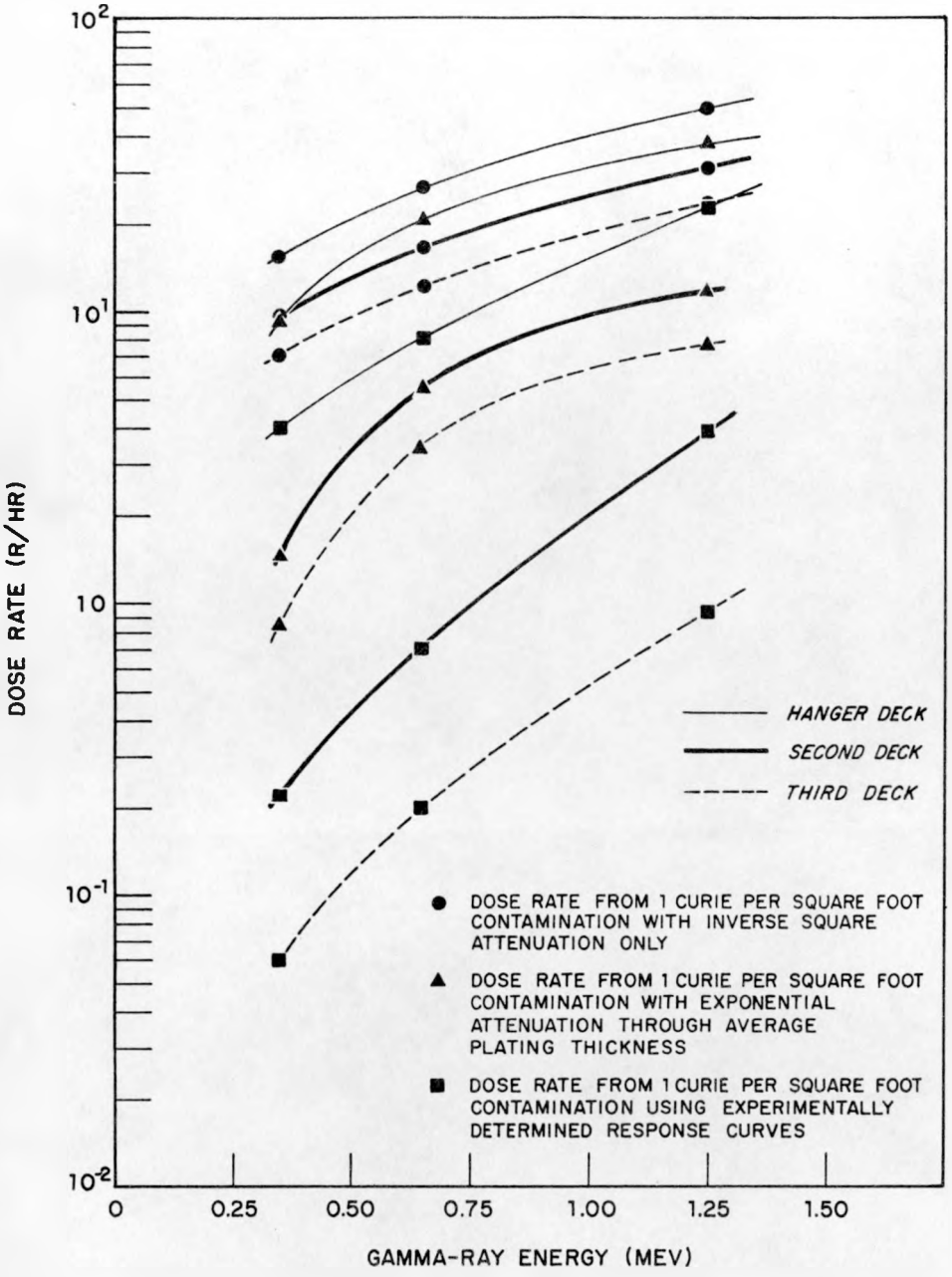

Fig. 9 Comparison curves of theoretical and experimental dose rates for three gamma-ray energies. These results are for the three decks under consideration in the "B" section.

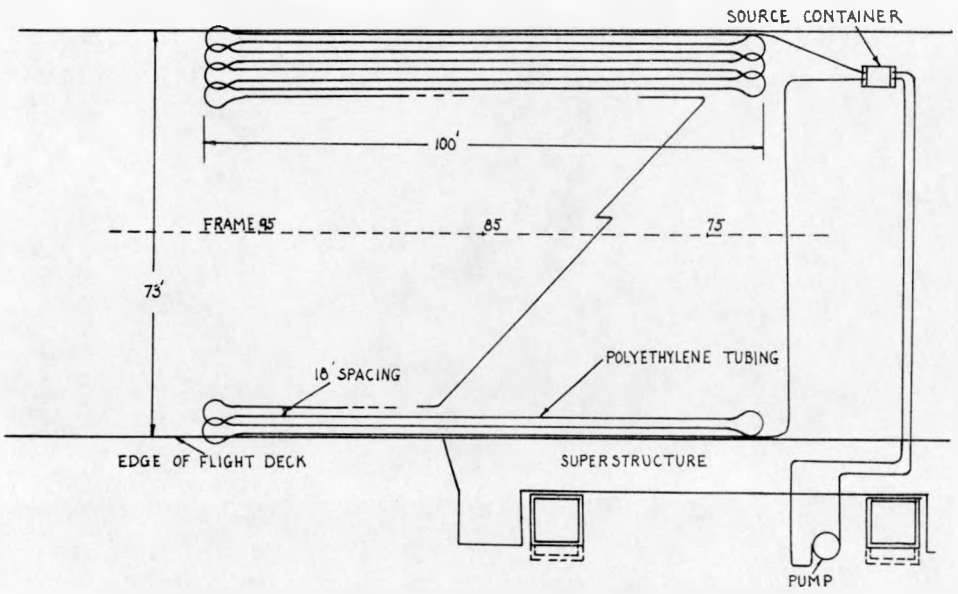

Fig. 10 Schematic drawing of experimental set-up for the distributed source experiment.

REFERENCES

1. Strope, W. E., History of the USS Independence at Bikini, NRDL AD-161 (o), September 1946.

2. Luxford, C. A. and Soole, B. W., Trials on the Penetration of Gamma Rays into the Compartments of H.M.S....., Preliminary Report A.R.L./R.1/R.640, September 1949. Secret; Soole, B. W., Final Report Part I., Characteristics of the Radioactive Sources and the Transmission of Gamma Rays Over the Sea, A.R.L./R.2/R.640, March 1950. Secret; Soole, B. W. and Luxford, C. A., Final Report Part II, Detailed Measurements in the Ship, A.R.L./R.3/R.640, August 1950. Secret.

3. Soole, Williams, and Dickenson, The Shielding Afforded by H.M. Ships against Gamma Radiation Emitted from Radioactive Surface Contamination, Preliminary Report A.R.L./R.1/R.651, September 1957. Secret.

4. Williams, J. H., The Protection Afforded by a Ship's Structure against the Gamma Radiation Emitted by an Atomic Explosion, AWEC/P(57), September 1957. Secret.

5. Beach, L. A., Theus, R. B., and Faust, W.R., Measurement of Penetration and Scattering of Radiation Aboard USS Randolph, NRL 4146, April 1953.

6. Beckelheimer, R. P. and Rexroad, R. E., Attenuation of 1.2 Mev Gamma Radiation by Soviet and U. S. Military Vehicles and U. S. Rail Equipment, C.R.L.R. 297, August 1953.

7. Rexroad, R. E., Drubar, D. L., and Peale, J. C., Experimental-Theoretical Attenuation of 1.2 Mev Radiation by Simple Structures, C.R.L.R. 326, September 1953.

8. Stanbury, G. R., Operation Hurricane Group Reports: The Penetration of the Gamma Flash into Anderson Shelters and Concrete Cubicles, FWE-76, August 1954. Secret R. D.

9. Malich, C. W. and Beach, L. A., Fallout Protection Afforded by Standard Enlisted Men's Barracks, NRL 4886, March 1957.

10. Malich, C. W. and Beach, L. A., Radiation Protection Afforded by Barracks and Underground Shelters, NRL 5017, September 1957.

11. Stewart, Chisholm, Crooks, and Gale, The Shielding Provided by a Brick House against the Gamma Radiation from a Uniformly Deposited Source - Experiments with Co^{60}, FWE-104, October 1955.

12. Home Office, Scottish Home Department, Assessment of the Protection Afforded by Buildings against Gamma Radiation from Fallout, 1957.

13. Graveson, R. T., Radiation Protection within a Standard Housing Structure, NYO 4714, November 1956.

14. Rexroad, R. E. and Schmoke, M. A., Pre-Test Plans for Dose Rate Build Up Factors Inside a Concrete Building, CWLTM-34-3, March 1958.

15. Berger, M. J. and Lamkin, J. C., Sample Calculations of Gamma-Ray Penetration into Shelters: Contribution of Skyshine and Roof Contamination, NBS 2827, February 1958.

16. Auxier, Buchanan, Eisenhauer, and Meuler, Experimental Evaluation of the Radiation Protection Afforded by Residential Structures against Distribution Sources, CEX-58.1, January 1959.

17. Shnider, R. W., Personnel Radiation Hazards Associated with Ships Immobilized by an Underwater Atomic Burst, USNRDL TR-5, February 1954. Secret R. D.

18. Cunningham, J. R., Wilson, R., and Bury, F. A., Protection Factors for Houses Using Radioactive Sources, DRCL 260.

19. Tomoeda, S., Kreger, W. E., Hastings, M. B., and Miller, W. G., Gamma-Ray Penetration into the Compartments of a Light Aircraft Carrier, USNRDL TR-343, July 1959.

19. RELATIVE CONTRIBUTIONS OF SCATTERED AND SECONDARY RADIATION INSIDE A REALISTIC CREW SHIELD

L. S. Burns, Jr.

General Electric Company
Aircraft Nuclear Propulsion Department
Evendale, Ohio

RELATIVE CONTRIBUTIONS OF SCATTERED AND SECONDARY RADIATION INSIDE A REALISTIC CREW SHIELD

by

L. S. Burns, Jr.

General Electric Company
Aircraft Nuclear Propulsion Department
Evendale, Ohio

Analytic calculations were made to compute the dose rate inside a crew shield as a function of energy of the emitted radiation and the angle of departure from the reactor shield. Scattering calculations were made by single scattering methods. Similarly, simplified calculations were made for (n,α) capture in air; inelastic scattering in air; thermal neutron capture in the crew shield; and thermalization of fast neutrons and capture of those neutrons in the crew shield. It is believed that this kind of study will prove highly useful in early planning stages of reactor shield design.

Last spring it became clear that the design phase of the ANP work was to undergo a major change. As a result of the change, it seemed wise to try and improve the technique of evaluating iterations in shield designs. The fault with the previous approaches lay in the nuclear criteria by which a design was judged to be good or bad. Designs were usually judged on the basis of the total dose rate at the front, side, and rear of a shield. These design points were generally chosen from experience or experiment and while they might well have been a fair criteria, a better criteria is clearly called for. In this study, an attempt was made to find a simple way to judge designs by evaluating the change in the dose rate inside of a realistic crew shield. It was known that it would not be possible to provide a completely general case for any crew shield but it was believed that if the total effect on the dose rate inside of a typical crew shield could be related to the type, energy and angle of emission of the radiation leaking from the reactor shield, this would be of benefit to shield designers. When Convair, Fort Worth, published the shield design of the CAMAL mission, the 54X-2 crew shield from their report was chosen as the typical crew shield for this study. In addition to the choice of the crew shield, the choice of separation distance from reactor center to crew shield was chosen to conform with the CAMAL study.

For this study, we have presented calculations for the principal known radiation contributors to the dose rate inside of the crew shield; air scattered gamma rays, air scattered neutrons, gamma rays from inelastically scattered neutrons, thermal neutron capture gammas from air, thermal neutron capture gammas in the crew shield, and the thermalization and capture of fast neutrons in the crew shield. The calculations that have been made are not necessarily the most accurate calculations that can be made today. They are typical of the

type of calculation currently performed by purely analytical methods. In the following dicussion of the methods used to achieve the curves presented in this report, we are simply point out the assumptions made and the techniques used in following out the calculations without embarking on a full scale methods-techniques discussion.

The scattering calculations of air-scattered neutrons and air-scattered gamma rays were made using the single scattered machine codes that have been in use in the GE-ANP Department[1] for some time. These programs are capable of calculating the dose rate at a shielded detector point in a homogeneous infinite medium from an anisotropic source. The source may be described by ten energy groups. The crew shield is assumed to be symmetrical about the source receiver axis and may be composed of one to five materials. For computing the neutron attenuation through the crew shield, it is necessary to provide the program with three relaxation lengths for each energy and each material used, one to be used through the shadow shield, one through the side wall of the crew shield, and one through the front wall. The relaxation lengths used were based on the total cross section of the crew shield materials at the average energy of the neutron arriving at the three sides of the crew shield after having been singly scattered from the beam of emerging monoenergy neutrons. The gamma ray scattering code requires fewer assumptions. The gamma ray code interpolates its own absorption coefficients from a table of coefficients and applies them to the impingent photons on the crew shield together with the buildup factors. From these codes we have calculated the dose rate inside the crew compartment from a conical beam of neutrons or gamma rays emitted from the reactor shield in a beam one degree wide. In both cases, it was assumed that there was no air attenuation.

The calculation of the gamma ray dose rate from inelastic scattering of neutrons was made using single scattering techniques with inelastic scattering cross sections replacing elastic scattering cross sections. The attenuation of the gamma rays entering the crew shield was entered as an exponential in the calculation just prior to the final summation of arriving dose rate over the polar angle at the detector. The neutron beam emitted from the reactor shield was treated as seven beams, each beam containing only those neutrons with energies in a one mev spectrum centered about 4, 5, 6, 7, 8, 9, and 10 Mev. The gamma rays excited by neutrons of these energies were computed by using the macroscopic inelastic cross sections from F. N. Watson[2]. The beam of neutrons emitted from the reactor shield was taken at several polar angles of emission thus providing the gamma ray dose rate inside of the shield from the angle of emission and the energy of the neutrons emitted from the reactor shield.

The calculation of the thermal neutron capture gamma rays from the nitrogen in the air was made by making some radical operations on the Monte Carlo work performed by Keller, Zerby, and Dunn[3]. The original work was done for an unshielded detector at separation distances of 25 and 65. This work was extrapolated at each energy and polar angle of emission to a distance of 93.5 feet. The extrapolation then provides new curves of dose rate versus angle of emission for several energies. These curves combined with curves showing the angles of arrival at the detector were used to compute the dose rate inside the crew shield. The angle of arrival of the dose rate at the detector was normalized to the total dose rate at the detector and the attenuation and buildup factors were applied at each angle. The result of these calculations are to provide dose rate inside of the crew shield as a function of the energy and angle of the emitted neutron.

Thermal capture in the crew shield walls was computed via the following route. First, the thermal flux arriving at the crew shield was computed by the method of R. Beissner[4] for the scattering of thermal flux in air. This flux was used to compute the flux inside the crew shield by assuming the flux outside of the shield represented an infinite plane source. The flux interior to the crew shield was transformed to the corresponding capture rates in the shield. These capture rates in each of the crew shield materials defined a gamma ray source strength, spectrum, and distribution in the shield. Using the kernel programs for attenuation through shields, a problem was set up in which the crew shield was considered to be the source,and the self shielding to the center of the shield was computed. Normalizing this calculation to the computations of the thermal flux arriving at the position of the crew box as a function of the angle of emission from the reactor shield yields the crew shield dose rate as a function of the angle of emission of the thermal neutrons.

The contribution of the fast neutrons thermalized and captured in the crew shield to the crew shield dose rate was computed by the following methods. First, a one dimensional, 19 level diffusion program was run. This program described the crew shield and its materials including the boron content of the crew shield. A source region of a monoenergetic source was described as the outside shell of a right circular cylinder representing the crew shield. This program was used to compute the flux from the single energy source along a radii of the cylinder. A flux was computed for each of the first six lethargy groups in turn or for fixed sources of 10 Mev, 6.0 Mev, 3.6 Mev, 2.2 Mev, 1.3 Mev, and .82 Mev. These fluxes were used to compute the capture rates in the hydrogen and boron in the crew shield. Again, as with the thermal capture problem in the air, this provided enough data to calculate with an attenuation kernel code, the dose rate at the center of the crew shield from the capture rates in the crew shield materials. The dose rate at the center of the shield was then associated with the air scattered fast neutron flux at the surface of the shield. This was done by computing the fast neutron flux at the surface, finding a point source in the source region of the diffusion program to give a flux equivalent to the fast neutron flux, deciding which energy group that flux most nearly fit into and normalizing the dose rate from that source energy to the flux outside the shield. Again, dose rate inside the shield was obtained as a function of the energy and angle leaving the reactor shield.

RESULTS

The final results of these calculations can be presented in two graphs; one for the dose rate inside of a crew shield as a result of the gamma rays that leave the reactor shield, and one for the dose rate inside of the crew shield as a result of the neutrons that leave the reactor shield. In both cases, we have the dose rate in rem/hr (using an RBE of 10) inside of the crew shield per source photon or neutron emitted/cm^2-sec within a conical beam one degree wide, where the angle is defined by the polar angle α. These curves may then be used as probabilities to determine the dose rate inside of the crew shield from any angular distribution or combination of angular and energy distributions. With a given angular distribution and spectrum emitted from the reactor shield, the dose rate inside of the crew shield becomes:

$$D(\rho,\alpha) = \rho^2 K\, f(E) \int_0^{\pi} D(\alpha,\rho)\, P(E,\alpha)\, dx$$

where $P(E,\alpha)$ = the dose rate inside of the crew shield in rem/hr-source neutron or photon-cm-sec, plotted for the angle of emission and the energy of departure from reactor shield.

$D(\rho,\alpha)$ = the neutron or gamma ray dose rate around the reactor shield at the polar angle α at ρ centimeters from the center of the core.

$f(E)$ = the fraction of the total dose rate in the energy interval $E - .5$ Mev $< E > E + .5$ Mev.

K = the dose rate to flux conversion.

ρ = the distance from the center of the core to the point at which the dose rate was computed.

While the greatest overall utility can be obtained by using these curves over a conical beam, in evaluating the effects of voids and other small disturbances in the overall pattern, a line beam that can be integrated over the solid angle of disturbance is needed. These probabilities can be applied to a line beam by dividing them by the area swept out by the conical beam:

$$2\pi \int_{\alpha}^{\alpha+1} \sin\alpha \, d\alpha$$

After this operation, the curves will approximate the probabilities for a line beam.

EVALUATION OF THE ACCURACY OF THE CURVES

The most obvious check on these calculations is to use them on the CAMAL system and make use of an entirely independent set of calculations. This was done. The overall crew compartment dose rate check was within a factor of two, with these calculations on the high side. The air scattering calculations for both gammas and neutrons were high. The calculation of crew shield capture secondaries was low by a factor of about 1.7. All things considered, this is a satisfactory agreement.

REFERENCES

1. "704 Program Report, Aircraft Nuclear Propulsion Shielding Program 10-0", J. W. Haffner, J. E. MacDonald, March 5, 1958.

2. LNP-NR-47 (1958), "The Significance of Two Recent Advances in Shielding Technology", Fifth Semi-annual ANP Shielding Information Meeting, Paper by F. N. Watson, May, 1958.

3. ORNL 2462, "Gamma Ray Dose Rates Resulting from Neutron Captures in Air", F. L. Keller, C. D. Zerby, W. W. Dunn, December, 1958

4. "A Study of Thermal Neutron Flux Distributions in Air", R. E. Beissner, Paper presented at the Fourth Semi-Annual ANP Shielding Information Meeting, November, 1957

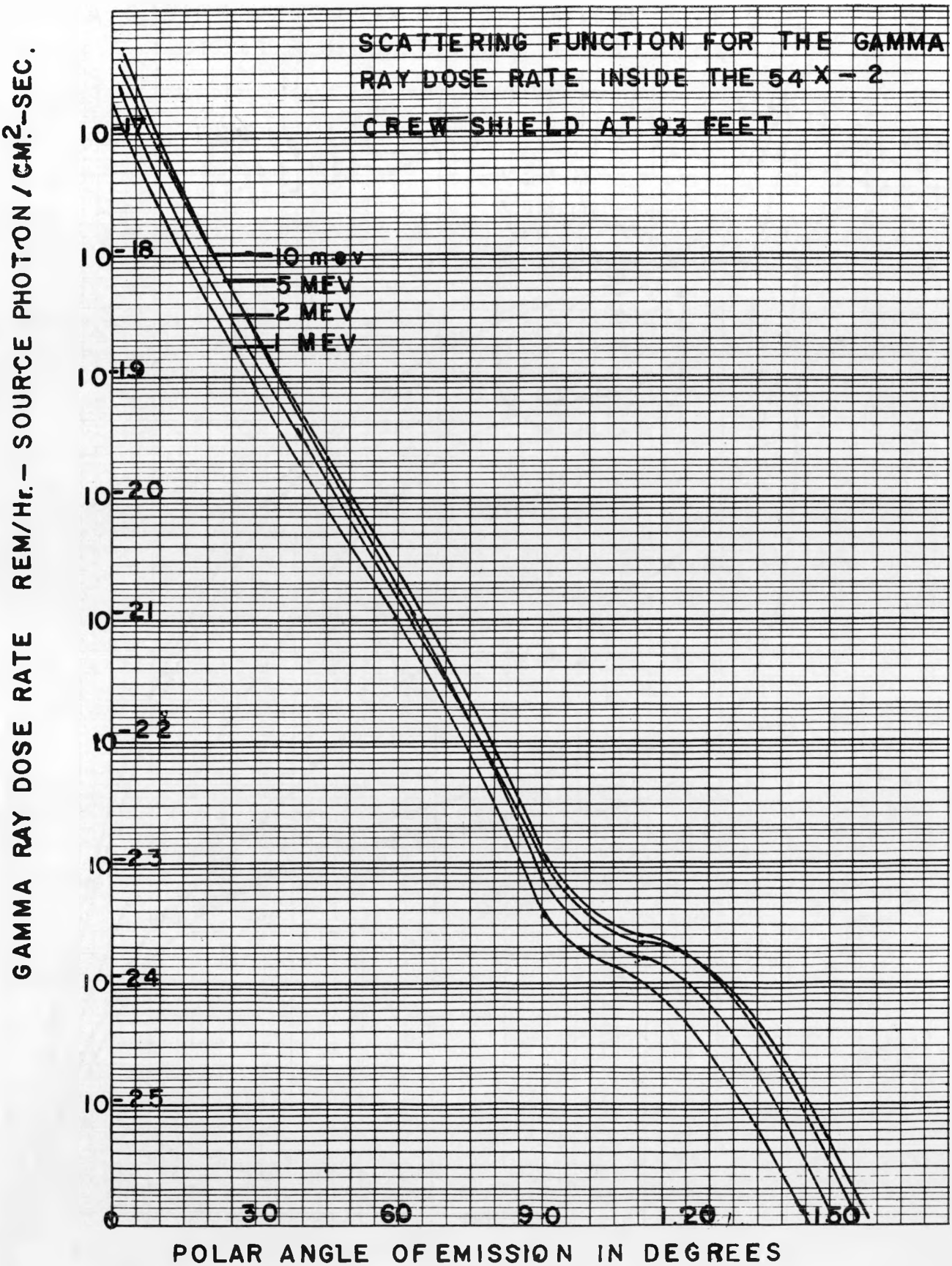
SCATTERING FUNCTION FOR THE GAMMA RAY DOSE RATE INSIDE THE 54 X – 2 CREW SHIELD AT 93 FEET
10 MEV
5 MEV
2 MEV
1 MEV
10-17
10-18
10-19
10-20
10-21
10-22
10-23
10-24
10-25
0
30
60
90
120
150
GAMMA RAY DOSE RATE REM/Hr. – SOURCE PHOTON / CM.2-SEC.
POLAR ANGLE OF EMISSION IN DEGREES

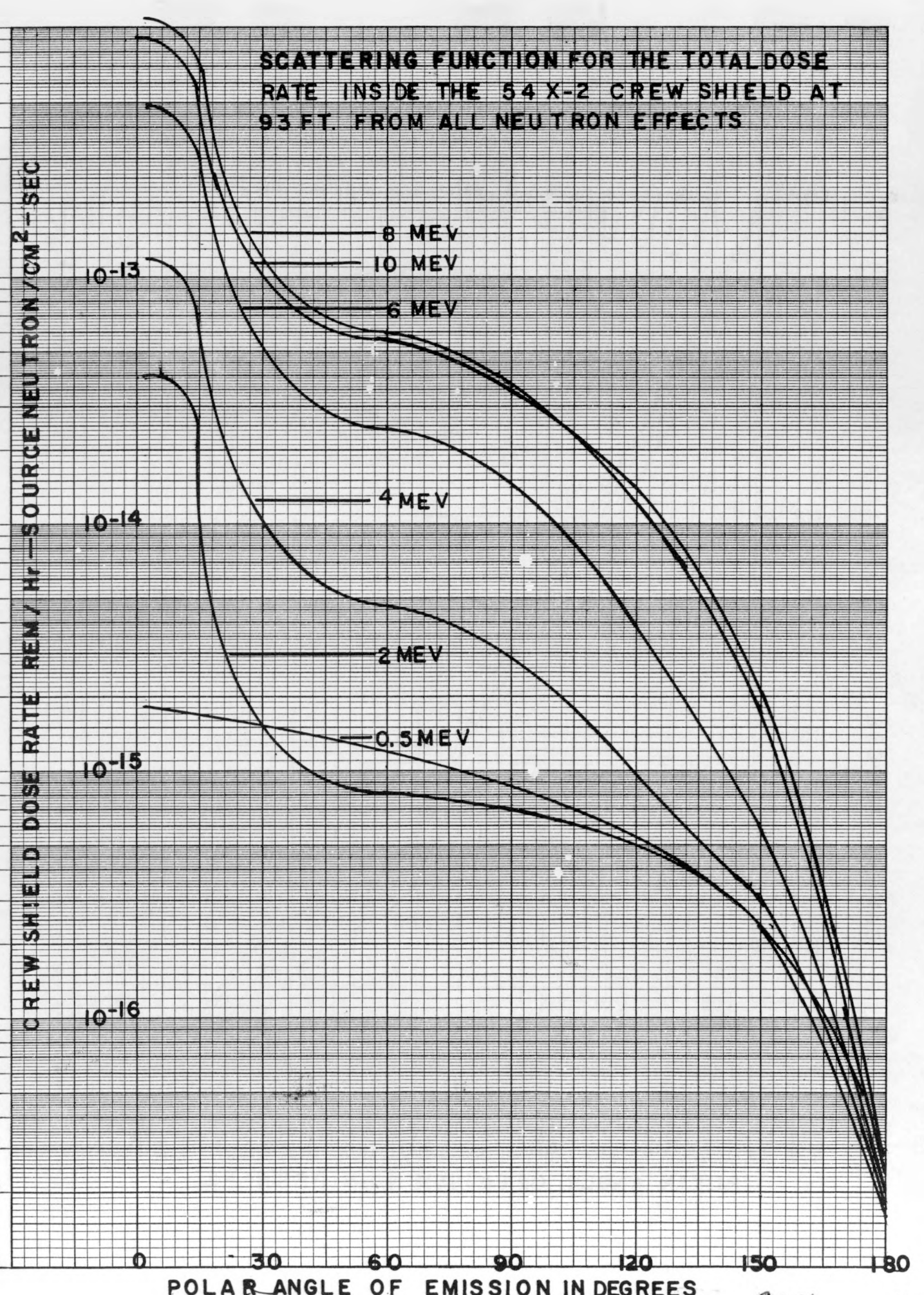
SCATTERING FUNCTION FOR THE TOTAL DOSE RATE INSIDE THE 54 X-2 CREW SHIELD AT 93 FT. FROM ALL NEUTRON EFFECTS
CREW SHIELD DOSE RATE REM/Hr—SOURCE NEUTRON/CM²—SEC
10-13
10-14
10-15
10-16
8 MEV
10 MEV
6 MEV
4 MEV
2 MEV
0.5 MEV
0
30
60
90
120
150
180
POLAR ANGLE OF EMISSION IN DEGREES

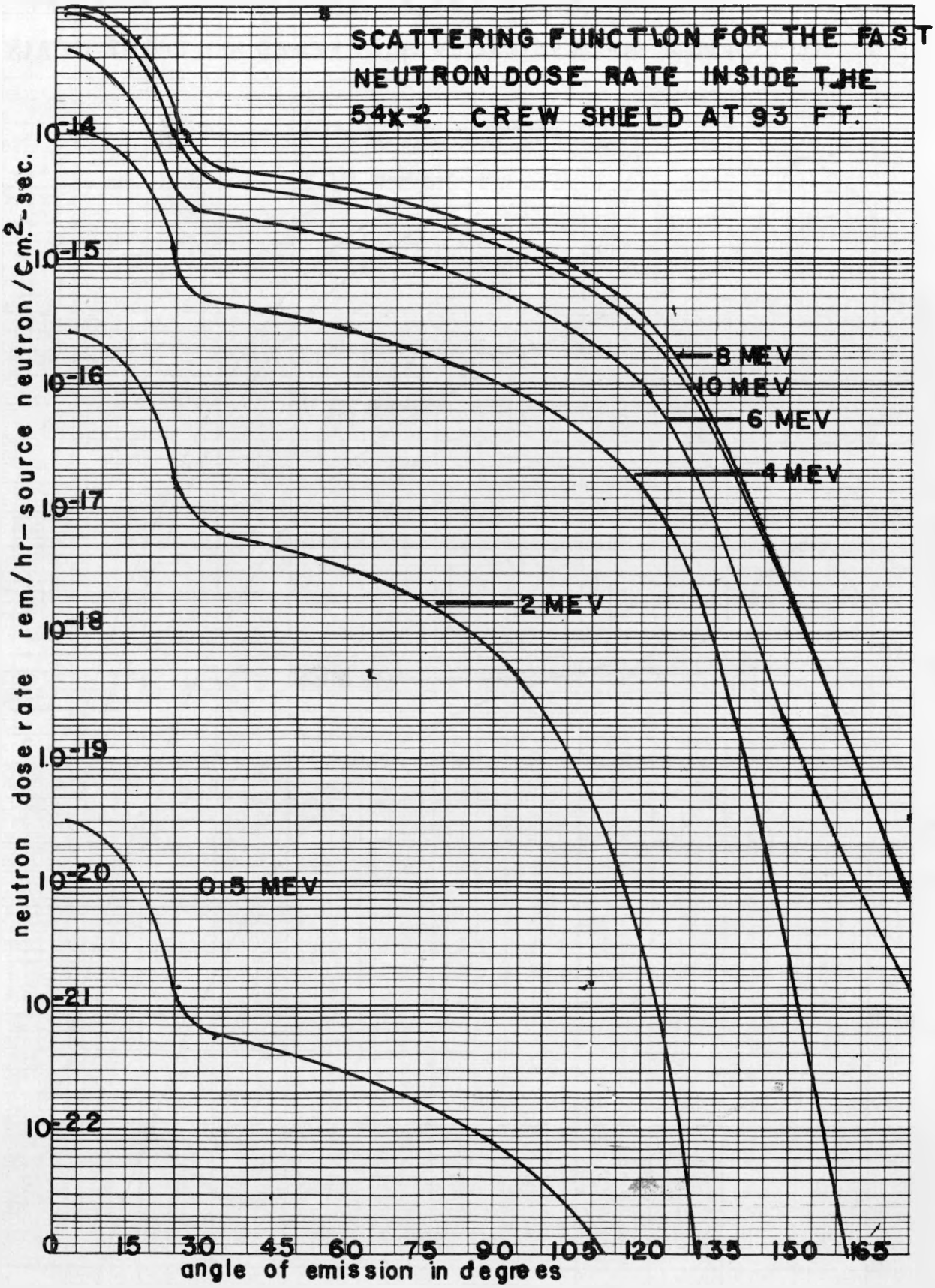
SCATTERING FUNCTION FOR THE FAST NEUTRON DOSE RATE INSIDE THE 54X-2 CREW SHIELD AT 93 FT.
neutron dose rate rem/hr-source neutron/Cm.²-sec.
10⁻¹⁴
10⁻¹⁵
10⁻¹⁶
10⁻¹⁷
10⁻¹⁸
10⁻¹⁹
10⁻²⁰
10⁻²¹
10⁻²²
8 MEV
10 MEV
6 MEV
4 MEV
2 MEV
0.5 MEV
0
15
30
45
60
75
90
105
120
135
150
165
angle of emission in degrees

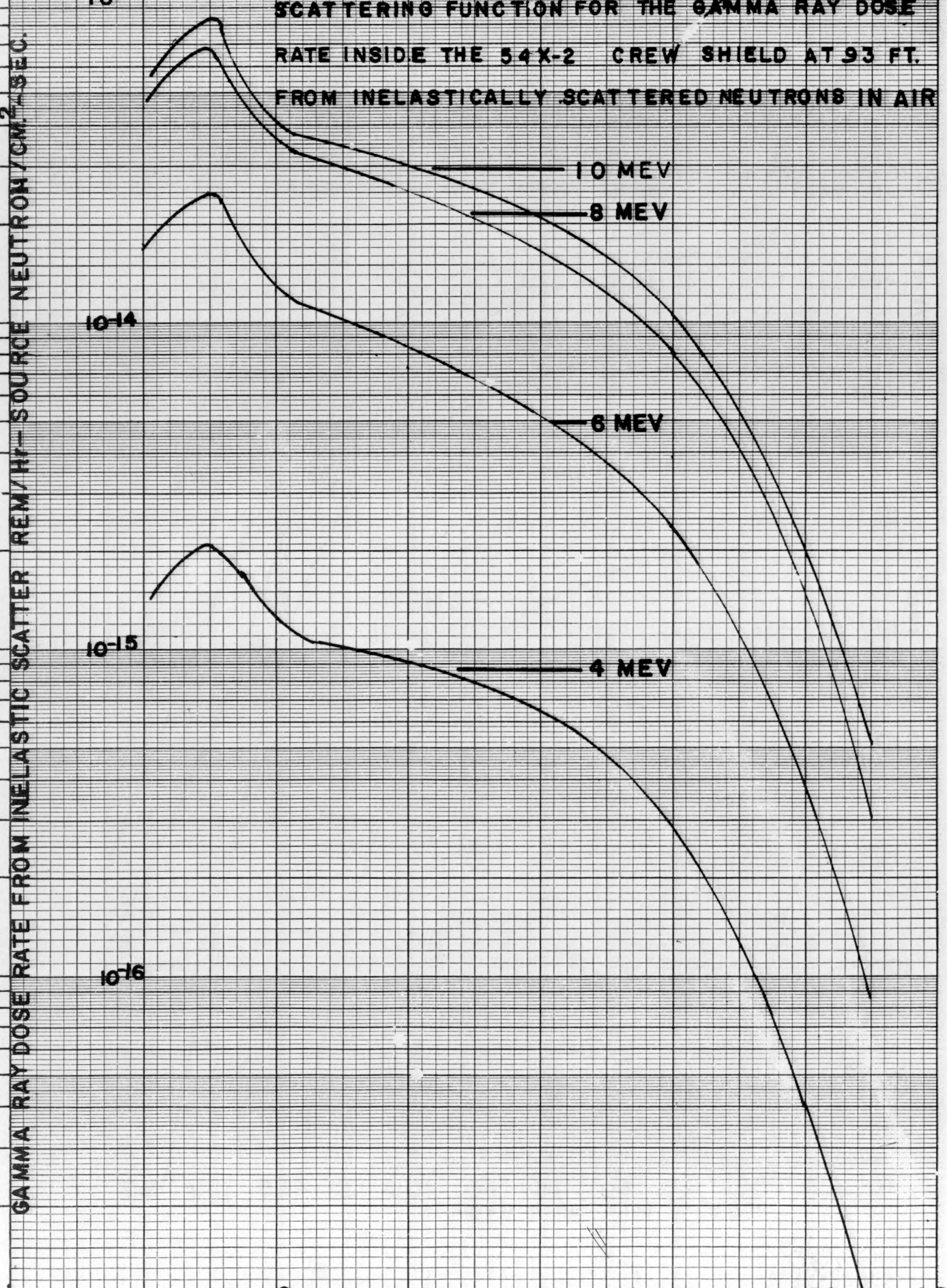
SCATTERING FUNCTION FOR THE GAMMA RAY DOSE
RATE INSIDE THE 54X-2 CREW SHIELD AT 93 FT.
FROM INELASTICALLY SCATTERED NEUTRONS IN AIR
10 MEV
8 MEV
6 MEV
4 MEV
10^{-14}
10^{-15}
10^{-16}
GAMMA RAY DOSE RATE FROM INELASTIC SCATTER REM/HR—SOURCE NEUTRON/CM.²SEC.

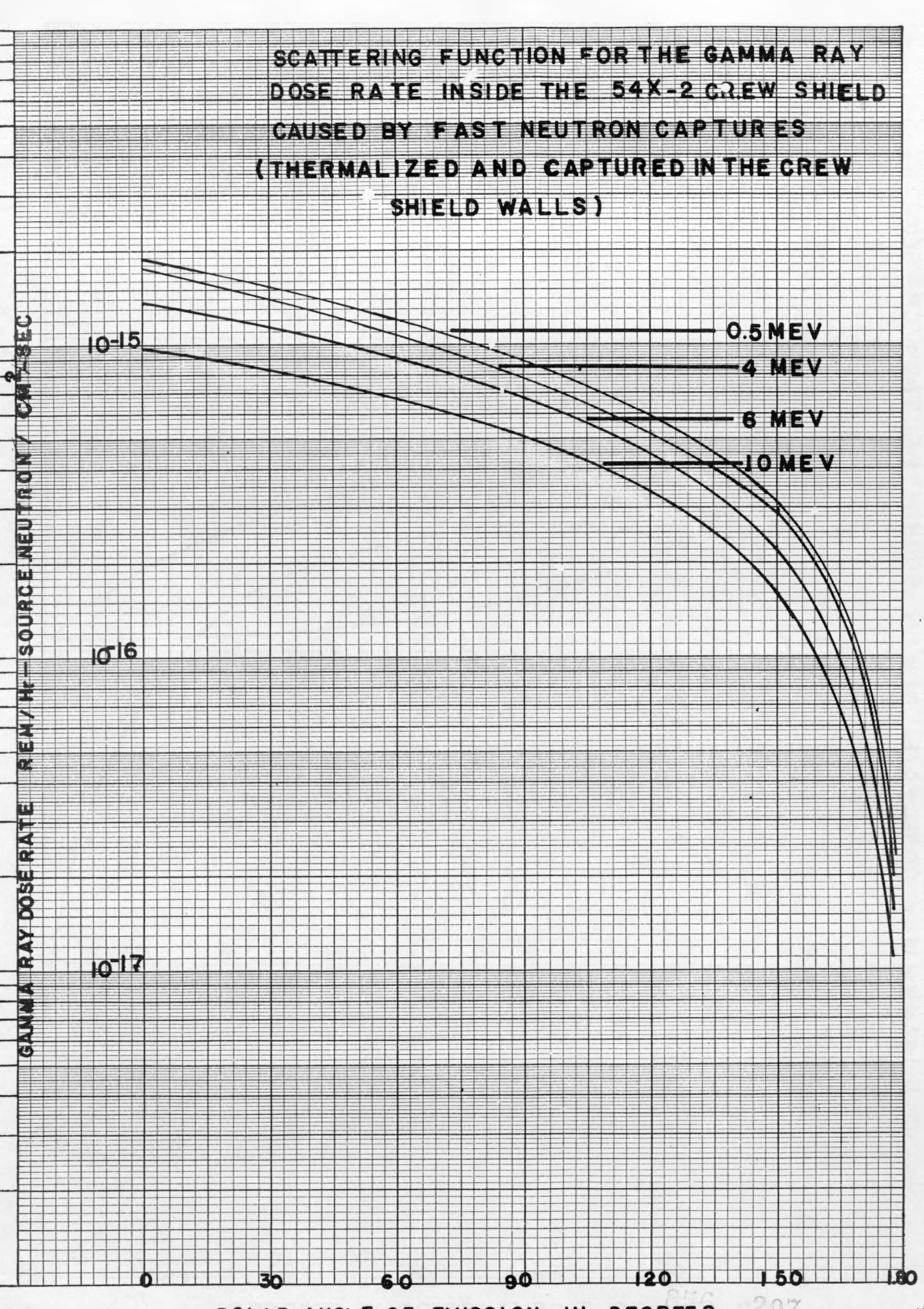
SCATTERING FUNCTION FOR THE GAMMA RAY DOSE RATE INSIDE THE 54X-2 CREW SHIELD CAUSED BY FAST NEUTRON CAPTURES (THERMALIZED AND CAPTURED IN THE CREW SHIELD WALLS)
GAMMA RAY DOSE RATE REM/Hr—SOURCE NEUTRON / CM^2-SEC
10^{-15}
10^{-16}
10^{-17}
0.5 MEV
4 MEV
6 MEV
10 MEV
0
30
60
90
120
150
180

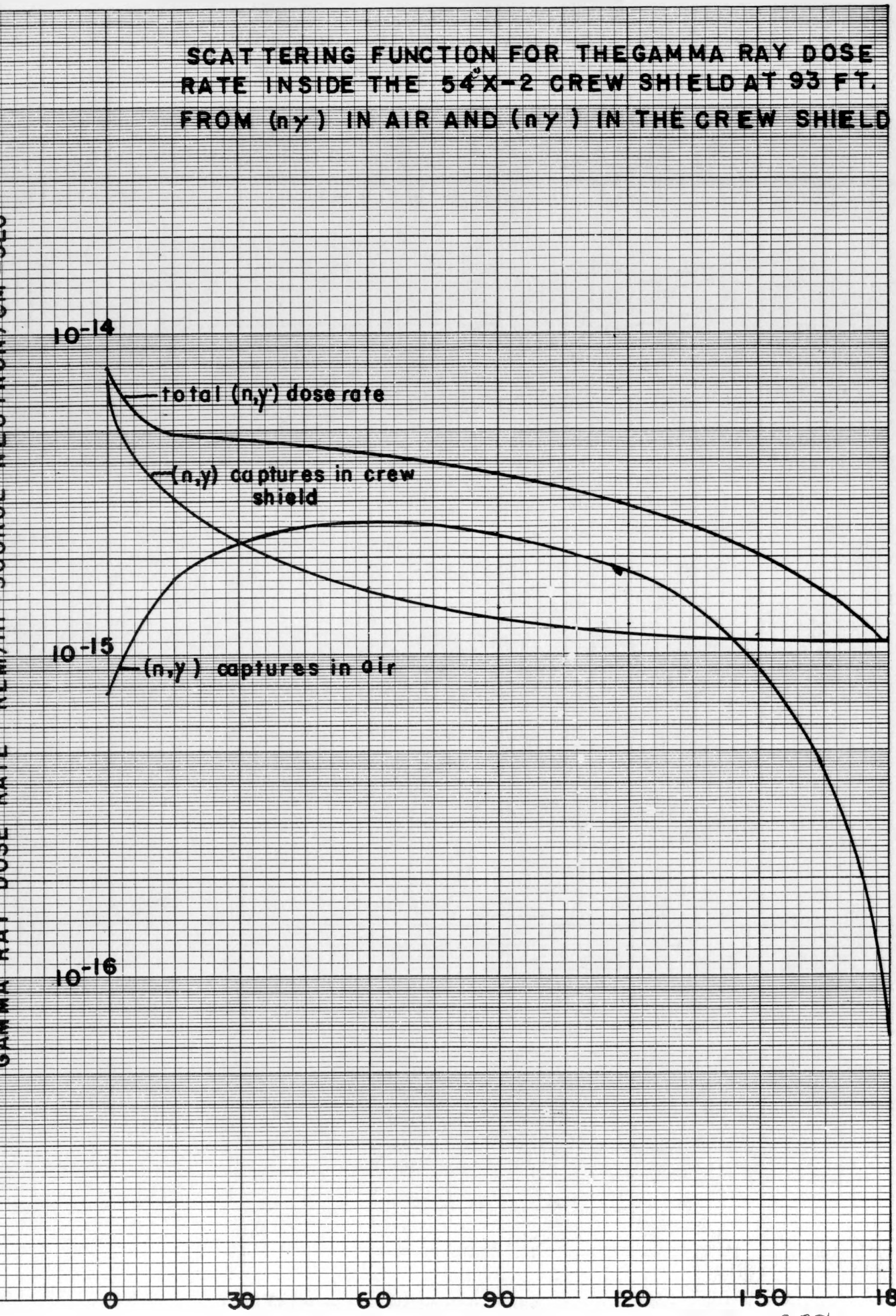
SCATTERING FUNCTION FOR THE GAMMA RAY DOSE RATE INSIDE THE 54° X-2 CREW SHIELD AT 93 FT. FROM (nγ) IN AIR AND (nγ) IN THE CREW SHIELD
GAMMA RAY DOSE RATE (REM/HR) PER UNIT SOURCE STRENGTH
10-14
10-15
10-16
total (n,γ) dose rate
(n,γ) captures in crew shield
(n,γ) captures in air
0
30
60
90
120
150
180
POLAR ANGLE OF EMISSION IN DEGREES

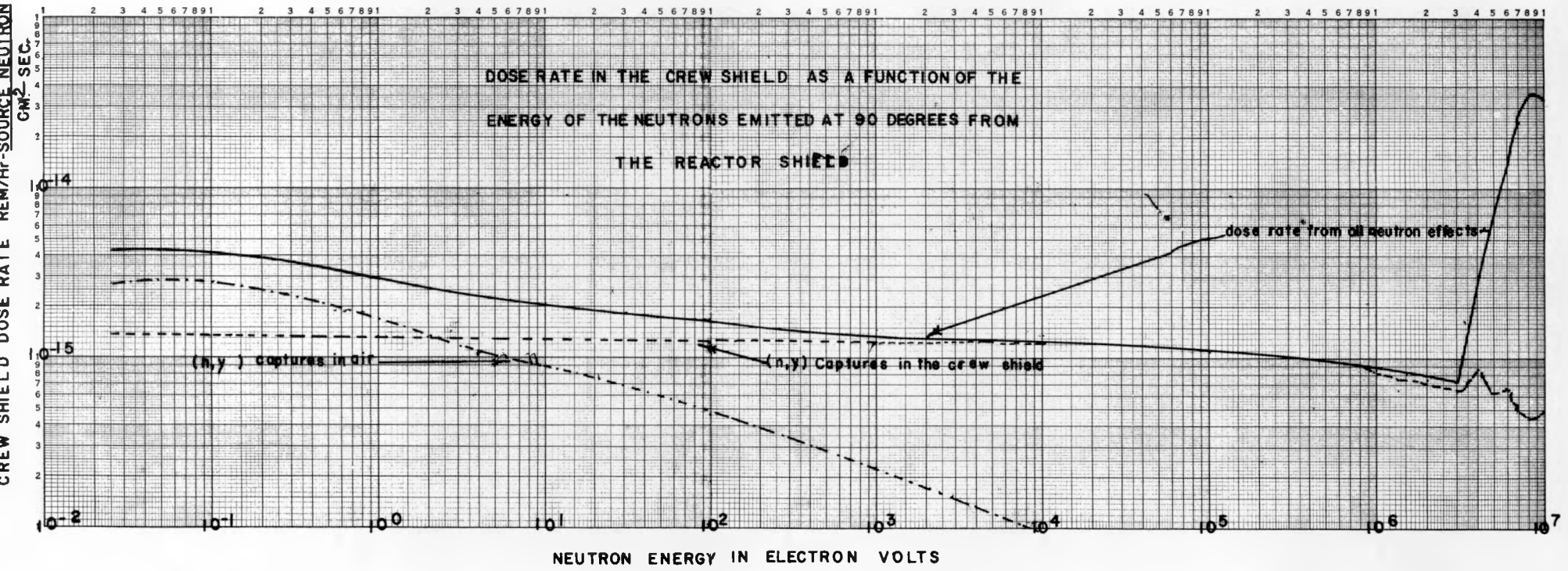
DOSE RATE IN THE CREW SHIELD AS A FUNCTION OF THE
ENERGY OF THE NEUTRONS EMITTED AT 90 DEGREES FROM
THE REACTOR SHIELD
dose rate from all neutron effects
(n,γ) captures in air
(n,γ) Captures in the crew shield
CREW SHIELD DOSE RATE REM/HR-SOURCE NEUTRON CM.² SEC.
NEUTRON ENERGY IN ELECTRON VOLTS

20. COMPARISON OF CALCULATED AND MEASURED WATER CENTERLINE DATA

A. W. Casper

General Electric Company
Aircraft Nuclear Propulsion Department
Evendale, Ohio

COMPARISON OF CALCULATED AND MEASURED WATER CENTERLINE DATA

by

A. W. Casper

General Electric Company
Aircraft Nuclear Propulsion Department
Evendale, Ohio

Dose rates and thermal fluxes have been measured in water both at the ORNL Bulk Shielding Facility and at the GE Source Plate Facility at Battelle Memorial Institute. The measured values are compared with point kernel calculations of the dose rates and thermal fluxes calculated by a combined diffusion theory - point kernel approach.

COMPARISON OF WATER CENTERLINE MEASUREMENTS WITH PREDICTIONS

The purpose of this study is to compare computations of attenuation of radiation in water with experimental measurements. Measurements made in water at the Bulk Shielding Facility at ORNL[1] are used in this study. Recent measurements of attenuation of radiation in water made at the GE-ANPD Source Plate Facility at BMI are also used.

The data taken at the Bulk Shielding Facility were measurements made in a large tank of water on the centerline of the Bulk Shielding Reactor. The large tank of water makes the infinite medium assumption used in the programs reasonable. The Bulk Shielding Reactor configuration was loading number 33. Figure 1 is a schematic representation of this reactor loading.

Programs now available[2,3] permit a wide variety of source descriptions. Program 04-2 permits only cylindrical source descriptions. In order to use this program, the rectangular source was replaced by an equivalent cylindrical source. The equivalent cylindrical source had the same length, volume, and uranium density as the actual source. Program 14-0 made it possible to describe the source as a set of 28 parallel lines located at the center of the actual fuel elements. The power distribution along these lines was made as nearly as possible that of the fuel elements. A third power description made use of Program 04-1 which allows a rectangular source description. This program makes it possible to use the given Bulk Shielding Reactor information in an accurate description of the power distribution. It was found that small differences in power distribution lead to large differences in computed gamma dose.

Measurements of both fast neutron dose rates and gamma dose rates are compared with computed values in Figure 2. At distances of 30 cm or greater, the measured fast neutron dose rates are 20 to 30 per cent greater than the computed values. The computed gamma dose rates include the 2.23 Mev secondary gamma dose rates from hydrogen. Measured values of axial thermal neutron flux were fitted by exponential functions and used as source terms. The computed gamma dose rate curve has a slightly steeper slope than a curve drawn through the measured gamma dose rates would have.

Figure 3 compares the computed gamma dose rates using each of the three source descriptions with the measured gamma dose rates. The cylindrical source description is the least accurate and gives results which differ most from the measurements. Programs 04-1 and 14-0 with their rectangular and line source descriptions, respectively, give better agreement with measurements than the cylindrical description.

Figure 4 compares the computed fast neutron dose rates with measurements. The graph compares fast neutron dose rates computed using Programs 04-1 and 14-0 with measurements. The cylindrical source description gives results almost identical with Program 04-1, and this is not shown in the figure.

Measurements were also made in the pool adjacent to the source plate at the GE-ANPD Source Plate Facility at Battelle Memorial Institute[4]. The pool is large enough so that the infinite medium assumption is reasonable. The active core of the source plate is a cylindrical plate about .02 inches thick and 28 inches in diameter consisting of uranium-235 of 93 per cent enrichment. Hence, the source can be accurately described in the point kernel programs as a plane circular source.

Figure 5 compares computed fast neutron dose rates, gamma dose rates, and thermal neutron flux with measurements. The measured fast neutron dose rates are 20 to 30 per cent greater than the computed values. Computed gamma dose rates include the secondary gamma dose rate contribution from hydrogen. The computed gamma dose rate curve has a slightly steeper slope than a curve drawn through the measured gamma dose rates would have. These two effects are similar to those observed in the comparison of computations with measurements made at the Bulk Shielding Facility. There is some indication that gamma dose rate measurements made with single ion dosimeters will be in better agreement with computed values.

The thermal neutron flux is computed by use of Program G-2[5] modified for shielding calculations. The thermal neutron to fast neutron ratio obtained from Program G-2 is used in conjunction with the fast neutron dose rates obtained from the point kernel programs to determine the thermal neutron flux. The computed values are about a factor of 2 low. These results are consistent with some earlier results by J. W. Haffner[6].

Adjustments in the kernels are being studied. It is hoped that these studies will lead to even better agreement between measured and computed dose rates in water.

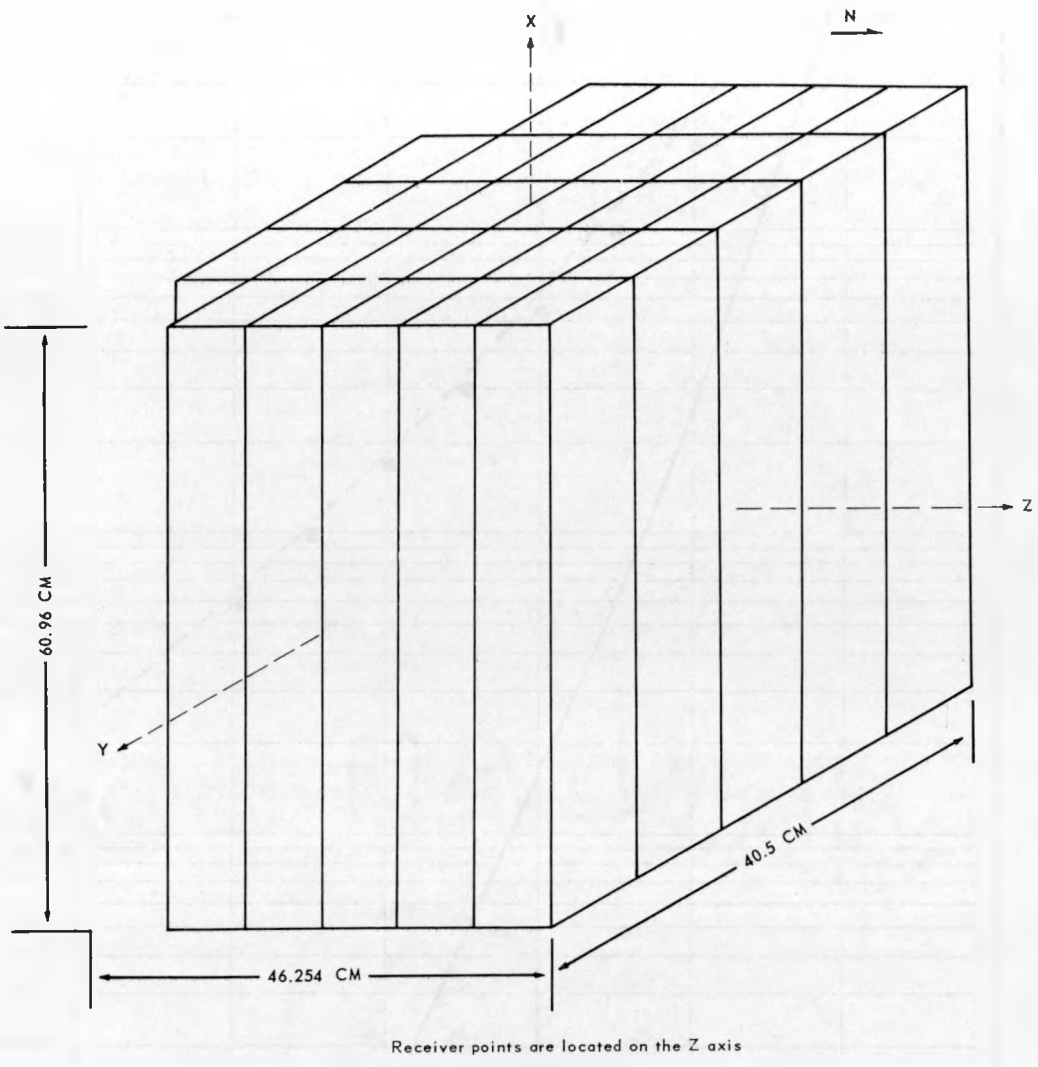

Fig. 1 – Schematic representation of the Bulk Shielding Reactor, loading number 33

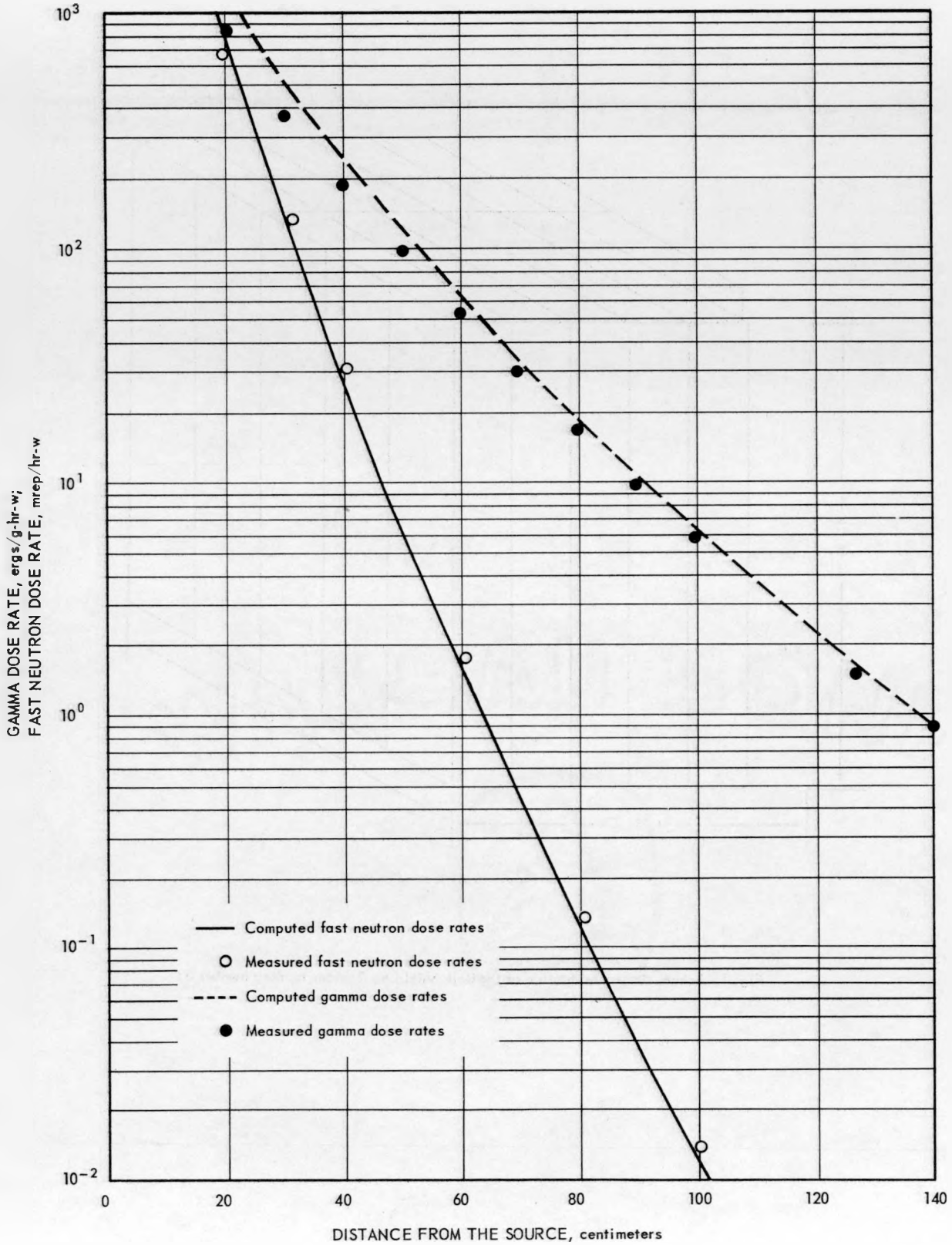

Fig. 2 – Attenuation of radiation on the centerline of the Bulk Shielding Reactor at ORNL

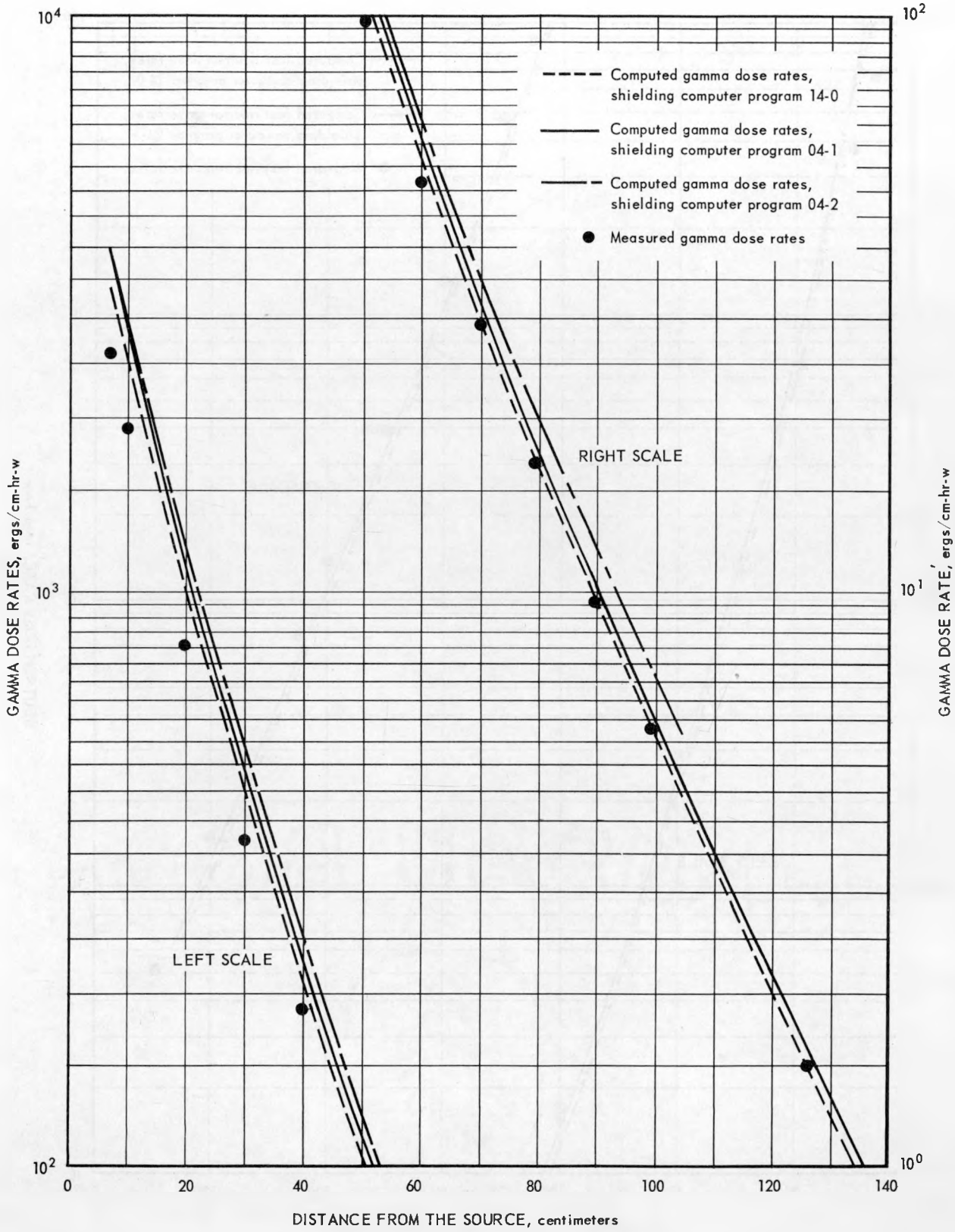

Fig. 3 – Gamma dose rates on the centerline of the Bulk Shielding Reactor at ORNL

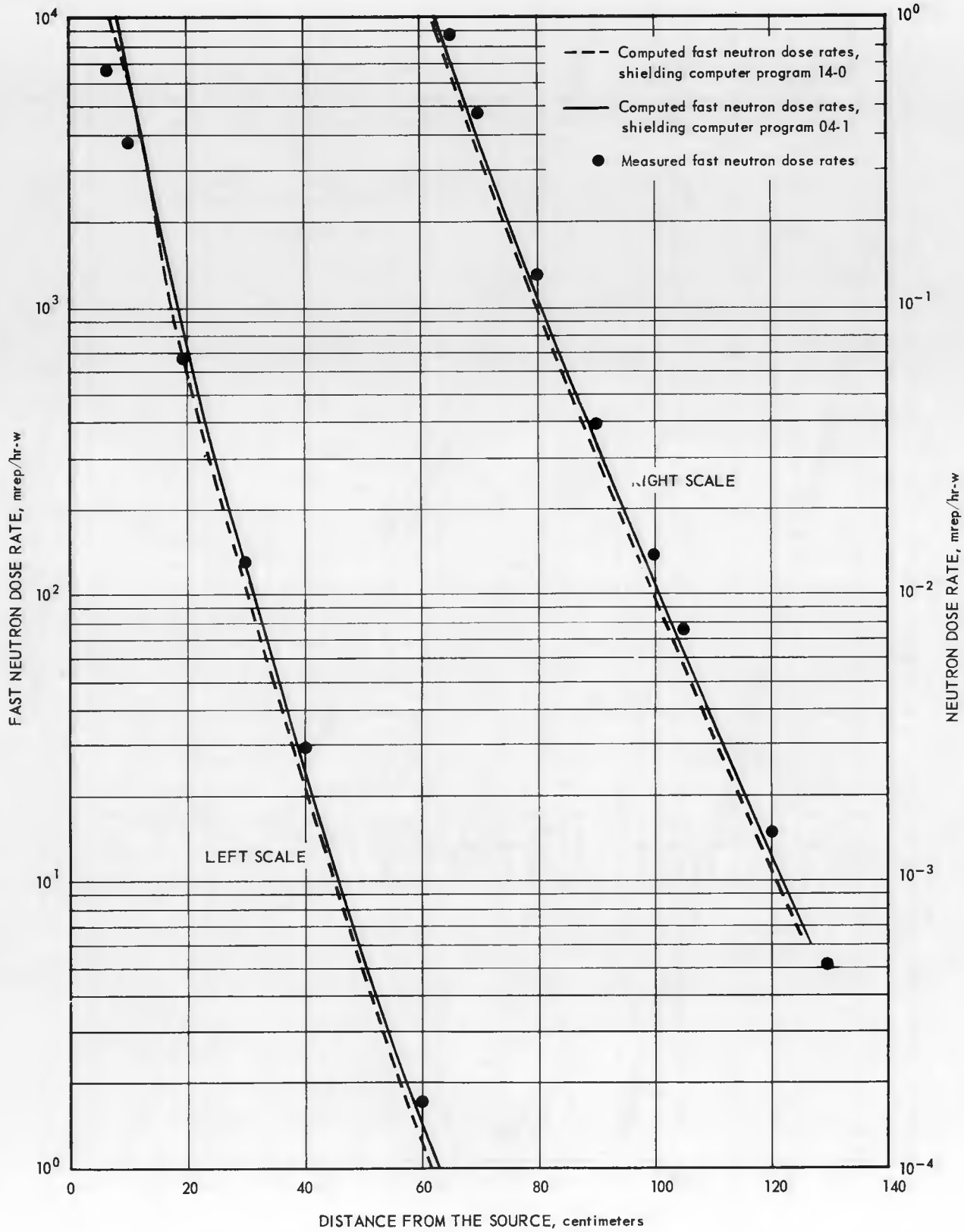

Fig. 4 – Fast neutron dose rates on the centerline of the Bulk Shielding Reactor at ORNL

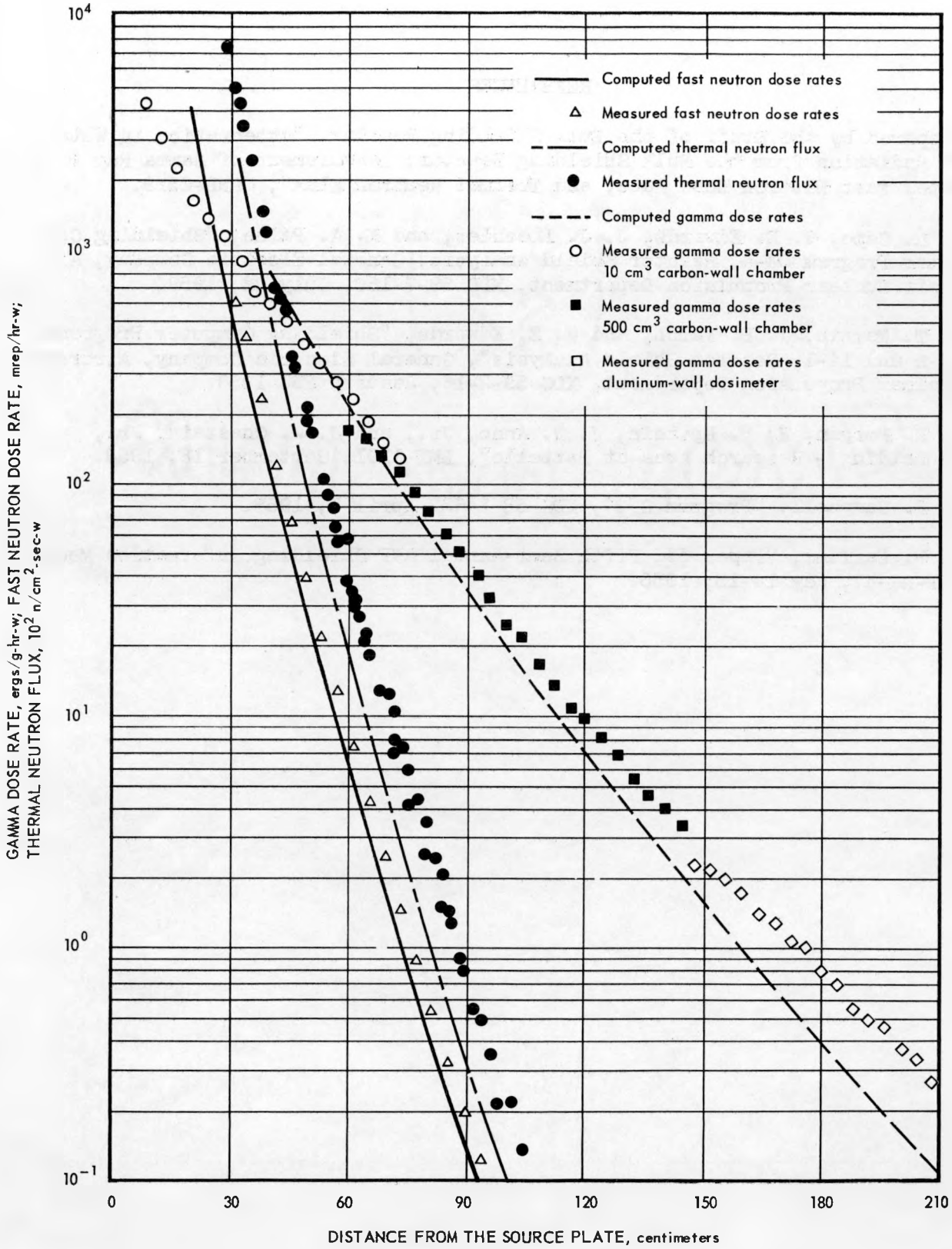

Fig. 5 – Attenuation of radiation on the centerline of the GE-ANPD source plate at Battelle Memorial Institute

REFERENCES

1. Prepared by the Staff of the Bulk Shielding Reactor, "Attenuation in Water of Radiation from the Bulk Shielding Reactor; Measurement of Gamma Ray Dose Rate, Fast Neutron Dose Rate, and Thermal Neutron Flux", ORNL-2518.

2. M. A. Capo, W. E. Edwards, J. J. Loechler, and K. A. Paine, "Shielding Computer Program 04-4, Reactor Shield Analysis", General Electric Company, Aircraft Nuclear Propulsion Department, XDC 59-7-150, July 22, 1959.

3. J. T. Martin, J. P. Yalch, and W. E. Edwards, "Shielding Computer Programs 14-0 and 14-1, Reactor Shield Analysis", General Electric Company, Aircraft Nuclear Propulsion Department, XDC 59-2-16, January 23, 1959.

4. W. R. Morgan, H. M. Epstein, J. N. Anno, Jr., and J. W. Chastain, Jr., "Shielding - Research Area at Battelle", BMI-1291, September 18, 1958.

5. D. J. Campbell, "Program G-2", XDC 58-4-63, April 5, 1958.

6. J. W. Haffner, "Paper 33, Fifth Semi-Annual ANP Shielding Information Meeting", LNP-NR-47, May 14-15, 1958.

21. CALCULATION OF NEUTRON SPECTRA FROM SLOWING DOWN MODELS

A. H. Barnett
J. R. Terrall

General Electric Company
Aircraft Nuclear Propulsion Department
Evendale, Ohio

CALCULATION OF NEUTRON SPECTRA FROM SLOWING DOWN MODELS

A. H. Barnett
J. R. Terrall
General Electric
Aircraft Nuclear Propulsion Department

14 September 1959

Abstract

Neutron slowing down models have for a long time been very useful to the reactor physicist in the calculation of neutron energy spectra, and perhaps they might be useful to the shield physicist. A slowing down model is a simple representation of the angle-integrated Boltzmann equation whereby energy loss in collisions is taken into account in some kind of approximation (which may be made quite good). Probably the greatest advantage in using a slowing down model lies in its replacement by a simple first order differential equation in energy, of the original integral equation for which there are no known mathematical methods of obtaining a solution in closed form. From this differential equation, explicit solutions for flux spectra can be calculated. The purpose of the investigation reported here is to exhibit several slowing down models, and to give an idea of their accuracy.

Slowing down models have for a long time been very useful to the reactor physicist in the calculation of neutron energy spectra, and perhaps they might be useful to the shield physicist. A slowing down model is a simple representation of the angle-integrated Boltzmann equation, together with the equation for slowing down density, whereby the redistribution of neutrons in energy, due to collisions, is accounted for in some kind of approximation which may be made quite good.

Whereas the flux-in-energy is almost directly proportional to all the up and down variations in energy of the neutron mean free path, there is a quantity whose variation is much gentler. This quantity is the number of neutrons, per unit volume per unit time, which slow down past a given energy as a result of collisions.

Without going into the lengthy details of the origin of the slowing down model equations, we will merely present them in order to demonstrate their utility. If we let $q(\vec{r},E)$ represent the number of neutrons in a volume element surrounding $\vec{r}$, which slow down, per unit time, past energy E then the model equations can be written:

$$-E\frac{\partial q}{\partial E} + \frac{\rho}{\lambda+\rho}\frac{\lambda}{\xi}q = \frac{\lambda}{\lambda+\rho}S$$

$$E\Sigma_s\phi = \frac{1}{\lambda+\rho}\frac{\lambda}{\xi}q + \frac{1}{\lambda+\rho}S$$

he great advantage of a model of this kind lies in its replacing the original ntegral equation in energy by a simple first order differential equation.

All quantities are functions of space location and of energy. Here ϕ is he angle-integrated flux of the Boltzmann equation:

$$\phi(\vec{r},E) \equiv \oint \Phi(\vec{r},E,\hat{\Omega})\,d\Omega$$

is a source of neutrons, Σ_s is the scattering probability, per unit length of ath, in the medium at $\vec{r}$, and λ and ξ are dimensionless functions of the icroscopic scattering cross sections which can be defined, for a given accuracy f over-all results, when the scattering properties (whatever they may be) of he medium are specified. In the case of scattering which is elastic, isotropic n the neutron-nucleus center-of-mass system, and constant in energy ξ reduces o the familiar reactor parameter — average loss in the logarithm of the neutron nergy in a scattering collision.

There are various models which can be devised, differing in their specifica- ion of the quantity λ. This quantity embodies the basic approximations in nergy.

Model	λ	λ (Hydrogen)	λ (Heavy nuclear mass A)
Modified Age (MA)	ξ	1	A/2
Wigner (W)	1	1	1
Greuling-Goertzel (GG)	ξ/γ	1	3/2
Fermi (F)	∞	∞	∞

fifth model has been devised at GE-ANPD but it is not shown since it is some- hat complicated for elements other than hydrogen.

The quantity ρ is defined in terms of absorption losses and the space deriva- ives of the directional current (transport losses), as they compare with the cattering density:

$$\rho \equiv [\Sigma_a\phi + \nabla\cdot\vec{J}\,]/\Sigma_s\phi = \Sigma_a/\Sigma_s + \nabla\cdot\vec{J}/\Sigma_s\phi.$$

Now, strictly speaking, we don't know ρ unless we have solved the Boltzmann equation in all its gory detail. However we are not totally in the dark because we can often make a shrewd guess about $\vec{J}$ by using our physical knowledge to define a quantity D, in terms of what we know about the neutrons' environment, such that

$$\vec{J}(\vec{r},E) \approx -D(\vec{r},E)\nabla\phi(\vec{r},E).$$

For some special modes of the spacial behavior of the flux, the current part of ρ will be independent of the flux and we can consider it as a given (space-and-energy-varying) parameter. This will allow us to find the energy spectrum $\phi(\vec{r},E)$ as it depends on this parameter. In other cases the current part will be small enough that errors in its specification will not be too strongly felt.

Since the slowing down models are only approximations, we should require that they pass certain minimum requirements. The simplest calculable case is that in which scattering is assumed to be elastic and isotropic in the neutron-nucleus center of mass system. Figures 1, 2, and 3 show the accuracy obtained by five different slowing down model calculations of neutron flux-in-energy in a reactor in which there is a fission source. If our reactor is assumed to be of homogeneous composition the flux escaping has the same variation in neutron energy as the flux in any particular volume element inside. (The magnitude, of course, depends on space location.)

The ratio curves plotted in the figures are to be considered as measures of accuracy while the flux ($\phi(E)$) curves show the relative importance of inaccuracies. For simplicity the parameter ρ has been assigned just two values — 0.01 and 0.10. Many cases of physical interest have values varying within this range.

Results for hydrogen moderation are not shown because, for this element, all the models except the Fermi model are exact (in the case of CMS-isotropic elastic scattering). Three elements, namely deuterium, lithium, and beryllium are shown, in order that certain trends with increasing moderator mass number can be inferred. We notice that the Wigner model is not more than about thirteen percent in error for the cases calculated. Also, as this model begins to deviate, thinking in terms of increasing moderator mass, the Greuling-Goertzel and T models get better (as does also the Fermi model, which is to be expected since it was devised specifically for moderators of high nuclear mass number). The Fermi model has been shown in the figures in order to demonstrate to just what extent a really simple picture can be relied on. As can be seen, it is not too accurate for the elements considered here.

In Figures 4, 5, and 6 we show calculations for regions in which there is no source, in contrast to Figures 1, 2, and 3. Here we have asked the question "What is the accuracy of the models given a certain number of neutrons slowing down past a given energy E_1?" Notice that the error scale is quite enlarged. The Wigner model is not too bad although the GG and T models are superior, especially for large losses.

Figure 1

NEUTRON SLOWING DOWN MODEL APPROXIMATIONS
IN THE CALCULATION OF DEUTERIUM MODERATED REACTOR FLUX

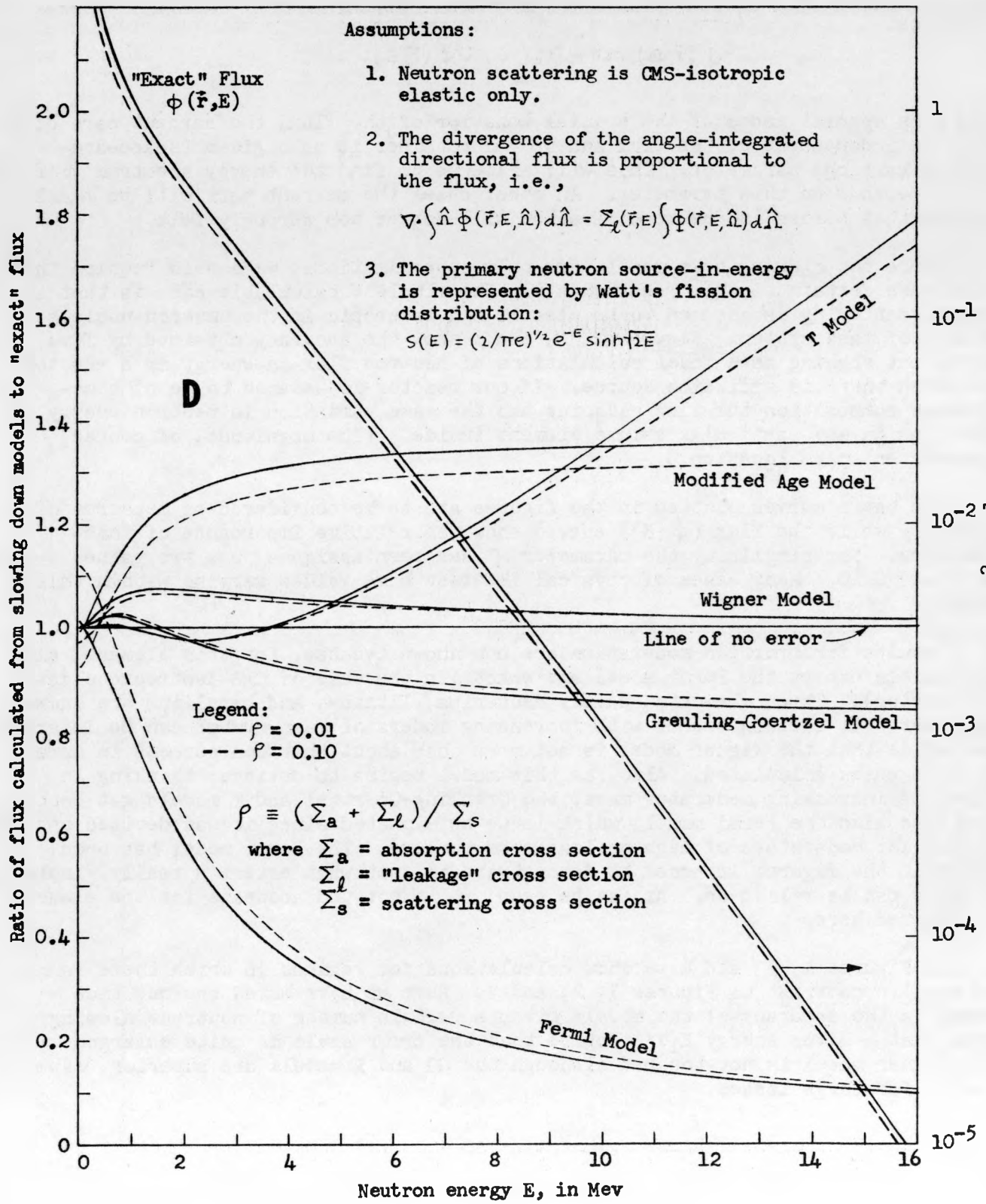

Figure 2

NEUTRON SLOWING DOWN MODEL APPROXIMATIONS
IN THE CALCULATION OF LITHIUM MODERATED REACTOR FLUX

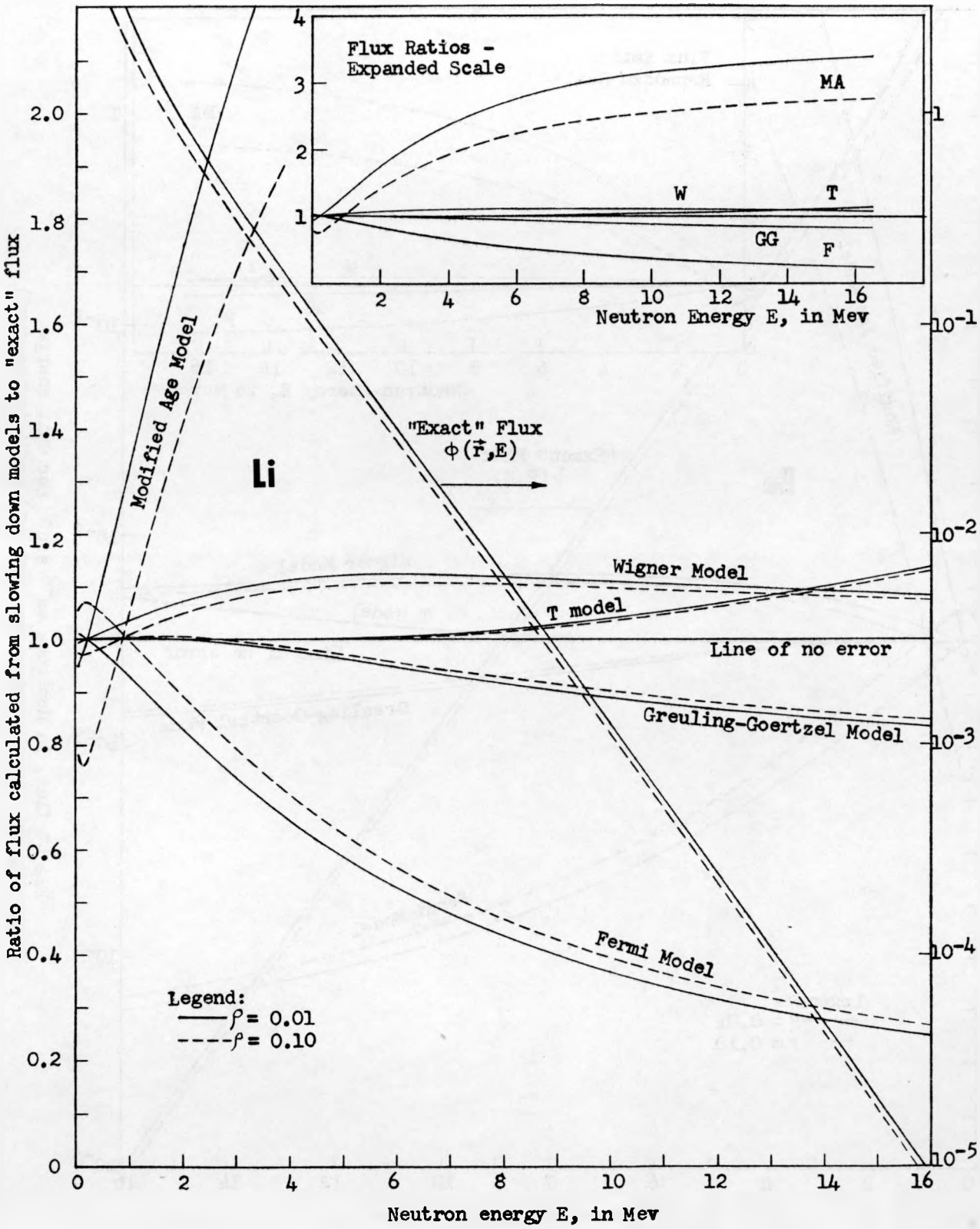

Figure 3

NEUTRON SLOWING DOWN MODEL APPROXIMATIONS
IN THE CALCULATION OF BERYLLIUM MODERATED REACTOR FLUX

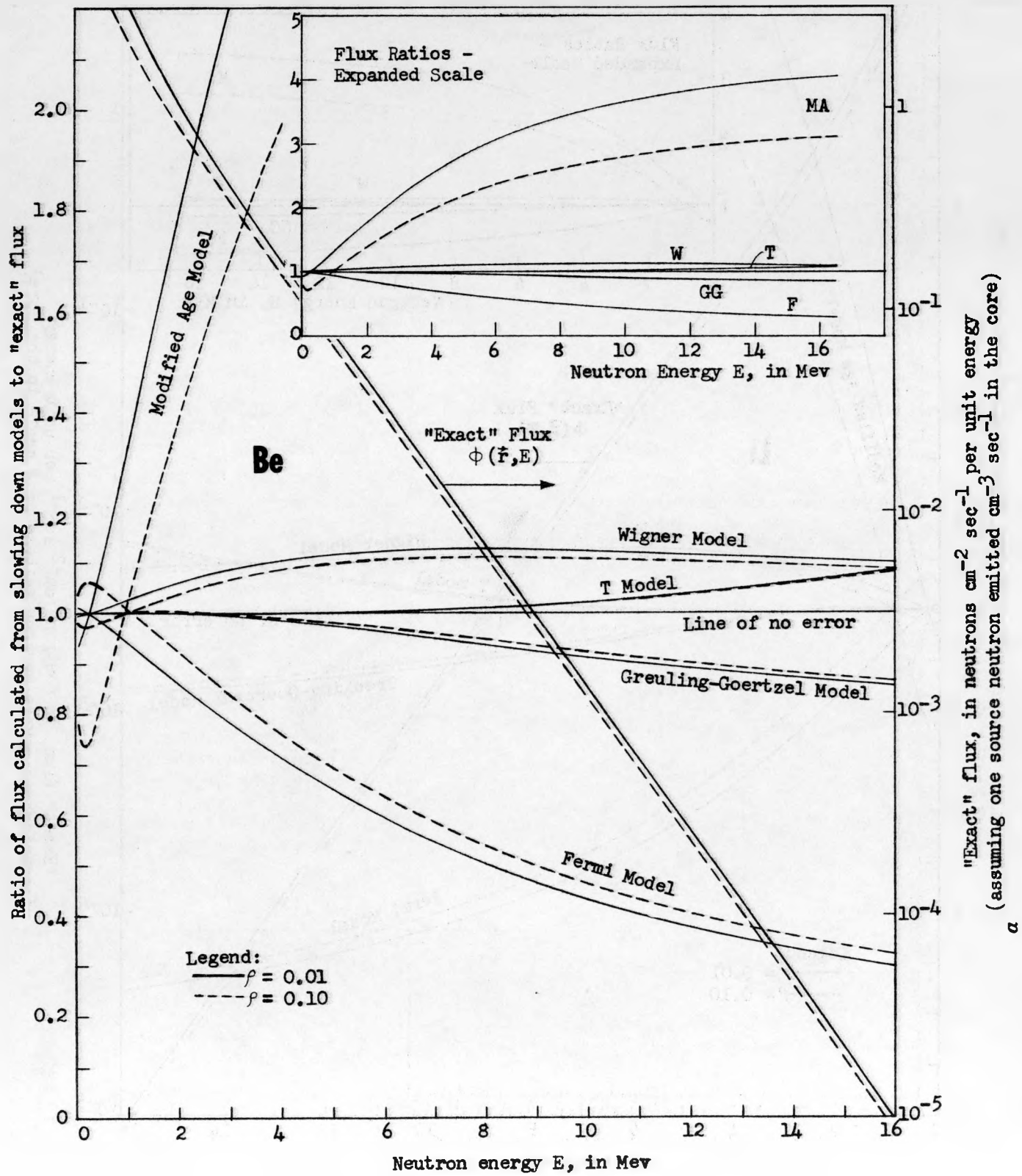

225

Figure 4

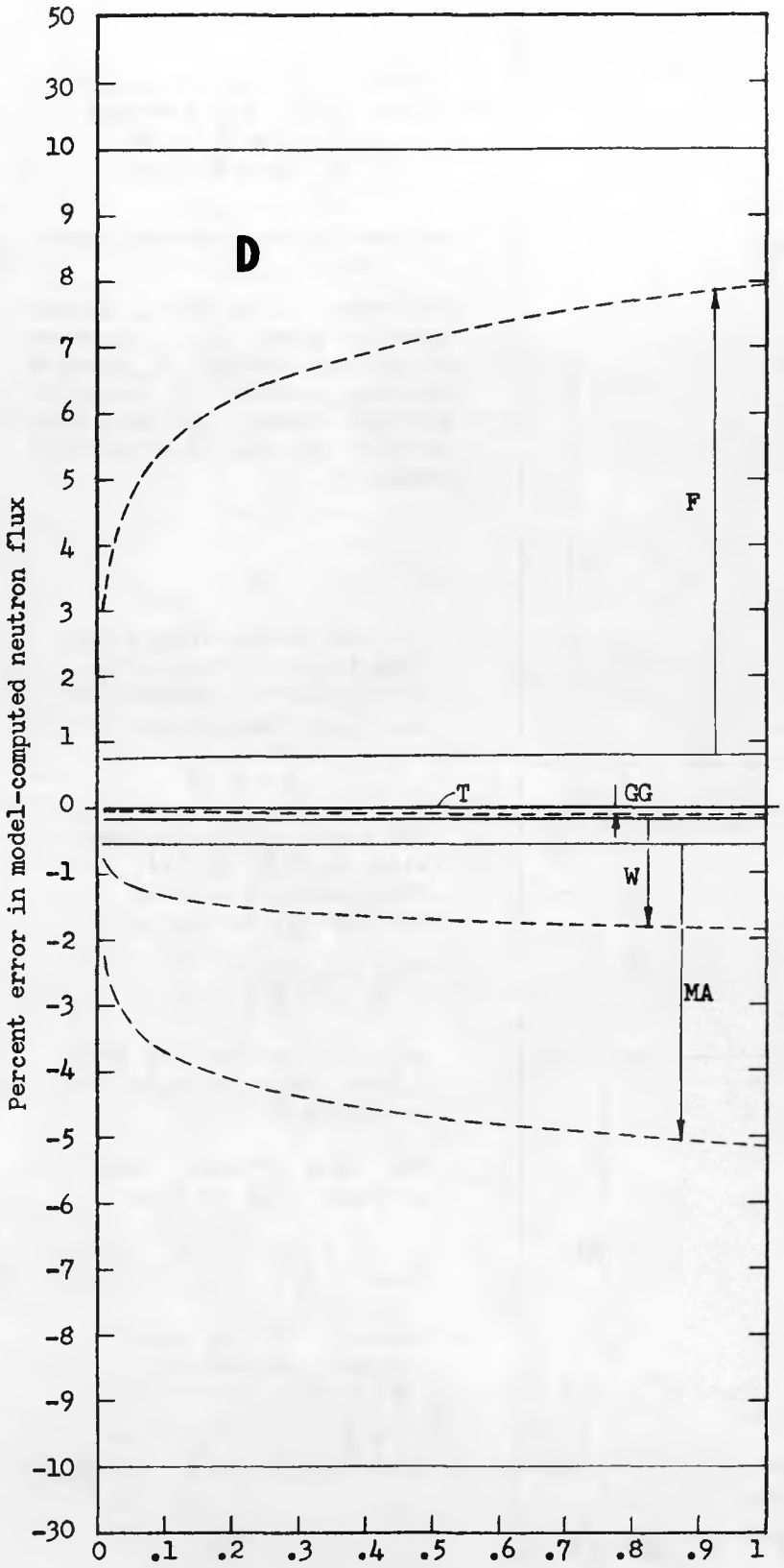

E/E_1 : Neutron energy in terms of prescribed energy (See explanation below title)

ACCURACY OF NEUTRON SLOWING DOWN MODELS FOR A REGION CONTAINING DEUTERIUM BUT NO FISSION SOURCE

The error in model-calculated flux is shown as a function of neutron energy E, given a certain number of neutrons per unit volume per unit time slowing down past a prescribed energy E_1.

For the graphs shown, the loss-to-scattering ratio $\rho \equiv \Sigma_L / \Sigma_s$ was assumed to have just two values:

—— $\rho = 0.01$

---- $\rho = 0.10$

The exact scattering density $\Sigma_s(\vec{r},E)\phi(\vec{r},E)$, for CMS-isotropic elastic scattering, varies as

$$\frac{1}{E_1}\frac{a}{\rho}\left(\frac{E_1}{E}\right)^{(1-\ )}$$

where a is obtained from a transcendental equation involving ρ.

The ratio of model flux to exact flux is then

$$\frac{a_m}{a}\left(\frac{E_1}{E}\right)^{(a\ -\ a_m)}$$

where a is the model computed parameter $(\rho/\xi)/(1 - \rho/\lambda)$.

Figure 5

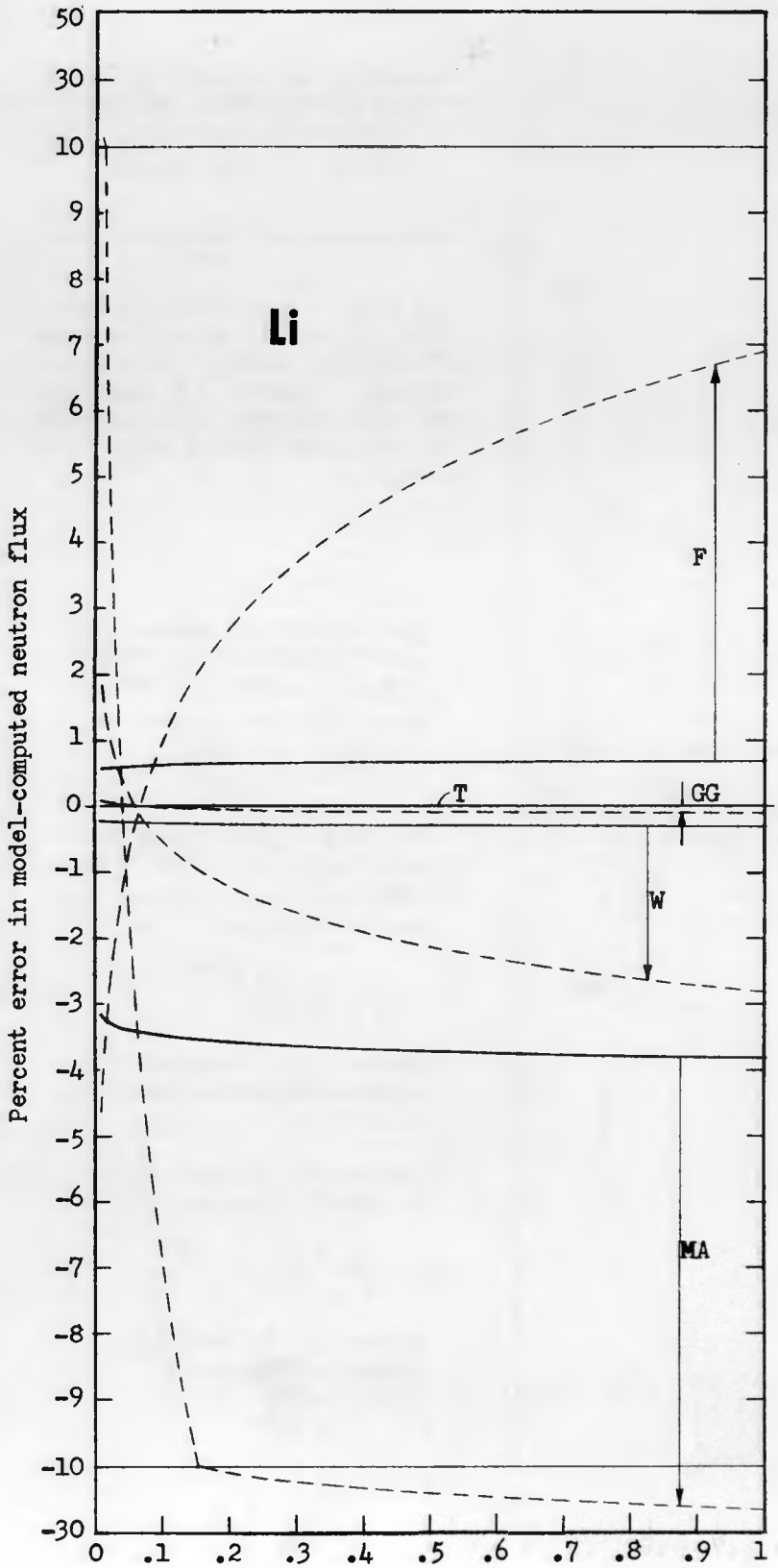

E/E_1 : Neutron energy in terms of prescribed energy (See explanation below title)

ACCURACY OF NEUTRON SLOWING DOWN MODELS FOR A REGION CONTAINING LITHIUM BUT NO FISSION SOURCE

The error in model-calculated flux is shown as a function of neutron energy E, given a certain number of neutrons per unit volume per unit time slowing down past a prescribed energy E_1.

For the graphs shown, the loss-to-scattering ratio $\rho \equiv \Sigma_L / \Sigma_s$ was assumed to have just two values:

—— $\rho = 0.01$

---- $\rho = 0.10$

The exact scattering density $\Sigma_s(\vec{r},E)\,\phi(\vec{r},E)$, for CMS-isotropic elastic scattering, varies as

$$\frac{1}{E_1}\,\frac{a}{\rho}\left(\frac{E_1}{E}\right)^{(1-a)}$$

where a is obtained from a transcendental equation involving ρ.

The ratio of model flux to exact flux is then

$$\frac{a_m}{a}\left(\frac{E_1}{E}\right)^{(a-a_m)}$$

where a is the model computed parameter $(\rho/\xi)/(1-\rho/\lambda)$.

227

Figure 6

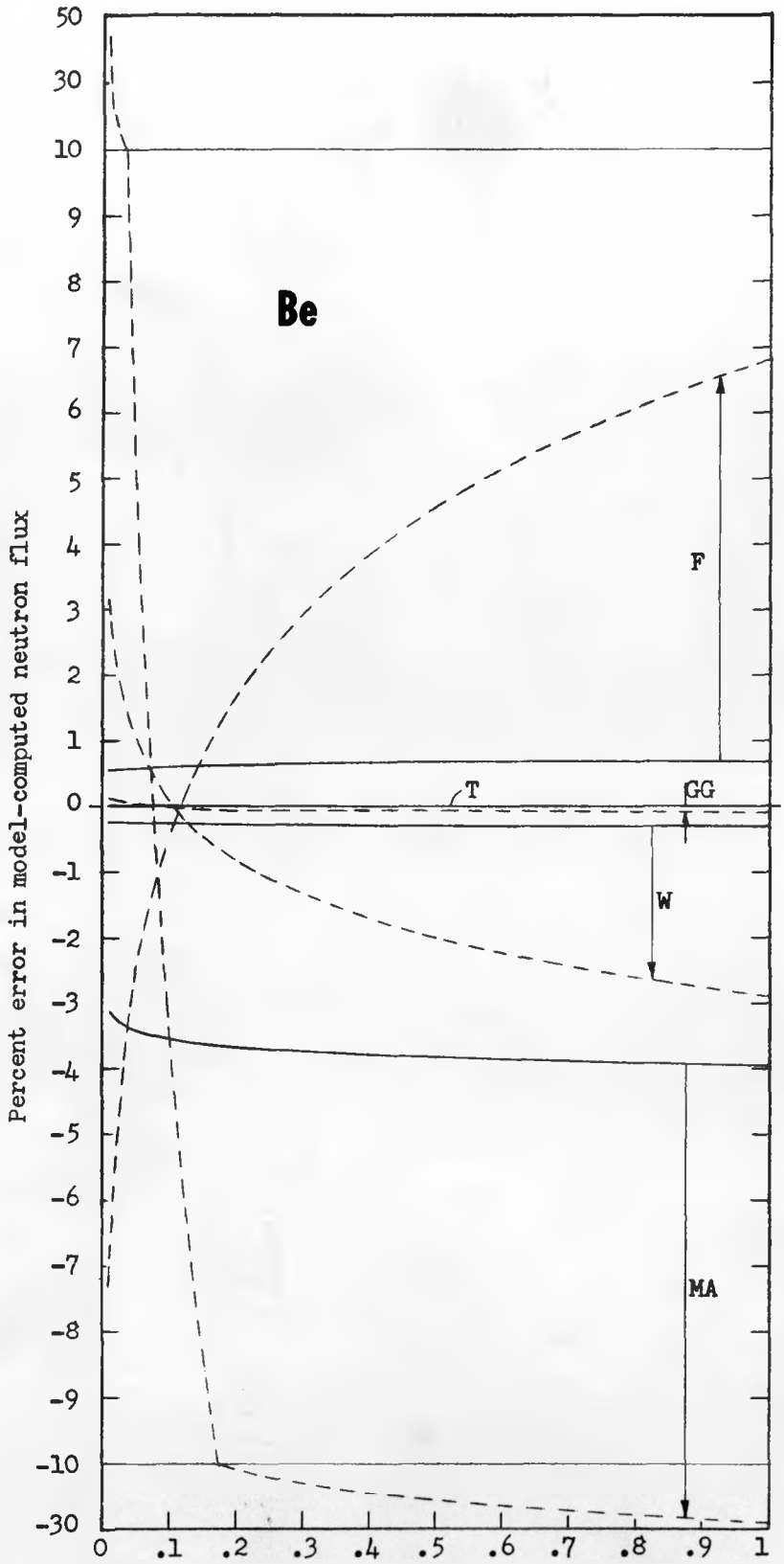

E/E_1 : Neutron energy in terms of prescribed energy (See explanation below title)

ACCURACY OF NEUTRON SLOWING DOWN MODELS FOR A REGION CONTAINING BERYLLIUM BUT NO FISSION SOURCE

The error in model-calculated flux is shown as a function of neutron energy E, given a certain number of neutrons per unit volume per unit time slowing down past a prescribed energy E_1.

For the graphs shown, the loss-to-scattering ratio $\rho \equiv \Sigma_L / \Sigma_s$ was assumed to have just two values:

—— $\rho = 0.01$

---- $\rho = 0.10$

The exact scattering density $\Sigma_s(\vec{r},E)\,\phi(\vec{r},E)$, for CMS-isotropic elastic scattering, varies as

$$\frac{1}{E_1}\,\frac{\alpha}{\rho}\left(\frac{E_1}{E}\right)^{(1-\alpha)}$$

where α is obtained from a transcendental equation involving ρ.

The ratio of model flux to exact flux is then

$$\frac{\alpha_M}{\alpha}\left(\frac{E_1}{E}\right)^{(\alpha - \alpha_M)}$$

where α is the model computed parameter $(\rho/\xi)/(1 - \rho/\lambda)$.